DISSERTATION

MULTI-SCALE & MULTI-RESOLUTION EXPERIMENTAL AND ANALYTICAL METHODS FOR MITIGATING BLAST RISK WITH BARRIER WALLS

Submitted by

Kellan M. Sullivan

Department of Mechanical Engineering

In partial fulfillment of requirements

For the Degree of Doctor of Philosophy

Colorado State University

Fort Collins, Colorado

Spring 2024

Doctoral Committee:

Advisor: Hussam Mahmoud
Co-Advisor: Christian Puttlitz

Benjamin Gadomski
Gaofeng Jia
Catherine Stephens
Genevieve Pezzola

ABSTRACT

MULTI-SCALE & MULTI-RESOLUTION EXPERIMENTAL AND ANALYTICAL METHODS FOR MITIGATING BLAST RISK WITH BARRIER WALLS

Over the last decade, interest in blast resistance and protection has increased as a result of the perpetual threat of terrorist groups around the world. In evaluating the Department of State (DOS) reports on terrorism since 2007, an estimated 330,000 fatalities and 430,000 injuries have been caused by terrorist attacks worldwide (2022). In the United States, various large scale explosive attacks have occurred over the years including the World Trade Center bombings in 1993, the Alfred Murrah Federal Building bombing in 1995, and the coordinated September 11th attacks in 2001. More recently, there has been a shift in the tactics of terrorist groups to use improvised explosive devices (IEDs) to target civilians due to regulations put in place after the September 11th, 2001, attacks that made it difficult for them to obtain a large amount of explosive material among other factors contributing the rise of terrorist activity. Attacks such as the Boston Marathon bombing in 2013 and the Madrid train bombing in 2004 demonstrate this shift in tactics. The upward trend of the use of IEDs around the globe since the September 11th, 2001, attacks presents a catalyst for a shift in research methods for blast mitigation techniques to provide protection to people rather than just structures. Therefore, developing methods to provide protection for people from blast effects is necessary to minimize the impact these terrorist groups have on our communities.

Of the existing blast mitigation strategies, perimeter walls or barriers are specifically advantageous in that they increase standoff distances and provide an obstacle to the propagation

path of the blast wave as well as primary fragmentation. The use of perimeter walls or barriers to protect structures has been well established in literature, however the use of barriers to protect people has not. The ability to predict airblast effects accurately and efficiently over a large variation in scaled ranges, within a complex environment, is important to characterize the potential severity of damage to structures and casualties among personnel in both military and civilian settings. Many different techniques have been used over the years to perform blast prediction of various airblast parameters such as pressure and impulse and blast resistant design research. While experimentation remains a valuable and powerful tool, in recent years, computational and numerical models have grown in popularity for their accurate evaluation capabilities. Advanced numerical software such as hydrocodes and computational fluid dynamic programs are often used to model airblast propagation and its impact on structures. However, in more complex environments, where blast loading in large areas of interest may occur, using high-fidelity computational modeling software could be inefficient due to the computing power required.

The goal of this dissertation was to develop a performance-based design framework for predicting the probability of survivability of a double-barrier system under blast loading, and the probability of different bodily injuries for personnel from the blast wave itself. In this dissertation, the gaps in research for protecting civilians from IED attacks in large open areas, understanding the impact of multiple barriers on the blast shockwave and pressures around the barriers, and investigating an absorption focused barrier were addressed. A combination of analytical, numerical, and experimental methods at multiple scales was used to develop and validate the various elements needed to conduct the performance-based design. This dissertation developed rapid computational models to predict the pressure field around a double-barrier system, analyzed a new barrier design that focuses on reducing the energy of the shockwave in order to protect

people, and accounted for the uncertainty and variability in multiple parameters to establish potential risk for various scenarios for both the barrier and for people.

The analyses combined numerical, analytical, and experimental methods at multiple scales, to create models to predict and assess the pressures associated with person-borne-improvised-explosive-devices (PBIEDS). The developed models used to predict and quantify the pressures around a rigid double-barrier system and the response of the wood barrier to blast loading were coupled with small- and full-scale experimental testing to validate and assess the accuracy and efficiency of the models. From the results of dissertation, it can be observed how the implementation of a double-barrier system can significantly reduce the pressures experienced around the barriers, which can lead to less potential for serious injury or damage from blast events. Additionally, it showed that the distance between the barriers plays a critical role in the pressures and therefore the potential for injury between the barriers. In addition, adopting an innovative approach to blast barrier design to consider the use of more lightweight, commonly available, non-rigid materials to increase the energy absorption to attenuate the blast shockwave rather than just reflect was proven to be beneficial.

ACKNOWLEDGEMENTS

I would first like to express my sincere gratitude and appreciation to my advisor, Dr. Hussam Mahmoud, for his guidance and support both academically and emotionally throughout the entirety of my Ph.D. studies. His technical guidance, encouragement, and patience always inspired and motivated me to overcome difficult times during my Ph.D. research. I am extremely fortunate to have him as my advisor and to have the opportunity to explore topics of interest with freedom and enthusiasm along with his support and guidance.

I would like to extend my gratitude and thanks to the rest of my PhD committee, Dr. Christian Puttlitz, Dr. Ben Gadomski, Dr. Gaofeng Jia, Dr. Catherine Stephens and Dr. Genevieve Pezzola for providing me with additional guidance, support, ideas, and critiques along the way. I am extremely thankful for the support and funding provided by Dr. Puttlitz and the Mechanical Engineering Department through assistantships. Dr. Puttlitz, thank you for always pushing me, believing in me, and providing me with the opportunity to explore my passions and go down a unique path. Additionally, I would like to thank Dr. Gadomski, you inspired me to pursue a Ph.D. so thank you for always believing in me and challenging me to be better.

Next, I would like to acknowledge the financial support of the Engineer Research and Development Center (ERDC) for the US Army Corps of Engineers. This support is greatly appreciated. I would also like to thank my coworkers in the Survivability Engineering Branch at ERDC including Dr. Jesse Sherburn, Mr. John Hoemann, Mr. Daniel Rios-Estremera, Mr. Billy Bullock, Mr. Dave Senior, Mr. Omar Flores, all the field technicians that helped during my experiments and so many more. I look forward to working with all of you.

Finally, I want to extend my thanks and appreciation to my family and friends. To my grandparents, Monty and Glenrose, for their support and love. I always appreciated you checking in on me and how things were going. My brother, Hunter, and my sister-in-law Karly, thank you for always cheering me on and making me smile. To my friends Izzy, Ben, Noel, and Mikayla thank you for listening to me for the last few years and for always pushing me on when things were tough. I could not have done it without you all!

DEDICATION

Dedicated first to God. Without You, I would never have had the opportunities or the strength to accomplish this.

Proverbs 16:3 & 1 Corinthians 10:31

Dedicated also to my parents, Brian, and Monique, for their unwavering support, faith, and love. Without you both I would not be where I am today. Thank you for everything-I love you so much!

TABLE OF CONTENTS

LIST OF TABLES

LIST OF FIGURES

CHAPTER 1 INTRODUCTION

1.1 Statement of the Problem

Terrorist groups around the world continually threaten the United States and nations across the globe. In evaluating the Department of State (DOS) reports on terrorism since 2007, an estimated 330,000 fatalities and 430,000 injuries have been caused by terrorist attacks worldwide (DOS, 2022). In the United States, various large scale attacks have occurred over the years including the World Trade Center bombings in 1993, the Alfred Murrah Federal Building bombing in 1995 (Figure 1-1a) and the coordinated September 11th , 2001 attacks (Figure 1-1b).

a) **b)**

Figure 1-1: a) Aftermath of Oklahoma City Murrah Federal Building Bombing in 1995 (Associated Press, 2022) and b) World Trade Center North and South Towers during the September 11th, 2001 attacks (ABC News, 2021).

Recently, there has been a shift in the tactics of terrorist groups to use improvised explosive devices (IEDs) to target civilians due to many different factors including more complex terrorist organizations, lone-wolf extremist attacks, and regulations put in place after the September 11 attacks that made it difficult for them to obtain a large amount of explosive material. Worldwide,

between 2010 and 2020, the use of IEDs has increased to accounting for more than 42% of all recorded explosive attacks (United Nations, 2020). These attacks resulted in over 170,000 casualties with civilians making up 80% of those harmed in IED attacks (United Nations, 2020). The Boston Marathon bombing in 2013 is a prime example of how terrorists have switched to targeting civilians and large groups of people. Figure 1-2 shows an example of a large population gathering at Michigan Stadium where multiple barriers could be used to control the movement of spectators and funneling of people to different areas for which this analysis is applicable.

Figure 1-2: Security checkpoint for Michigan Stadium (Arnold, 2010).

While concerns of direct losses, such as infrastructure damage and mass casualties, from such events have gained substantial interest, the indirect social and economic effects add to the burden and impact of these events. For example, after the September 11th, 2001, attacks, air travel and security were changed worldwide to provide new security measures such as taking shoes off at the airport and going through security checks at sporting events which are now common security measures. Today, around $9.3 billion is spent on the Transportation and Security Administration (TSA) every year (DHS, 2023). Due to this transition in attack strategies, existing protection

techniques and research topics may not provide the best approach for protecting civilians from explosive attacks.

Over the last decade, interest in blast resistance and protection for civil and critical infrastructure has increased as a result of the perpetual threat of terrorist groups. As large buildings have been the target of many of the explosive terrorist attacks, previously conducted research has focused mainly on protecting and designing structures to be more blast resistant and reduce damage through testing of different building design modifications and protection methods (Stewart & Netherton, 2008; Gebbeken & Döge, 2010; Lee & O 'Toole, 2014; Zhu & Khanna, 2016b, 2016a; Xiao et al., 2017; Pezzola, 2018; Khan et al., 2019; Taha et al., 2019). Retrofitting, utilization of advanced materials, geometric manipulation, and implementation of barrier systems, are the main strategies used to protect structures and people from blast loading. Of the different strategies, many are not economically feasible to be utilized in civilian settings due to social and financial costs.

Of the existing strategies to protect structures from blast loading, perimeter walls and barriers, are specifically advantageous in that they increase standoff distances and provide an obstacle to the propagation path of the blast wave as well as primary fragmentation. Common types of barriers include soil or rock-filled baskets and reinforced concrete walls which have many different configurations including the T-walls, H-walls, and Alaska barriers. Literature on the effectiveness of barriers in mitigating the effects of blast waves on structures has been well published and researched in a variety of settings (Beyer, 1986; Bahei-El-Din & Dvorak, 2008; Belegundu & Rajan, 2008; Dharmasena et al., 2008; Goel & Matsagar, 2014; Xiao et al., 2017; Taha et al., 2019). Many different tools such as numerical finite element analysis (FEA), shown in Figure 1-3a), have been used to assess the effectiveness of different types of barriers. Other studies

included experimental testing to evaluate the impact changes in the material and the geometry of a barrier can have on making the barrier more effective as shown in Figure 1-3b) (Hussein, 2019; Hussein et al., 2020).

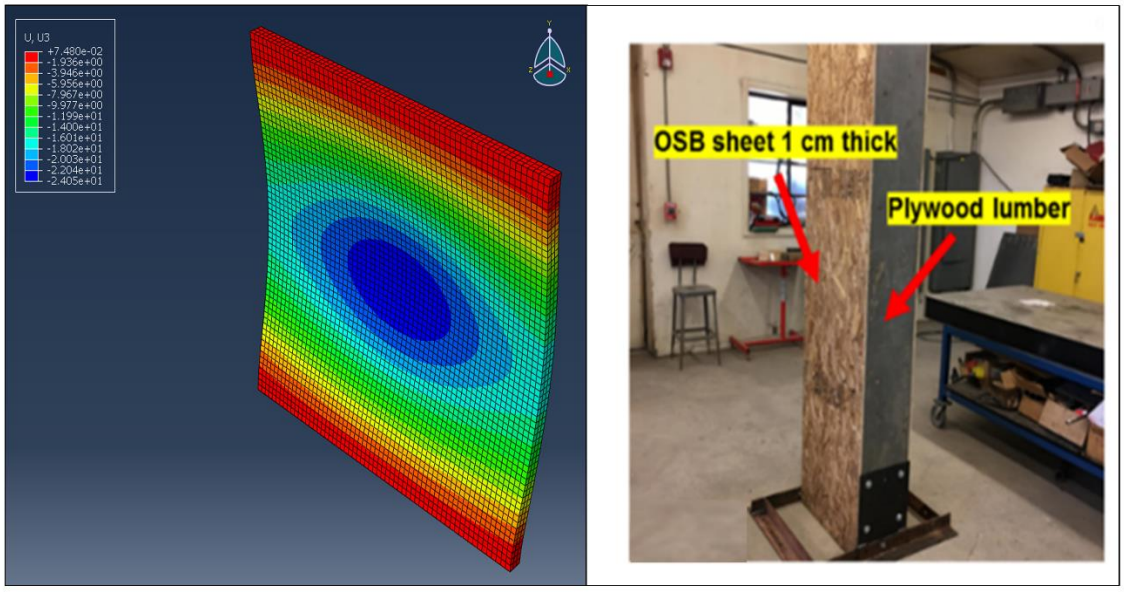

a) **b)**

Figure 1-3: a) Finite element analysis of steel wall in ABAQUS and b) Experimental blast test set up for a composite wall (Hussein, 2019; Hussein et al., 2020).

This dissertation addresses gaps in existing research on protecting people from explosive events in large areas using multiple barriers. The goal is to establish a performance-based design framework that combines analytical, numerical, and experimental methods to assess the performance of a double-barrier system and the potential for human injuries while accounting for various uncertainties in the assessment parameters.

A numerical model was developed to predict the pressure fields from person-borne-improvised-explosive-devices (PBIEDS) around a double-barrier system in open areas in which large crowds are present and where people are compartmentalized in order to control the crowds. The validity of the pressure predictions and blast wave parameters are assessed through small-

scale experimentation. Pressure predictions from the numerical model were used to train an artificial neural network (ANN) to allow for more computationally efficient predictions of the blast loads around a double-barrier system for a variety of blast loading environments. A barrier design to protect people and absorb the shockwave was then assessed using a finite element model of a barrier to determine for what scenarios it met the assumptions of the ANN. To evaluate the validity and accuracy of the developed finite element model, both the pressure predictions and the barrier design were evaluated using full-scale experimentation. Finally, the developed components were combined to achieve the overall object of the study of conducting performance-based design where probabilistic analysis and development of fragility and damage criteria of both the blast barriers and personnel located in the blast vicinity was completed. That analysis could provide a design spectrum to potentially be utilized in event set up to protect and deter potential terrorist threats.

1.2 Objectives and Scope of Research

The vast majority of blast mitigation and protection research mainly focuses on protecting structures and infrastructure either through structural modification and design or through the implementation of a blast barrier or perimeter wall. Techniques such a retrofitting, material manipulation, and geometrical manipulation of the structure are examples of modifications that are used to design a structure to be more blast resistant (Goel & Matsagar, 2014b; Pezzola, 2018; Trasborg, 2014). Commonly used perimeter barriers such as Alaska barriers and T-walls are large, robust, and immobile which is not ideal for use in public settings due to the restrictions and costs they impose on the public.

Providing protection to people from an explosive attack is not the same as providing protection to structures. The human body does have a relatively high tolerance to pressure that

varies with magnitude and duration of exposure to the wave, but this pressure wave can still cause significant damage to the body in the form of primary injuries (DOD, 2008). The best way to prevent injury would be to implement a barrier to increase the standoff distance from the charge as well as it provides an obstacle in the path of the blast wave. However, current barriers can significantly amplify the blast pressure as it reflects off the surface of the barrier causing further damage to the human body (DOD, 2008).

Current blast mitigation research does not explore providing protection to people in large open areas where a single barrier would not be sufficient to guide the movement of a large population group and provide protection against a PBIED level threat in places such as sporting arenas, security checkpoints, and political events where people are compartmentalized or funneled between barriers or walls for crowd control. Understanding how the blast wave moves around multiple barriers and how the blast wave could cause human injuries is critical for public safety. Additionally, current barrier styles are not ideal for protecting the human body due to their size and amplification of the blast pressure they cause as a result of the shockwave reflecting off the surface of the barrier (DOD, 2008).

To address these gaps in existing literature, a comprehensive framework for predicting blast loads and their impact on people in large urban areas against blast attacks was developed in this dissertation. The main objective is to conduct performance-based design to predict the probability of survivability of a barrier to blast loading and the probability of injury from the blast wave itself.

This dissertation includes the development of a numerical hydrocode model of a double-barrier system to predict the pressures in front, between, and behind the barriers for various blast loading scenarios. Small-scale experimental tabletop testing was conducted to validate the pressure

predictions of the hydrocodes and establish an efficient, cost-effective, and repeatable testing method for predicting airblast parameters. Artificial intelligence in the form of an ANN model was trained from the hydrocode numerical model predictions to capture the blast wave propagation and peak pressures around a double-barrier system. However, in the hydrocode dataset used to train the ANN and therefore in the corresponding ANN predictions, it is assumed the barriers are rigid and remain intact during the blast event. It is therefore important to validate such an assumption using finite element models (FEM) and explosive testing for a barrier designed to protect people and focus on absorption of the shockwave. In this study, FEM was utilized to allow for investigation of the localized behavior of a barrier system and its failure mechanisms for large scale blast events. Full-scale experimental testing was used to validate the response of the barrier tested in the FEM model. Finally, probabilistic analysis and performance-based design was conducted to obtain damage criteria for barriers and for people from the results of the ANN and the FEM. Through utilization of a single-degree-of-freedom model scaled to the barrier characteristics determined in the FEM and field experiments, fragility, and damage for different intensities of blast loading on the barriers will be established. Thresholds for different blast injuries was used to assess the pressure predictions from the ANN and the results of the damage analysis of the barrier. The different elements of the framework, including numerical methods, experimental methods, and design implications are illustrated in Figure 1-4.

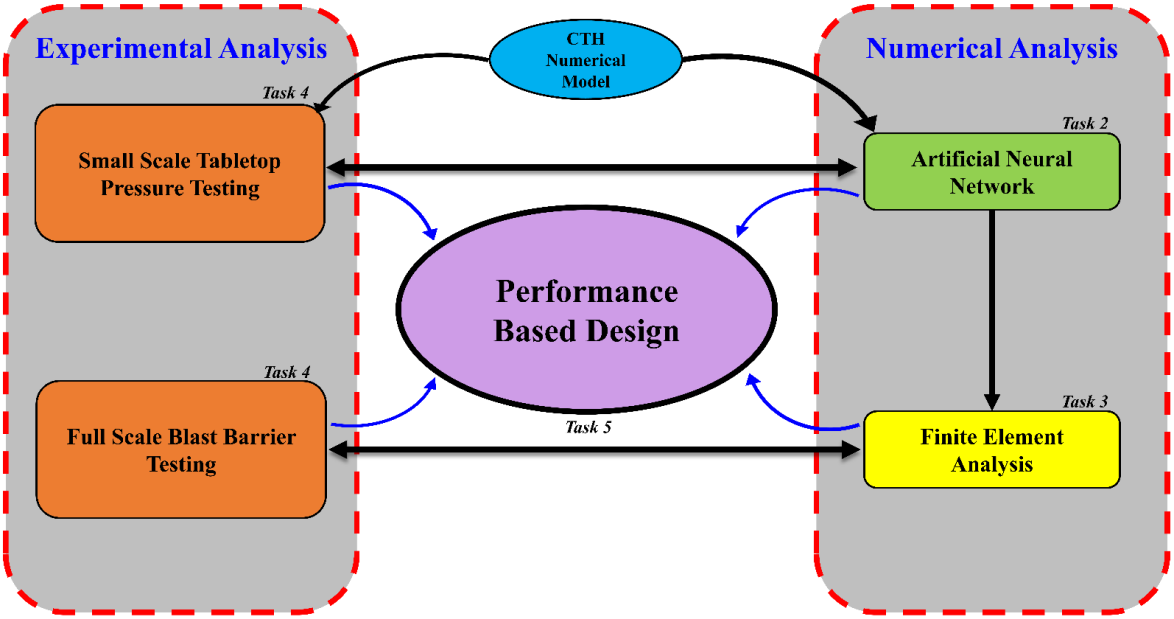

Figure 1-4: Framework for the blast mitigation design for human protection.

The above objectives require the following tasks and subtasks to be accomplished:

- Task 1: Conduct Comprehensive Literature Review
  - Explore the characteristics of an explosive hazard.
  - Acquire knowledge of neural networks and the use of neural networks in blast analysis.
  - Analyze current blast mitigation techniques for structures and people.
  - Develop understanding of explosive effects on human bystanders.

- Task 2: Establish Neural Network with Barriers for Blast Analysis
  - Conduct simulations to predict pressure in large areas with various positions of a cluster of barriers using hydrocode.
  - Develop, train, and test, a neural network from hydrocode simulations to predict pressure-histories in the vicinities of the barriers in open areas.
  - Validate the output of the neural network against high resolution hydrocode models.

- Task 3: Configure and Investigate Barrier for Blast Mitigation
  - Develop barrier design that is mobile and aesthetically appealing.
  - Develop finite element model for the barrier design.
  - Perform response, failure, and slipping and tipping analyses on barrier design using FEA to finalize wall design.

- Task 4: Validate Blast and Barrier Damage Models Using Field Experiments
  - Conduct field experiments to verify results of the FEA.
  - Conduct tabletop scaled experiments to verify results of the ANN.
  - Establish a procedure for small-scale tabletop testing for blast analysis problems.

- Task 5: Risk Analysis and Optimization for Minimal Barrier Damage and Injury Levels
  - Conduct simulations utilizing neural network to test a variety of barrier network scenarios.
  - Utilize performance-based assessment to analyze the effectiveness of different barrier networks.
  - Develop fragility curves for a variety of variables pertaining to the barrier network and human survivability. (i.e., standoff distance, charge weight, etc.).
  - Use the developed neural network with FEA to establish optimal barrier clustering configuration for specific blast scenarios and injury levels.

1.3 Organization of Dissertation

The dissertation is outlined in eight chapters to address the main objective along with the specific objectives of each component according to the highlighted scope. Chapter one introduces the motivations, problem statement and the objective of the research. Chapter two provides the background and literature review in reference to the topics within this dissertation. The chapter starts by providing an overview of blast loading characteristics. That is followed by a discussion on the basics of artificial neural networks in a general sense as well as in the context of blast loading. From there the effects of blast loading on structures and on people is summarized. At the end of chapter two, the current blast mitigation techniques for protecting people and structures are discussed.

In chapter three, small-scale tabletop testing is presented. The objective of the tests is to understand the behavior of the shockwave as it interacts with multiple barriers and establish a new method of performing blast testing. A double-barrier system is scaled down to fit on the tabletop

surface to assess the blast parameters of pressure and impulse. Pressure time histories are recorded for the experiments to validate the pressure predictions made by the hydrocode simulations with the same set up. Additionally, a new small-scale testing technique and procedure were developed as a part of this testing.

Chapter four presents the development and testing of the artificial neural network for blast prediction around the double-barrier system. The objective of ANN development is utilizing machine learning for rapid prediction to allow for more efficient predictions of important blast parameters. The hydrocode simulations, validated with the testing in chapter three, were used to build a numerical dataset used to train the neural network. The simulation environment along with the modeling techniques are presented. An overview of the basics of ANNs and training are discussed before the development of the ANN used in this study. The dataset developed in chapter three using the hydrocode simulations was utilized to train the ANN. A variety of model parameters were explored to determine optimal parameters such as training algorithm, number of layers, and number of nodes in each layer. The final ANN is presented and evaluated as well.

The objective of chapter five and six are to investigate the application of an absorption focused barrier and its effectiveness for PBIED threats. Chapter five concentrates on the finite element model of the blast barrier. The ANN in chapter four assumes the barriers in the double-barrier system remain rigid and fixed. To validate this assumption and assess the application of the barrier on the field, a model was created to assess the response of a barrier to various blast scenarios. A non-rigid, wood-sand sandwich style barrier was developed and presented. The results of the FEM analysis were used to determine at testing matrix for full-scale experimental barrier

testing in chapter six and provided structural properties necessary to complete the performance-based design in chapter seven.

Chapter six pertains to conducting full-scale experimental testing of the wood barrier designed in chapter five with the FEM analysis to meet the combined objective between chapters fix and six. Specifically, pressure time history and displacement magnitudes were recorded as part of the testing to assess the response of the barrier and the accuracy of numerical pressure predictions. The results of the testing are compared to the FEM results in chapter five to assess how accurate the model was in predicting the response of the wood barrier subjected to blast loading.

Finally in chapter seven, the overall main objective of conducting the performance-based design was completed. First, probabilistic analysis is used to evaluate the performance of the wood barrier subjected to blast loading. A single degree of freedom (SDOF) model is developed and scaled to match the results of the FEM from chapter five and the response of the barrier in chapter six. The ANN from chapter four is used to predict peak pressure on the wall. Second, predictions for human injury in the form of primary blast injury is conducted using probabilistic analysis as well. Fragility curves for the survivability of the barrier and the injury potential are presented for a variety of blast events.

Chapter eight provides a summary of the research done in this dissertation highlighting the most important findings of the study. Design recommendations and the contribution of this

research to the field of blast mitigation prediction and protection is emphasized. Finally, future research recommendations and requirements on related topics is presented.

CHAPTER 2: BACKGROUND AND LITERATURE REVIEW

2.1 Introduction

This chapter provides a comprehensive literature review of blast loading characteristics, basics of neural networks, the effects of explosive attacks on structures and human bystanders, and blast mitigation techniques. Blast loading characteristics including blast wave formation, blast wave behavior in different environments and blast modeling codes and standards are presented first. Then, information on the basics of neural networks is presented in a general sense as well as in the context of blast loading. Additionally, the effects of blast loading on structures including the wave-wave and wave-surface interaction are explained further. The effects of the blast wave on humans are presented here as well. Finally, a literature review of the current blast mitigation techniques for people and structures is discussed.

2.2 Explosive Threats and Motivations

Throughout human history, terrorism has been experienced around the world driven by a variety of goals including publicity, sympathy, monetary reward, religious motivations, or political gain (Dusenberry, 2010). Explosives are a preferred weapon of choice as they are highly destructive, relatively easy to obtain and fabricate, as many of the ingredients are readily available at most farm and hardware stores, and they can be rather mobile (DHS, 2006, 2021). Conventional weapons are those that cause significant damage to life and property, but not on the same scale as nuclear, chemical, and biological weapons. Nuclear, chemical, and biological weapons are known for large scale mass destruction (Lahiri & Ho, 2011). Specifically, the use of improvised explosive

devices (IEDs) has been on an upward trend around the globe in frequency and magnitude since the September 11th, 2001, attacks. An IED is a "homemade" bomb or explosive device and consists of many components that include an initiator, switch, main charge, power source and a container (DHS, 2021). They typically include projectile material or "enhancements" including nails, glass, and metal fragments (DHS, 2021).

Explosive materials are typically classified into two categories: high explosives and low explosives. High explosives (HE) are "condensed" explosives that create shockwaves when they are detonated. HEs are classified further based on how sensitive to initiation they are. Primary explosives are easier to detonate from a spark or impact (Cormie et al., 2019; Pezzola, 2018). Secondary explosives are less sensitive and harder to detonate than primary explosives (Cormie et al., 2019; Pezzola, 2018). Tertiary explosives are a combination of explosive compounds and are usually cheaper than military grade explosives (Cormie et al., 2019). Low explosives (LE) deflagrate, or burn rapidly, to produce a pressure pulse with a smaller amplitude and longer duration than HE (Cormie et al., 2019; Pezzola, 2018). Examples of HE and LE are summarized in Table 2-1.

Table 2-1: Examples of HE and LE (Cormie et al., 2019)

Type of Explosive	Classification	Examples	Known IED Use
High Explosives	Primary	Lead azide, mercury fulminate	-
	Secondary	Dynamite, TNT, Semtex, RDX, C-4	Irish Republican Army Bombings
	Tertiary	Ammonium Nitrate and Fuel Oil (ANFO)	Oklahoma City Bombing 1995
Low Explosives	-	Smokeless powder, propellants (black powder), pyrotechnics	Olympic Park Bombings 1996

Due to the regulations and controls instituted on what one can buy and who can buy dangerous material, terrorists have manufactured their own home-made explosive (HME), from widely available chemicals such as fertilizer and hydrogen peroxide (Cormie et al., 2019). In large quantities, HME detonates and behaves similar to HE (Cormie et al., 2019). The damage caused by an IED can range drastically depending on the attack scenario. The explosive's size, construction, location, and type of explosive material all influence the impact it can inflict (DHS, 2021). Table 2-2 lists common IED devices and their typical explosive mass.

Table 2-2: Common IED Explosive Threats and Safe Evacuation Distances *modified from:* (DHS, 2006).

Threat Description		Explosive Mass (TNT Equivalent)
	Pipe Bomb	5lbs 2.3kg
	Suicide Belt	10lbs 4.5kg
	Suicide Vest	20lbs 9kg
	Briefcase/Suitcase Bomb	50lbs 23kg
	Sedan	1,000lbs 454kg
	Passenger/Cargo Van	4,000lbs 1,814kg
	Small Moving Van/Delivery Truck	10,000lbs 4,536kg
	Semi-Trailer	60,000lbs 27,216kg

IEDs transported inside vehicles such as cars, trucks, vans, trains, and airplanes, are known as vehicle-borne improvised explosive devices (VBIEDs). VBIEDs tend to have large amounts of explosives and can cause catastrophic mass-casualty events. Person-borne improvised explosive devices (PBIEDs) such as suicide vests or suitcases are usually less powerful than VBIEDs but could be more deadly as they can be detonated very close to the intended targets (Cormie et al., 2019; DHS, 2006)). The Madrid commuter attacks in 2004 and the Boston Marathon Bombing in 2013 are two examples of the level of casualties PBIEDs attacks can inflict.

2.3 Blast Loading Characteristics

2.3.1 Blast Wave Formation

When an explosion occurs, a rapid release of energy takes place. A powerful expansion of the gaseous products of the explosive (detonation products) occurs, and the surrounding air is forced out of the occupied volume. As a result of this expansion, the surrounding air is compressed creating a shock wave or blast wave. This blast wave propagates radially outwards, decreasing in pressure as it travels from the center of the explosion. A negative phase is created from the over-expansion of the gas, due to the momentum of the gas, resulting in the pressure near the end of the blast wave falling below normal atmospheric pressure (Bueno et al., 2018; Cormie et al., 2019). This creates suction resulting in the air moving back toward the explosion center. Eventually the flow reaches equilibrium where the pressures reach normal atmospheric pressure (Bueno et al., 2018; Cormie et al., 2019). The impact of the negative phase is dependent on the scenario and size of the explosive but for smaller charges the negative phase of the blast wave is negligible as its effects are much smaller in comparison with the positive phase (Goel, 2015). The shape of an ideal

blast wave due to an explosion in free air is presented in Figure 2-1 where the wave instantaneously reaches a peak overpressure (P_{so}) and quickly decays back to ambient pressure (P_o). The time of arrival of the blast wave is denoted as t_a, the duration of the positive phase is t_o, the duration of the negative phase of the blast wave is t_o^-, the area under the positive region of the curve is the peak positive impulse i_s, and the area under the negative region of the curve is peak negative impulse is i_s^-. The blast wave in free air is described by the Friedlander's equation as shown in Equation 2.1 (Friedlander, 1946).

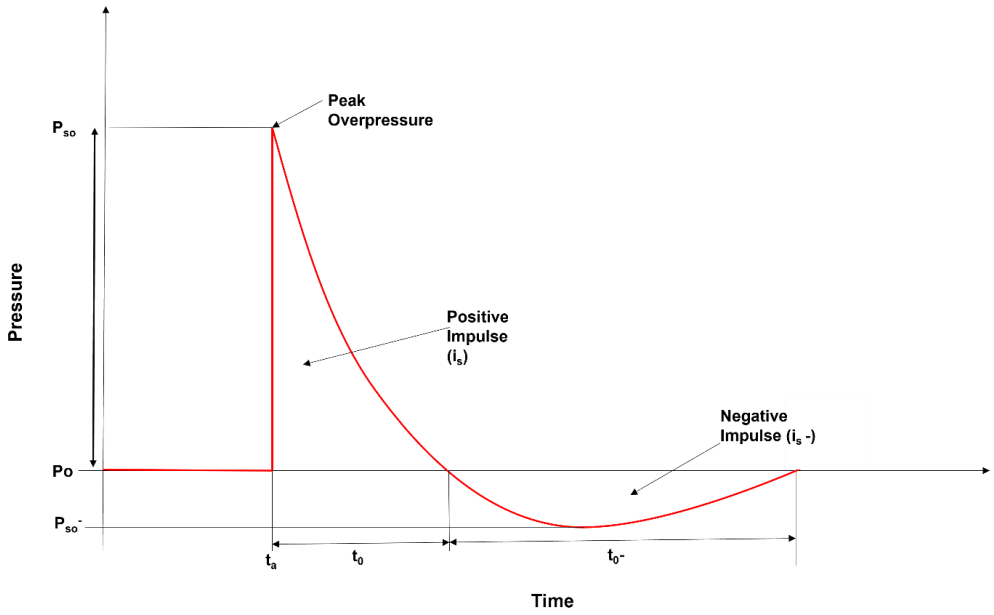

Figure 2-1: Typical graphic for a blast wave pressure-time history in free air.

$$P(t) = P_{so}\left(1 - \frac{t}{t_0}\right)e^{\left[-b\frac{t}{t_0}\right]} \tag{2.1}$$

Where b is a decay coefficient and t is time, which starts at the arrival of the pressure where $t = t_a$.

2.3.2 Blast Wave Behavior in Open versus Confined Spaces

The blast wave characteristics depend on the size, shape, and explosive material inside the explosive itself and can be affected by the surrounding environment, wave-wave, and wave-structure interactions. There are two main types of blast environments: unconfined and confined. Unconfined explosions are classified into three types: free air burst, air burst and surface burst (DOD, 2008). Confined explosions are classified into three types as well: fully confined, fully vented, and partially vented (DOD, 2008). Unconfined and confined explosions can be subdivided based on the blast loading produced. These blast loading categories are summarized in Table 2-3 (DOD, 2008).

Table 2-3: Blast Loading Characteristics for Different Environments (DOD, 2008)

Charge Confinement	Category	Pressure Loads
Unconfined Explosions	1. Free Air Burst 2. Air Burst 3. Surface Burst	a. Unreflected b. Reflected
Confined Explosions	4. Fully Vented	c. Internal Shock d. Leakage
	5. Partially Confined	c. Internal Shock e. Internal Gas d. Leakage
	6. Fully Confined	c. Internal Shock e. Internal Gas

The blast loading characteristics summarized in the table are described further below.

Unconfined Explosions-

Free Air Burst- free air burst explosions occur at a point high above the ground surface (DOD, 2008). In this type of explosion, the shock wave propagates away from the center of the detonation without any intermediate amplification of the wave before striking a structure (DOD, 2008). If the free air blast is in an open field with no structures to strike, the pressure load will be unreflected and will behave as described above in Figure 2-1. If the free air blast hits a structure, the pressure

and impulse of the wave are amplified by the reflection of the blast wave on the structure as illustrated in Figure 2-2. The structure is then loaded by the reflected pressures and impulse, not the incident pressure and impulse.

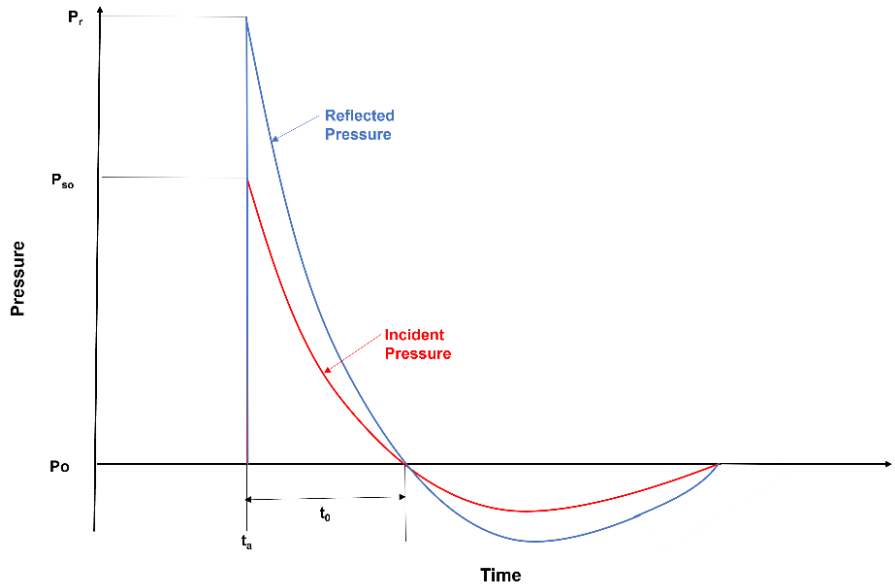

Figure 2-2: Typical reflected pressure-time history compared to incident pressure-time history.

The peak pressure and impulse of both the incident and reflected blast waves for a free air blast vary based on the distance from the center of the explosive to the point of interest, size of the charge, and the type of explosive material being used (DOD, 2008). Figure 2-3 shows the positive phase properties for a spherical charge at sea level in free air in terms of the scaled distance *Z* and TNT equivalent weight of the charge *W* from the Unified Facilities Criteria (UFC) 3-340-02 manual. The UFC 3-340-02 is a manual overseen by the United States Army Corps of Engineers (USACE) and Department of Defense (DOD). It was developed to present methods of design for protective construction used in facilities for development, testing, production, storage, maintenance modification, inspection, demilitarization, and disposal of explosive materials (DOD, 2008). The UFC 3-340-02 provides methods for establishing blast load parameters and for

calculating dynamic response of structural elements to a variety of explosions (DOD, 2008). The scaled distance Z is commonly used to report blast parameters as defined in Equation 2.2

$$Z = \frac{R}{\sqrt[3]{W}} \tag{2.2}$$

Where R is the distance from the center of the explosive to the point of interest in either feet (imperial units) or meters (metric units), and W is the equivalent TNT weight of the charge in pounds-force (imperial units) or kilograms (metric units).

The TNT conversion factors for different materials are defined based off the explosive material's specific energy and TNT's specific energy as defined in Equation 2.3. The specific energies and TNT equivalent conversion factors of the more commonly used explosive materials are listed in Table 2-4.

$$W_{EFF} = \frac{Q_E}{Q_{TNT}} W_E \tag{2.3}$$

Where W_{EFF} is the effective charge weight, W_E is the weight of the explosive in use, Q_{TNT} is the mass specific energy of TNT and Q_E is the mass specific energy of the explosive in use.

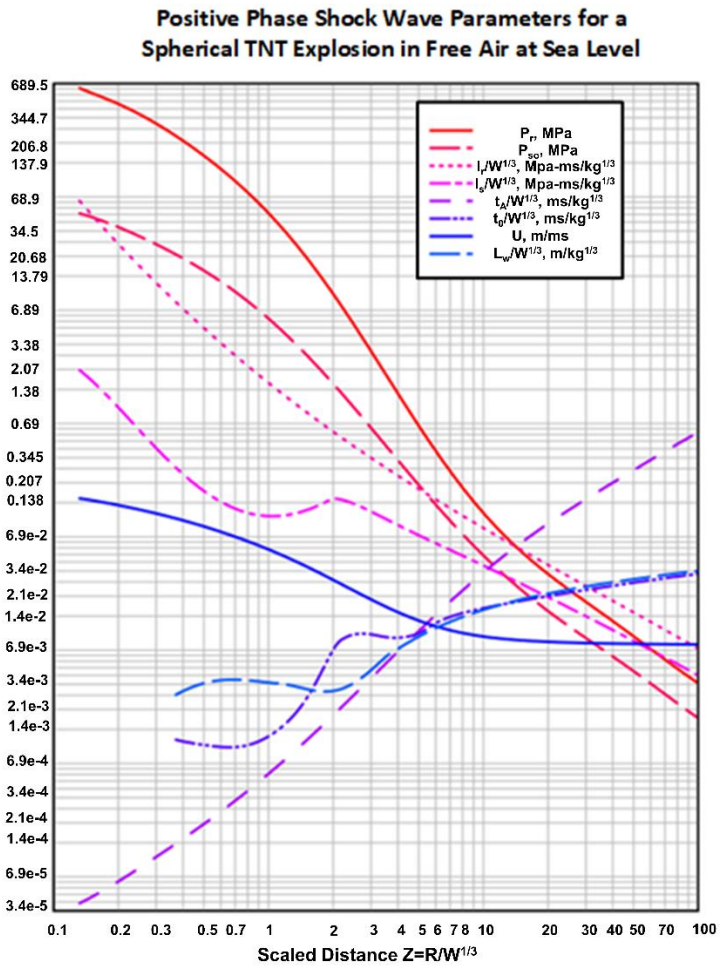

Figure 2-3: Blast wave parameters versus the scaled distance for the positive phase of spherical free air detonation of TNT *modified from:* (DOD, 2008).

Table 2-4: Conversion factors for common explosives (Cormie et al., 2019)

Explosive	Mass Specific Energy [kJ/kg]	TNT Equivalent
Nitroglycerin (liquid)	6,700	1.481
C4 (91% RDX)	-	1.19-1.37
HMX	5,680	1.256
Semtex	5,660	1.250
RDX (cyclonite)	5,360	1.185
Composition B (60% RDX 40% TNT)	5,190	1.148
TNT	4,520	1.000
Blasting gelatin	4,520	1.000
ANFO (94% ammonium nitrate, 6% fuel oil)	3,932	0.870
60% nitroglycerin dynamite	2,710	0.600

Air Burst- in an air burst explosion, the point of detonation is located at a distance above the ground, such that the ground reflections from the blast wave will occur before the incident blast wave arrives at the structure of interest (DOD, 2008). The incident wave combines with the ground reflections to form a "Mach Front" as shown in Figure 2-4 (DOD, 2008). Further discussion of the Mach front and reflection amplification is continued in section 2.4.1 below.

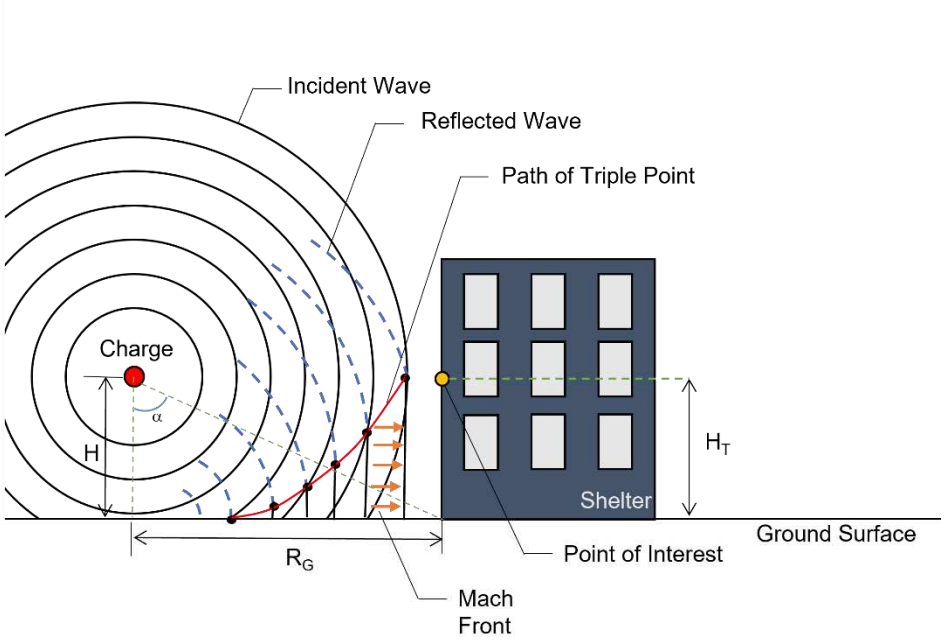

Figure 2-4: Air Burst Blast Environment *modified from:* (DOD, 2008).

Surface Burst- a surface burst explosion will occur when the point of detonation is located near or on the ground causing the reflected wave from the ground to merge and amplify the incident shock wave (DOD, 2008). Due to the amplification of the incident wave, an increase of approximately 1.8 times greater in blast wave parameters is observed compared to free air burst parameters for a given standoff distance (Cormie et al., 2019). A surface burst explosion environment is illustrated in Figure 2-5.

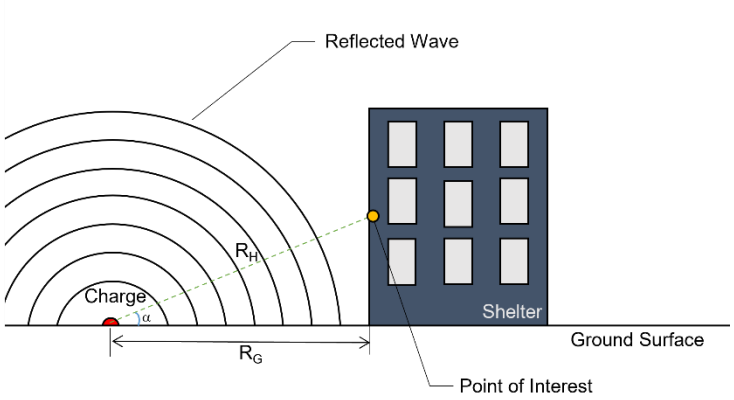

Figure 2-5: Surface Burst Blast Environment *modified from:* (DOD, 2008).

Confined Explosions-

Fully Vented Explosion- fully vented explosions take place inside structures or immediately adjacent to a barrier with at least one surface open to atmosphere (DOD, 2008). The initial wave is amplified by the structure and is fully vented along with the detonation products of the explosive into the atmosphere in the form of a shockwave (DOD, 2008).

Partially Vented Explosion- in a partially vented explosion, an explosion occurs within a structure that has small or limited size openings (DOD, 2008). The amplified initial wave and detonation products are vented to the atmosphere after a finite period of confinement inside the structure (DOD, 2008).

Fully Confined Explosion- fully confined explosions occur when an explosion is totally contained by the barrier structure and the shock loads are not vented to the atmosphere (DOD, 2008). Any pressure vented will be low in magnitude and only impact the immediately surrounding structures (DOD, 2008). The difference between the three classifications of confined explosions is depicted in Figure 2-6.

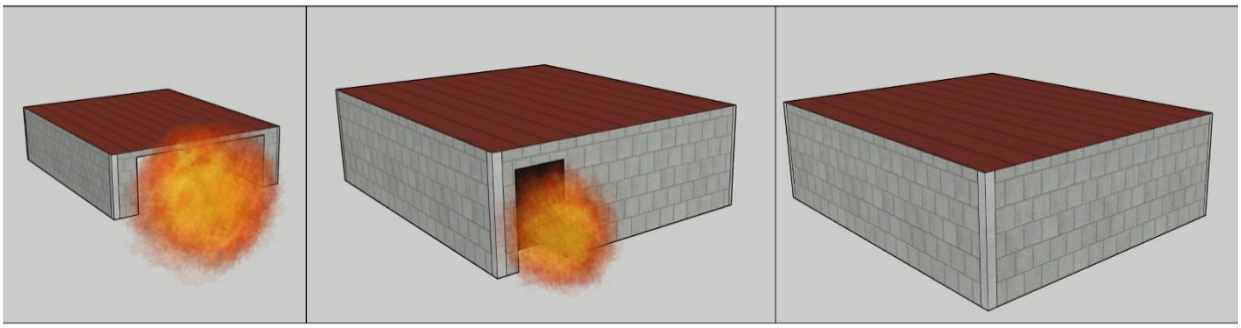

Figure 2-6: a) Fully Vented Confined Explosion, b) Partially Vented Confined Explosion, and c) Fully Confined Explosion.

2.3.3 Representation of Blast Loads in Codes and Standards

Many manuals and codes have been developed for the design of blast resistant structures (DHS, 2003; DHS, 2006; DOD, 1990; DOD, 1986; Goel, 2015). These manuals range in focus from design methods and protection recommendations to standards and codes. The United States government has released numerous manuals including FEMA-426, FEMA-453, UFC 3-340-02 and TM5-1300 on how to design and protect structures from potential explosive attack. FEMA-426 is the Reference Manual to Mitigate Potential Terrorist Attacks against Buildings. It is provided by the DHS to enhance the performance of buildings and infrastructure to blast and chemical, biological, and radiological (CBR) threats. The manual presents methods for calculating risk for threat assessment, guidance on protection measures, and design recommendations. It provides guidance on site layouts as well as integration techniques for structural, architectural, building envelope, and nonstructural aspects (DHS, 2003). FEMA-453 is the Design Guidance for Shelters and Safe Rooms manual. It focuses on the planning and design of safe rooms and shelters to provide protection in the case of a manmade threat of chemical, biological, radiological, or explosive nature (DHS, 2006). This manual focuses on standby systems that do not provide protection on a continual basis and can be employed after a warning has been issued.

The UFC and the TM5 manuals present protective design guidance and development for facilities against accidental explosions or other threats. The UFC 3-340-02 manual was discussed in section 2.3.2. The UFC 3-340-01 is the Design and Analysis of Hardened Structures to Conventional Weapons Effects. This manual is restricted for government use due to the sensitivity of the materials. The TM 5-1300 manual is one of the most widely used manuals for designing structures to protect against blast effects before the UFC manuals were published (DOD, 1990). The goal of this manual was to derive blast wave parameters to be used to design structures against blast loading, as well as provide the design procedures and construction details for steel and concrete structures. Blast load design parameters, design steps, calculation methods, and design equations, graphs, tables, and figures are included for free-air burst, air burst, and surface burst explosions. It was intended to be used by structural engineers involved in designing hardened facilities (DOD, 1986; Goel, 2015). It provides air blast pressure time histories and a simplified method, using a triangular pulse, for the incident and reflected pressures, for evaluating blast loading on multi-story buildings. The Interagency Security Committee (ISC) Risk Management Process was developed in 1995 by Executive Order 12977 with the purpose of developing longstanding construction standards for buildings and infrastructure that require blast resistance (ISC, 2021). The ISC developed a risk management process for federal facilities to determine the risk of any federal facility and the level of protection it must meet (ISC, 2021). The higher level of risk a facility faces, the higher the baseline level of protection must be (ISC, 2021).

Other standards and manuals have been developed by industry and experienced engineers for blast design of structures. The Handbook for Blast Resistant Design of Buildings provides a single reference for architects, designers, and engineers when designing blast resistant facilities to meet standards such as the American Society of Civil Engineers (ASCE), American Concrete

Institute (ACI), and American Institute of Steel Construction (AISC) codes (Dusenberry, 2010). The ASCE Blast Protection of Buildings standard presents the minimal requirements for new and existing buildings that could potentially be subject to effects of blast loading from accidental or malicious explosions (ASCE, 2009). Many of the codes and manuals specify that the level of protection is a balance between risk and cost. Higher levels of protection result in more detailed design and therefore higher construction costs (ASCE, 2009). Other factors such as capacity levels, site location, and emergency response time all are important risk factors to consider as well.

2.4 Methods for Modeling Blast Loading

2.4.1 Empirical, Semi-empirical and Numerical Methods

Analysis of blast loading has a long history dating back to World War II (Goel, 2015; Kennedy, 1946). Even the limited amount of research and data that existed before then was kept classified due to its sensitivity concerning the general public (Hopkinson, 1915; Cranz, 1926). Many analytical and experimental studies took place after World War II to study two main objectives. Firstly, to understand the nature of the blast wave and its characteristics and secondly, to examine effects of blast loading on the structural response. Stoner and Bleakney (1948) conducted free air experiments with TNT and Pentolite charges of various shapes and reported the resulting pressures. Goodman (1960) complied the free air blast data of spherical charges. Baker (1973), Swisdak (1975), and Kinney and Graham (1986) provide good summaries of blast wave characteristics. Kingery (1966) analyzed the air blast parameters for hemispherical surface blasts. Dewey (1962), Jack (1965), Wenzel and Esparza (1974) analyzed normally reflected pressures in reference to the incident blast pressure. Later the use of models and experimental data were used

by researchers such as Brode (1955), Henrych (1980), Kingery and Bulmash (1984) and Smith and Hetherington (2014) to create expressions for blast peak overpressure for free air explosives. Others such as Chapman, Rose, and Smith (1995), Remennikov and Rose (2005) and Jankowiak et al. (2007) utilized numerical simulations, hydrocodes and other commercially available simulation codes to model blast waves for comparison with experimental data or for studying the effects on structures and buildings. The methods for prediction of the blast wave parameters and the effects on structures are divided into three approaches: 1) Empirical (or analytical), 2) semi-empirical and 3) Numerical (Goel, 2015).

Empirical or analytical methods are evidence or experimental data-based approaches used to study and interpret the results of experimental work. They are essentially finding correlations between the experimental data that are treated as the results of the experimental work (Goel, 2015). The main advantage to empirical methods is speed and simplicity (Dusenberry, 2010). However, since all empirical equations are based on the availability of data, the accuracy tends to diminish in near field explosion (Dusenberry, 2010; Goel, 2015; A. G. Razaqpur et al., 2012). The most common empirical blast model is the Kingery-Bulmash model. Kingery and Bulmash (1984) derived high degree polynomial equations to predict air blast parameters for spherical and hemispherical charges ranging between 1kg to 400,000kg (CONWEP, 1991; Goel, 2015; Hussein, 2019). The equations are widely accepted and utilized for free air explosions. The peak incident pressure and impulse, positive phase duration, and time of arrival are calculated using these equations. CONWEP, is a fast-running tool that provides estimates for a variety of blast and fragmenting threat effects. ConWep calculates blast effects using the Kingery Bulmash equations and is made available through the U.S Army Corps of Engineers (USACE) Protective Design Center (PDC). The blast parameters found from the Kingery-Bulmash equations is then used to

iterate and find the decay coefficient (b). This is then used to plot pressure values at various time steps finally creating a pressure time history applied to the structure of interest (Goel, 2015; Hussein, 2019). Another commonly used empirical tool is the Single Degree of Freedom Blast Design Spreadsheets (SBEDS) developed by the USACE PDC. It was developed to design and analyze structures subjected to blast loading using equivalent single degree of freedom (SDOF) systems. The user should define the resistance function of the material and structural system and run a SDOF analyses. Many of the government manuals such as the UFC-340-02 and TM5-1300 provide graphical charts and empirical equations to calculate blast effects for a variety of materials, shapes, and threat environments.

Semi-empirical methods utilize a physics-based model to compute blast parameters (Dusenberry, 2010). These methods rely on extensive data and are limited to configurations and charge weight ratios for which data are available (Dusenberry, 2010; Goel, 2015). Advantages to a semi-empirical method are that the accuracy is typically better than empirical methods and it has quicker run times compared to more detailed numerical techniques. However, they are still seen as less accurate on average due to the lack of empirical data available for correlation (Miller et al., 2010).

Numerical modeling offers many advantages over empirical or semi-empirical methods when it comes to modeling blast loading and dynamic material behavior. Reduced cost of experimental testing, faster completion of analysis, and complete response data for discrete points in the simulation are a few reasons numerical simulation has become such a powerful tool in engineering analysis and design. Numerical methods are based on mathematical equations that describe the basic laws of physics such as conservation of mass, momentum, and energy (Goel, 2015). The physical behavior of materials is described by constitutive relationships that are

commonly used in Finite element analysis (FEA) and CFD (Goel, 2015). FEA is a powerful computational tool that allows for complex real-world engineering problems to be approximately solved by discretizing the problem into a finite number of elements and solving constitutive relationships. FEA has the capabilities to predict internal stresses and strains that are difficult to measure experimentally, perform failure analysis on structures, identify crucial parameters involved in failure and evaluate impulsive loading responses on a structure (Goel, 2015). If coupled with a computational fluid dynamics (CFD) approach, the response of deformable structures, fluid flow, and wave-wave, or wave-structure interaction can be analyzed as well. Analysis of impulsive blast loading on a structure using FEA is more commercially available with the advancement and development of many different computer software packages.

Hydrocodes are a computational continuum tool that simulates the response of both solid and fluid material under a variety of conditions. These programs are used to study very fast, very intense loading on materials and structures such as shock waves (Zukas, 2004). Since hydrocodes can numerically simulate high energy wave propagation phenomena and model structural dynamics, they are useful for modeling a wide variety of physical phenomena, including fluid-structure interactions, collisions, explosions, shock hardening and impact (Zukas, 2004). Hydrocode modeling requires three things to determine the forces acting on the mesh in each time step: the Newtonian laws of motion, the equation of state and the constitutive model. The Newtonian laws of motions are a set of differential equations for the conservation of momentum, conservation of mass, and conservation of energy. The equation of state relates the pressure to the density and internal energy (Collins, 2002). It is what accounts for the compressibility effects that occur during highly dynamic conditions. The constitutive model relates the stress to a combination of strain, strain rate effects, internal energy, and damage to describe the effects of deformation, a

change in shape or strength properties (Collins, 2002). Many hydrocodes have been developed over the years with a variety of schemes and approaches to accomplish different modeling capabilities.

Lagrangian hydrocodes define the mesh to represent the geometry of the problem. The vertices of the mesh are attached to the material and move with the material as the material is acted upon by forces. This results in the cells becoming deformed in shape and size as they remain fixed to the material (Collins, 2002). This is illustrated in Figure 2-7a). Mass, momentum, and energy are transported by the material flow, but the mass within an individual cell remains invariant so the changes in density are caused by the change in cell volume (Collins, 2002). Typically, a finite element or smooth particle hydrodynamic (SPH), also known as free Lagrangian, numerical techniques are used (Pierazzo et al., 2008). An advantage to using a Lagrangian hydrocode is it can be significantly less computationally expensive in CPU and memory due to the reduced meshing requirements. Common Lagrangian hydrocodes include LS-DYNA, ABAQUS, and EPIC.

LS-DYNA is a general-purpose finite element program used in a variety of industries developed by Livermore Software Technology Corporation (LSTC) (Hallquist, 1998). It has the capability to simulate complex real-world engineering problems and has been validated for modeling blast simulations. It has a coupled structural response analysis with CFD making it ideal for highly dynamic problems such as automobile crash simulations. ABAQUS is an explicit finite element analysis software package. It can analyze high speed (short-duration dynamics) and has a reputation of having accurate analysis with plastic deformation and discontinuous problems. Similar to LS-DYNA it has been validated for modeling blast loading and is a coupled structural response analysis with CFD.

In contrast, Eulerian hydrocodes define the mesh fixed in space and the material flows through the mesh. This is illustrated in Figure 2-7b). In this case, the mesh is defined to include the entire space of interest and mass, momentum, and energy all flow across the cell boundaries (Collins, 2002). Unlike Lagrangian hydrocodes, the volume of an individual cell is invariant and the change in mass of the cell is what causes the change in density (Collins, 2002). A finite difference or finite volume technique is typically used in Eulerian hydrocodes (Pierazzo et al., 2008). CTH is the most prominent Eulerian hydrocode. CTH, is a two-step Eulerian based hydrocode developed at Sandia National Laboratories capable of modeling multidimensional, multi-material, large deformation shock wave physics (McGlaun et al., 1990; Schmitt et al., 2017). It is a blast prediction hydrocode that solves the conservation equations in a two-step process similar to LS-DYNA and ABAQUS, however, it is not a coupled solver the way LS-DYNA and ABAQUS are. Eulerian codes such as CTH are widely used in shock physics analysis due to their ability to handle large deformations, robustly unlike the Lagrangian which can cause mesh tangling in large deformation (Pierazzo et al., 2008).

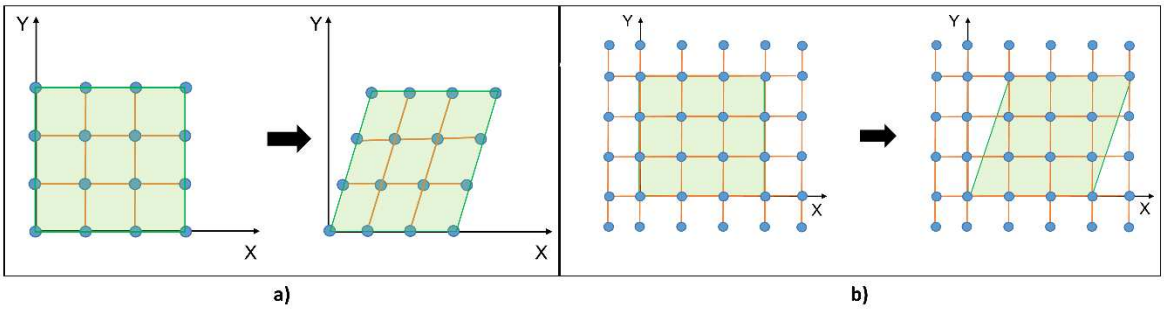

Figure 2-7: a) Lagrangian and b) Eulerian description of mesh.

2.4.2 Neural Networks and Surrogate Models

Surrogate Modeling- Hydrocodes and other computational modeling software are powerful tools used in engineering research. Software such as CTH, LS-DYNA, and ABAQUS can be very efficient and accurate in specific cases. The accuracy of computational models depends highly on

the parameters of the simulation such as mesh size, complexity of the simulation environment (i.e., loads and boundary conditions), computational cost, and memory requirements. When there are multiple simulation cases to be considered, such as different charge weights, charge heights, and differing standoff distances, or other scenarios such as optimization, risk analysis, and sensitivity analysis the computational demand could increase substantially. A surrogate model is an alternative method for modeling the outcome of complex problems when a solution is not as easily computed using a hydrocode or computational modeling software.

A surrogate model is an analytical model that mimics the input-output behavior of complex systems as closely as possible. These models approximate the behavior of the systems, while alleviating the burden of running computationally expensive simulations. Developing such models requires input and output data from computer simulations from a specific design space. Using a data-driven approach, commonly known as black-box modeling, the specific input and output data is used to "train" the surrogate model to produce accurate results to a reasonable precision. These types of models rely solely on the input-output relationship, while the internal workings of the model are typically not known or understood. Commonly used forms of surrogate models are genetic algorithms (GAs), response surface models (RSMs) and artificial neural networks (ANNs).

Introduction to Artificial Neural Networks- Artificial neural networks are an alternative method for modeling more complex simulation environments. ANNs have been used in a variety of fields in design optimization, classification, pattern recognition, and prediction problems (Remennikov & Rose, 2007). The advantage of using an ANN rather than a simulation model, is that ANN, as a surrogate model, can develop complex non-linear relationships between input variables and corresponding outputs.

ANNs are a form of artificial intelligence that are inspired by the biological neural networks in the brain. Similar to the biological model in which it is derived from, an ANN is an assembly of many highly connected processing units, often referred to as nodes or neurons. The neurons are the basic processing elements of both a biological and a neural network as illustrated in Figure 2-8a). The strength of the connections between each individual neuron is represented by numerical values known as weights (Remennikov & Rose, 2007). The actual connections model the axons and dendrites of a biological neuron while the connection weights represent the synapses that control the input signals. A positive weight corresponds to excitatory synapses while negative weight models inhibitory ones (Jain et al., 1996). A typical artificial neuron or node in a neural network computes a weighted sum of the inputs, x_j for j=1, 2, …, n and generates an output, called the signal, of either 0 or 1 depending on if the sum is found to be above the activation threshold θ. The neuron output O is given by the following relationship:

$$O = f\left(\sum_{j=1}^{n} w_j x_j\right) = f(S) \tag{2.4}$$

$$O = \begin{cases} 1 & \text{if } S \geq \theta \\ 0 & \text{otherwise} \end{cases} \tag{2.5}$$

Where w_j is the weight associated with the *jth* input and f is the activation (transfer) function. This is shown in Figure 2-8b).

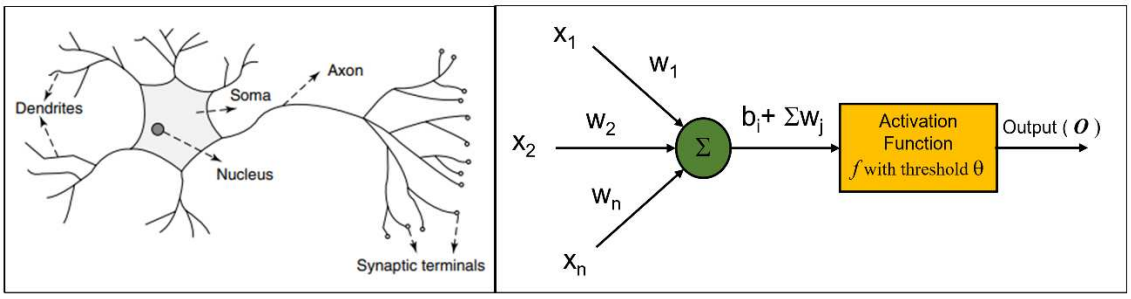

a) **b)**

Figure 2-8: a) Biological neuron (Jain et al., 1996) vs. b) artificial neuron.

This activation function captures the nonlinear characteristic exhibited by neurons by using functions such as a threshold function, piecewise linear, sigmoid, or Gaussian as shown in Figure 2-9. The most used type of activation function in ANNs is sigmoid. The sigmoid function switches a node between a low and high states. It is a strictly increasing function that exhibits smoothness and has the desired asymptotic properties to achieve the desired nonlinear behavior (Furrer & Thaler, 2005; Jain et al., 1996).

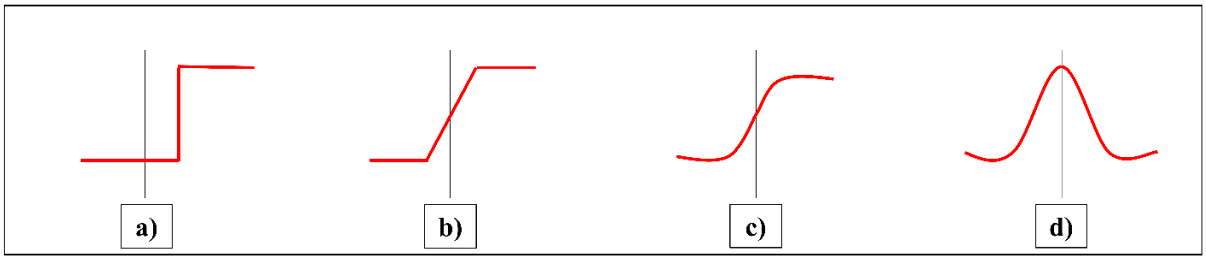

Figure 2-9: Different types of activation functions a) threshold, b) piecewise linear, c) sigmoid, and d) Gaussian. *modified from:* (Jain et al., 1996).

Neural Network Architectures - the basic architecture of an ANN consists of three types of neuron layers: input, hidden and output. Depending on the connection pattern or architecture and how data is propagated through the neurons and layers, ANNs are categorized into two categories:

- Feed-forward networks
- Recurrent networks

In feedforward networks, the connections do not form a cycle, data travels in one direction only from input nodes, to hidden node layers, and finally to the output nodes (Jain et al., 1996). Data processing can exist on multiple layers but there are no feedback connections so no backtracking through multiple segments will take place before an output is produced (Jain et al., 1996). Feedforward networks are static in that they produce a single set of output values rather than a sequence of values from a given input (Jain et al., 1996). Feedforward networks are memory-less as their response to a specific input is independent of the previous network state (Jain

et al., 1996). Recurrent networks have feedback connections present that form a directed cycle, so data can propagate forward and backwards. This allows them to be dynamic systems that continue to change rather than reaching a stable state. When a new input is presented, the neurons compute an output. Due to the feedback connections, the inputs at each neuron are then modified and the activation values are changed causing the network to enter a new state.

The feedforward network can be classified further as single layer or multi-layer networks. Single layer neural network contains no hidden layers. This means that no computations are done, and the inputs are sent to the output nodes. This type of network is suitable for linear regression analyses (Furrer & Thaler, 2005). The most widely used network is the multi-layered perceptron (MLP) network. An MLP consists of one or more hidden layers placed between the input and output layer as shown in Figure 2-10 (Dayhoff, 1990). Typically, each node in a lower layer is connected to every node in the higher layer in a fully interconnected design. The input layer feeds each of the nodes on the first hidden layer, the outputs of the first hidden layer then feed into each of the second hidden layer nodes and so on. This network structure allows for more complex equations and non-linear relationships that cannot be accurately modeled using a linear regression. The larger the number of hidden layers and nodes in each layer, the more capable the MLP will be in accurately capturing a complex input-output relationship (Furrer & Thaler, 2005).

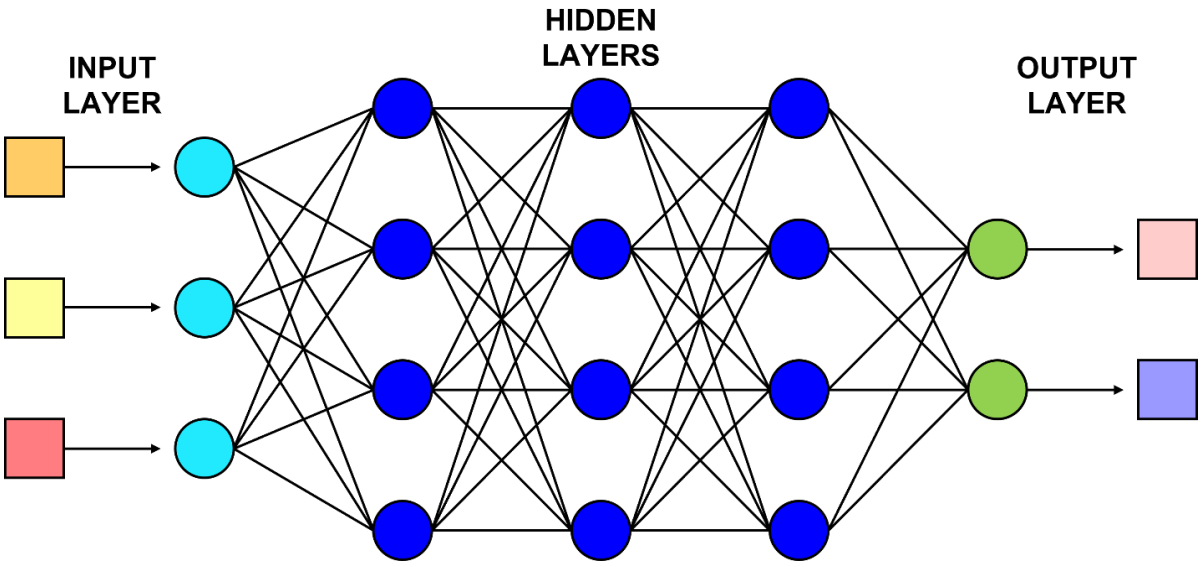

Figure 2-10: Multi-layered feedforward neural network diagram.

Neural Network Learning & Training - in an ANN, learning refers to the method of modifying the weights of the connections, the biases, and the activation thresholds between the nodes of the network. The network "learns" or is "trained" by adjusting the parameters in an iterative process. The learning process has three distinct pieces that determine how the training will take place. First, the learning paradigm determines how the neural network will learn. Second, the learning rule determine how the parameters are updated and third, a learning algorithm refers to the procedure in which learning rules are used for adjusting the weights (Jain et al., 1996).

Learning Paradigms - there are three main learning paradigms: supervised learning, unsupervised learning, and reinforced learning. In supervised learning, a set of inputs and corresponding outputs is provided to the network. The error between the calculated outputs and the desired outputs are found for each node in the output layer. These errors are then used to determine the weight adjustments according to the specific learning rule. This process is repeated until the parameters for each of the nodes are adjusted to obtain the desired output with a specified level of accuracy (Remennikov & Rose, 2007). The term "supervised" originates from the fact that the desired

outputs for each node are provided by an external "teacher." In contrast, in unsupervised learning or self-organization the network is provided with just the inputs to develop a learning pattern of its own. An output unit is trained to respond to clusters of patterns within the input (Abraham et al., 2005; Dongare et al., 2012). In this paradigm, it explores the underlying structure in the data, and correlations between patterns in the data, and organizes patterns into categories from these correlations (Jain et al., 1996). Reinforcement learning is an intermediate of supervised and unsupervised learning. In this structure, the learning machine does some action on the environment to determine how to maximize a numerical reward signal. The learner is not told which actions to take, as is in most forms of machine learning; instead, the learner must discover which actions to take based on the reward or critique proved on the correctness of the calculated output. The adjustment of parameters is made until an equilibrium state has been reached. In general, supervised learning focuses on a task, unsupervised learning focuses on data, and reinforcement learning focuses on adapting to the network environment.

Learning Rules - there are four major learning rules: error correction, Boltzman, Hebbian and competitive learning. Boltzman and competitive learning are not utilized in single and multiple layer perceptron neural networks so they will not be discussed in this study.

Error-Connection - during the training process, the calculated output $\boldsymbol{O}$ from the network may not be equal to the desired output $\boldsymbol{d}$. The basic principle behind the error-correction learning rules is to use the error between the desired output and the calculated output ($\boldsymbol{d}$-$\boldsymbol{O}$) to adjust the weights, biases, and activation threshold parameters. The overall goal is to gradually reduce and eventually minimize the errors between the two outputs. The back propagation algorithm and the perceptron algorithm are examples based on the error-correction principle. The back-propagation algorithm is the most common training algorithm used for MLP training.

The back-propagation algorithm is the most straightforward algorithm as it utilizes the steepest descent method to update the weights and biases (Remennikov & Rose, 2007; Yu & Wilamowski, 2016). It can be used for large neural networks as it does not require the calculation for the Hessian matrix, the matrix of second derivatives of the error function. However, it has the slowest convergence and requires many iterations to find a solution. In the back propagation algorithm, the weights and biases are initialized as random values. The value from the *ith* neuron x_i in a feedforward network with a back-propagation learning rule is determined by following (Pilkington & Mahmoud, 2016):

$$s_i = \sum_{j=1}^{n} w_j x_j \tag{2.6}$$

$$x_i = f(s_i) \tag{2.7}$$

For more networks with more hidden layers, the threshold, possibly the bias, value for the *ith* neuron, b_i is added to Equation 2.8 and is conducted between two neurons of adjacent layers (Pilkington & Mahmoud, 2016).

$$s_i = b_i + \sum_{j=1}^{n} w_j x_j \tag{2.8}$$

To increase accuracy of the network, back-propagation alter the weights and biases to minimize either the mean square error (MSE) between the calculated output and the desired output or the objective/loss function (Pilkington & Mahmoud, 2016). The level of the adjustment is dependent on the gradient of the objective function with respect to the weights and biases. The partial derivatives of objective function ∇f with respect to each individual parameter is calculated using the chain rule, one layer at a time, iterating backwards from output layer, hidden layer(s) and ending with the input layer. The gradient shows how much the parameter needs to change (positive or negative) to minimize the error. This difference is then fed backwards into the network to update all the weights and biases depending on the training algorithm chosen. This process is repeated to

iterate the parameters until the error is minimized. Equation 2.9 shows how the weights are updated using the back-propagation algorithm where α is the training rate.

$$w_{k+1} = w_k - \alpha \nabla f \tag{2.9}$$

The parameters in the neural network can be trained in two different modes: online or batch. In the online method, the parameter updates are calculated for each input data sample, and they are individually modified after each sample. In the batch method, the parameter updates are computed for each input sample and then stored during one pass through the training set, which is called an epoch (Abraham et al., 2005). At the end of the epoch, all the contributions for each parameter are added and then the parameters will be updated with a competitive value. This method adapts the weights with a cumulative parameter update, so it will follow the gradient more closely (Abraham et al., 2005).

Hebbian - the oldest learning rule is Donald Hebb's postulate of learning in 1949. This learning rule states that if two neighboring neurons are both activated or both deactivated, the weights between these neurons should increase proportional to the product of the input and output. For neurons operating in the opposite phase, the parameter should decrease (Wilamowski, 2009). If there is no correlation, the parameter should remain unchanged. The training process begins by initializing the parameters to zero, unlike the back-propagation method where the initial parameters are set to random values. The Hebbian rule can be described by Equation 2.10 and 2.11.

$$w_{ij}(new) = w_{ij}(old) + x_i O_j \tag{2.10}$$

$$\Delta w = xO \tag{2.11}$$

Where w_{ij} is the weight between the *i-th* and *j-th* neurons, x_i is the signal on the *i-th* input and O_j is the output signal. The Hebbian learning rule can be utilized in both supervised and unsupervised paradigms for different network architectures.

Training - the goal of the training process is not to just minimize the training error, it is to minimize the error for when the network is used with data that is not in the training set (Furrer & Thaler, 2005). The data can be from past events/experiences or from computer simulations where the output is known and will form a basis on which outcomes from future similar events can be predicted (Pilkington & Mahmoud, 2016). The data should be divided into three categories: training data, validation data, and testing data (typically 70, 15, and 15% respectively). First the training data is utilized to establish patterns, reducing the training error over multiple iterations while the validation and testing data serve as data used to minimize the generalization error (Furrer & Thaler, 2005; Pilkington & Mahmoud, 2016). The training process is part of the whole process of creating a neural network illustrated in Figure 2-11.

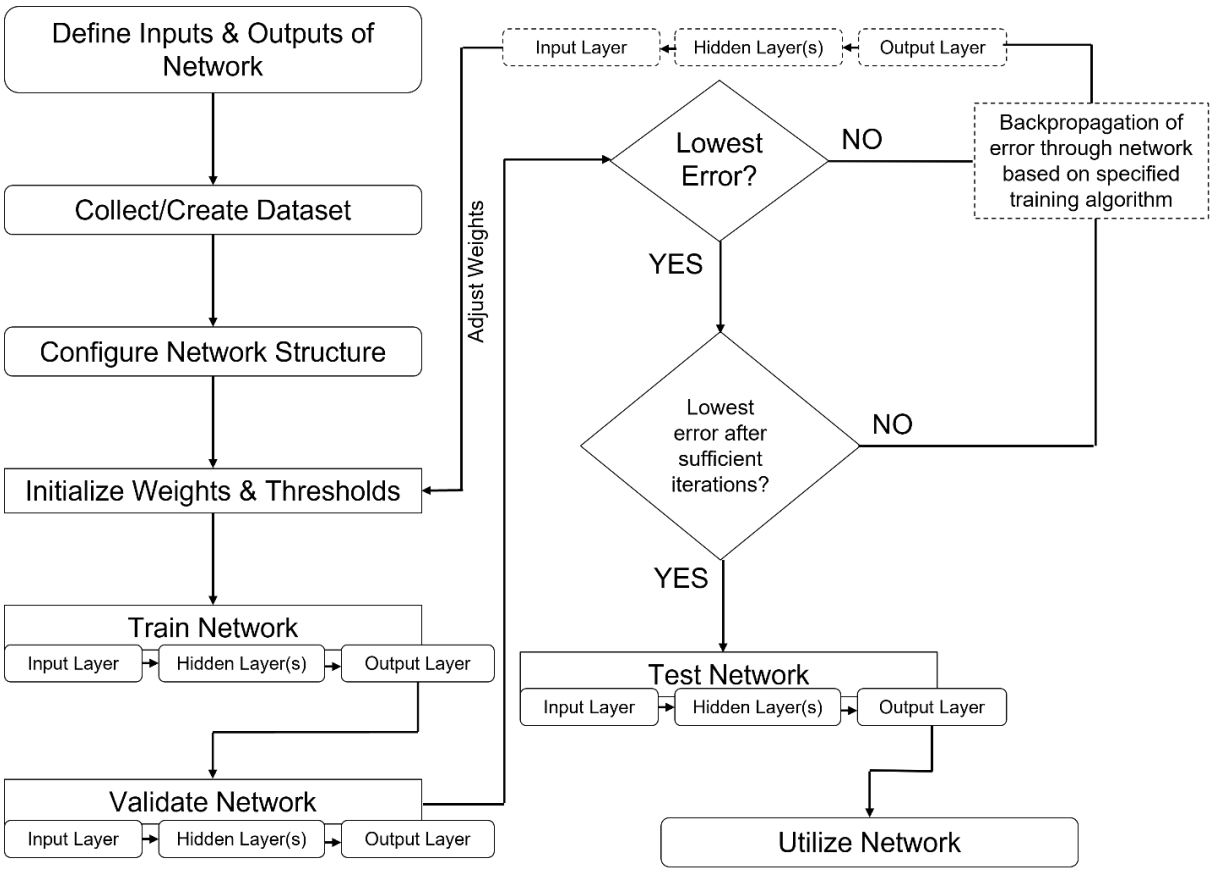

Figure 2-11: Design process for creating an artificial neural network *modified from:* (Pilkington & Mahmoud, 2016).

As previously discussed, the back-propagation algorithm is the most commonly used scheme for training a neural network. However, back-propagation does have some drawbacks. Due to the random initialization of the weights and biases, often it gets stuck at a local minimum rather than finding a global minimum. There are various methods and algorithms that are used in training neural networks, but the main four types of optimization algorithms are gradient descent, Newton's method, conjugate gradients, and Levenberg-Marquardt.

Newton's method is a second-order training algorithm that utilizes the Hessian matrix to find better training directions for adjusting the weights. It requires fewer steps than the steepest descent method to reach a minimum, but it has drawbacks concerning the Hessian matrix. First, the solution found is not guaranteed to be a minimum. It is only a minimum if the Hessian matrix

is positive definite. If the Hessian matrix is not positive definite, a maximum may be found as the function evolution may not be reduced at every iteration as it does towards a minimum. Second, even though the use of the Hessian matrix requires fewer steps to find the minimum of the error function, the calculation of the exact Hessian matrix and its inverse are very computationally expensive. In comparison to the steepest descent method, it converges much quicker but is unstable and can be extremely expensive. The governing equation for Newton's method is shown in Equation 2.12, where H is the Hessian matrix and k is the index of iterations.

$$w_{k+1} = w_k - H^{-1}\nabla f \tag{2.12}$$

The conjugate gradient method is meant to be an intermediate method between the steepest descent or gradient descent method and Newton's method. The search direction and step size are chosen more carefully as to accelerate the slow convergence of the steepest descent method and to avoid the computational complexity of the Hessian matrix used in Newton's method. The training direction is along the conjugate directions from the conjugate gradient. Generally, the conjugate directions, d^k are found by setting the initial direction ($d^0 = -\nabla f$) as the negative gradient and is updated according to Equation 2.13, using a conjugate parameter γ that is calculated differently depending on the method chosen (Møller, 1993). The governing equation for updating the weights is shown in Equation 2.14 where η_k is the training rate usually found by line minimization.

$$y_{k+1} = \nabla f_{k+1} + \gamma y_k \tag{2.13}$$

$$w_{k+1} = w_k + y_k \eta_k \tag{2.14}$$

This method has proven to be effective in training large neural networks as it does not have the computational expense of calculating the Hessian matrix. There have been many modifications to the conjugate gradient algorithm to create "scaled" conjugate gradient methods that utilize

pieces of other methods. For example, combining the conjugate method with the quasi-Newton method or the Levenberg-Marquardt to "scale" the gradient to avoid the line search (Møller, 1993). Another approach to limit the computational expense of the training algorithm is to approximate the inverse of the Hessian matrix with first derivative information rather than compute the exact Hessian. The quasi-Newton method does exactly that using different approximation formulas including finite difference approximations, Broyden-Fletcher-Goldfarb-Shanno (BFGS), Davidon-Fletcher-Powell (DFP), and symmetric rank one formulas (Griva et al., 2008). The inverse Hessian is approximated by another matrix B_k which uses the first partial derivatives of the error function. Equation 2.15 is used for quasi-newton methods by replacing H^{-1} with B_k, which updates each iteration based on the formula chosen.

$$w_{k+1} = w_k - B_k \nabla f \tag{2.15}$$

This method is faster than the steepest descent and conjugate gradient methods and does not have the same computational complexity as Newton's method. However, similar to Newton's method, quasi-Newton methods are not guaranteed to find a minimum unless B_k is positive definite.

The Levenberg-Marquardt (LM) algorithm also known as the damped least squares (DLS) method is used to minimize a nonlinear function. This method has been adapted to minimize an error function that arises from a squared error criterion such as Equation 2.16.

$$E = \frac{1}{2}\sum_{i=1}^{n} u_i^2 \tag{2.16}$$

where u is the vector of all the error terms ($u_i = \boldsymbol{d} - \boldsymbol{O}$) and n is number of outputs. The LM method blends the steepest descent method and the quasi-Newton method to develop a fast and stable training algorithm. The method inherits the speed of the quasi-Newton method and the stability of the steepest descent method (Yu & Wilamowski, 2016). Typically, it is not as fast as

the quasi-Newton methods, but it does provide stability that quasi-Newton methods lack. The basic idea of the LM algorithm is using a combined training process such that a steepest descent algorithm is used for more complex curvature and is augmented with a quasi-Newton approach when the local curvature can be approximated with a quadratic and speed up the convergence significantly. This algorithm uses the gradient and the Jacobian matrix rather than the Hessian matrix. The Jacobian matrix for the weights is defined as follows

$$J_{i,j} = \frac{\partial u_i}{\partial w_j} \tag{2.17}$$

Where i=1,…a and j=1,…b where a is the number of instances in the dataset and b is the number of parameters in the neural network (Nguyen et al., 2021). The size of the Jacobian matrix is [a, b]. This algorithm is only used for small or medium sized neural networks as the Jacobian matrix storage can become very large as the size of the neural network increases (Yu & Wilamowski, 2016). The gradient is then

$$\nabla f = J^T u \tag{2.18}$$

The Hessian can then be approximated as

$$H \approx J^T J + \mu \boldsymbol{I} \tag{2.19}$$

Where μ is the always positive combination coefficient and $\boldsymbol{I}$ is the identity matrix (Nguyen et al., 2021; Yu & Wilamowski, 2016). The update rule of the Levenberg-Marquardt algorithm is then

$$w_{i+1} = w_i - (J_i^T J_i + \mu \boldsymbol{I})^{-1} J_i u_i \tag{2.20}$$

When the combination coefficient μ is small, the equation becomes the update equation for quasi-Newton method. When μ is large, the equation becomes the same as the steepest descent method (Nguyen et al., 2021; Yu & Wilamowski, 2016). Table 2-5 summarizes the convergence rates and complexities of the various training algorithms.

Table 2-5: Summary of Neural Network Training Algorithms (Møller, 1993; Yu & Wilamowski, 2016)

Training Algorithm	Convergence	Computation Complexity
Backpropagation/EBP/Steepest Descent	Stable, slow	Gradient
Newton	Unstable, fast	Gradient & Hessian
Conjugate Gradient	Unstable, fast	Conjugate & Conjugate Gradient
Quasi-Newton	Unstable, fast	Jacobian
Levenberg-Marquardt	Stable, fast	Jacobian

2.4.3 Application in Blast Research

ANNs have been used in a variety of different engineering fields including geotechnical, structural, material behavior, and finite element analysis (BERRAIS, 1999; Shahin et al., 2004). They are powerful tools that have started to gain popularity in blast research over the years as a fast method for predicting blast loading. Remennikov and Mendis (2006) developed and tested an ANN model for predicting blast loads in single city street. The MLP developed had input variables of street width, building height, distance along the street, height of point of interest above the ground with output variables of pressure and impulse. A dataset of 49 different analyses were gathered to train and validate the network. It was found that the four layer back-propagation network with two hidden layers with eight nodes in each hidden layer produced the best predictions. The ANN produced overpressures and impulses that matched the CFD predicted values but was much more efficient. In a follow up study, Remennikov and Rose (2007) developed an ANN to predict the pressure behind a single barrier and to predict the effectiveness of the barrier for varying parameters. The five parameters to train the input data were wall height, distance behind the wall, charge height above the ground, point of interest height above the ground, and standoff distance. The ANN model was used to develop contour plots of the overpressure and impulse adjustment factors to simplify the prediction process (Remennikov & Rose, 2007). It was found that the ANN developed could predict air blast loading scenarios with a single barrier.

Similarly, Flood et al. (2008 & 2009) proposed a new ANN-based modeling approach to model blast waves with a barrier and a structure behind the barrier as the target of interest. A radial gaussian (RGIN) neural network was used as it performs well for problems with large training sets. After training from a large experimental dataset, it was found that the model could predict peak pressure accurately over a wide range of values with a correlation of 0.996.

Two other studies were presented in the paper that were ongoing research at the time at the Air Force Research Laboratory to determine how the neural network can be extended to model more complicated problems. The first study was using the developed ANN to predict the time-wise evolution of pressure. Specifically, the goal was to determine how pressure changes over time across the surfaces of a barrier, the ground between the barrier and the building, and the front and top surfaces of the building itself (Flood et al., 2009). Two additional inputs were added to the study: the lateral distance from the centerline of the building (x) and the bomb charge weight (W). The goal of this study was to allow the user to view the time-wise progress of the blast wave over the critical surfaces in the system. The second study was the development of a coarse grain method (CGM) approach to ANN and simulation modeling for blast loads. The focus of the study was to develop a simulation tool that has the versatility of CFD simulations, but the speed that is an order of magnitude faster (Bewick & Flood, 2010; Flood et al., 2009). Another study done by Bewick and Chen used the previously develop ANN to predict blast wave parameters such as peak pressure, impulse, time of arrival, and positive phase duration on different surfaces of buildings protected by simple barriers (Bewick & Chen, 2011). The ANN techniques were trained with hydrocode simulations from DYSMAS. Peak pressure and time of arrival on the side walls were found to have the most accurate results while the impulse and duration were less accurate. The ANN was able to accurately predict pressure, time of arrival and duration for the roof, but impulse

still had poor correlation. It was found that in general, the peak pressure and the time of arrival had better prediction from the ANN, while impulse and positive phase duration have higher levels of nonlinearity that is more difficult to predict (Bewick & Flood, 2010; Bewick & Chen, 2011). Bewick et al. (2011) found that the use of non-scaled input parameters led to improved correlations between target values and predictions. Another three-dimensional neural network was applied to predict peak pressure by Kang and Park (2023). Kang and Park (2023) utilized a convolutional neural network, often used in image processing, to predict peak pressure between buildings with an explosive located at one end of the buildings. Dennis et al. (2021) developed a neural network to predict the peak specific impulse for confined internal blast environments depending on the charge mass, point of interest coordinates, and charge coordinates. Confined internal environments are highly complex and the prediction of this type of loading requires specific computational software to capture the reflection and coalescence of multiple shock fronts. The goal of this study is to develop a fast-running predictive tool that can be used to assess the effects of an explosive attack on crowded internal environments. A feed forward backpropagation neural network structure with five inputs, two hidden layers, and a single output was used to model the complex nonlinear internal blast waves. Another study by Dennis et al. (2023) developed a direction-encoded neural network to predict peak pressure in a variety of domains with multiple barriers. Holgado et al. (2022) developed a deep neural network (DNN) to predict the impulse, pressure, load duration, and time of arrival for different charges when considering nine different inputs. This study analyzed the effects of charge shape, scaled standoff distance, and scaled height of burst (HOB) of the charge on the corresponding blast parameters. The results were validated against CFD models and experimental data which showed the DNN model accurately predicted the impulse however there were large variations in the pressure.

The studies mentioned above demonstrate that ANNs can be used to predict blast wave parameters accurately and efficiently for different blast environments.

2.5 Explosive Effects on Structures and Human Bystanders

2.5.1 Impact of Blasts on Structures

Reflection, Diffraction and Amplification - when a blast wave encounters another surface, it will behave similar to any other light or sound wave, it will reflect from it and depending on the geometry and size, diffract around it, or transmit through the surface (Cullis, 2001; McVay, 1988). The air applies the same external force to the surface that the surface applies to the air, creating a change in momentum. This change in momentum results in the pressure being increased above the incident pressure. This result is called the reflected wave or reflected overpressure (Cormie et al., 2019; Dusenberry, 2010). The magnification of the reflected pressure varies with respect to incident pressure, as well as the proximity, robustness, geometry, and material characteristics of the impacted structure or object (Cullis, 2001; Dusenberry, 2010). One of the most important parameters when considering reflection is the angle of incidence α, which is the angle of the blast wave on the surface of the target structure. By convention, when the blast wave is normal or perpendicular to the surface of the structure, α is equal to zero. When α is 90°, there is no reflection, and the incident pressure loads the structure (Cormie et al., 2019). Typically, between angles of 0° and approximately 40°, regular reflection will occur. After 40°, Mach reflection takes place. This phenomenon occurs in an air blast scenario (Cormie et al., 2019). Figure 2-12 shows the concepts of regular reflection and Mach reflection.

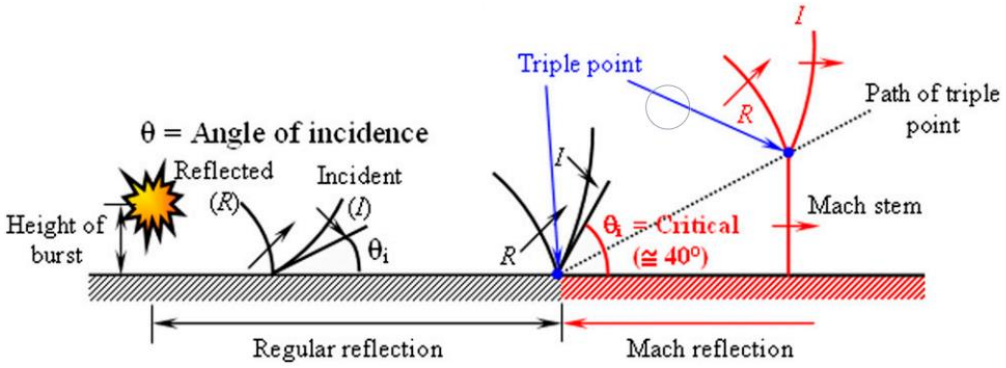

Figure 2-12: Regular reflection for $0° \leq \alpha \leq 40°$ and Mach reflection for $\alpha \leq 40°$ (Goel & Matsagar, 2014).

In an air blast scenario, initially described in section 2.2, the detonation occurs above the ground at a certain distance so that the initial shock wave reflects off the ground surface before the initial wave reaches the structure. The ground reflection and incident shock waves combine to form a "Mach front." The Mach front is assumed to be a uniform pressure as there are small fluctuations along the height of the Mach front that can be ignored. The further away from the detonation, the higher the height of the Mach front. This increase in height is referred to as the "path of the triple point" which is the intersection of the incident, reflected, and Mach waves. Everything below the height of the triple point is assumed to be loaded with a uniform pressure while everything above will be loaded with varying pressures which is an interaction of the incident and reflected waves (Goel & Matsagar, 2014; Pezzola, 2018). To calculate the blast loads that a structure would be subjected to in an air blast scenario, the UFC manual must be utilized to find the peak reflected pressure $P_{r\alpha}$ based off the angle of incidence α, and the scaled height of the charge H, from Figure 2-3. The angle of incidence can be found with Equation 2.21 where R_G is the distance on the ground from the location of the charge to the point of interest.

$$\alpha = \tan^{-1}\left(\frac{R_G}{H}\right) \tag{2.21}$$

The reflected impulse at the ground of the structure, $i_{r\alpha}$, can be found using the UFC manual based on the angle of incidence α, and the scaled height of the charge *H* using Figure 2-13 . The blast wave parameters for the Mach wave can then be computed using Figure 2-2 with $P_{r\alpha}$ as the new value for the peak incident pressure and $i_{r\alpha}$ as the new value for the peak incident impulse.

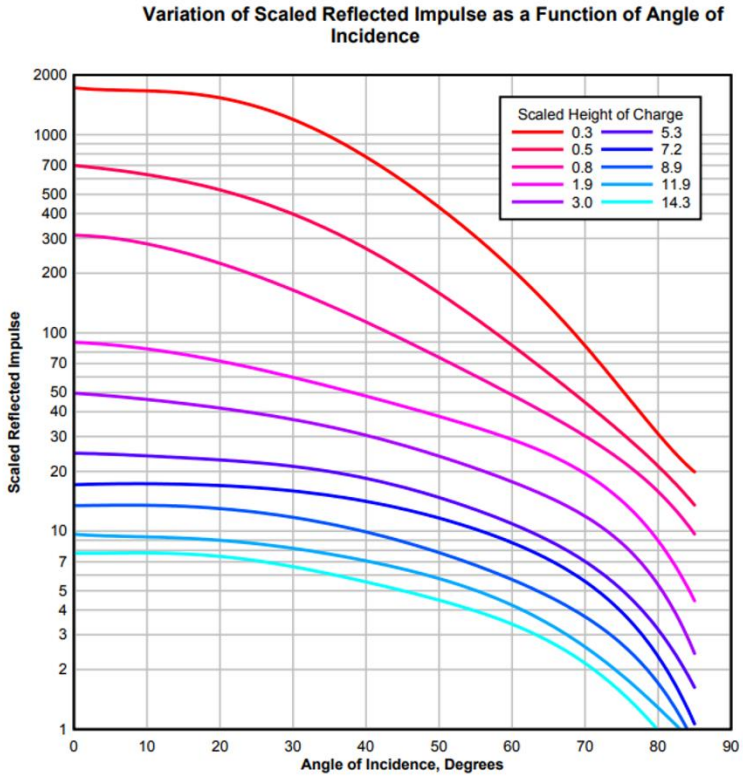

Figure 2-13: Reflected Impulse for different scaled heights and angle of incidence from: (DOD, 2008).

A surface blast scenario was discussed in section 2.2. In a surface blast scenario, the point of detonation is located near or on the ground causing an immediate reflection wave to form from the ground and merge and amplify the incident wave. The UFC manual can be used to find the blast parameters for a surface burst in a similar fashion to that of air burst calculations. The distance between the charge and the point of interest, R_H can be found using Equation 2.22 below where R_G is the distance along the ground between the charge and the point of interest and *H* is the height of the charge.

$$R_H = \sqrt{R_G^2 + H^2} \tag{2.22}$$

The scaled distance Z_H can be found using Equation 2.2 by replacing R with R_H. This can then be used to find the angle of incidence α and the incident overpressure P_{so} using Figure 2-14 for hemispherical charges. If the charge is not hemispherical, the UFC manual provides blast parameter data for other surface blast category charges of different shapes (DOD, 2008). Using Figure 2-15, the angle of incidence, and peak incident overpressure, the reflected pressure coefficient $C_{r\alpha}$ can be found. The peak reflected pressure $P_{r\alpha}$ is then determined using Equation 2.23. This can then be used in the same manner as it was for an air burst scenario to find Z and the rest of the blast parameters (DHS, 2005; Pezzola, 2018). Other manuals and reports have recorded calculations for additional parameters such as clearing times, dynamic pressures, as well as other approaches for finding the reflection coefficients and reflected blast parameters (ASCE, 2009; Cormie et al., 2019; Ngo & Mendis, 2007).

$$P_{r\alpha} = C_{r\alpha} * P_{so} \tag{2.23}$$

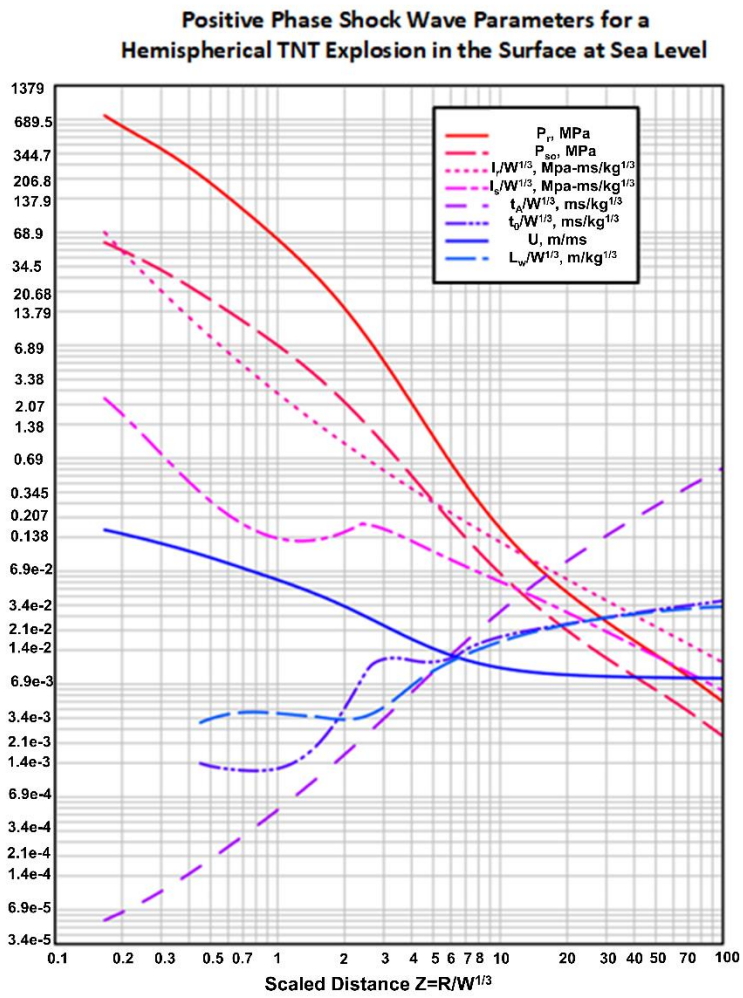

Figure 2-14: Positive Phase Blast Wave Parameters for Hemispherical Surface Blast *modified from:* (DOD, 2008).

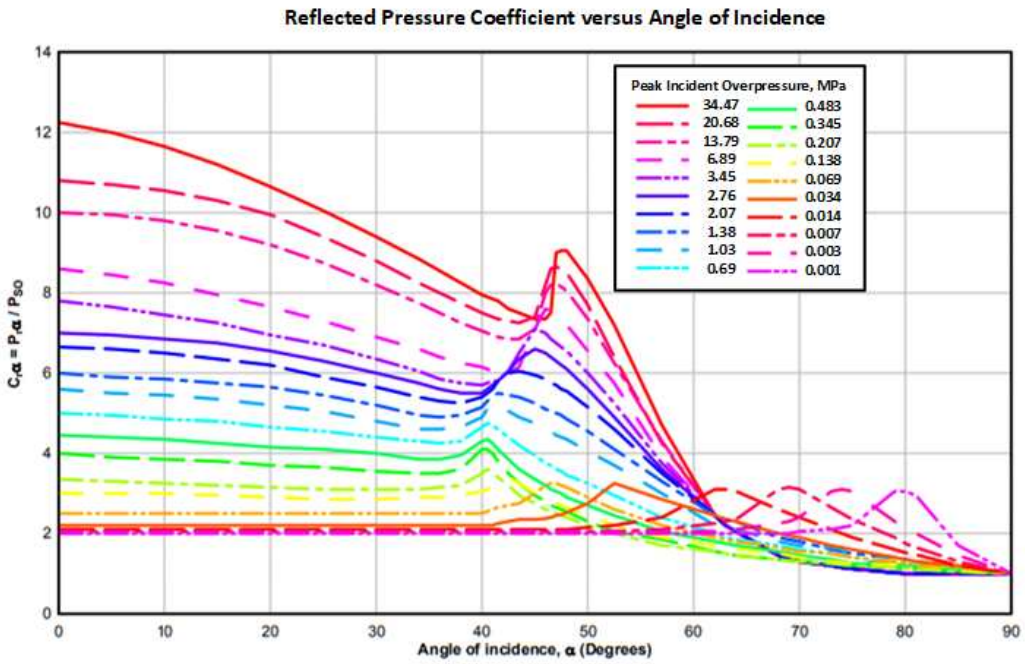

Figure 2-15: Reflected Pressure Coefficient for various peak incident pressures and angle of incidence *modified from:* (DOD, 2008).

Structural Response- blast wave exerts an impulse on the exterior surfaces of the structure or object. This force can cause movement and deformations as the energy is absorbed or dissipated. This creates a complex, dynamic, or impulsive response off the structures which is a function of many variables including time, pressure, proximity, and material.

Blast loading could result in different failure modes such as flexure, direct shear, breaching, or punching shear (Ngo & Mendis, 2007). Both local and global responses can occur from blast loading. Localized structural responses are related to the close-in effects of the explosion, resulting in localized shear and flexural failures in the closest structural components. The structural components near the explosion can experience high pressure and short duration loads, which typically allows them to be analyzed by the impulse rather than the peak pressure, which is associated with the longer duration blast pressures (ASCE, 2009; Razaqpur et al., 2009). The resulting localized shear failure occurs in the form of punching, spalling, and breaching due to the

impact of fragments with the structure (ASCE, 2009; Ngo et al., 2007). Since the structure does not have adequate time to deform, the pressure cannot do any work. This means the strength of the structure is less important compared to the ductility to resist the blast energy (ASCE, 2009; Razaqpur et al., 2009). Global structural behavior occurs at lower pressure ranges and higher durations. The longer duration of the blast wave may exceed that of the response time of the structure which causes the response of the structure to be dependent on both the pressure and the impulse of the explosion, but mainly the pressure (ASCE, 2009; Ngo et al., 2007; Razaqpur et al., 2009). Typically, global failure modes are either in the form of bending (flexure) or direct shear.

Structural materials are known for being affected by extreme loading conditions. The high loading rates and large inelastic deformations that occur as a response to blast loading can cause drastic changes in material properties. Blast loading is applied over a significantly shorter duration than many other common loading scenarios which causes high strain rates on the scale of 10^2-10^4 s^{-1} (Thornton & Colangelo, 1985). High strain rates can have a significant effect on a material's strength and dynamic behavior. Structural elements often exhibit higher strengths when subjected to dynamic blast loads than in static loading conditions (Dusenberry, 2010; Thornton & Colangelo, 1985). Material testing demonstrates an increase in strength is in response to the strain rate sensitivity under high strain rate dynamic loading. Malvar & Crawford (1998), Ngo et al. (2007), and Grote et al (2001) are a few studies performed on the high strain rate effects on concrete. It was found that the dynamic increase factor does significantly increase for high strain rates. It was found that the energy absorption capacity significantly increased with higher strain rate (Malvar & Crawford, 1998). Dowling and Harding (1967), Kong and Remennikov (2011), and Meyers (1982) analyzed the effects of high strain rates on several types of stainless steels and mild steels.

Strength increases could range from 9-50% varying with strain rate, type of steel and structure. However, the tensile strain does not experience the same increase in capacity (Dowling & Harding, 1967; Kong et al., 2011; Marques, 2012; Razaqpur et al., 2009). In order to accurately predict increase in strain, more sophisticated material models, such as the Johnson-Cook model or the Karagozian & Case model, are necessary to represent the behavior of the structural material under such conditions when using finite element methods (Dusenberry, 2010).

The analysis and protective design of structures to resist blast loading may be accomplished through a variety of analytical and numerical approaches. Pressure-Impulse charts (P-I charts), single degree of freedom (SDOF) model analysis, multiple degree of freedom (MDOF) model analysis and finite element analysis (FEA) are common approaches to analyze and predict structural response to blast loading.

P-I charts – P-I charts summarize the performance characteristics of different elements, structural or nonstructural, in response to different blast loading based on peak pressure and impulse. The curves on a P-I chart correspond to the thresholds for various levels of protection. As seen in Figure 2-16, there are two asymptotes that occur. One that corresponds to the minimum impulse for all greater peak pressures and the other to the minimum peak pressure for all greater impulses that correspond to a specific performance threshold (ASCE, 2009; Dusenberry, 2010). The pressure and impulse combinations that lie to the left and below of a P-I curve will correspond to better performance while anything above or to the right of the curve will correspond to worse performance. P-I charts are derived using data from a database or available test data and are usually presented as a nondimensional, normalized set of axes to allow for use in a greater range of element responses (ASCE, 2009; Dusenberry, 2010).

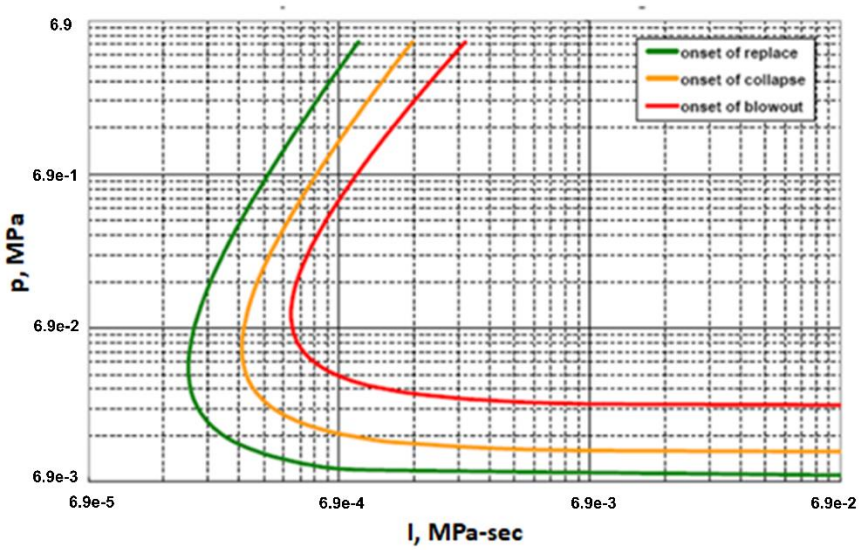

Figure 2-16: Pressure-Impulse (P-I) Diagram *modified from:* (ASCE, 2009).

Single degree of freedom (SDOF) – SDOF models are commonly used to simplify the analysis of the structural response. SDOF models are used for predicting dynamic response of structures subjected to blast loading due to the simplicity and less computationally expensive solution. They require the use of explicit time stepping numerical integration algorithms along with governing equations to represent the elastic and inelastic behavior of the element (ASCE, 2009; Dusenberry, 2010). SDOF methods are described in many structural dynamics textbooks and courses as well as the US Army Technical Manuals (ASCE, 2009; Dusenberry, 2010; Sisemore & Babuška, 2020). The structure can be idealized as an equivalent SDOF spring-mass system. To determine the response of the structure, the solution to Newton's equation of motion for a triangular impulse load is found. Equation 2.24 is the governing second order differential equation for Newton's equation of motion.

$$m\ddot{x} + c\dot{x} + kx = F(t) \tag{2.24}$$

Where $\boldsymbol{m}$ is the mass, $\boldsymbol{c}$ is the damping coefficient, $\boldsymbol{k}$ is the stiffness, and $\ddot{x}$, $\dot{x}$ and x are the acceleration, velocity, and position of the system. The force $F(t)$ is represented by a triangular

linear pulse that is scaled to the magnitude and duration of the positive phase of the Friedlander equation shown in Equation 2.1. This is illustrated in Figure 2-17 and Equation 2.25.

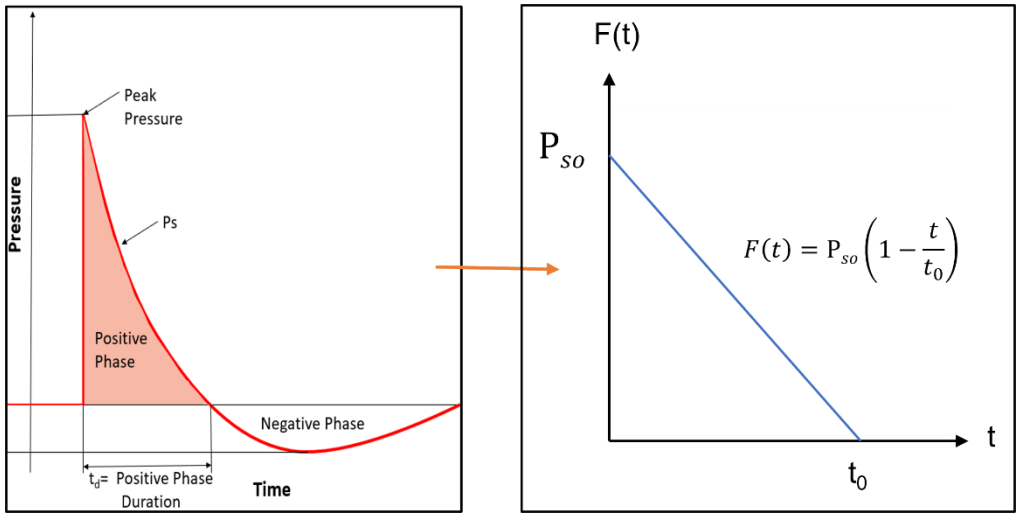

Figure 2-17: Triangular linear load simplification typically used in blast loading scenarios.

$$F(t) = P_{so}(1 - \frac{t}{t_0}) \tag{2.25}$$

Damping is typically ignored in blast loading as it has little to no effect on the system response since the peak response of the wave, which governs design, occurs within milliseconds from the onset of the blast (Hussein et al., 2020; Sisemore & Babuška, 2020). The response of the undamped SDOF system subjected to triangular impulse is as follows:

$$x(t) = \frac{P_{so}}{k}(1 - \frac{t}{t_0} - \cos(\omega t) + \frac{1}{t_0\omega}\sin(\omega t)) \qquad 0 \le t \le t_0 \tag{2.26}$$

$$\dot{x}(t) = \omega \sin(\omega t) - \frac{1}{t_0} - \frac{\cos(\omega t)}{t_0} \qquad 0 \le t \le t_0 \tag{2.27}$$

$$x(t) = x(t_0)\cos\big(\omega(t - t_0)\big) + \frac{\dot{x}(t_0)}{\omega}\sin(\omega(t - t_0)) \qquad t \ge t_0 \tag{2.28}$$

Where $\omega = \sqrt{\frac{k}{m}}$ is the natural frequency of the system, t_0 is the positive phase duration and P_{so} is the max overpressure. The accuracy of these approximate models depends highly on

choosing the appropriate SDOF system to represent the governing failure mechanism of the element (ASCE, 2009; Dusenberry, 2010).

Multi-degree of freedom (MDOF) may be more complex than SDOF models and require numerical tools such as finite element methods to derive the mass and stiffness matrices for systems with large number of DOFs. For this reason, MDOF analyses may be performed using a variety of dynamic response analysis software programs (ASCE, 2009; Dusenberry, 2010). Any MDOF analyses must have a sufficiently small timestep to guarantee numerical stability so it can accurately represent all potential modes of failure (ASCE, 2009; Dusenberry, 2010). Explicit dynamic finite element methods have proven to be effective in determining the response of a structure to blast loading. However, they require sufficient modeling resolution and small-time steps to capture the high frequency, near range effects of the shock wave blast loading and the structural response (ASCE, 2009; Dusenberry, 2010). The critical time step is related to the wave speed of the material and least dimension of the finite element model (ASCE, 2009; Dusenberry, 2010). This results in the equation of motion being solved at each node using the current geometry and material properties at that location at a specific point in time. Implicit methods require the equations of motions to be solved simultaneously through matrix methods which can be very efficient in linear systems. Explicit solvers which use the displacement, velocities, and accelerations from previous timesteps are typically more efficient and accurate in nonlinear systems. The model estimates the response at the end of the time step and then corrects the model to further improve the results in future time steps (ASCE, 2009; Dusenberry, 2010).

2.5.2 Casualties and Fatalities from Blast Loads

The blast shock wave can cause significant damage to the human body. Since each blast is unique based on several factors including charge material, size and shape, the impact can cause a

variety of short- and long-term health effects. Humans can experience severe injuries or even death directly from the blast wave, structural collapse, or projectile debris because of an explosive event. The injuries imposed on the body due to an explosion are split into four categories based on what directly caused the injury and how it affected the body.

Primary Blast Injuries- Primary blast injuries are a direct effect of the blast and blast wave. They take place when the blast overpressure reaches the person and exerts its demand on the body. Primary blast injuries usually happen within tens of meters of the explosive epicenter where the highest-pressure levels of the blast wave can occur (Wolf et al., 2009). Primary injuries mostly involve air-filled organs and air-tissue or air-fluid interfaces. Human tolerance to blast overpressure is relatively high and tests have shown the tolerance to vary with both magnitude and duration of the blast wave, as well as the orientation of the person relative to the blast front (DOD, 2008). The shorter the exposure to the elevated pressure of the shock wave, and the farther away from the explosion, the lower impact on the human body due to a lower magnitude of pressure. Survival is dependent on the mass of the human, where survival of babies will be different than it will be for small children which will be different from that of grown men and women (DOD, 2008). Some of the most common primary injuries are lung and organ damage to the auditory system, gastro-intestinal tract, pulmonary system, and the brain. Threshold values and criteria for primary blast injuries have been developed and contested since the 1960s (Denny et al., 2021, 2023)

Ruptured ear drums are one of the most common primary blast injuries occurring in up to 47% of survivors (Yeh & Schecter, 2012). The tympanic membranes of the auditory system have the lowest pressure threshold for injury. Fifty percent of exposed eardrums rupture at a pressure of

103.42 kPa (15 psi) at short duration, fast rising pressures (DHS, 2005; Hussein, 2019). Temporary hearing loss can occur at much lower pressure levels. McCann (2018) determined the pressure required to cause severe ear damage for different explosive blast settings. Three tests including a game cannon, C-1, and detonation cord were assessed to determine the pressure levels created by each and the likelihood of damage each could create. It was found the game cannon, used during football games, produced a maximum pressure of around 2kPa (0.3psi) resulting in a 160dB noise level. If this level was experienced for 1.75 sec it could risk creating temporary hearing damage in the football spectators especially in close vicinity to the cannon (McCann et al., 2018). The pressure thresholds for eardrum rupture from C-1 and detonation cord were tested using sheep eardrums. It was found that the threshold pressure was between 42-44kPa (6.09-6.38psi). Table 2-6 lists the probability of eardrum rupture for different peak overpressure values (Lees & Mannan, 1996).

Table 2-6: Probability of eardrum rupture for varying peak overpressures (Lees & Mannan, 1996)

Probability of Eardrum Rupture [%]	**Peak Overpressure**	
	psi	**kPa**
1	2.4	16.5
10	2.8	19.3
50	6.3	43.4
90	12.2	84.0

Primary blast injury involving the pulmonary system and the gastro-intestinal tract are rare, occurring in only about 0.3-0.6% of survivors (Yeh & Schecter, 2012). Pulmonary blast injury occurs in the form of spalling or implosion at the level of the alveoli in the lungs. Spalling occurs when a denser medium is displaced or fragmented into a less dense medium (Yeh & Schecter, 2012). In the case of the lungs, this would mean an alveolar hemorrhage. Implosion is the opposite in which a less dense medium is displaced into a more dense medium (Yeh & Schecter, 2012). An air embolism from the alveoli into the vascular system is an example of implosion and accounts

for a high number of deaths in blast events in which it occurs (DHS, 2005; Lozano, 2016; Yeh & Schecter, 2012). Though rare, pulmonary blast injury has a mortality rate of 11% (Yeh & Schecter, 2012). Gastro-intestinal injury occurs more commonly in internal or underwater explosions (Yeh & Schecter, 2012).

One of the more common fields of research in blast loading and blast injuries is traumatic brain injury (TBI). TBI has received increasing attention over the years due to the impact on military personnel and as it is now one of the most common blast injuries. Though classified as a primary injury, it can occur from secondary or tertiary blast injuries as well (Hussein, 2019). Research studies have shown that as the blast shock wave passes to the brain through blood vessels, long term neurological problems can be caused, this means that protecting the head with a helmet will not prevent the cells from damage (Cernak et al., 2001; Cernak & Noble-Haeusslein, 2010). The level of traumatic brain injury can range from a mild concussion to penetrating injury meaning the effects could be temporary or could cause permanent disability. Brain trauma can be difficult to diagnose as it does not have to be related to any direct head injuries (Hussein, 2019). Research over the years has worked to develop better personal protective equipment (PPE) and helmet technology to minimize the possibility of bodily injuries, however, it is still a challenge to protect the head from such injuries(Curley et al., 2011; Gupta & Przekwas, 2013; Hussein, 2019).

Bowen et al. (1968) estimated the human tolerance to free field and reflected blast overpressures for different orientations of the body. Some of developed curves for the perpendicular orientation are shown in Figure 2-18 and Figure 2-19 are commonly referenced for blast injury and survivability prediction. The curves are based on a 70kg man for a single blast wave.

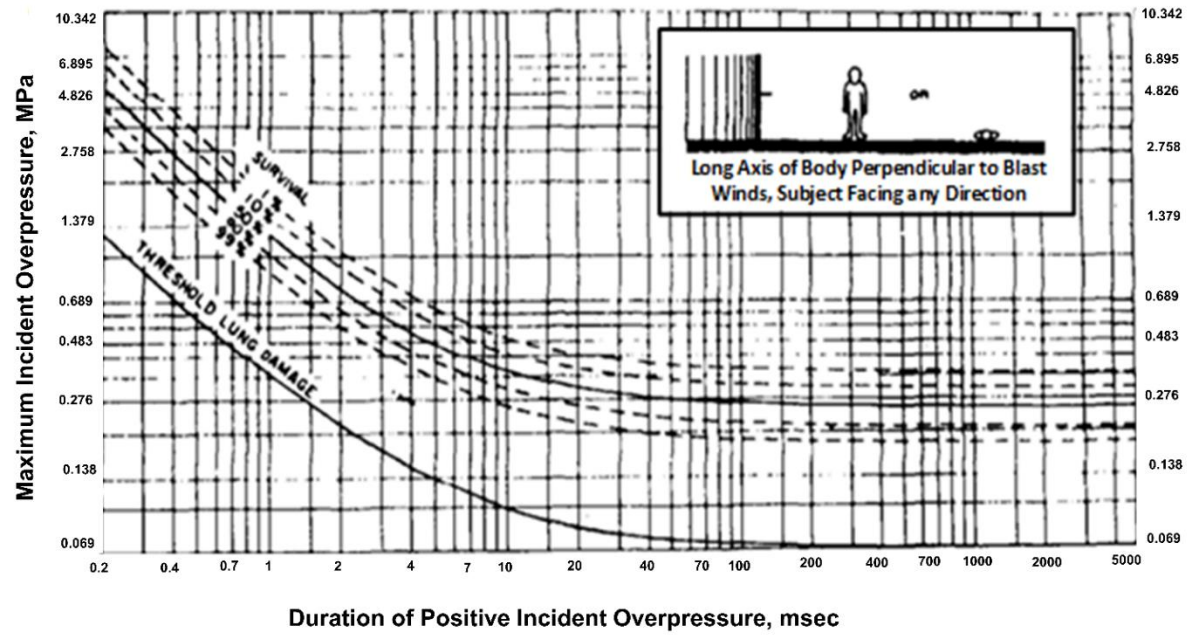

Figure 2-18: Estimated survival curves for free field where long axis of the body is perpendicular to the direction of propagation of the shock blast wave *modified from*:(Bowen et al, 1968).

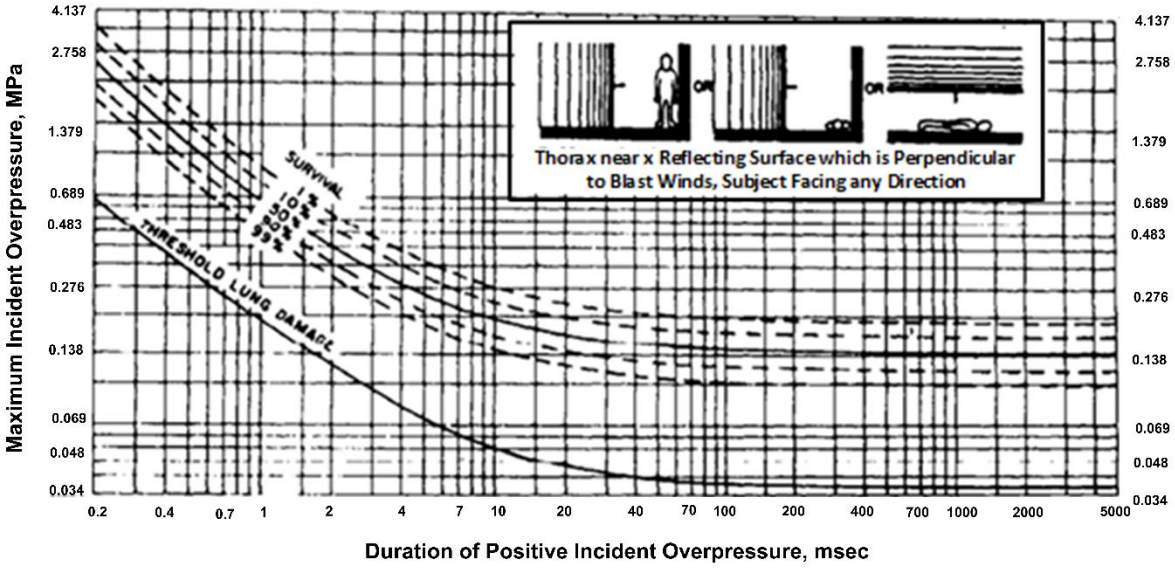

Figure 2-19: Estimated survival curves for blast situations where the man is near a reflecting surface and the long axis of the body is perpendicular to the direction of propagation of the shock blast wave *modified from:* (Bowen et al, 1968).

Secondary Blast Injuries- Secondary injuries are caused by debris or shrapnel physically displaced or propelled by the blast or blast wave. The fragments associated with secondary injuries are

classified as primary or secondary fragments. Primary fragments are typically small, high-speed fragments that cause penetrating injuries and perforation of vital areas of the body (DHS, 2005; Lees & Mannan, 1996). The level of injury from primary fragments relates to the fragment area to weight ratio and velocity. As the area to weight increases, the velocity necessary to have 50 percent probability of penetrating the human skin increases (DOD, 2008). Secondary fragments, which are normally larger and have greater mass, can travel at significantly lower velocities than the primary fragments, but still cause serious bodily harm. Secondary fragments can cause a combination of blunt and penetrating injuries (Wolf et al., 2009). Since these fragments are being propelled by the blast wave, the distance in which these fragments can travel and cause injury can reach up to thousands of meters (Wolf et al., 2009). The serious injury thresholds for different body parts depending on fragment velocity and mass are shown in Figure 2-20. The penetrating injuries from the primary fragments (shrapnel that are a part of the weapon) and secondary fragments (those that are the result of the explosion) are the leading cause of death and injury in military and civilian terrorist attacks (DePalma et al., 2005). Overall human tolerance to fragment impact is very low (DOD, 2008).

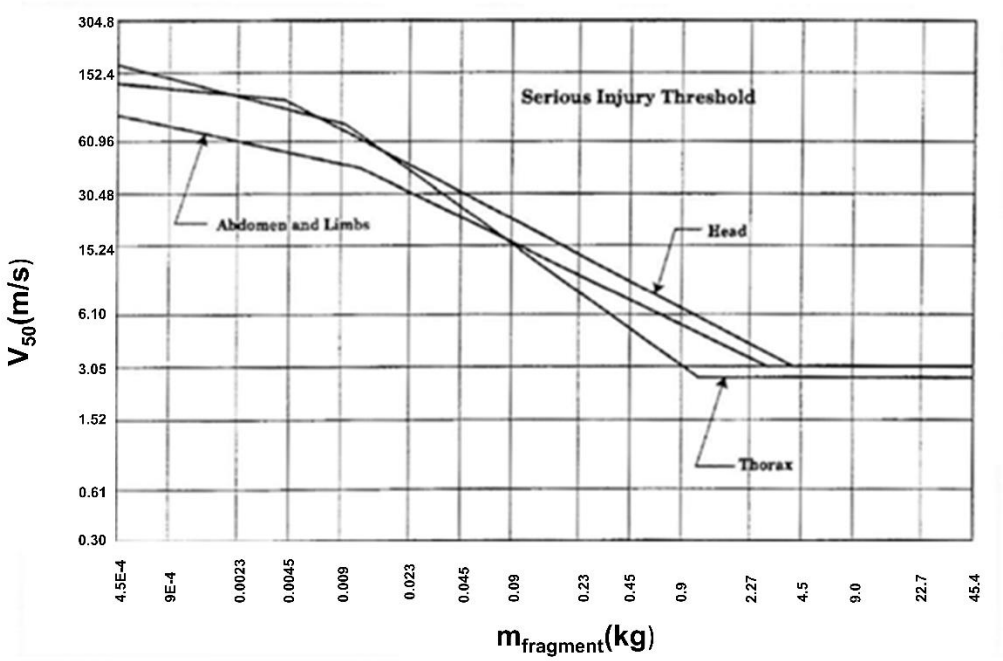

Figure 2-20: Serious injury thresholds from fragment impact *modified from:* (DOE, 1981).

Tertiary Blast Injuries- tertiary injuries are the injuries caused by bodily translation or displacement by the force of the peak overpressure. Blunt trauma injuries such as closed head injuries, blunt abdominal trauma, tissue contusions or fractures are common tertiary injuries. The extent of the injuries depends on several factors such as the type of surface impacted, area of the body involved, and velocity of impact (Lozano, 2016). Due to the delicate nature of the human head, translation damage criteria are often reported based on skull fracture and concussion likelihood (DOE, 1981). Studies show that the probable safe impact velocity is around 3.048 meters per second (mps) (10 feet second (ft/s)). As the velocity increases, the likelihood of serious bodily injury increases. At 5.486mps (18 ft/s), there is a 50 percent probability of skull fracture and at 7.010mps (23 ft/s) the probability is near 100 percent (DOD, 2008) as shown in Figure 2-21 below.

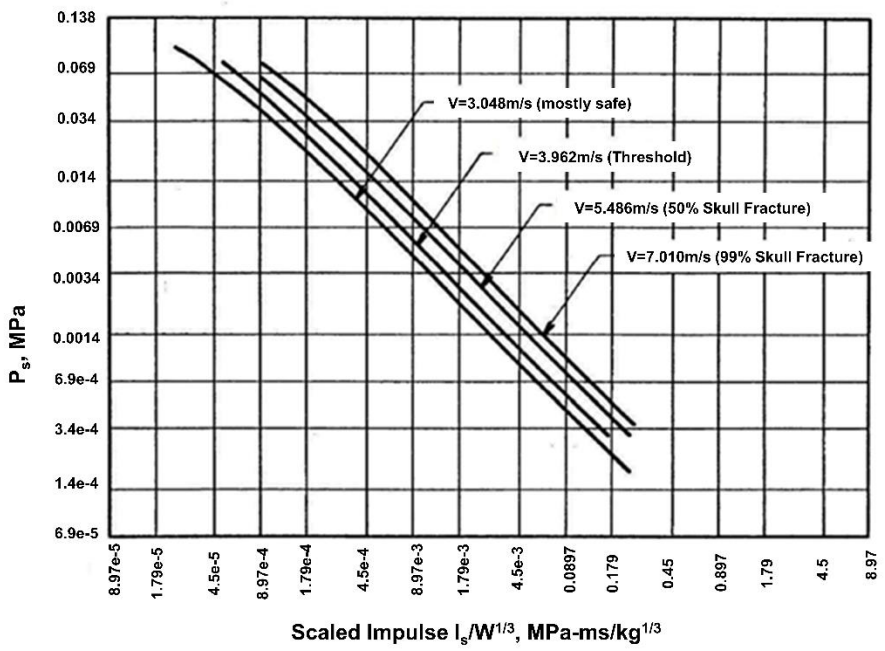

Figure 2-21: Pressure vs Impulse skull fracture probability curves *modified from:* (DOE, 1981).

Another cause of tertiary injuries is structural collapse. The collapse of structures causes a higher rate of death due to crush and compartment injuries (DOD, 2008). Crush syndrome is a condition caused by an excessive compressive force applied to a muscle or tissue for an extended period, causing compromised local circulation (Gonzalez, 2005). The resulting muscle and tissue damage will cause the release of toxins into the body, which can lead to life threatening complications such as renal failure or heart attack (Gonzalez, 2005). Compartment syndrome results from the compression of a closed osteofascial compartment that causes the intercompartmental pressure to increase resulting in significant pain that appears out of proportion to the injury (DePalma et al., 2005; Via et al., 2015). The leg and forearm are most frequently affected but it can occur with hands, feet, and buttocks (Via et al., 2015). If the pressure is not surgically relieved quickly, local tissue necrosis and permanent disability may occur (DePalma et al., 2005; Via et al., 2015). Crush injuries and fractures are common causes of compartment syndrome (DePalma et al., 2005; Via et al., 2015).

Quaternary Blast Injuries- quaternary injuries refer to the miscellaneous injuries that are caused directly by the explosion but are not classified as primary, secondary, and tertiary injuries (Wolf et al., 2009). This includes burns, asphyxiation, inhalation of foreign substances, exposure to toxic chemicals, radiation, and biological weapons (Wolf et al., 2009). Crush injuries are sometimes classified as quaternary blast injuries as well. This includes psychological effects such as post-traumatic stress disorder as well.

2.6 Blast Mitigation Techniques for Protecting Structures and Human Bystanders

When it comes to providing protection against blast loading, research tends to focus on protecting structures since they have been the main target of terrorists for decades. Many techniques for protection and design of structures have been developed over the years. On the other hand, methods for protecting people are minimal, especially within non-military public settings.

2.6.1 Protection Methods for Structures

Extensive research has been completed on methods for protecting structures from blast loading. Research conducted on how to make a structure more blast resistant and how to create a barrier are the most common forms of research. Both methods of protection follow very similar paths when it comes to research and improving the designs. Material manipulation, reinforcement or cladding, and geometric manipulation are common techniques researchers have developed for new blast resistant structures.

Structures - over the years as technology has improved, researchers have continued to look for ways to understand and improve blast resistance of structures through material or geometric

manipulation. The use of composite materials has grown in popularity in blast resistance. Numerous studies have been completed using experimental methods or finite element methods to investigate the effects of FRP composites to strengthen concrete and masonry structures for blast resistance. Buchan & Chen (2007) provided an extensive review of studies completed on FRP and polymer composite effects on concrete and masonry structures. Research has shown that retrofitting using FRP, and polymer can significantly increase the blast resistance of a concrete structure (Buchan & Chen, 2007; Pezzola, 2018). Glass fragments can cause large casualties and serious injury. Stewart and Netherton (2008) developed fragility and reliability curves for different window glazing systems for a variety of explosive weights to be used in probabilistic risk assessment. The use of blast resistant laminated glass or glazing can significantly reduce the level of injury caused by glass fragments; however, it is not very transparent making visibility more difficult. Khanna and Zhu (2016a, 2016c) developed a laminated glass that has a transparent glass fiber reinforced composite interlayer. When tested, it could survive medium to high intensity blast loading without fragmentation (Chen et al., 2012; Zhu & Khanna, 2016a, 2016b).

Other studies are looking for ways to increase energy absorption to limit the propagation and duration of the blast wave. Sandwich structures are a common design choice when it comes to blast resistance. Sandwich structures are a composite structure that consists of two sheets of high-ductile materials to resist and reflect the blast shock wave. The core or interlayer of the sandwich structure is made of a high compressible, low-density material such as foams or other porous material to absorb the shock wave (Hussein, 2019; Hussein et al., 2020a; 2020b). Figure 2-22 illustrates the components of the sandwich structure.

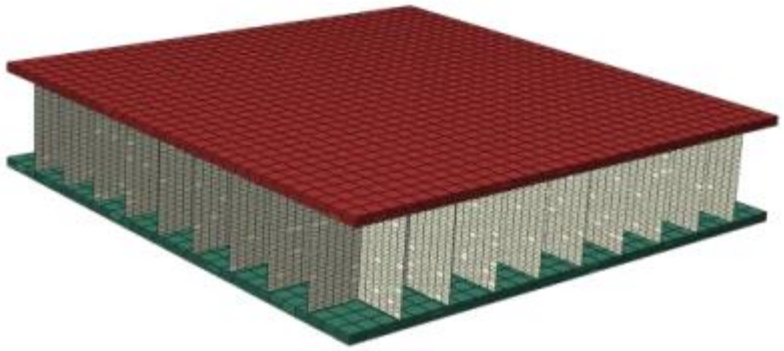

Figure 2-22: Sandwich Structure Blast Resistant Panel (Dharmasena et al., 2008).

Lee and O'Toole (2014) examined the design of a honeycomb core structure for sandwich panels for energy absorption during blast loading. Using FEA, the study found that the face-sheet and core sheet thicknesses are critical to uniform permanent deformation. The optimal thickness for the core sheets were similar with the inner core thickness of 0.2 mm (0.008in) and outer core was found to be 0.4mm (0.02in). The face sheet thicknesses differ significantly at 26.6 mm (1.05in) for the back sheet and 2mm (0.07in) for the front sheet. It was found the nonuniformity of the deformation pattern impacts how much energy is absorbed from the wave. If the sheet thicknesses are not optimal, nonuniform deformation of the honeycomb core can occur which tends to increase the total energy applied to the structure and the rigid body velocity (Lee & O 'Toole, 2014).

Dvorak and Bahei-El-Din (2008) analyzed the effect of design modifications on the blast resistance of sandwich plates. Four designs were tested with different core interlayers that included a structural foam, polyurethane interlayer, elastomeric foam interlayer, and a combination of both polyurethane and elastomeric foam. FEA was used to complete the analysis for the response of the sandwich panels. It was concluded that the use of interlayers is beneficial to the performance of the sandwich panels under blast loading by reducing kinetic energy, increasing energy absorption, and reducing the compression of the inner core and plate deflection (Bahei-El-Din & Dvorak,

2008). The use of a polyurethane or elastomeric foam interlayer or even a combination of both, increases the performance significantly from the original sandwich panel with a normal structural foam core.

Drdlova et al. (2015) investigated the response of energy absorbing materials as potential core materials for sandwich structures. Two porous materials based on expanded glass and ceramics were mixed with polymeric binders to create new blast wave absorbers. Experimental and numerical modeling concluded that the glass-based absorber exhibited lower potential for energy absorption than the ceramic absorber (Drdlová et al., 2015). The ceramic absorber increased the strength as well as decreased the dynamic deflection of the structure over all by 26.2%.

Gebbeken and Döge (2010) investigated the effects that structure shape had on blast loading. They analyzed a variety of shapes including square, long rectangular, circular, cylindrical, pyramid and hyperboloid to compare the peak reflected pressure each structure experienced. It was found that to reduce loading on the structures the number of reentrant corners needed to be minimized. These corners enhance the reflection and amplify the blast loading on the structures (Gebbeken & Döge, 2010). Further they conclude that convex shapes perform better than concave shapes. This is due to the angle of incidence on a convex shape increasing more rapidly than it does on a planar surface resulting in a faster decay rate of the reflected pressure (Gebbeken & Döge, 2010; Goel & Matsagar, 2014a). Ultimately, it was observed that to reduce design loads, normal reflections should be avoided with simple geometry.

Perimeter Walls or Barriers – making a structure more blast resistant can be an expensive affair between detailed design, material manipulation and hardening, geometric design, and site layouts

(ASCE, 2011; Dusenberry, 2010; Goel & Matsagar, 2014). An alternative protection method is to create a barrier. Barriers act to mitigate blast loading and blast wave propagation in two ways. First, as a standoff barrier to increase the distance between the explosion and the intended target structure and second, as an obstacle to the propagation of the blast wave. Maintaining a sufficient standoff distance is often one of the most effective methods of protection from blast loading (Lee & O 'Toole, 2014).

Goel and Matsagar (2014) discussed and reviewed the properties of a barrier, geometry, and material which had been determined by previous studies. It was concluded that a sacrificial layer integrated into a structure that is made of lightweight, energy absorbing materials are recommended to avoid fragmentation and lower the peak reflected overpressure. Sacrificial walls that have lightweight energy absorbing materials such as metal foams, polymeric foams, or something similar sandwiched between two stiffer layers, results in less energy transferred to the parent structure (Goel & Matsagar, 2014a). It was found that the surface of the wall facing the explosion should be vertical for as far as possible.

Xio et al. (2017) developed a method for predicting the effectiveness of a barrier using numerical analysis to overpressure-time histories behind the barriers. Experiments for three different barriers were conducted and the peak overpressure and impulses were recorded. The numerical models were validated with the results of the physical tests. It was found in this study that the barrier effectiveness depends on the design and arrangement of the barriers. The effectiveness was based on if the blast effects behind the wall had been reduced. Generally, of the three designs tested, the barrier configuration with a canopy attached to the front surface of the wall with a 45° angle of inclination and orientated toward the charge performed the best in overpressure reduction. All three configurations reduced impulse to a nearly identical amount.

Beyer (1986) at the Naval Civil Engineering Laboratory developed a preliminary design criterion for vertical cantilever barriers where the explosive is immediately behind the wall. Ten total tests were conducted with three canopy styles and three charge weights. All barriers were not damaged, and the canopies were all blown away from the wall for all tests. The design criteria were presented in terms of the peak overpressure, total impulse and scaled distance are presented in graphical form for different scaled heights and angles.

Historically, natural materials such as soil or sand have often been used for protection purposes. Both have been used for many different purposes including providing protection from floods, fires, and shock absorption in civilian and military applications. This is the main motivation behind a HESCO barrier. A HESCO barrier is wire or steel mesh container filled with sand or soil. These individual containers are stacked to form a wall. Another common barrier material is concrete or reinforced concrete. Reinforced cement concrete (RCC) panels or T-walls are a commonly used structure for protection and blast mitigation. Figure 2-23 shows typical T-wall and HESCO barriers.

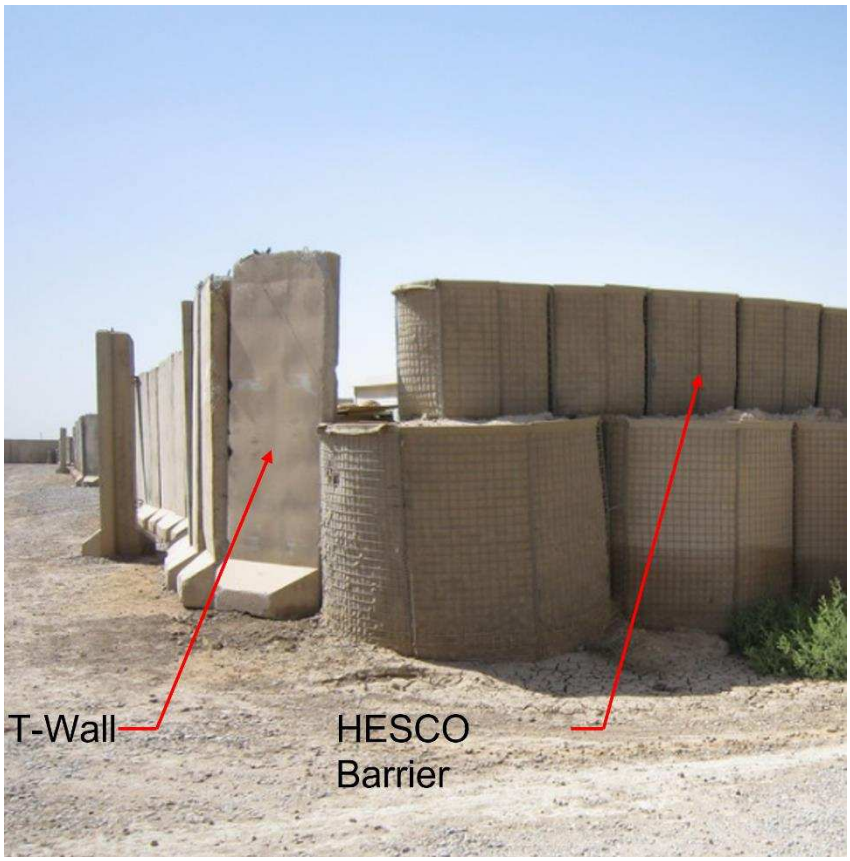

Figure 2-23: T-Wall blast barrier and HESCO barrier filled with sand (Sherman, 2011).

In a study conducted by Trasborg (2014), the construction and economic benefits of using precast panels rather than site-cast panels for concrete sandwich panels were explored. Pre-cast sandwich panels are ideal systems to meet both protection and environmental criteria developed by the U.S. Army. Initially, precast panels failed to meet the hazardous and blowout levels of protection standards. The tests completed showed the improvement of ductility from local un-bonding of the longitudinal reinforcements and the results illustrated the relationship between increasing ductility, resistance, and local un-bonding length (Trasborg, 2014).

In a study conducted by Khan, Farooq, and Usman (2019) the response of RCC panels to blast loading was investigated to determine the effect of steel strips on the resistance of the existing structures. Simulations of the effects of integrating the steel strips were completed for two charge

weights based on previous terrorist attacks. It was found that the steel strips increased the blast performance of the RCC panels, and the strips significantly reduced the deflection and pressures for both charge weights tested (Khan et al., 2019).

Hussein (2019) developed a barrier made from low-tech common materials. The sandwich structure design was utilized with two orientated strands board (OSB) face sheets and a sand interlayer to act as an absorbing layer. The barrier was modeled using FEA and SDOF methods as well as tested experimentally to validate the models. The results of the study demonstrated that the simple barrier could effectively reduce the pressure behind the wall, while limiting fragmentation and shrapnel due to the absorbing nature of the sand layer. It was found that the mass of the structure had the largest role in absorbing the blast shock energy (Hussein, 2019; Hussein et al., 2020a; 2020b).

Similar to structural design, the shape of barriers has been a popular research topic in hopes to find the optimal geometry for protection. Belegundu & Rajan (2008) developed an approach for optimizing the shape of metal plates subjected to blast loading using FEA. The finite element model utilized the CONWEP function in LS-DYNA to create a blast load and to minimize the dynamic deflection and plastic strain of the aluminum plate. By varying the number of design variables, model envelope size and limitations, and symmetry of the problem the optimal shape of the plate varied. The plate mass and max plastic strain varied minimally between the different models.

Taha et al. (2019) investigated the effects of changing the shape of concrete structures against comp-B explosions using the hydrocode simulations. Concrete walls of flat, convex, and concave shape were tested to determine the effects of changing the angle of curvature on the effectiveness of the barrier in mitigating blast loading. Gages were placed along the top, middle

and bottom of the front and back surface of each of the walls. The results showed that changing the shape of a barrier to a convex curve with a 60° angle of curvature had the best performance in mitigating blast wave effects. The peak pressure at all gage locations in the simulations were significantly lower for the 60° convex barrier than it was for all gage locations for the other barrier shapes modeled. Only the peak pressure at gage location three along the top of the front surface, on the convex 50°, concave 50° and the flat wall were less than the 60° convex wall. The internal energy of the convex wall with 60° curvature was the highest of all walls modeled confirming the results of the pressure findings. As the internal energy of the barrier increases, the resistance to blast loads increases resulting in the pressures behind the barrier wall decreasing (Taha et al., 2019).

2.6.2 Protection Methods for Human Bystanders

When it comes to protection against blast loading for people, the current research trend is to protect people inside buildings by protecting the structure with a barrier, or by implementing techniques of blast resistant structural design. Similar design ideas for barriers to protect structures can be applied to protecting individuals which involves the use of specialized materials, sandwich designs, and reinforced coatings (Lahiri & Ho, 2011). The limiting factor of current strategies developed for protecting structures is they focus on reflection of the shock wave or absorption of the shock wave to the point of plastic deformation and failure of the cladding or wall structure (Goel & Matsagar, 2014a).

Reflection off a barrier can be detrimental to mitigation and protection of humans as it could increase both the duration of loading and the magnitude of loading humans may experience if the wave is reflected on them. Diffraction and absorption are better approaches to mitigating the duration and magnitude of the pressure wave as it does the opposite of reflection by mitigating the

duration and magnitude of the blast wave. Studies such as Hussein et al (2019; 2020a; 2020b) and Taha et al. (2019), provide background on material and geometric manipulation of barriers that could be utilized in protecting people in large open areas due to the reduction of pressure and level of protection behind a barrier found in those studies.

2.7 Summary

This chapter presented a comprehensive literature review on five different topics that include explosive threats, blast loading characteristics, modeling methods, explosive effects on structures and humans, and mitigation techniques for structures and humans. A summary of the main findings of the literature review are listed below.

- Terrorist organizations around the globe utilize explosives to achieve a variety of goals due to the highly destructive nature of explosives as well as ease of fabrication and availability of components.
- IEDs have a large variation of size, shape, and type of explosive that all drastically influence the impact it can inflict.
- The UFC 3-340-02 is a manual overseen by USACE that provides methods for establishing blast load parameters such as pressure and impulse. The manual provides methods for calculating dynamic response of structural elements to a variety of explosions ranging in shape, size, and confinement.
- There are a variety of analytical, empirical, and numerical methods for modeling blast loading and its effects that range in accuracy and efficiency. ANNs are a common tool in blast mitigation for modeling a complex blast scenario from existing data.

- When a blast shock wave interacts with a structure it has an impact on the blast wave and on the structures. Reflected blast shock wave parameters can be calculated using methods shown in the UFC 3-340-02. Models such as SDOF, MDOF or FEA can be used to assess the structural response to the blast load.
- The blast shock wave can cause significant damage to the human body either from the blast wave itself, projectile debris and fragmentation, or resultant structural collapse. The injuries imposed on the body due to an explosion are split into four categories based on what directly caused the injury and how it affected the body.
- Extensive research and methods for protecting structures from blast loading have been developed over the years. Material manipulation, integration of reinforcement or cladding and geometric manipulation are the most common techniques for either improving the structure itself or designing a barrier to protect the structure from certain attacks.
- Minimal research has been done on the effects of multiple barriers on the blast shockwave in external open areas.
- Minimal research has been made available to the public on how to protect people in large open areas where primary and secondary injuries to a blast event could occur without any protection. Both the duration and magnitude of pressure are important factors in the degree of injury of human bystanders and need to be minimized as much as possible.

CHAPTER 3: SCALED FIELD EXPERIMENTATION OF DOUBLE-BARRIER NETWORK IN BLAST MITIGATION

3.1 Introduction

As the threat of terrorist bombings has grown around the globe, the awareness for blast analysis and the threat and impact of explosive attacks on people and the built environment has increased considerably over the last few decades. Due to the use of improvised explosive devices, infrastructure such as government buildings and embassies are no longer the only targets. Large gatherings of people for concerts, political rallies, or sporting events are targets for terrorist bombings that can result in mass casualties. One of the simplest ways to provide protection and increase survivability against these attacks is to implement compartmentalization barriers (for fragmentation protection) or perimeter barriers (to enforce standoff).

Providing a barrier can not only increase protection from fragmentation and enforce standoff but also reduce the energy and pressure experienced behind the barrier as it provides a physical obstacle to the propagation path of the blast wave. Numerous studies have been done over the years to understand the impact a barrier has on the blast shock wave. Different shapes, sizes, and materials have been tested to determine new innovative ways to provide protection to structures (Bahei-El-Din & Dvorak, 2008; Dharmasena et al., 2008; Hussein et al., 2020a). Various studies have been done to assess the effect of different barrier shapes in confined settings such as shock tubes and internal environments (Epstein & Kudryavtsev, 2012; Gan et al., 2022; Hajek & Foglar, 2015; Ivanov et al., 2019; Kumar R & Pathak, 2021; Niollet et al., 2015). However, little research has been done on the effects of multiple barriers on the blast shockwave in external open areas.

Accordingly, it is imperative to develop a clear understanding of the effect of multiple barriers on airblast pressure through analytical, numerical, and experimental testing. Analytical and numerical methods have grown in popularity over the years because of their accurate and rapid evaluation capabilities. In many cases, however, experimental testing remains a necessary method for verifying these models so they can be further used in extensive parametric studies. Issues of scale, equipment capacity, and availability of research funding continue to limit the extent of full-scale blast testing that is possible. Therefore, it is important to explore the use of small-scale testing as a more cost effective and rapid way of testing.

Busch et al. (2016) used small-scale airblast experiments on clay soils to compare experimental results to numerical predictions. It was found that using explosive masses between 0.9 and 100 g showed the numerical model is good as a first estimate but does not capture the post peak response well. Rose et al. (1995) used a 1:10 scale experimental set-up to assess the effects of having no barrier and having a barrier present in a blast scenario. The charge used was 75 g (0.17lbs) of TNT, which, at full scale, would represent a vehicle bomb. The results were used to create contour plots of the pressure and impulse behind the wall to quantify the impact of a barrier. It was found that the blast experiments can be successfully performed at a 1:10 scale, with consistent results compared to previous experimentation from other studies. Rickman and Murrell (2007) used small-scale blast tests on a tabletop as described in Ohrt et al. (1998) to create experimental results that could be used to develop a new method for predicting pressure relief. The small-scale experiments involved a single, nonresponding, rectangular structure with pressure gauges mounted in the structure. The charge size was kept the same, and the scaling of the building was adjusted to represent different blast events of interest for the development of the pressure relief prediction method. The experimentation was able to validate the new methodology for predicting

the onset and magnitude of pressure relief on a directly loaded wall. The experiments showed good agreement with the pressure and impulse values as compared to the methodology developed in the study. Bevins et al. (2003) tested the effects of having a soil berm between a barrier and the structure of interest to further reduce the blast wave or secondary fragments from the explosion. In that study, the berm was found to have little to no effect on reducing the pressure further but did reduce the impulse. Smith et al. (1992) performed small scale experiments at a 1:45 scale for a variety of tunnel shapes and venting for cubicles. The small-scale experiments were compared to larger-scale experimental results and were found to have a good correlation between the results for peak overpressure comparison. It was found that slightly larger experiments, such as 1:30 or 1:40 scales, could give more satisfactory results.

This chapter presents the use of a reusable tabletop system for small-scale airblast experiments, allowing for efficient and repeatable testing in a condensed setting for multiple scenarios. The main focus is understanding and predicting the behavior of the blast shockwave as it interacts with multiple rigid barriers to verify the predictions made by hydrocode simulations of the same set up and to establish a new method of testing airblast parameters such pressure and impulse. When it comes to reporting blast parameters, often pressure and impulse are used. Human injury thresholds from blast events are commonly presented in terms of pressure. Therefore, as the major focus of this effort is to understand how the use of perimeter barriers can reduce the potential injury to people, pressure was the main blast parameter investigated. In this chapter, three different wall configurations were used to investigate how the presence of a double-barrier system affects the shockwave and subsequent observed pressures around and behind the barriers. The explosives used were hemispherical and elevated spherical C4 charges. Pressure gauges are used to read

pressure in front of, between, and behind the barriers on the tabletop. The airblast effects, such as pressure and impulse, from the scaled experiments are presented and compared to the predictions using a hydrocode model for validation.

3.2 Numerical Hydrocode Simulations

Prior to conducting the tests, a two-dimensional numerical model of the double-barrier system was developed to establish an understanding of the expected behavior of the airblast pressure. The numerical models provided a baseline prediction of the experimental results as well as the final experimental configuration and testing matrix. The two-step Eulerian-based hydrocode, CTH, which has been used extensively in blast modeling and has been well validated for complex blast scenarios (Flood & Bewick, 2010; Homan et al., 2013; McGlaun et al., 1990; Needham, 2009; Schmitt et al., 2017; Zapata & Weggel, 2008) was used in the analysis. Two identical rigid barriers were utilized to represent perimeter barriers with varying distances, *d*, separating them, as shown in Figure 3-1.

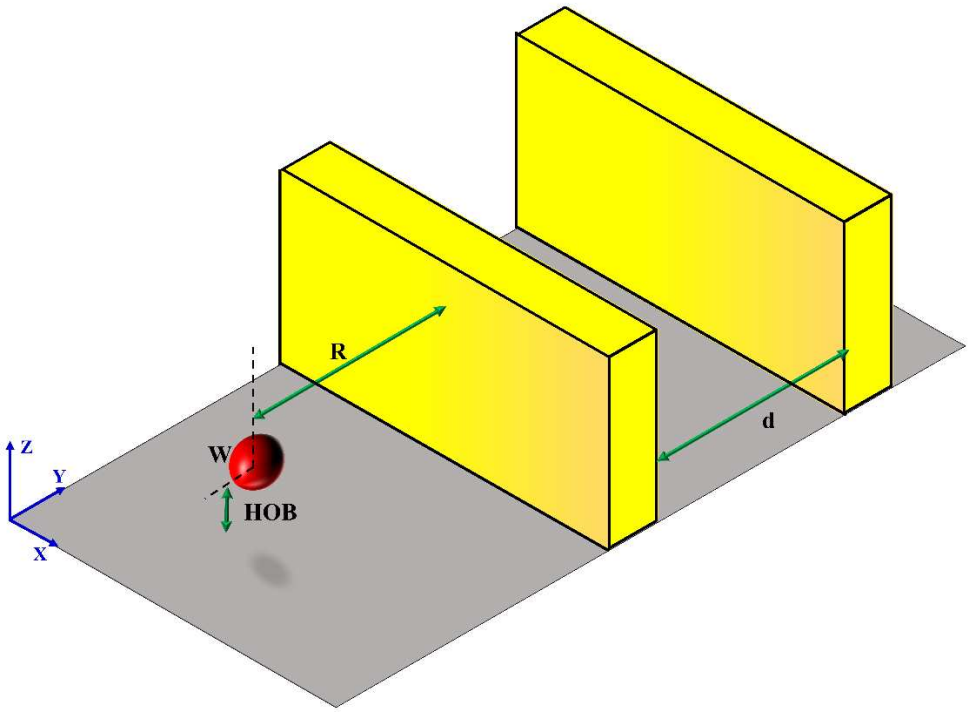

Figure 3-1: CTH model and experimental setup diagram with corresponding inputs.

The walls in the 2D numerical models were considered infinitely long to avoid considering wrap around effects. Clearing over the top of the barriers was accounted for, however. The walls remained fixed and rigid in the model. The varied inputs to create the numerical models are summarized in Table 3-1.

Table 3-1: Input parameters for the numerical model.

Parameter	Unit	Description
W	kg	Weight of explosive charge in lb. of Trinitrotoluene (TNT)
HOB	m	Height of burst of charge. 0: hemispherical, bottom detonated charge >0: spherical, center detonated charge
Z	$m/kg^{1/3}$	Scaled standoff distance of the front surface of the first wall to the charge center (Equation 3.1)
d	m	Distance between the two barriers

The scaled distance, *Z*, was calculated from the charge weight, *W*, and the distance from the center of the charge to the point of interest, *R*, using Equation 3.1.

$$Z = \frac{R}{\sqrt[3]{W}} \tag{3.1}$$

The two-dimensional cylindrical (2DC) axisymmetric domain was created for the largest distance between walls *d* and the largest scaled distance, *Z,* to be tested that allowed for the full expansion of the blast wave without any interference of the boundaries. A high-resolution flat mesh that allowed for 40 cells across the radius of the charge of the explosive was used for the area of data collection inside the domain, while a biased mesh that extended to the end of the domain outside the area of data collection, with larger cells was used to reduce computational costs. An equation of state (EOS) was required for each material modeled to accurately simulate the relationship between pressure and density of a material. In this study, the air was modeled with SESAME, which is the general tabulated EOS in CTH for air (Schmitt et al., 2017). The Jones-Wilkins-Lee (JWL) is the widely used EOS for detonation products of explosives (Lee et al., 1968). The JWL EOS constants for TNT were taken from the literature (Dobratz, 1981). The ideal burn model of HEBURN was used to fully detonate the explosive in each simulation.

3.3 Experimental Tabletop Testing

3.3.1 Testing Materials and Testing Matrix

A reusable tabletop developed by the U.S. Army Engineer Research and Development Center (ERDC) (Hoemann, 2023) was used to perform the small-scale testing and validate its results against the CTH model. The tabletop was a 2.44 m (8 ft) by 3.66 m (12 ft) steel table, as shown in Figure 3-2. A hole was machined at 1.22 m (4 ft) in the long direction (Y) and 1.22 m (4 ft) along the short direction (X). This hole allows for a replaceable 98.43mm-diameter (3 7/8 in.), 4.76 mm-thick (3/16 in.) steel puck to be placed under the charge. The dimensions of this hole

(and steel puck) were previously determined after extensive modeling of the table was conducted, where the detonation train and a range of charge weights were explicitly modeled (Hoemann, 2023). In these models, the size of the puck was varied until the damage from the detonation was contained to only the puck and not the table. The concept of the puck allows for this table to be reusable, as the only thing that needs to be replaced from experiment to experiment is the puck itself. During experiments, the damaged puck was expelled downwards after the shock wave translates past the puck. This timing of puck expulsion was verified in proof-of-concept testing and computational modeling (Hoemann, 2023).

Figure 3-2: Steel rectangular table used for small-scale testing of a) free fields and b) multi-wall experiments.

Using Equation 3.1, the full-scale setup was scaled down to 1/6 scale to fit on the tabletop. The small-scale test matrix, along with associated full-scale values, is shown in Table 3-2, where "FF" means free field testing where no walls were attached to the table. The walls used in the experimental program were 304.8 mm (12 in.) high and 25 mm (1 in.) thick. The walls were designed to run the width (2.44 m) of the table to avoid wave wrap around effects to match the set up in the 2D numerical model described previously. The walls were cut to size from a 2.44 m (8

ft) cold-rolled steel plate, and holes were tapped on one edge for the screws to connect through in the bottom of the table.

Table 3-2: Full and small-scale test matrix.

Experiment Number	W [kg]	W_{Scaled} [g of C4]	HOB [m]	HOB_{Scaled} [mm]	Z [kg/m$^{1/3}$]	d [m]	d_{Scaled} [mm]
1	18.14	65.63	0	0	2.58	FF	FF
2	18.14	65.63	0.91	152.4	2.58	FF	FF
3	18.14	65.63	0	0	2.58	1.22	203.2
4	18.14	65.63	0.91	152.4	2.58	1.22	203.2
5	20.41	73.83	0	0	2.97	FF	FF
6	20.41	73.83	0	0	2.97	1.68	279.4
7	22.68	82.03	0	0	2.22	FF	FF
8	22.68	82.03	0	0	2.22	2.90	482.6
9	13.61	49.22	1.3	0	2.63	FF	FF
10	13.61	49.22	1.3	212.7	2.63	2.90	482.6

The experiments were chosen to minimize the number of holes drilled in the table while allowing for the desired data collection. The holes drilled for the pressure gauges were 25.4 mm (1 in.) and threaded with fine threads to hold the gauge mount. Nine 14.3 mm (9/16 in.) holes for each wall location were drilled in the table. Then, the 12.7 mm (1/2 in.) socket head screws were used to attach the walls to the table.

3.3.2 Instrumentation

Eight model HKS-375 pressure gauges manufactured by Kulite Semiconductors, Inc., were installed in different locations in the table depending on the test. The pressure gauge thresholds ranged from 172.4 kPa (25 psi) - 1723.7 kPa (250 psi) depending on the location on the table to prevent the pressures from exceeding the ideal range of each gauge (between 10% - 50% of the gauge maximum threshold). Gauge P1 was installed to capture the incident pressure and was located on the opposite side of the charge from the walls at a distance of 3H where H is the height of the walls of H = 305 mm (12 in). Gauges P2-P8 were spaced around the walls for each experiment, as shown in Figure 3-3, where *d* is the spacing between the walls.

Table **3-3** summarizes the different wall ranges and spacing for each of the 10 experiments.

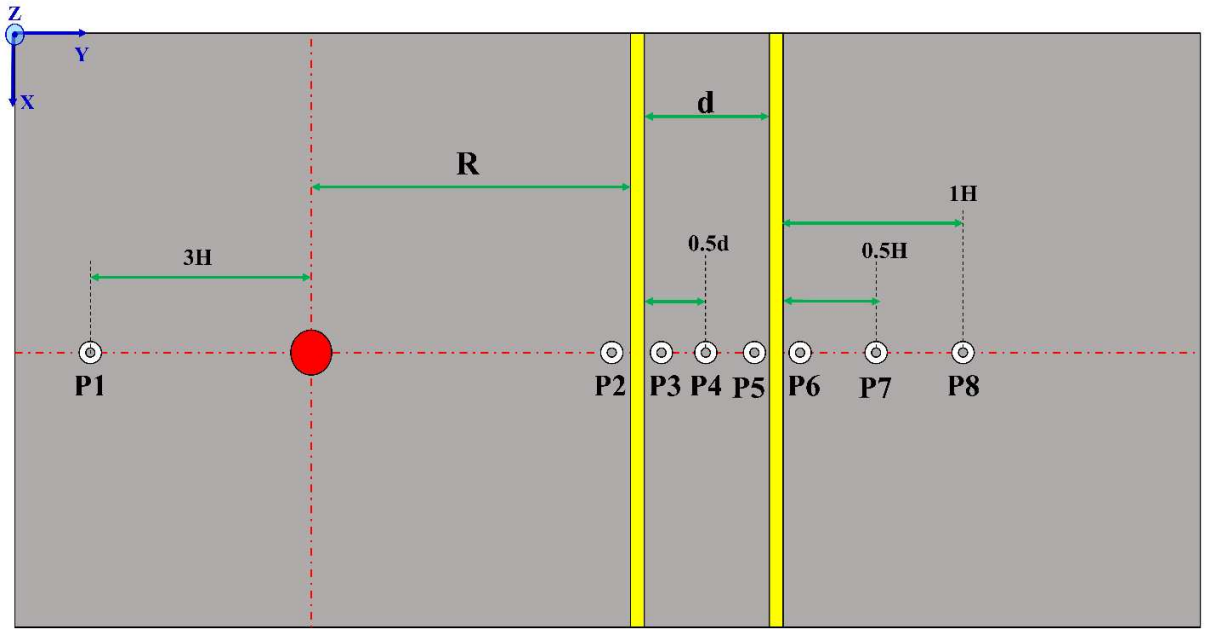

Figure 3-3: Pressure gauge location general diagram where H is the wall height.

Table 3-3: Wall Locations for Each Experiment Labeled from Figure 3-3.

Experiment Number	R [mm]	d[mm]
1	FF	FF
2	FF	FF
3	1041.4	203.2
4	1041.1	203.2
5	FF	FF
6	1244.6	279.4
7	FF	FF
8	965.2	482.6
9	FF	FF
10	965.2	482.6

Three high speed Phantom video cameras were used to capture a variety of views of the tabletop testing. Cameras one and two were inside a structure facing the table to capture the long edge (Y) image of the table and a close up on the walls, as shown in Figure 3-4. The tripod legs of both cameras were secured with sandbags. Camera one was set to capture the whole table view with a 1280x800 resolution and 4,000 frames per second (fps) frame rate. Camera two captured a close-in view of the walls and the shockwaves interaction with the walls. The resolution of camera two was 1280x800 with 4200fps. Camera three (640x480 resolution and 4000fps) was located along the long axis of the table in the field to capture the short edge (X) image of the table, as shown in Figure 3-5. All cameras had a popup tent placed over them to protect from any rain or weather that could occur during testing.

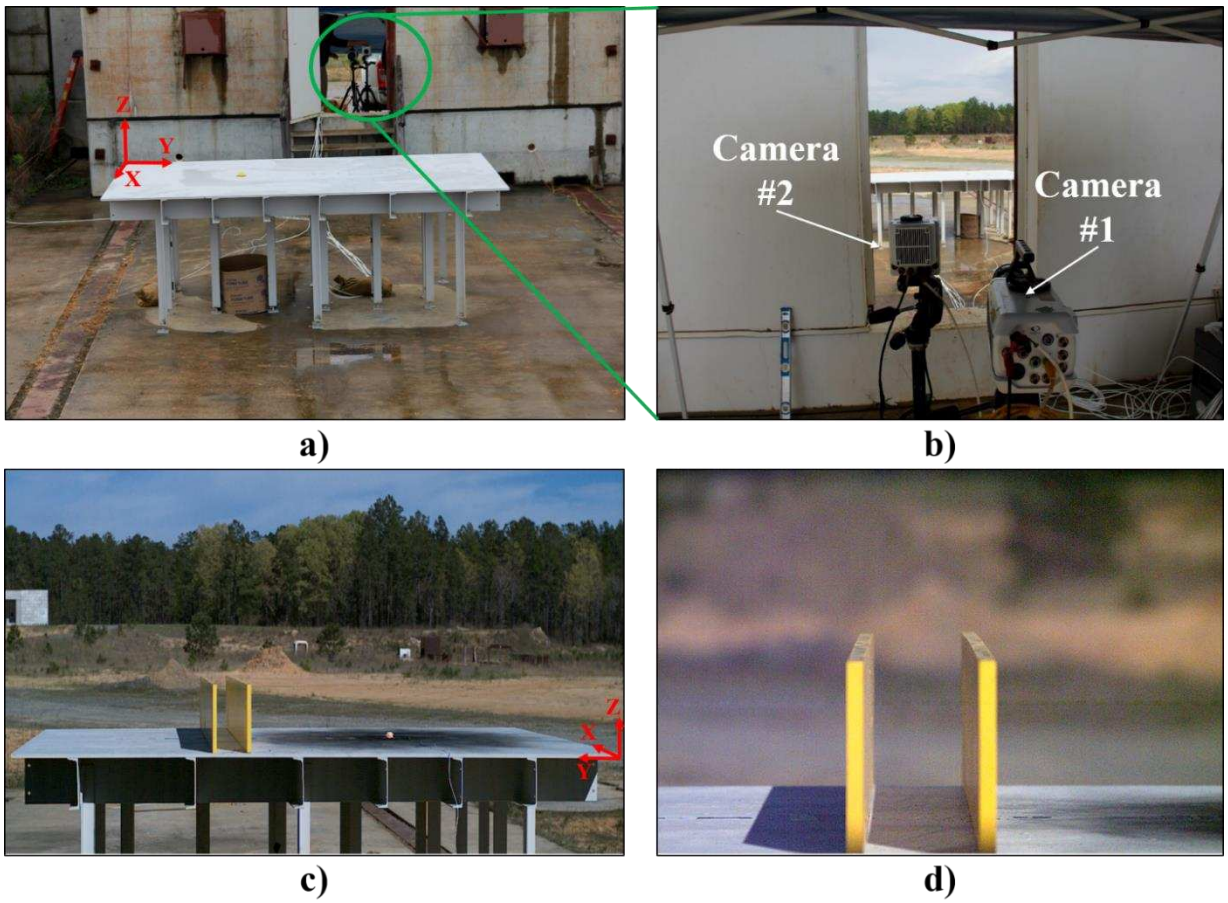

Figure 3-4: a) Location of cameras one and two, b) point of view of cameras one and two and the individual views of c) camera one and d) camera two.

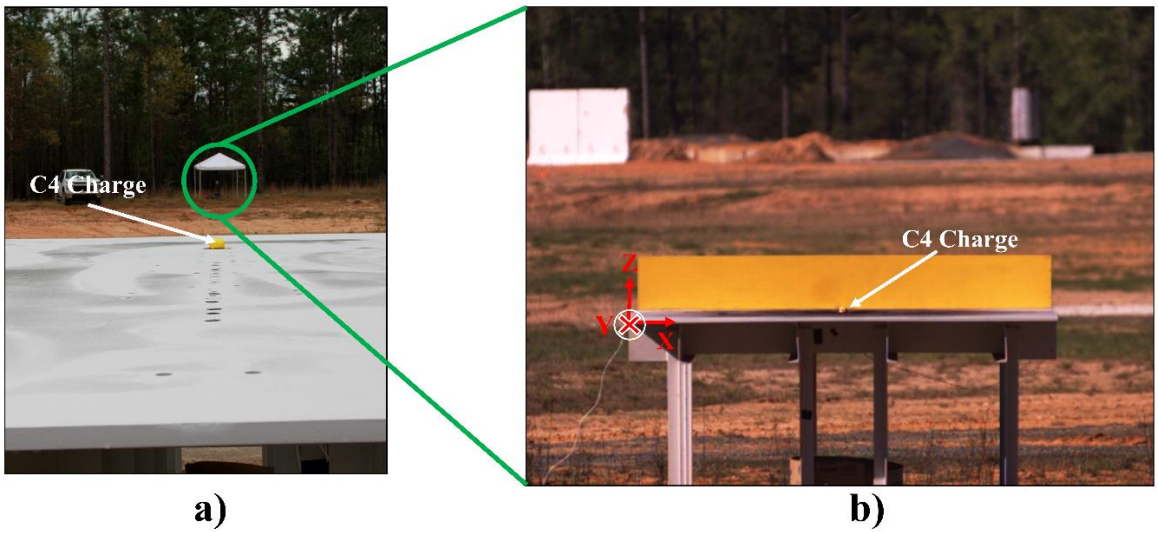

Figure 3-5: a) Location of camera three and b) view of camera three.

3.3.3 Experimental Procedure

Composition C4 was used as the primary explosive. Each charge was measured out on a scale and recorded before being molded into a hemisphere or sphere using plastic molds to ensure the correct radii. Each charge was then taped with electrical tape to allow for easier handling during testing and to help retain the shape. An RP-81 exploding bridge wire detonator (EBW), manufactured by Teledyne Energetics, which is equivalent to a #8 blasting cap, was used as the detonator for all experiments (Teledyne, 2023). For the hemisphere experiments, the charges were bottom detonated. To accomplish this, the EBW was glued into the pucks, as shown in Figure 3-6a). This allowed for the top of the EBW to be flush with the top of the puck so it would be in contact with the bottom of the C4 charge when the C4 was placed on top of the puck, as shown in Figure 3-6b). The puck was then placed in the tabletop with the top of the puck and EBW flush with the surface of the table, and the charge was centered on the puck based off markings on the top surface of the puck. The break wire to trigger the recording of the cameras and instrumentation was attached to the charge, and the EBW was tied into the firing line. This process was repeated for each hemisphere experiment.

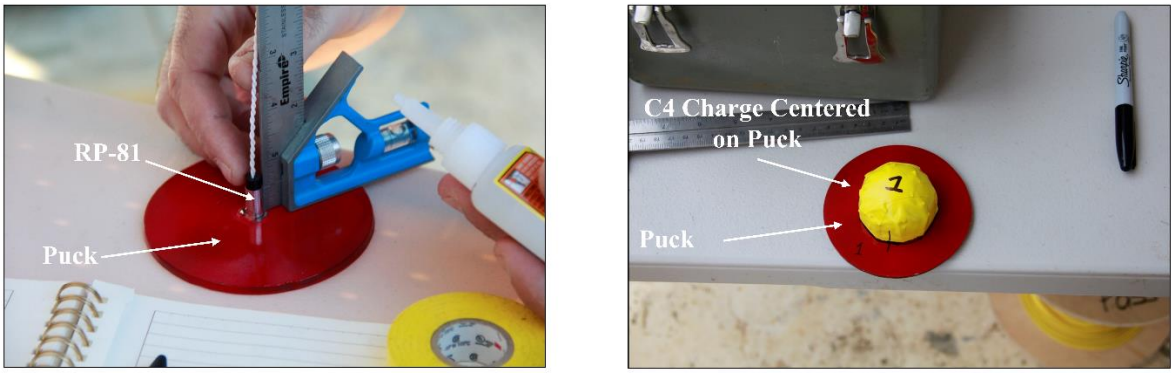

Figure 3-6: Tabletop charge set up for hemispherical charges with a) Bottom view of the puck, EBW (RP-81) glued to puck to guarantee top of EBW was flush with top of puck and b) charge centered on puck so EBW just contacts the bottom of C4 charge.

For the elevated spherical experiments, to match existing literature and the existing numerical models, the charge was center detonated. While the intention was to center detonate, due to the scale and reality of initiation methods, a true center detonation cannot be achieved. To accomplish as close to a center detonation as possible, the EBW was pushed into the spherical charge as shown in Figure 3-7a) until the bridged header sleeve was the only part of the EBW remaining outside of the charge. The elevation of the charge was created with a low-density foam that has no impact on the shock wave. Since the height of burst (HOB) was at the center of the charge, a hole was cut out of the foam for the charge to sit on, so the center of the charge was at the correct height. The charge was then placed in the foam, so the EBW was directionally facing toward the gauges and walls to maximize the amount of energy in that direction. Similar to the hemisphere experiments, the break wire and firing line were then attached after the low-density foam has been centered on the puck and the charge has been placed.

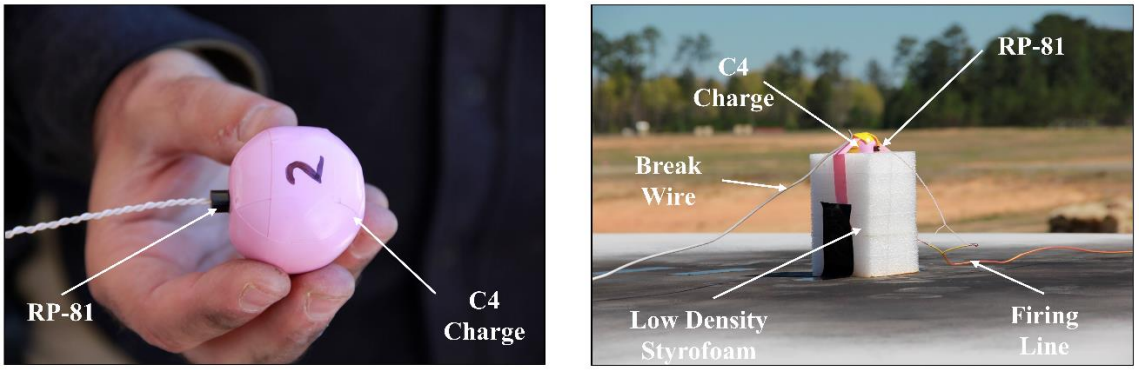

a) b)

Figure 3-7: Tabletop charge set up for spherical charges with a) EBW pushed into charge to center detonate and b) charge resting in low-density foam so EBW and center of charge was at designated HOB.

3.4 Results and Discussion

The results of all experiments are presented and discussed herein. Three to four experiments for each scenario in Table 3-2 were completed to assess the repeatability and accuracy of the results. Free-field experiments were completed without the walls on the table to obtain baseline data to compare in order to assess how effective the walls were in reducing the shockwave. The results comprise of visual inspection as well as pressure-time histories. The pressure data was recorded for all experiments at eight-gauge locations and analyzed in multiple ways to assess the results and the accuracy of the numerical model.

3.4.1 Visual Observations

Analysis of the high-speed video of the experimental testing was completed using the three camera angles. The detonation of Experiment 3 is depicted in Figure 3-8. As shown in Figure 3-8, camera three provided a view that allowed the shape of the shockwave to be analyzed. Figure 3-8a) depicts the viewpoint of camera three before the detonation of the charge. A hemispherical charge

created a symmetric hemispherical shockwave as it expanded, as shown in Figure 3-8b) and Figure 3-8c), where the shock-front is delineated in white-dashed lines to better illustrate its shape and location. Camera two captured the shockwave interaction with the wall. Figure 3-8d) depicts the viewpoint of camera two zoomed in on the walls before the detonation of the charge. In Figure 3-8e), the shockwave can be seen approaching the wall and still maintains its hemispherical shape. Figure 3-8f) shows how the shockwave has passed over the first wall, and a portion of the shock-front is wrapped over the top, while the remaining part continues to pass over the second wall. Due to the wrapping of the shockwave over the first wall, reflections and amplifications of the pressures take place in between the walls. This will be explored further in the rest of this chapter.

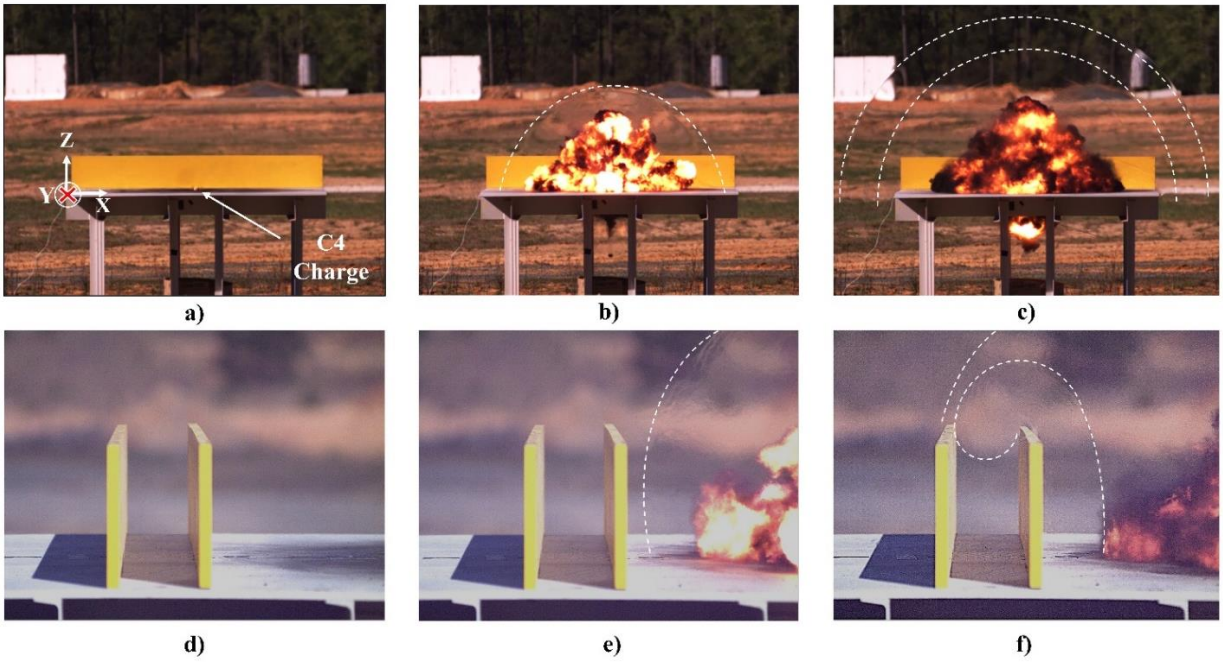

Figure 3-8: Screenshots from high-speed cameras during blast experiments on a tabletop system for Experiment 6 from a) camera three: before detonation, b) camera three: 750 µs after detonation, c) camera three: 1750 µs after detonation, d) camera two: before detonation, e) camera two: 500µs after detonation, and f) camera two: 1250µs after detonation.

3.4.2 Pressure and Impulse Time Histories

The results of the experiments were found to be repeatable, with the most variation occurring at P1 due to the impact of the fireball. Having a pressure gauge inside the fireball can

drastically impact the reading on the gauge due to detonation products and high temperatures (Tyas, 2018). Gauges P2-P8 were not affected by the fireball and had less than a 10% difference on average for percent error between experimental shots and less than a 34.47 kPa (5 psi) difference between experimental shots on average. Table 3-4 shows the average difference and average percent error between shots for all experiments across all gauges.

Table 3-4: Average variation in experimental pressure for pressure gauges P1-P8 across all experiments.

Gauge	Average Percent Error [%]	Average Difference [kPa]
P1	9.79	37.23 (5.40 psi)
P2	8.47	33.65 (4.88 psi)
P3	5.24	4.27 (0.62 psi)
P4	4.18	3.45 (0.50 psi)
P5	6.43	7.58 (1.10 psi)
P6	6.48	1.38 (0.2 psi)
P7	6.17	1.65 (0.24 psi)
P8	3.56	1.03 (0.15 psi)

For the sake of clarity on the graphs, in this section, only two experiments (Experiment 4 and Experiment 6) were used for the pressure and impulse time histories to compare to the numerical modeling results. The rest of the data can be found in the appendix. Experiment 4 was a sphere of 65.6g (0.145lbs) of C4 elevated to a HOB of 152.4mm (6 in.), as shown in Figure 3-7b). Figure 3-9a) shows the measured pressure-time histories from Experiment 4 for select pressure gauges, plotted alongside the pressure-time histories at the same location and charge setup obtained from the numerical model. The pressure-time histories shown in this figure were P1 (free field gauge), P2 (gauge in front of wall 1), P4 (gauge in between wall 1 and wall 2), and P7 (gauge located behind wall 2 at a distance equal to half the wall height H). The largest variation across all experimental shots, between the experimental data and numerical model, was observed in P1 to be 41.0%. As previously mentioned, this could be due partly to the fireball interacting with the gauge.

Another reason the experimental peak pressure was potentially higher than the numerical predicted peak pressure could be due to the directionality of the EBW, which was not included in the CTH models. Gauges P2-P8 showed good agreement with the peak pressure predicted by the numerical model with the largest percent difference of 11.5% at P2. Gauges P4 and P7 experienced an even smaller error, which was below 6%. Figure 3-9b) shows the pressure-time history for pressure gauges P1, P2, P4 and P7 from Experiment 6, a hemisphere of 73.83g (0.16lbs) of C4 with an HOB of 0mm, as shown in Figure 3-5b). Similar to the results from Experiment 4, a variation between the numerical model and experimental pressure at P1 was observed; however, it was not as large as that of Experiment 4 with a percent error of 32.4%. Numerical pressure predictions for the remaining pressure gauges were all within 10.7% of the experimental results, showing overall good agreement for gauges unaffected by detonation products. When the durations and pressures were analyzed and compared to the Bowen injury curves (Figure 2-18 and Figure 2-19), the pressures experienced between the barriers and behind the barriers were all very low but due to the durations of the elevated pressure there was potential for ear drum damage and slight risk of lung damage. This will be explored further in Chapter 7.

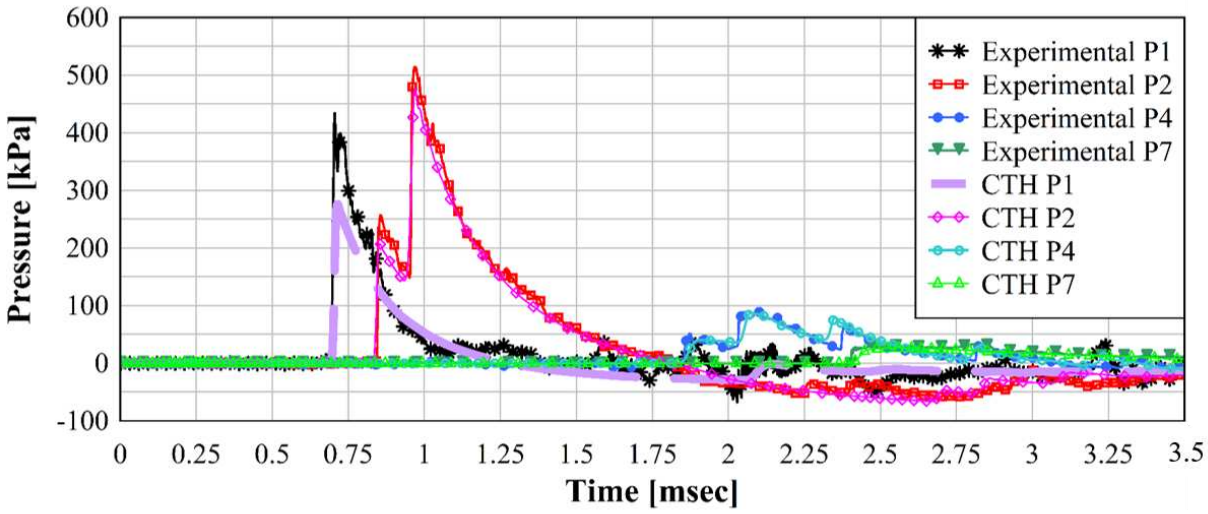

a)

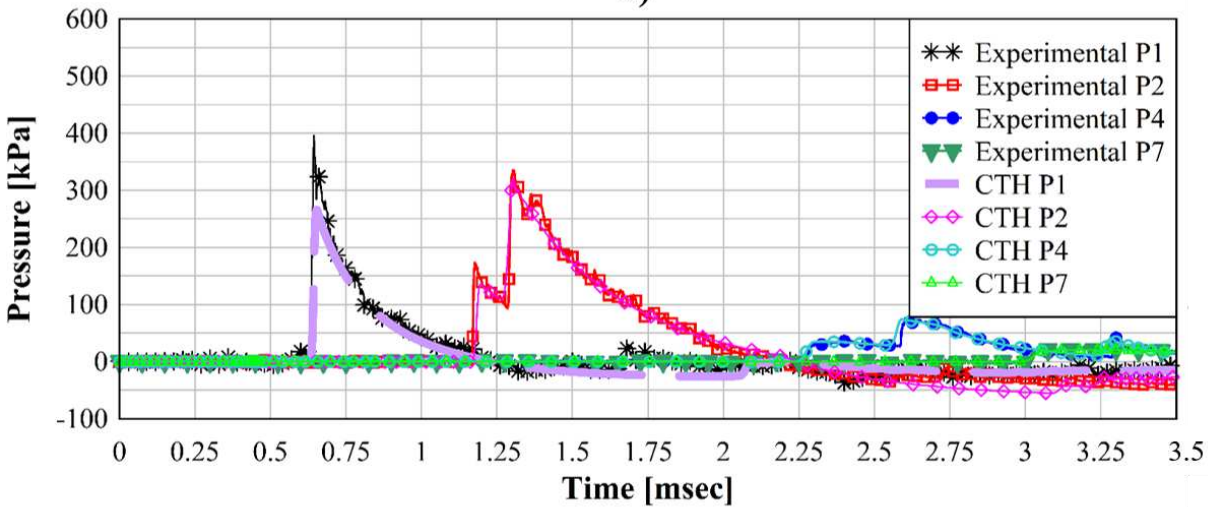

b)

Figure 3-9: Pressure time history curves for P1, P2, P4, and P7 for a) Experiment 4 and b) Experiment 6.

Though pressure predictions were the main objective of this study, impulse is an important blast characteristic to consider as it represents the energy in the system. Figure 3-10a) and Figure 3-10b) depict the impulse-time histories for Experiment 4 and Experiment 6, respectively. The impulse-time histories for all pressure gauges for the numerical model match those of the experiment closely. The agreement between the numerical model and experiment shows the ability of the numerical model to accurately simulate the energy of the event and accurately simulate the

behavior of shockwave propagation across a multiple barrier system. The largest error between CTH predictions and the experimental shots shown in Figure 3-10a) and Figure 3-10b) occurred at P1 with a 18.7% and 25.6% error for Experiment 4 and 6, respectively. All the other impulses had less than 20% error. This showed that using a 2DC simulation domain for a barrier width to charge size ratio close to 1, at the scaled distances investigated, was appropriate despite the barriers not being infinitely wide.

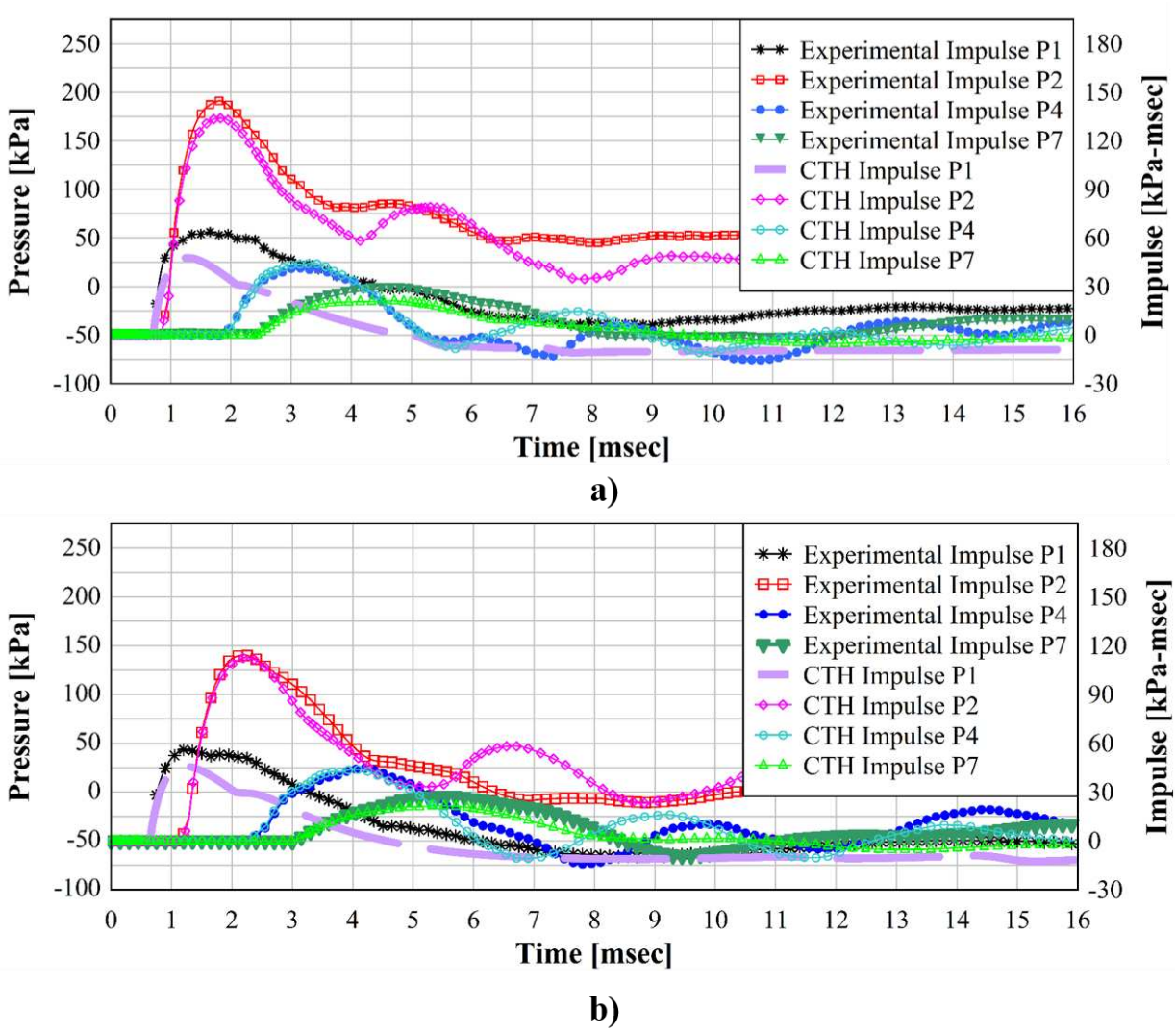

Figure 3-10: Impulse-time history curves for tracers P1, P2, P4, and P7 with axis on right side of graph for a) Experiment 4 and b) Experiment 6.

3.4.3 Peak Pressure Comparisons

The peak pressures were obtained from the pressure-time history for each experiment conducted. The peak pressures for each gauge were plotted as a function of scaled distance in Figure 3-11 for all wall experiments. The grouping of the symbols in each graph shows the repeatability from experiment to experiment with the same setup, as there were three shots for each experiment. The largest variation between experiments was 20.12% at P1 in Experiment 1, as shown in Figure 3-11a). After evaluation of the video, P1 was well inside the fireball which could be one of the possible causes of the variation in the pressure readings. Of the data, 88.2% were within 34.5 kPa (5 psi) of each other, with 58.8% of those with a variability above 34.5 kPa (5 psi) being at P1.

Figure 3-11a) and Figure 3-11b) show the results for Experiments 3 and 4, which were a 65.6 g (0.145lbs) hemisphere surface burst and 65.6 g (0.145lbs) sphere with an HOB of 152.4 mm (6 in.), respectively. As illustrated in the figures, the maximum pressures at each gauge differ between the sphere and hemisphere experiments. P1 and P2 were higher for Experiment 4 compared to Experiment 3, as expected due to the reflections that occur off the ground from a HOB > 0 mm. P1 experienced a 40.8% increase from Experiment 3 to Experiment 4 while P2 experienced a 22.3% increase. Experiment 6, the 73.83g hemispherical charge results are shown in Figure 3-11c). P1 has a large discrepancy again, ranging between 21.1%-32.4% error between experimental pressures and the CTH predications. Analysis between the rest of the data for gauges P2-P8 and the numerical predictions for P2-P8 show the accuracy of the CTH model outside the fireball with the largest percent error being 21.0% for P3 between shot A and CTH. Variation between the three experimental tests for Experiment 6 for each gauge P1-P8 was less than 14.0%

difference showing that the testing method produced similar results between repeated shots. Experiment 8 was an 82.03g (0.18lbs) hemisphere and is shown in Figure 3-11d). Similar to all the other experiments with walls on the tabletop, the CTH predictions were similar to the experimental tabletop tests. The variation between the three experimental tests for Experiment 8 for each gauge P1-P8 was less than 16.8% difference. The results of the smallest charge of a 49g (0.11lbs) sphere from Experiment 10 are shown in Figure 3-11e). In both Figure 3-11d) and Figure 3-11e), P5 has an increase in max pressure in front of the second wall compared to the other two gauges in the middle of the walls. This is examined more in the next section. Across all experiments, 96.70% of all experimental pressure readings were within 68.9 kPa (10 psi) of the other experimental pressures for the same test. This shows the repeatability of the tabletop testing method. When comparing the experimental results with the CTH predictions, 93.90% of the experimental pressure readings were within 34.5 kPa (5 psi) of the CTH predictions.

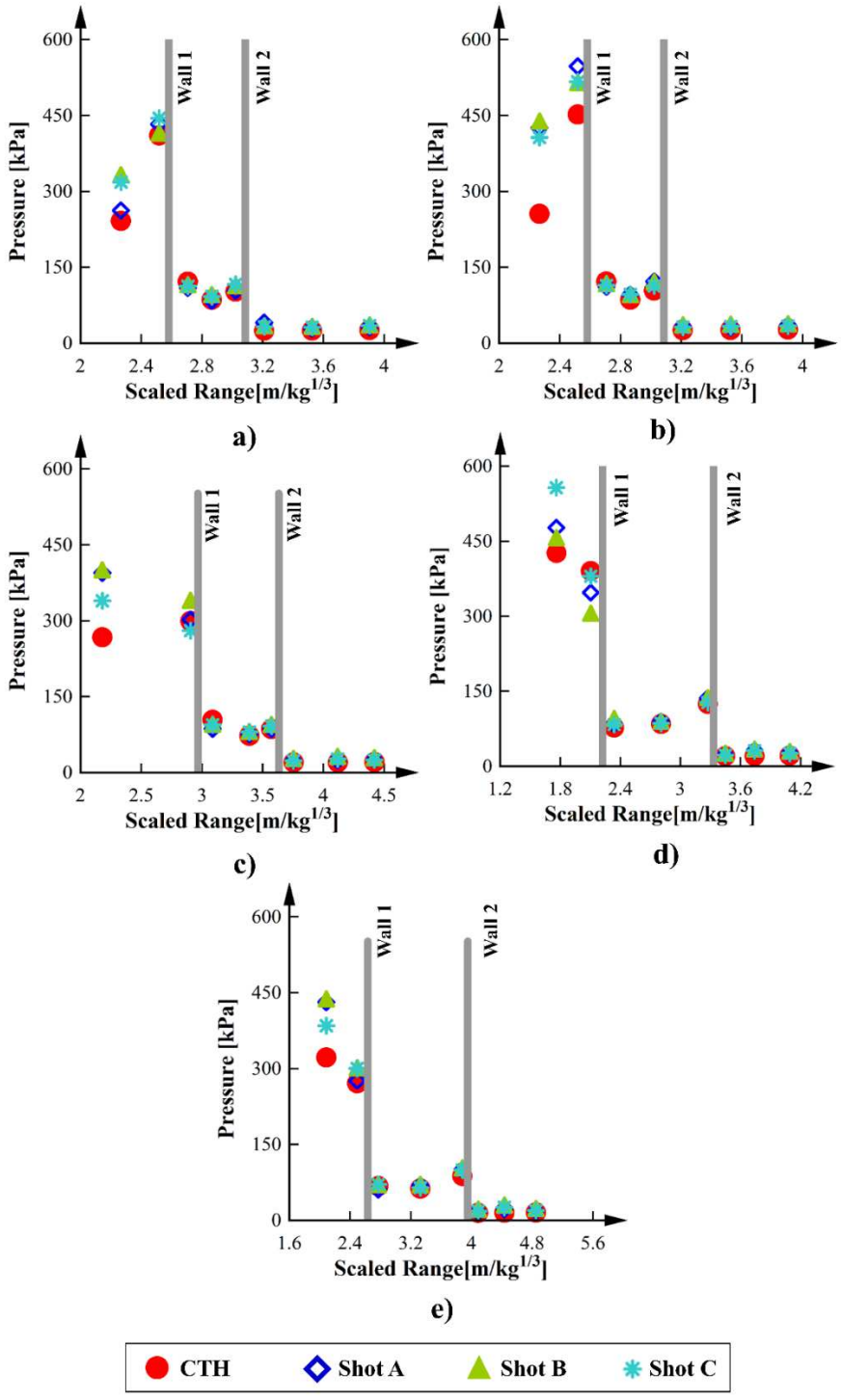

Figure 3-11: Peak pressure trend comparison for gauges P1-P8 between CTH models and experiments for a) wall Experiment 3, b) wall Experiment 4, c) wall Experiment 6, d) wall Experiment 8, and e) wall Experiment 10.

To address the effectiveness of the barriers in reducing pressures, a comparison of the free field pressures to the wall experiment pressures is shown in Figure 3-12. The wall experiments were normalized to the free field averages in order to assess how effective the walls were in reducing the pressures of the blast shockwave. For all experiments shown in Figure 3-12, gauge P1 normalized pressures were around one, as expected. This was due to P1 being a free field gauge and not being affected by the presence of the walls on the other side of the table. Gauge P2 normalized pressures for all experiments in Figure 3-12 at around or above two. In Figure 3-12b), P2 normalized pressures were 1.92, 2.32, 2.17, and 2.19 for CTH, Shot A, B, and C, respectively. The normalized pressure at P2 was amplified compared to the free field due to the reflection of the pressure off the front of wall one. This amplification was expected and is well researched. Graphs and methods to determine the amplitude of the expected reflective amplification are published in the UFC-3-340-02 (DOD, 2008).

Normalized pressures for P3-P8 were below one for most experiments. As predicted, this means the maximum pressure recorded in the wall experiments was lower than that recorded in the free field experiments. Therefore, the walls were successful in reducing the pressure faster and at smaller scaled ranges closer to the charge than just letting the shockwave pass without any barriers. In Figure 3-12a), P3 pressures for Experiment 3 were, on average, 56.5% of the free field values. This means the peak pressure at P3 was reduced by close to 50% with the inclusion of the double-barrier system compared to no walls. Additionally, in Experiment 3, P6 pressures were, on average, 25.8% of the free field values. The inclusion of the double-barrier system reduced the peak pressures by approximately 75% compared to no walls. When comparing the pressures between the two walls and behind both walls, the pressure behind both walls was again reduced

by about half of the pressure between the two walls. The pressures between the barriers were again compared to pressure threshold values for ear drum damage and lung damage from the Bowen injury curves and literature values. Based on the duration of the pressure waves, the pressure experienced between the barriers could potentially lead to ear drum damage or a slight potential of lung damage due to the pressures experienced. This will be further explored in Chapter 7 of this dissertation.

Experiments 8 and 10, however, have an increase in pressure at P5. As shown in Figure 3-12d) and Figure 3-12e), the pressure for the wall experiments at P5 was either equal to or above the free field experiments. This increase in pressure was believed to be due to the reformation of the blast wave behind the first wall or the reflection and stagnation of the pressure shockwave between the two walls. Blast wave reformation can begin behind the first wall. The wave can be completely reformed at two wall heights behind the structure at certain scaled distances. The walls in Experiments 8 and 10 were 482.6 mm (19 in.) apart which was 1.6 times the height of the wall at 304.8 mm (12 in.). This larger distance compared to Experiments 3, 4 and 6 allows for more reformation between the walls, resulting in a higher pressure in front of wall two.

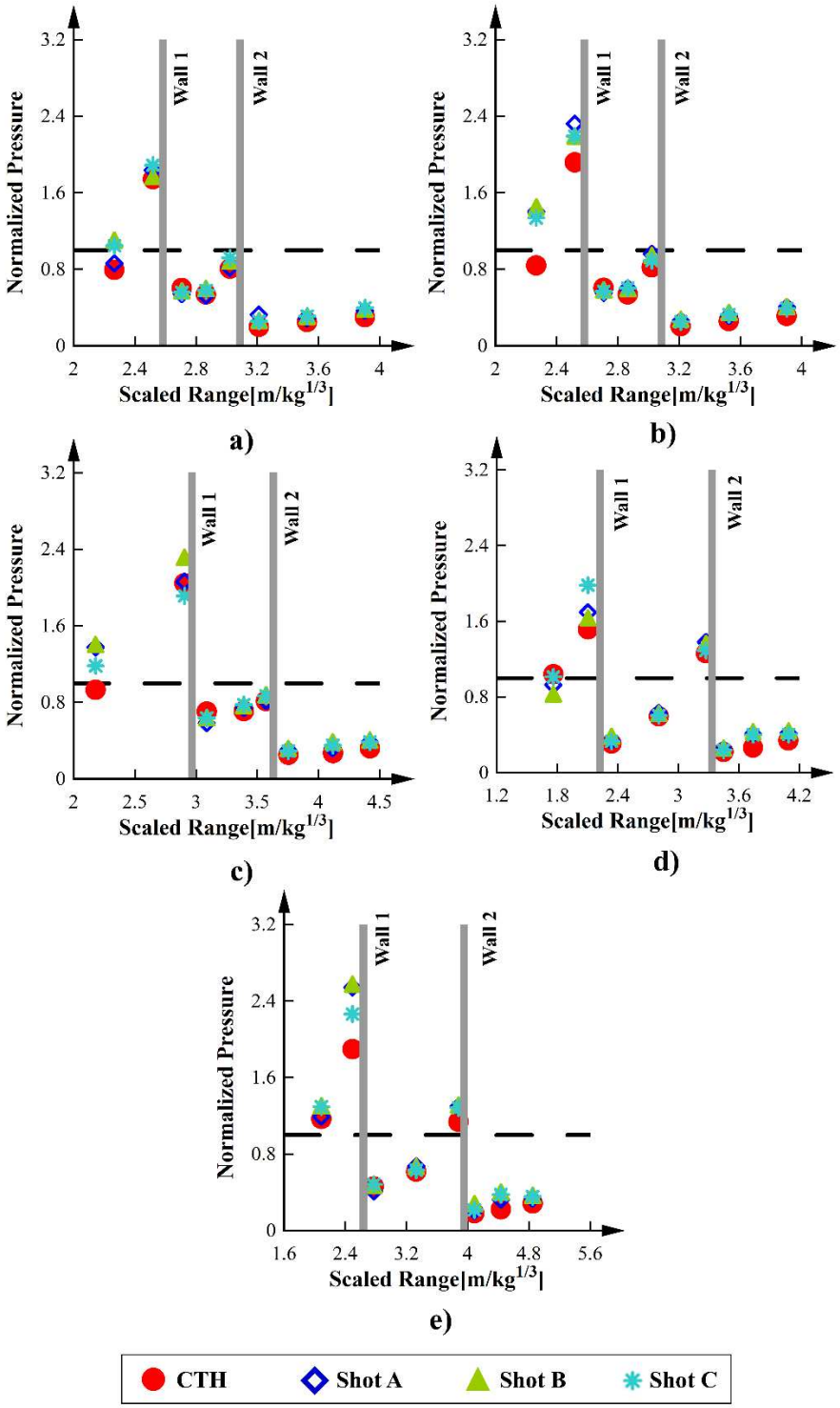

Figure 3-12: Peak pressure trend comparison normalized to the corresponding free field for gauges P1-P8 for experimental a) Experiment 3, b) Experiment 4, c) Experiment 6, d) Experiment 8, and e) Experiment 10 with walls in place.

Table 3-5 summarizes the average pressure reductions between free field and wall experiments for gauge P5 for each set of experiments. This summary is shown for gauge P5 because P5 was the pressure gauge in front of the second wall, where the importance of the distance between the two barriers can be analyzed and has the largest impact. As shown in Table 3-5, the difference between the peak pressures measured in free field experiments and the pressure with the double-barrier system, was significantly larger in Experiment 8, for an average difference of 33.35 kPa (4.84 psi), and Experiment 10, for an average difference of 22.29 kPa (3.23 psi). The difference in Experiments 8 and 10 was not only larger in magnitude, the difference, from the corresponding free field Experiments 7 and 9 was positive, meaning the pressures were amplified rather than reduced as they were for Experiments 3, 4, and 6.

Table 3-5: Pressure reductions between free field and wall experiments for P5.

FF Experiment #	**Wall Experiment #**	**FF AVG Pressure [kPa]**	**Wall Pressure AVG [kPa]**	**Average Peak Pressure Reduction [kPa]**
1	3	126.66 (18.37 psi)	109.56 (15.89 psi)	-17.1 (-2.48 psi)
1	4	126.66 (18.37 psi)	117.07 (16.98 psi)	-9.59 (-1.39 psi)
5	6	107.21 (15.55 psi)	89.46 (12.98 psi)	-17.75 (2.57 psi)
7	8	98.80 (14.33 psi)	132.15 (19.17 psi)	+33.35 (4.84 psi)
9	10	77.15 (11.19 psi)	99.44 (14.42 psi)	+22.29 (3.23 psi)

When analyzing Figure 3-11 and Figure 3-12, the gauges directly behind the first barrier (P3) and in the middle of the two barriers (P4) saw a reduction in pressure as those values were below a normalized pressure of 1.0. It was P5 that has the significant increase. Overall, for gauges P3, P4 and P5, the pressure on average was reduced from the free field experiments. However, the

amount of reduction was dependent on the gap size between the barriers. When observing the results in Figure 3-12 and Table 3-5, one can conclude that the larger gap between the two barriers allowed for increased pressures between the barriers. The impact of the gap size on the peak pressures in between the barriers is summarized in Table 3-6 as an average of the three gauges.

Table 3-6: Pressure reduction relative to distance between barriers for gauges between the two barriers.

FF Experiment #	Wall Experiment #	Distance Between Barriers [mm]	Average Normalized Pressure for Gauges 3, 4 and 5
1	3	203.2	0.66
1	4	203.2	0.69
5	6	279.4	0.74
7	8	482.6	0.80
9	10	482.6	0.77

Experiments 3 and 4 saw the most reduction between the barriers with an average normalized pressure of 0.66 and 0.69, respectively. The gap between barriers in Experiments 3 and 4 was the smallest at 203.2 mm (8 in). Experiment 6 was the next best with an average normalized pressure of 0.74 with a 279.4 mm (11 in.) gap between barriers. While Experiments 8 and 10 had the largest gap of 482.6 mm, which could contribute to the reformation of the wave behind the first barrier and the larger pressure at P5 as mentioned and analyzed above. The average pressure for Experiments 8 and 10 were at 0.80 and 0.77, respectively, which was elevated when compared to Experiments 3, 4, and 6. It can be concluded that a larger gap resulted in not only a larger increase in pressure in front of the second barrier, but also an elevated average pressure between the barriers.

3.5 Summary and Conclusions

The main objective of this chapter was to present a new method of testing airblast parameters and scenarios using small-scale experimentation on a table and assess the pressure predictions of the hydrocode model that will train the ANN in chapter four. This method of testing allows for efficient, accurate, and repeatable testing, providing a powerful way for engineers to investigate airblast and the impact it has on structures. Numerical models were created using the hydrocode CTH for predicting pressure around a double-barrier system in chapter three. Results from the completed experimentation were compared and analyzed to assess the effectiveness of a double-barrier system in reducing the blast shockwave pressure in a large open area, the repeatability of the small-scale testing on a table and the accuracy of the numerical model. The following conclusions can be drawn from these experiments:

- Tabletop small scale experimental testing allowed for repeatable data to be collected in an efficient manner (up to 15 shots / day were conducted). Of all experimental data shots, 90.6% were within 34.5 kPa (5 psi) of each other with the vast majority of those above 34.5 kPa (5 psi) being at the free field gauge.
- Tabletop testing procedure was an effective way to investigate the blast effects on multiple structures in a small-scale environment.
- Tabletop experimental data matches pressure predictions from the CTH numerical model validating the accuracy of the CTH model for training the ANN in Chapter 4. CTH predicted 96.7% of pressures within 68.9 kPa (10 psi) of experimental averages, and 93.90% of the remaining pressures were within 34.5 kPa (5 psi).
- Experimental data impulse-time histories were close to the CTH model, showing that the CTH model correctly captures the energy of the system.

- Multiple walls were effective in reducing the pressure shockwave much faster than no walls. A single wall reduced the pressure by 50.0%, and a second wall reduced it by almost 74.9% for the configurations investigated.
- CTH models can accurately predict the maximum pressure trends for a variety of charge sizes and standoffs with multiple walls present when compared to the experimental data collected.

CHAPTER 4: ARTIFICIAL NEURAL NETWORK WITH BLAST BARRIERS FOR BLAST ANALYSIS PREDICTION

4.1 Introduction

Predicting airblast effects over a large variation of scaled ranges within complex environments is important to characterize the potential severity of structural damage and personnel injury. In recent years, computational and numerical models have grown in popularity for their accurate evaluation capabilities. Advanced numerical methods are often used to model airblast propagation and its impact on structures. However, in more complex environments, where blast loading in large areas of interest may occur, using high-fidelity computational models can be inefficient due to the computational time required. Artificial neural networks are becoming popular across many engineering fields due to their ability to produce accurate results in a rapid, computationally efficient manner.

Of the current research that utilizes ANNs for blast prediction and mitigation, most focus on predicting blast parameters in an open area or behind a single barrier or structure. Many existing studies approach the problem from a plane view as it provides a good depiction of the overall domain, much like a drone image or aerial view. However, the assumptions made about the domain in order to perform the analysis from the plane viewpoint potentially ignore important physics associated with shock wave propagation and interaction with any objects present. A plane view ignores the height variation of the flow field, which can become important when looking at human injury potential due to the variability in heights in a random population of people. Ignoring the height variation means the height of burst of the charge cannot be accounted for, which can influence the blast characteristics (DOD, 2008; Swisdak, 1975). Most importantly, a plane view

assumes an infinitely tall barrier in the path of the shock wave which accounts for clearing effects around the sides of the barrier but not over the top of a barrier. In some instances, this assumption can be acceptable. For example, in a large building or structure, the blast wave must travel a large vertical distance before reforming on the other side, and therefore will not have much impact on the magnitude of the reformed wave. In other instances, however, such as perimeter walls or barriers (T-walls, Alaska barriers, or Hesco barriers) the blast wave only has a short vertical distance to travel before reforming on the other side, and it is expected that this will have a large effect on the objects behind the walls due to the magnitude of the pressure and impulse of the reformed blast wave.

This chapter presents the development of an ANN to predict the peak pressure from a blast wave in front, between and behind multiple perimeter barriers, accounting for realistic barrier heights. First, a hydrocode simulation model that predicts the pressures around a double-barrier system from a blast shock wave is presented. This model will allow us to understand the impact that a double-barrier system can have on the blast shock wave and how the spacing of those barriers can be best manipulated to provide better protection for military and civilians in the vicinity of an explosion. Second, the actual development of the ANN model through optimization of the model parameters is presented and analyzed. Finally, the final ANN model is presented and tested against high resolution hydrocode simulations. The advantage of an ANN model is that it allows for accurate and reliable predictions to be made quickly and easily while providing a unique perspective on the blast analysis problem of a double-barrier system. Such a model can then serve as a fast-running engineering tool for military and civilian applications where the assessment of multiple barriers is necessary for protection from blast propagation.

4.2 Double-Barrier Hydrocode Model

The hydrocode CTH was utilized to generate the training dataset for the ANN. This study was not meant to provide a detailed characterization of the wave interaction with a double-barrier system. The CTH model was used as a method for creating a training dataset of a double-barrier system to accomplish the main goal, which was to develop an ANN for rapid prediction of the pressures experienced around a double-barrier system. CTH, a two-step Eulerian-based hydrocode developed at Sandia National Laboratories, is capable of modeling multidimensional, multi-material, large deformation, and strong shock wave physics (McGlaun et al., 1990; Needham, 2009; Schmitt et al., 2017). CTH has been used extensively in blast modeling and has been well validated for complex blast scenarios (Bewick & Flood, 2010; Homan et al., 2013; Zapata & Weggel, 2008). In this study, two identical barriers were utilized with varying distances separating them (Figure 4-1). The dimensions of the barriers were chosen based off the motivations of the study to be 0.1524 m thick (6in), 1.8288 m high (6ft), and infinitely long to avoid having to consider wrap around effects. This assumption can be made for a large number of perimeter barrier configurations and scaled distances due to the typical length of barriers relative to the charge size seen in real world applications. The height of the barriers was chosen to be slightly taller than the average male at 1.8288 m. The idea was to develop a barrier to be used in a public setting without intruding on the lives of civilians as much as something similar to the large concrete barriers typically used by various government departments that range in height between 1.5-3 m and vary in thickness between 15.24-30 cm. The corresponding inputs for the model are summarized in Table 4-1.

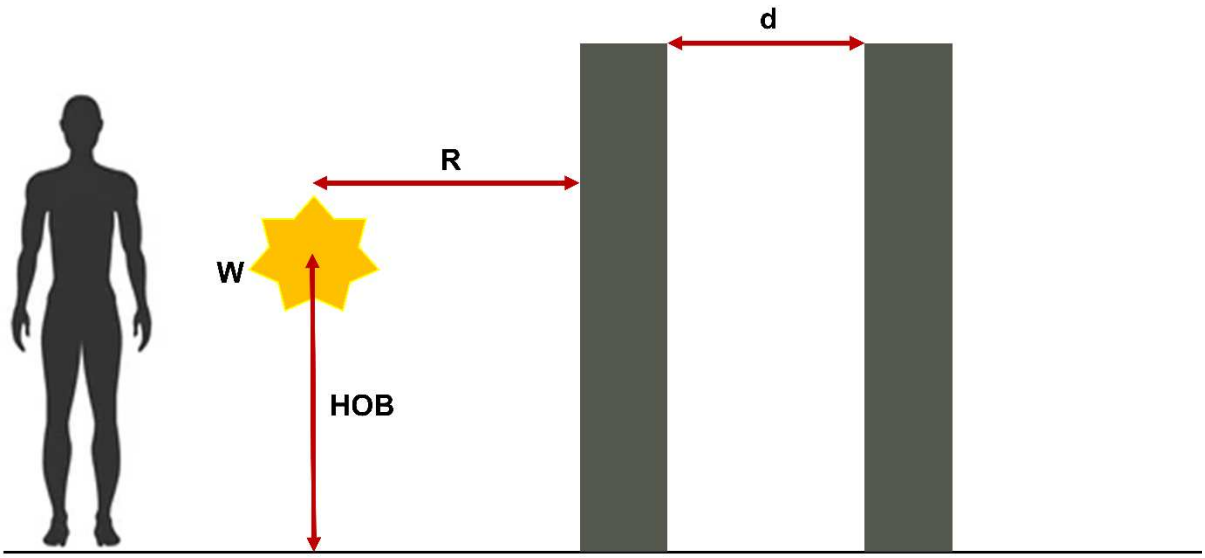

Figure 4-1: CTH model diagram with corresponding inputs and tracer points.

Table 4-1: Neural Network Input Parameters

Parameter	Unit	Description
W	kg	Weight of explosive charge of Trinitrotoluene (TNT)
HOB	m	Height of burst of charge.
Z	m/kg$^{1/3}$	Scaled standoff distance of the front surface of the first wall to the charge center (Equation 4.1)
d	m	Distance between the two barriers

The scaled distance Z was calculated from the charge weight W and the range to the point of interest R using Equation 3.1. A 2D domain was created for the largest distance between walls (d=3.66m or 12ft) and largest scaled distance (Z=5.95 m/kg$^{1/3}$ or 15 ft/lb$^{1/3}$) that allowed for the full expansion of the blast wave without any interference of the boundaries. A high-resolution flat mesh that allowed for 40 cells across the radius of the charge of the explosive was used for area of data collection inside the domain, while a biased mesh that extended to the end of the domain outside the area of data collection with larger cells was used to reduce computational cost. This division of the mesh is illustrated in Figure 4-2.

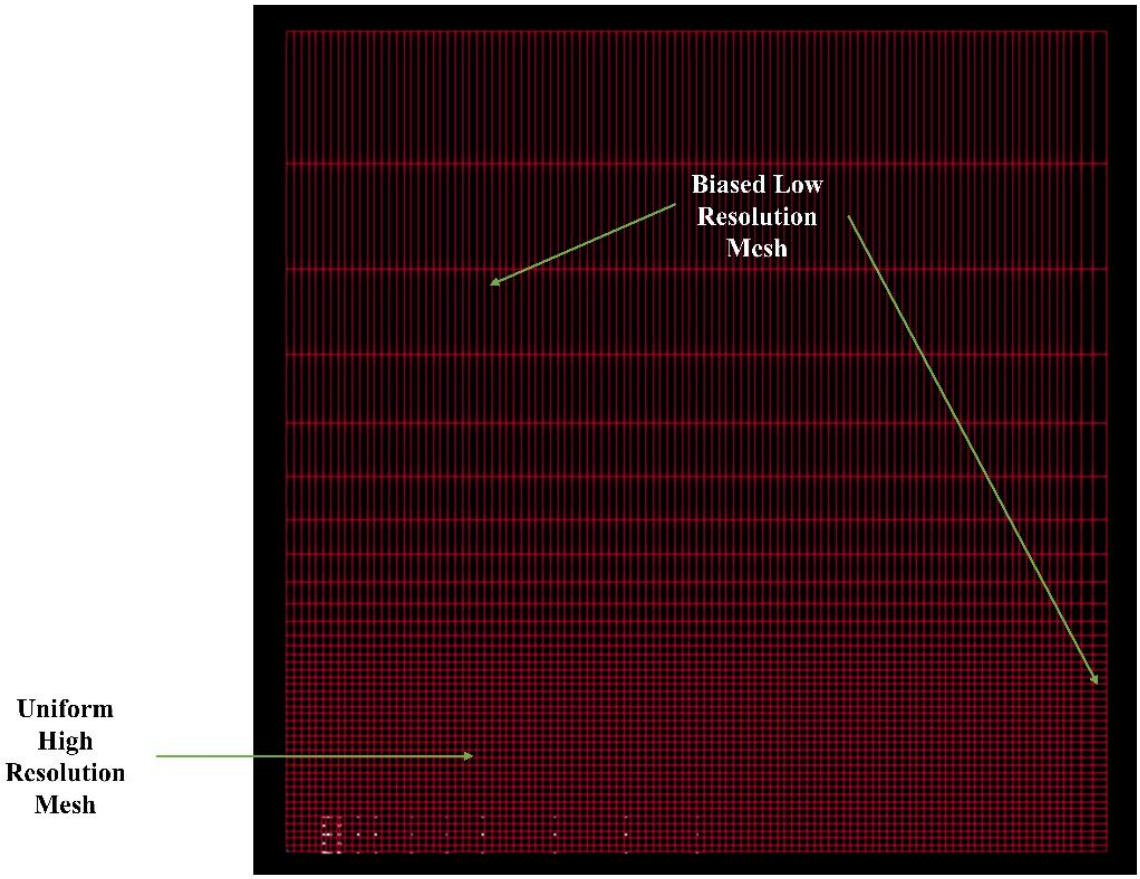

Figure 4-2: CTH simulation domain showing the difference in the high resolution and low-resolution biased mesh.

An equation of state (EOS) was required for each material modeled to accurately simulate the relationship between pressure and density of a material. In this study, the air was modeled with SESAME which is the general tabulated EOS in CTH for air (Schmitt et al., 2017). The Jones-Wilkins-Lee (JWL) is the widely used EOS for detonation products of explosives (Lee et al., 1968). The JWL EOS constants for TNT were taken from literature (Dobratz, 1981). The ideal burn model of HEBURN was used to fully detonate the explosive in each simulation.

The range for each of the inputs is summarized in Table 4-2. The charge weights (W) were chosen to represent person-borne improvised explosive devices (PBIEDS). The charge weights of 2-22kg (5-50lbs) are a PBIED level threat according to the UFC 3-340-02 manual (DOD, 2008).

A PBIED threat level is associated with the weight of explosives that a single person can carry in various forms. As the threat was a PBIED threat to be transported and used by a single individual, the HOB ranged from 0- 1.5m (0-5ft) to represent different heights that different charges could be placed, in reference to the height of the average male. For Z, the values were ranged between 1.19-5.95m/kg$^{1/3}$ (3-15ft/lb$^{1/3}$). A low boundary for Z of 1.19m/kg$^{1/3}$ was chosen as values smaller than Z=1.19m/kg$^{1/3}$ are considered to be "close-in blast" and has potential to become a breaching problem. The high boundary for Z was chosen to be large to assess a variety of distances that people could be standing at in the event of a blast allowing the authors to assess the impact of pressure on them if they were even far away. Finally, the gap distance d was varied from 0.61-3.66m in order to test various gaps that could fit a single person or even a vehicle between the barriers.

Six hundred thirty simulations were conducted to model all the combinations between the different variables shown in Table 4-2. Pressure measurements were calculated at 60 different tracer locations for each of the 630 simulations as depicted in Figure 4-3. The various tracer locations allow the full-blast environment in front of, between, and behind the barriers to be characterized. Tracers were placed in front of the first barrier, incrementally at $0.25d$, $0.5d$, and $0.75d$ between the walls, and in the free field behind the second barrier at 0.5, 1, 2, 3, 4, 6, 8, and 10 times the wall height spaced evenly along the height of the walls. Five tracers were evenly spaced along the height of the barrier for the front and back surfaces of the barriers. Tracers between the barriers and behind the second barrier in the free field only had three tracers located at ground level, half the barrier height and at barrier height. For each one of the 60 tracers, a full pressure time history was reported from CTH.

Table 4-2: Neural Network Test Matrix

Parameter	Range	Increments
W [kg]	2.27-22.68	2.27, 4.54, 6.80, 9.07, 13.61, 18.14, 22.68
HOB [m]	0-1.52	0, 0.91, 1.52
Z [m/kg$^{1/3}$]	1.19-5.95	1.19, 2.38, 3.57 4.76, 5.95
d [m]	0.61-3.66	0.61, 1.22, 1.83, 2.44, 3.05, 3.66
Total Scenario Count		**630**

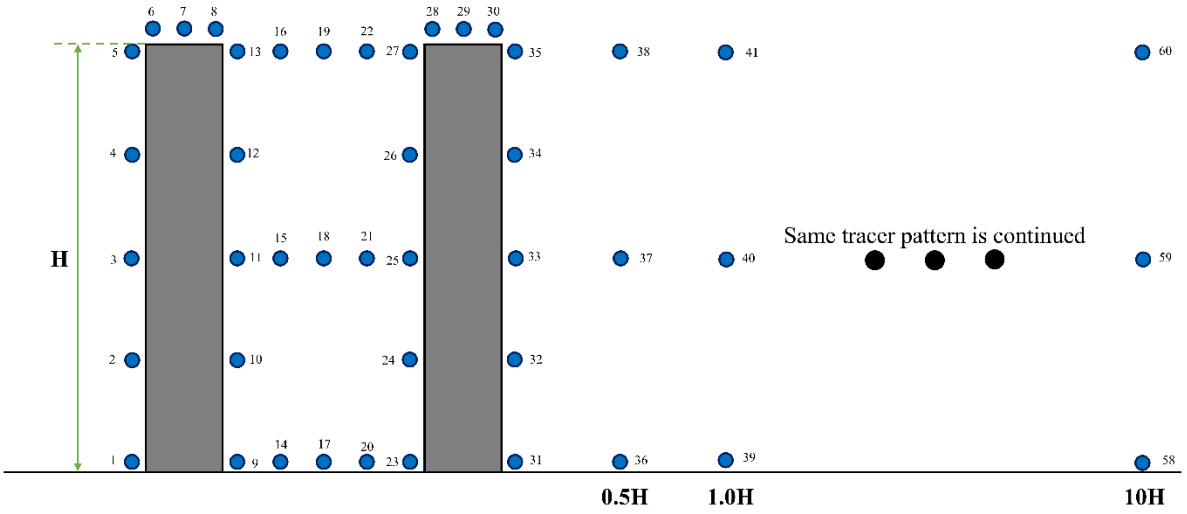

Figure 4-3: Pressure output location diagram for CTH simulations.

An example of a time history for tracer 1 is shown in Figure 4-4. The initial peak was when the blast wave hits the front surface of wall one and the second peak was a reflection off the wall. The maximum pressure for each of the tracers for each of the 630 simulations was extracted to be used as the training points for the artificial neural network explained in the rest of this chapter.

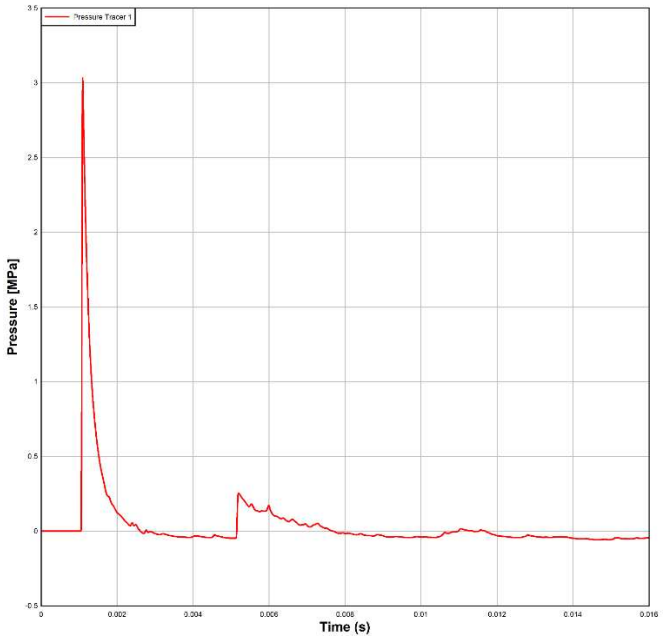

Figure 4-4: Pressure Time History for Tracer 1 from a CTH simulation.

4.3 Double-Barrier Artificial Neural Network Model

ANNs are a form of artificial intelligence inspired by the biological neural networks in the brain. Similar to the biological model from which it was derived, an ANN assembles many highly connected processing units, often referred to as nodes or neurons. The basic architecture of an ANN consists of three types of neuron layers: input, hidden, and output. The input layer contains the independent variables (input variables), and the output layer contains the dependent or predicted values (output or target variables). Typically, the input, hidden, and output layers are all connected, as shown in Figure 4-5. The strength of the connections between neurons is represented by numerical values known as weights. To determine those weights, the network must be trained. As shown in Figure 4-5, each node has weights and biases associated with it. Typically, the weights and biases are initially defined as random values and are subsequently determined as training takes place.

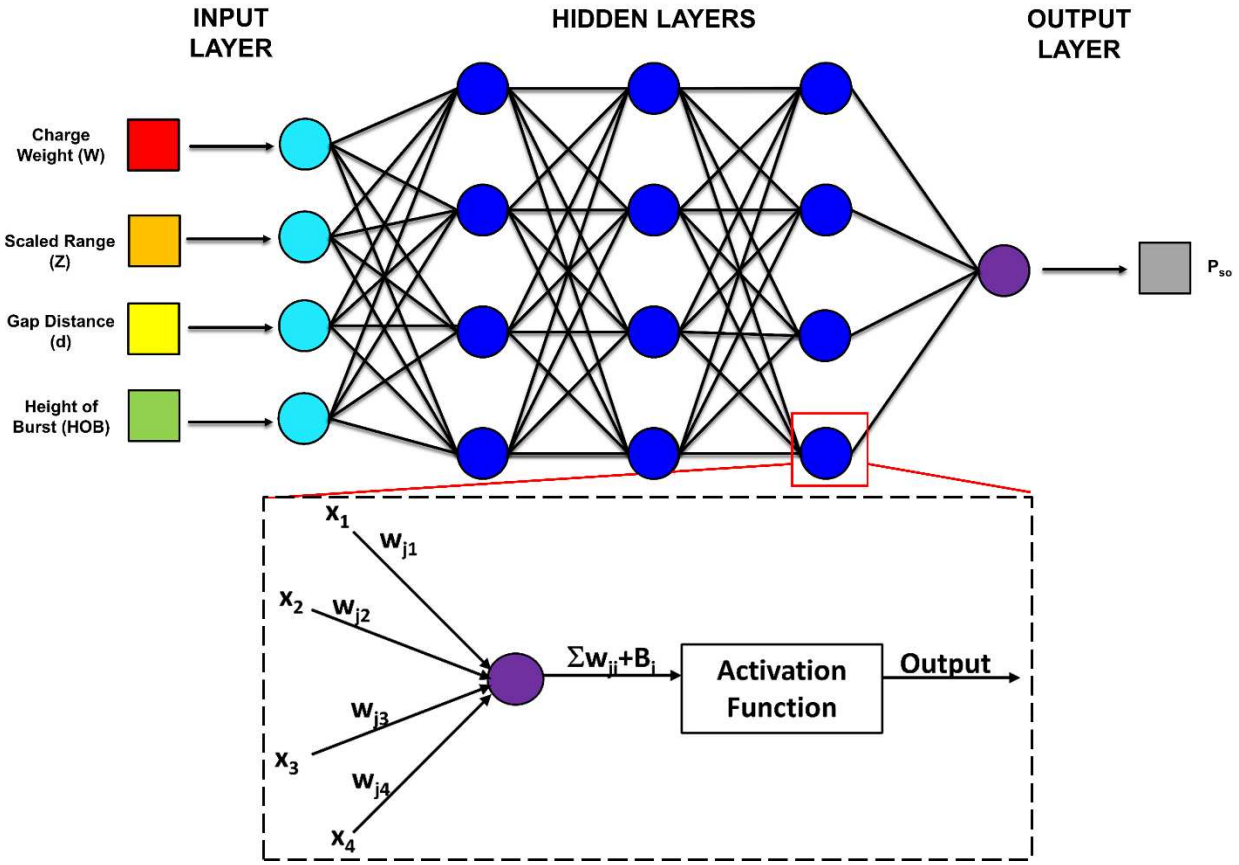

Figure 4-5: Multi-layered feedforward neural network diagram.

In the model definition stage, the inputs and outputs of the problem are defined and a dataset that will be used for training is created. During this stage, the network structure is determined, including how many nodes, layers, and what activation functions are used. Of the many steps to create an ANN, one essential step in the design process of an ANN is training, which is completed in the model development stage. The goal of the training process is not just to minimize the training error but to minimize the error when the network is used with data that is not in the training set.

A supervised training approach provides known inputs and outputs to the network. Patterns in the data are learned through iterations of network weights and bias adjustments and model

output validation against the data. Supervised training is commonly used in multi-layer perceptron (MLPs) feedforward networks like the one shown in Figure 4-5. Feedforward means the data travels in only one direction from input nodes to hidden node layers and finally to the output nodes. Feedforward MLPs that are trained with backpropagation are the most popular neural networks and are commonly used in pattern recognition and data analysis problems (Pilkington & Mahmoud, 2016). In the backpropagation training algorithm, the gradient or derivatives of the objective function, or error function, are calculated using the gradient descent method first in the output layer, then the hidden layer(s) and finally the input layer. The output error is propagated backwards toward the input layer updating the correlations (weights and biases) between neurons (Pilkington & Mahmoud, 2016).

There are different training algorithms that have been successfully used in various applications, including Newton's method, gradient descent, Bayesian Regularization, and Levenberg-Marquardt. In this study, five different training algorithms were assessed to evaluate each algorithm's influence on determining the lowest mean square error (MSE) for the network. All five training algorithms are summarized in Table 4-3. All of these are optimization methods that approach the minimization of the error in different ways to reach the desired input-output relationship.

Table 4-3: Select Neural Network Training Algorithms for Backpropagation (Pilkington & Mahmoud, 2016)

Parameter	Description
Bayesian Regulation (Geman et al., 1991; Neal, 1992)	Determines the maximum probability for the weights' values during training. Consists of a utility (lowest MSE), network 'likelihood' model (Levenberg Marquardt for this study), and priors (distributions from previous iteration components)
Levenberg Marquardt, LM, (Gavin, 2019)	Uses Gauss-Newton if approximated function values are close to optimal values. Otherwise, uses Levenberg Marquardt.
Scaled Conjugate Gradient, SCG, (Møller, 1993)	Uses gradient descent to determine direction of descent but uses a line search technique to determine the step size in that direction.
One Step Secant, OSS, (Constantinescu et al., 2008)	Integrates SCG and a Quasi-Newton method. Aims to find the point where the gradient is zero and updates with each iteration.
BFGS Quasi-Newton Method (BFGS) (Broyden, 1970; Fletcher, 1970; Goldfarb, 1970; Shanno, 1970)	Form of Quasi-Newton method that approximates the inverse Hessian and uses a line search technique to determine the direction of steps.

In building and training a feedforward MLP, the dataset should be divided into three distinct categories: training data, validation data and testing data. Commonly, the default distribution is 70% training, 15% validation, and 15% testing (Pilkington & Mahmoud, 2016). During training, the algorithm utilizes the dataset to minimize the error between the desired output from the hydrocode simulation and the calculated output from the developed ANN. In this study,

MSE was used as the objective function to assess the accuracy of the ANN predictions. The validation dataset was then used to assess performance of the model trained on the training dataset and was reported after each iteration. Validation error was used to prevent the overlearning or overfitting of the model, as well as to fine-tune the model's parameters including the number of hidden layers. Finally, the testing data was then used to give an unbiased view of how well the training process performed in minimizing error. The testing data provides the best picture of the expected error from the trained model as it is a completely independent dataset from the validation and training datasets that are used to modify the model parameters during training. The inputs can range from 1 to any number *m* of user-defined values, however, a larger number of user-defined inputs requires more training data due to the higher model complexity. For example, if a problem has two independent variables, each with three training data points for each independent variable across the range of that variable in the problem domain, then there are nine data points in the training dataset, as shown in Figure 4-6a). However, that leaves a large gap between each training data point for the model to interpolate with no data. Instead, if five training data points are used, that increases the number of data points in the training dataset to 25, which can provide better coverage of the problem domain as depicted in Figure 4-6b). This creates an increase in the number of data points needed or at least preferred for each independent or input variable. This can create a limit to the number of independent variables that can be managed due to the number of data points in the training dataset needed.

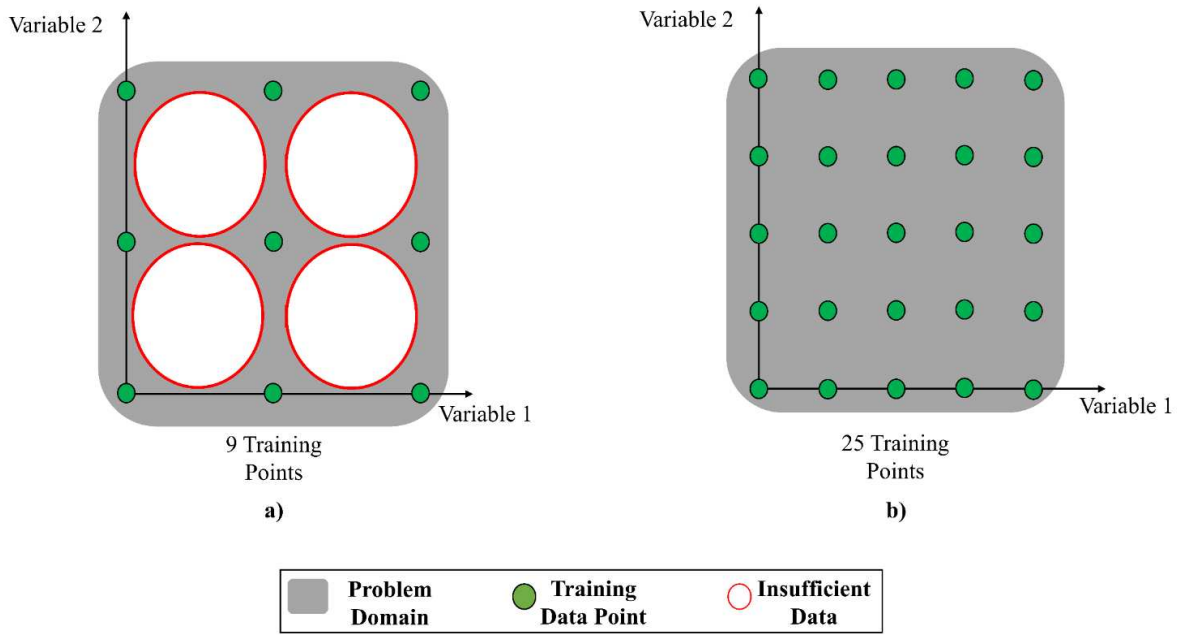

Figure 4-6: Model resolution for training data set for a) 9 training examples versus b) 25 training examples.

Similar to the inputs, the output **Y** can range to any number of user-determined values; however, most of the time there are fewer outputs than inputs. Y_i can be considered the known target values while y_i indicates the approximated values created by the network. The learning tool or training algorithm adjusts the weights, **W**, in order to minimize the MSE, or objective function, ***E***, between the approximate **y**, and the target value **Y**, as shown in Equation 4.1, where *n* represents the number of output values.

$$MSE = \frac{1}{n}\sum_{i=1}^{n}[y_i - Y_i]^2 \tag{4.1}$$

For complex networks with hidden layers, the value of the ith neuron, x_i in a feedforward network is.

$$x_i = f(s_i) \tag{4.2}$$

where s_i, the combination of the biases and the weights, is defined in Equation 4.3. In that equation, b_i is the bias of the i^{th} neuron, and W_{ji} is the weights between the i^{th} and j^{th} neuron of adjacent layers (Svozil et al., 1997; Werbos, 1990).

$$s_i = b_i + \sum_{j=1}^{i-1} W_{ji} x_j \tag{4.3}$$

The relationship between the input and output of a neuron is referred to as the transfer or activation function. Commonly used examples are tan-sigmoidal, logarithmic sigmoidal, linear, rectified linear unit (ReLU), or radial basis functions. As an example, the function for a logarithmic sigmoidal transfer function is shown in Equation 4.4, where *s* is defined above in Equation 4.3, and *e* is the base of the natural logarithm.

$$f(s) = \frac{1}{1+e^s} \tag{4.4}$$

4.4 Results and Discussion

4.4.1 CTH Simulations of Double Barrier System

Overall, the CTH model was used as a method for creating a training dataset for a double-barrier system to accomplish the main goal, which was to develop an ANN for rapid prediction of the pressures experienced around the double-barrier system. Even though this study was not meant to provide a detailed characterization of the wave interaction with a double-barrier system, it is important to understand how the blast shockwave interacts with the double-barrier system. Figure 4-7 depicts the blast wave at different times during the CTH simulations used to train the ANN.

Figure 4-7a) shows the hemispherical blast shockwave as it approaches the first barrier. The shockwave then contacts the first barrier reflecting off the front surface amplifying the pressure in front of the barrier and wrapping around the top to apply a load to the back of barrier one as shown in Figure 4-7b). The blast wave then interacts with both barriers in the gap between walls as part of the shockwave begins to pass over and wrap around the top of barrier two in Figure 4-7c). Between the barriers a complex flow field can be seen as multiple waves are intersecting and overlapping with each other to amplify and reflect off the barrier surfaces. The pressures experienced between the barriers are highly dependent on multiple factors including charge weight, standoff distance, and the gap distance between the barriers which is part of the reason so many tracers in the study were put in the gap to characterize the peak pressures at different locations. Finally, Figure 4-7d) shows the shockwave after it has passed the second barrier and has reformed after hitting the ground. Multiple wave fronts can be seen in front, between and behind the barriers demonstrating the complex flow field and variety of pressures experienced due to a double-barrier system.

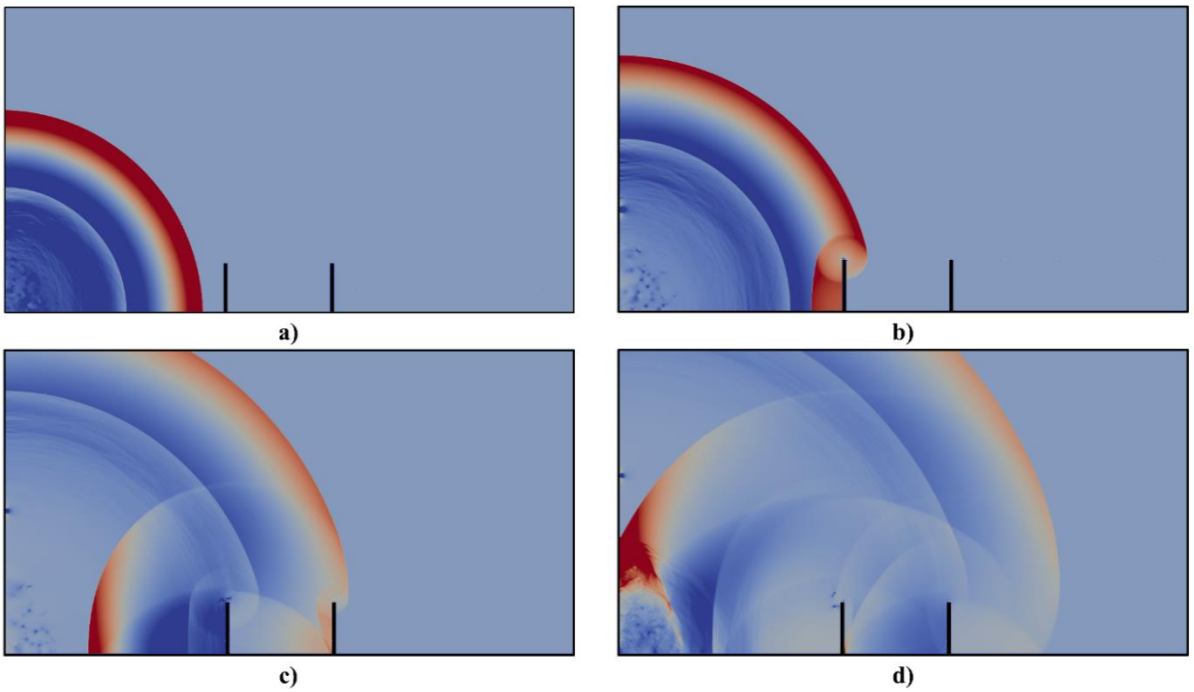

Figure 4-7: Blast shockwave expansion in CTH simulation for a double-barrier system where red is high pressure, dark blue is low pressure, and light blue is normal atmospheric pressure for a) before impacting the first barrier, b) passing over the first barrier, c) shockwave fully engaged in the gap and passing over the second barrier, and d) wave reformation after clearing the second barrier.

4.4.2 Network Performance Assessment

The neural network was built using the deep learning toolbox in MATLAB (2022). The toolbox provides a framework for designing and implementing deep neural networks and includes a host of training algorithms, in addition to what is listed in Table 4-3. The CTH dataset was uploaded as separate matrices for input parameters (4x630) and target outputs (60x630). The training dataset was randomly divided into three categories for training, validation, and testing, as previously mentioned. Inside the toolbox, the network architecture and performance parameters were manipulated to test the effects of each parameter on the accuracy of the model and determine the optimal combination. Similar to Remennikov and Rose (2005), different size networks were analyzed by varying the number of hidden layers and the number of hidden nodes. The four

parameters that were varied for each network are summarized in Table 4-4. The original network was set with two hidden layers, with 50 hidden neurons in both layers.

Table 4-4: Network Parameters Varied for Performance Assessment and Network Optimization

Parameter	Range
Number of Hidden Layers	1-3
Number of Hidden Nodes	10, 20, 30, 40, 50, 75, 100
Training Algorithm	See Table 1
Transfer Function	Logarithmic Sigmoid, Tangent Sigmoid, ReLU, Radial Basis, Linear

For each network, the data was cycled through multiple times in order to reach an acceptable level of MSE. One cycle, where all the training data has been cycled through once, is known as a single epoch. Error histograms were analyzed to verify that there were no outliers in the data during training of the individual tracers. While the training MSE assesses how well the ANN fits the training dataset, the validation MSE was used to assess performance of the model compared to a different dataset set aside from the training data and was reported after each iteration. This metric shows if the model needs further adjustment.

Depending on the complexity and non-linearity of the problem and the structure of the ANN model, different scenarios can occur when it comes to the training and validation errors, which are shown in Figure 4-8 for a three hidden layer ANN using the default parameters in the MATLAB toolbox. One scenario is that the magnitude of both the training and validation error is high as shown in Figure 4-8a). This indicates underfitting of the data, which means the model is unable to accurately fit the data (Barinov et al., 2023). Typically, this occurs when there is too little data for building the network or when trying to use a linear model with non-linear data. To

address underfitting, model complexity can be increased by adding layers and neurons, increasing iterations, trying different training algorithms, or by providing more data to train the model. In contrast, Figure 4-8b) shows an example of overfitting in the data. The training error is low, but the validation error is high. Overfitting occurs for different reasons, but the most common are training for a long period of time or the model being too complex for the dataset. Using a regularization method, simplifying the model architecture, and implementing early stopping parameters to avoid long training can prevent overfitting (Ying, 2019). When the model produces a good fit, both the validation and training errors will be low, and the validation error will be slightly above the training error, as shown in Figure 4-8c) and, for clarity, zoomed in at Figure 4-8d). The error curve in Figure 4-7c) decreases slowly at the beginning and rapidly at the end. Although this is unusual for a typical MSE curve, it is not uncommon. Similar curves to Figures 4-7c) and 4-7d), that have a decreasing trend until the point that training is terminated, can be found in Awad et al (2016) and Mustafa et al (2012). The results of the training with this shape loss curve may not have the optimal learning schedule but the ultimate result of achieving a low MSE and meeting other performance metrics of the network resulted in pressure predictions with good agreement with CTH and experimental validation in Chapter 3 of this dissertation.

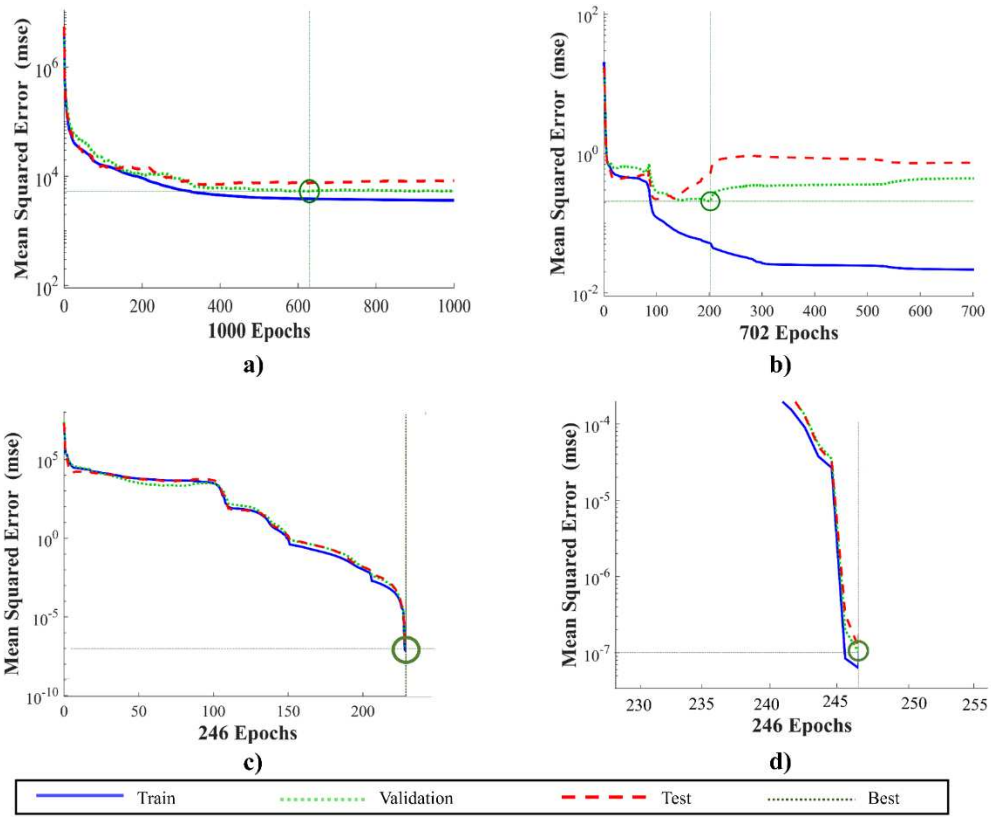

Figure 4-8: Performance Error of Tracer 1 for a) three hidden layers of 10 nodes each to show an underfitting model, b) three hidden layers of 100 nodes each to show an overfitting model, c) three hidden layers of 50 nodes each to show a good fitting model, and d) a zoomed in view of c) to show the validation error is above the training error.

Varying the training algorithms, introduced previously, was the first alteration explored in the network parameters. It was observed during training that the number of iterations needed to reach the lowest MSE varied a significant amount for the different training algorithms. Figure 4-9 shows the average number of iterations needed to reach the lowest MSE for each training algorithm and the average time to complete training across all tracer points. The Levenberg-Marquardt algorithm used the fewest number of iterations, an average of 21 iterations, in order to reach the lowest MSE and took the least amount of time to train in just 2.5 minutes. Bayesian Regularization and BFGS Quasi-Newton required the largest number of iterations to reach the lowest MSE,

averaging 923 iterations and 573 iterations, respectively. For both algorithms, that correlated to longer training and termination times.

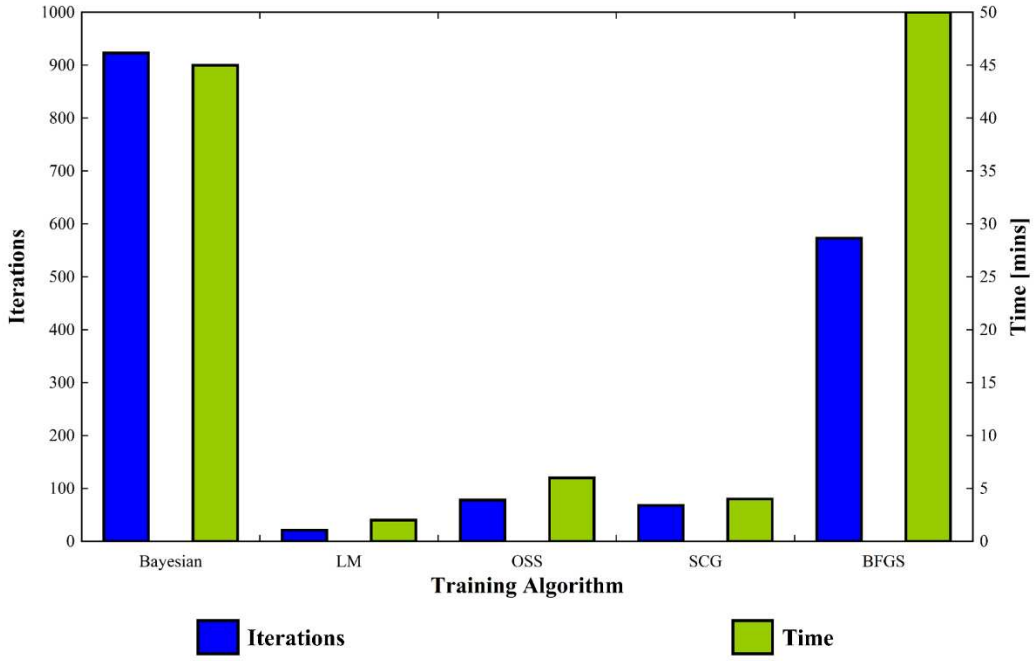

Figure 4-9: Average number of iterations to reach the lowest mean square error for varying training algorithms for tracers used in parameter assessment.

Figure 4-10a) shows the comparison of the resultant error between the different training algorithms tested. The error shown is the average error and lowest error across all tracers. The BFGS Quasi-Newton method was the least accurate, with a 21% lowest error, while Bayesian Regularization and Levenberg-Marquardt were the most accurate, at 4% and 5% lowest error, respectively, making them the most applicable for this network prediction. Bayesian Regularization performed the best out of all the training algorithms across all tracer locations.

Another network parameter that was varied was the transfer function of the hidden layers. Figure 4-10b) illustrates the accuracy of the different transfer functions. The default function within the MATLAB ANN toolbox was tangent sigmoid, which performed well with the lowest

error across all tracers of 5%. Logarithmic sigmoid performed similarly to tangent sigmoid, with the lowest error of 4%. The linear transfer function was the least accurate, with a 46% lowest error.

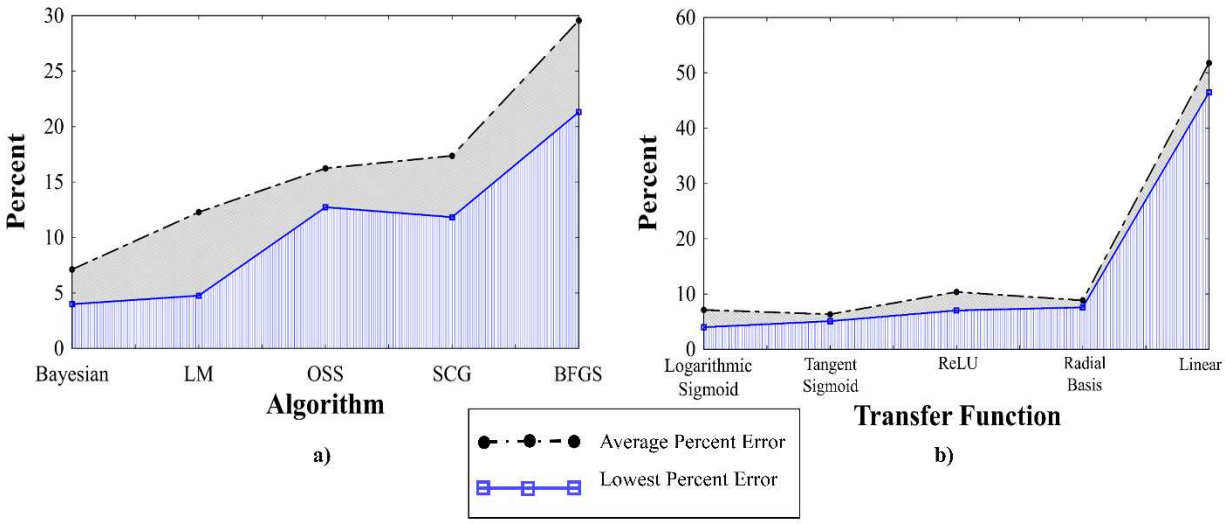

Figure 4-10: Comparison between the networks percent errors a) for varying training algorithms and b) varying transfer functions.

4.4.3 Alterations to Network Architecture

For further assessment of the network structure, Bayesian Regularization and logarithmic sigmoid were kept as the training algorithm and transfer function for consistency in comparison between the different networks. The model was adjusted for one, two, and three hidden layers while varying the number of hidden neurons in each layer between 10 and 100, as listed in Table 4. Figure 4-11a) and Figure 4-11b) show how those changes affected the resulting models' percent error for the varying number of hidden neurons and hidden layers, respectively. The percent error increased with fewer layers and fewer neurons in those layers. With only five neurons in each layer, the lowest percent error reached was 47%, while with an increase to ten neurons or higher, the lowest percent error was on average 7%. The changes in the average and lowest percent error with the number of neurons were due to shift in prediction accuracy at one or more data points.

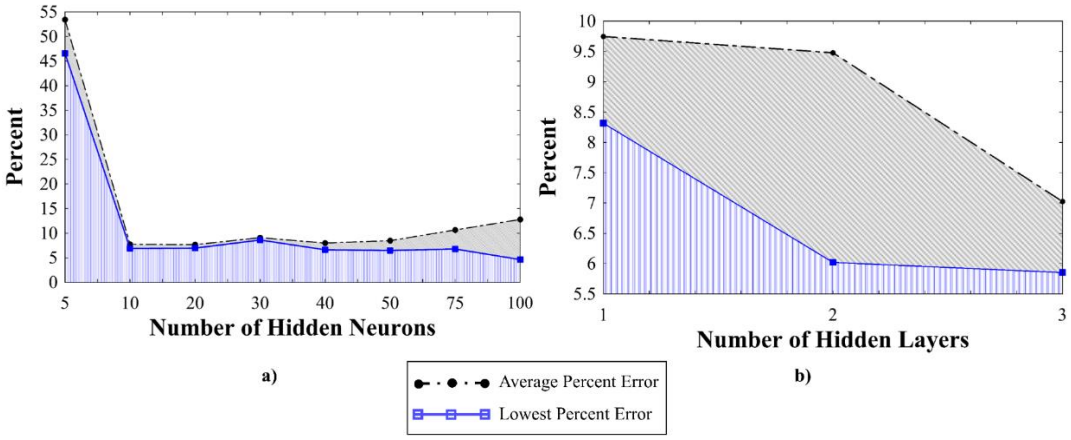

Figure 4-11: Comparison of network percent errors with varying number of a) hidden neurons and b) hidden layers.

4.4.4 Final Network Design

After evaluating the variation of network parameters and network structure, it was found that at least ten neurons were needed for more accurate results when using Bayesian Regularization. Theoretically, to produce the lowest MSE, a large number of nodes and multiple hidden layers would be ideal. However, due to the long run times of Bayesian Regularization, a larger network will cause the training time to increase exponentially, resulting in an unpractical network. Choosing the number of hidden neurons becomes a balance between lowering the network percent error and maintaining a reasonable run time (Pilkington & Mahmoud, 2016).

Ultimately a network with three hidden layers with 50 hidden neurons in each layer with a logarithmic sigmoid transfer function was chosen as the final network structure. Bayesian Regularization was chosen as the training algorithm, resulting in a data separation of 85 % (536) training and 15% (94) testing, as Bayesian does not require a validation phase. Regularization is a technique used in neural networks to prevent overfitting and improve the generalization performance of the model. The validation error calculated in training can be used as a form of

regularization in which the model is adjusted to fine tune the parameters of the model. Since Bayesian Regularization has its own regularization programmed into the algorithm, the validation phase was not used. The final network diagram from the MATLAB toolbox is shown in Figure 4-12. Figure 4-13 shows the performance for the final network that produced the highest overall accuracy. At each one of the tracers shown, the training shows a good fit, as both the testing and training tracked together and overall had a low MSE.

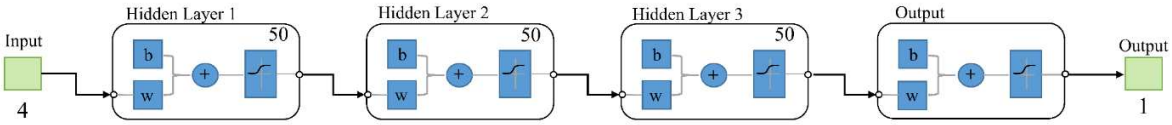

Figure 4-12: ANN structure for final model.

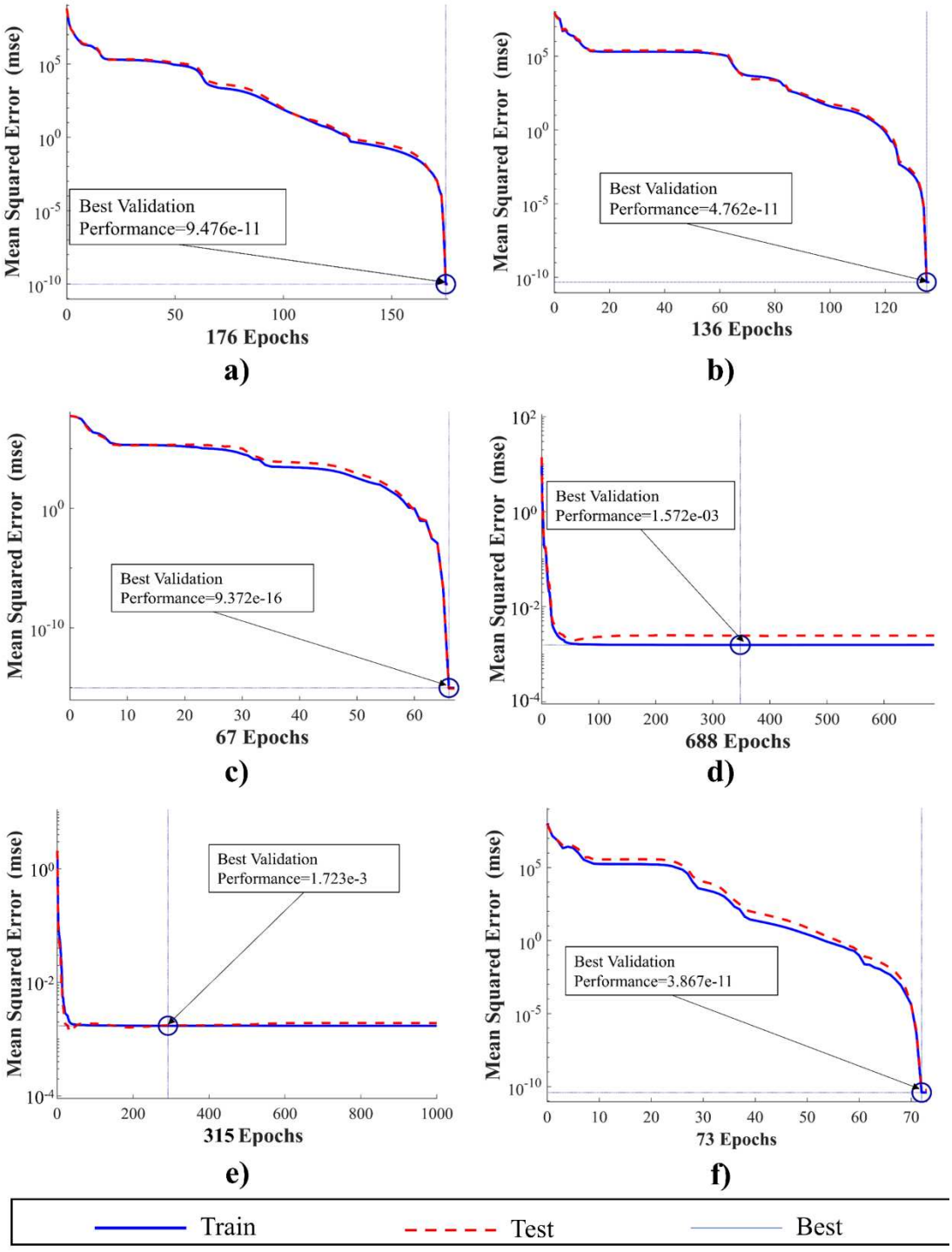

Figure 4-13: Performance of a) Tracer 1, b) Tracer 18, c) Tracer 23, d) Tracer 37, e) Tracer 39 and f) Tracer 50.

The final model was employed to predict the pressure for two random test cases within the data range not in the original training dataset, as shown in Table 4-5. These test cases were run through both the trained neural network and CTH to compare the results of both.

Table 4-5: Neural Network Parameter Assessment Tests

Test Number	**W [kg]**	**HOB [m]**	**Z [m/kg$^{1/3}$]**	**d [m]**
1	9.07 (20lbs)	0	1.98 (5 ft/lb$^{1/3}$)	0.91 (3ft)
2	22.68 (50lbs)	0.91 (3ft)	2.58(6.50 ft/lb$^{1/3}$)	2.13 (7ft)

Figure 4-14 shows the ANN predicted pressures and the CTH predicted pressures versus the tracer number in the domain. The pressures have been normalized to results from a CTH simulation for the same charge weight and HOB with no walls present (a value greater than 1.0 indicates that the pressure was higher compared to the simulation without walls at the same tracer location, and a value less than 1.0 indicates that the pressure was lower compared to the simulation without walls at the same location). The final ANN produced accurate results for both tests when compared to the CTH predictions. In Figure 4-14a) and Figure 4-14b), the first five tracers can be seen to have a normalized peak pressure greater than 1.0. This was due to the reflections caused by the barriers being present versus the incident pressure from the baseline test. Reflections of the surface perpendicular to the direction of travel, such as the barriers in this test series, will result in much higher reflected pressure and impulse (DOD, 2008). For the remaining tracers, the normalized pressure was close to 1.0 or dropped below 1.0. Reformation and reflection of the blast waves off the ground surface can occur due to the presence of a barrier. This was due to the change in direction of the wave when it interacts with the barrier which could result in higher pressures as seen in the spike between tracers 20-30 in Figure 4-14b). The reduction of pressure below 1.0 is expected as these tracers were between or behind the barriers which protects them from

experiencing the undisturbed incident wave but rather, they see a reduced pressure due to the barrier being present.

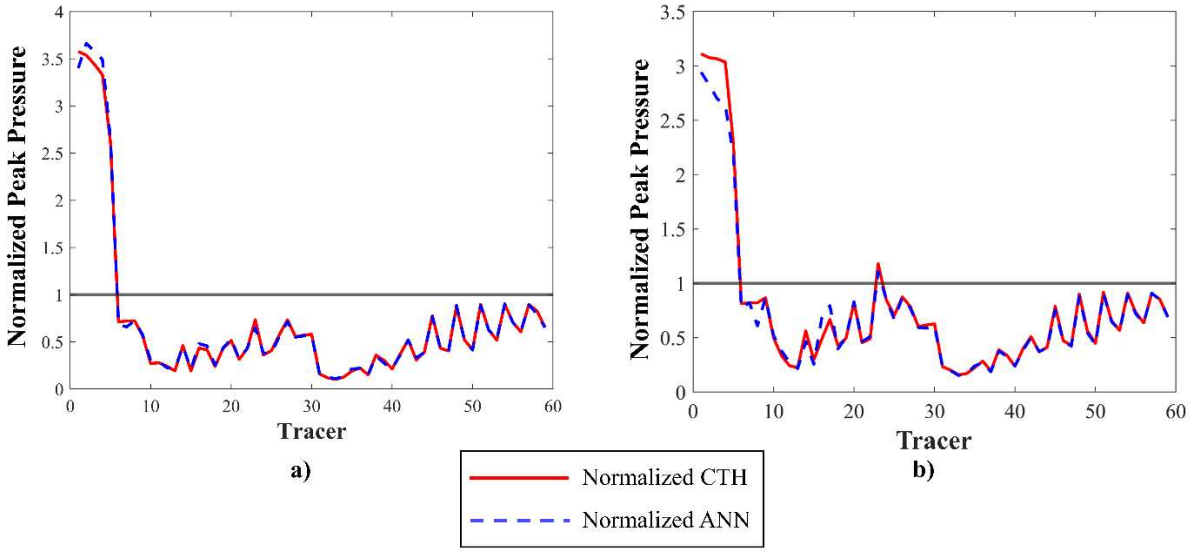

Figure 4-14: Normalized peak pressure predictions from ANN and CTH hydrocode for each tracer location a) Test 1 and b) Test 2.

Statistical and performance metrics are presented in Figure 4-15, Table 4-6, and Table 4-7. In Figure 4-15, the ANN predicted pressures were plotted versus the CTH predicted pressures to show the correlation between the predictions and the target outputs. The coefficient of determination, R^2, which describes how well the outputs match the targets, was close to one (or unity) in both tests, as desired for an accurate model.

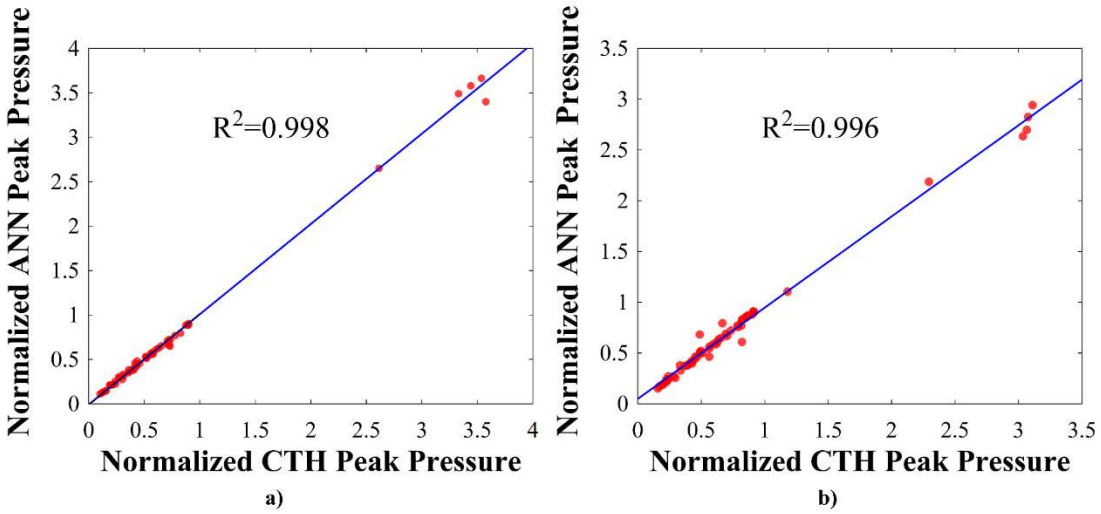

Figure 4-15: Normalized peak pressure predictions from CTH hydrocode versus ANN for a) Test 1 and b) Test 2.

The statistics for the overall network are summarized in Table 4-6. The MSE measures the average difference between the predicted and the target values. This metric is commonly used to assess the performance of a model as it heavily penalizes for large errors due to the square. For both test cases, MSE was less than 237 kPa^2 (5 psi^2), showing that there was minimal error in both ANN models. The mean absolute error (MAE) measures the average absolute difference between the prediction and target values but does not penalize for large errors as MSE does. The average MAE for both test one and test two was less than 6kPa (1 psi), again showing the network was able to accurately predict pressure for the tests input.

Table 4-6: Performance for both test cases for ANN versus CTH

Test Number	R^2	MSE [kPa^2]	MAE [kPa]	Average Error [%]
1	0.998	105.46 (2.22 psi^2)	4.45 (0.65psi)	3.73
2	0.996	199.95 (4.21 psi^2)	5.90 (0.86 psi)	5.15

The average errors summarized in Table 4-6 prove the ANN was successful in generalizing the inputs to accurately predict for tests inside the data range. Table 4-7 presents the variation in the percent error across the whole model. In test 1, 93.2% of tracers had less than 10% error from the CTH predictions. The targets were predicted with good accuracy, and all points in the model were predicted within the desired <20% error range. Test 2 had good accuracy with target prediction as well; however, there were 5% of tracers predicted outside the desired <20% error range.

Table 4-7: Performance Variation for Finalized Network for Peak Pressure Predictions

Test Number	**Percentage of Data Points Predicted within Percent Error Range [%]**		
	E<10	**10≤E<20**	**E≥20**
1	93.22	6.78	0.00
2	84.75	10.17	5.09

When comparing the ANN to the CTH model, computational cost was an important factor to analyze as well. A single CTH simulation took an average of 42 minutes to run with 4400 cores, resulting in a total of 3080 CPU-hours. The trained ANN produced predictions in less than 30 seconds using a laptop with 14 cores, resulting in 0.16 CPU-hours.

4.5 Summary and Conclusions

In summary, this chapter's main goal was to develop an ANN that could accurately predict the peak pressure in an environment with a double-barrier system in the path of the shock wave. The numerical dataset of pressure measurements was created using the hydrocode CTH to train and test the network. The developed ANN provides a unique perspective on airblast analysis using

artificial neural networks as it allows for the analysis of a double-barrier system to protect against blast shock wave propagation, which has little existing research in the field. Using the MSE as the main parameter to determine accuracy, five different neural network algorithms were compared for the training of the network including Bayesian Regularization, Levenberg-Marquardt, One Step Secant, Scaled Conjugate Gradient, and BFGS Quasi-Newton Method. The following conclusions and summaries can be drawn from the analysis:

- An ANN surrogate model was used to create predictions of peak pressure from a blast shockwave from a PBIED threat around a double-barrier system using the input parameters of charge weight (W), height of burst (HOB), scaled standoff distance (Z), gap distance between barriers (d).
- The use of a double-barrier system was evaluated to understand the impact more than one barrier would have on the pressure shockwave for use in large scale open areas where a single barrier would not provide sufficient protection for people in the vicinity of a blast.
- The hydrocode CTH was used to model a complex blast shockwave flow field with a double-barrier system to predict pressure in-front, between and behind those barriers to understand the impact the system could have on protecting people in the vicinity of a blast.
- A dataset of 630 simulations with pressure time histories for 60 tracer points in each simulation was created from the CTH model. This dataset was used to train the artificial neural network model.
- After manipulating network parameters and structure to assess the effects of a variety of characteristics on the models' prediction capabilities and performance, a reliable network was created.

- A 3-layer network with 50 hidden neurons each using a Bayesian Regularization training algorithm and a logarithmic sigmoid transfer function trained on an 85-15 training-testing split was found to predict multiple test scenarios above 90% accuracy as the final network structure.
- The final trained network predicted multiple test scenarios above 90% accuracy. Less than 10% have a difference greater than 34.5 kPa (5psi).
- The developed ANN can produce predictions with high accuracy and high statistical performance with significantly less time and memory requirements than the hydrocode simulations used to train the network.
- This model provides both military and civilian settings with a fast-running engineering tool to analyze the impact of a double-barrier system on hemispherical and spherical air blast scenarios.

CHAPTER 5: FINITE ELEMENT ANALYSIS OF NON-RIGID BLAST BARRIER

5.1 Introduction

The ANN developed in the previous chapter for a double-barrier system assumed the barriers in place remained rigid and fixed for all blast scenarios in the data range from Z=1.19m/kg$^{1/3}$-5.95m/kg$^{1/3}$ (3ft/lb$^{1/3}$-15ft/lb$^{1/3}$). This assumption needs to be validated to determine what types of barriers these models can be used for. Through the years, many different types of barriers have been utilized and researched for better blast protection (Bahei-El-Din & Dvorak, 2008; Dharmasena et al., 2008; Hussein et al., 2020). A wood-sand-wood sandwich style barrier is an attractive alternative to the large, robust, and immobile concrete barriers such as T-walls and Alaska barriers due to it being built of readily available materials for a more lightweight, and expedient style barrier.

In order to determine the performance of the wood barrier in these scenarios, the response of the barrier must be determined. Unlike in Chapter 3, the response of the barrier is not scalable like blast parameters of pressure and impulse, so the use of the tabletop is not applicable. Many techniques have been used over the years to perform blast prediction and mitigation research (Goel, 2015; T. Ngo et al., 2007). Numerical modeling offers many advantages over empirical or semi-empirical methods when it comes to modeling blast loading and dynamic material behavior. Reduced cost of experimental testing, faster completion of analysis, and complete response data for discrete points in the simulation are a few reasons numerical simulation has become such a powerful tool in engineering analysis and design. In recent years, computational and numerical models have grown in popularity for their accurate evaluation capabilities.

This chapter presents a finite element model (FEM) to predict the response of a modified wood sandwich barrier to a blast shockwave. The FEM of the barrier will be used to address part of the objective of assessing the application of an absorption focused barrier for PBIED threats. By investigating the barrier through FEM, an understanding of the response of the designed barrier in different blast scenarios can be determined. The results of this study will then be used to determine a test matrix for full scale experimentation to validate the findings of the FEM in a subsequent chapter.

5.2 Finite Element Model of the Barrier

5.2.1 Wood Wall Design

T-walls and HESCOS are commonly used in military settings as perimeters walls around army bases to provide protection to the people and equipment inside the base. Numerous studies have been completed both numerical and experimental on the use of reinforced cement concrete (RCC) for barriers (Khan et al., 2019; Taha et al., 2019; Trasborg, 2014). However, these barriers are large, robust, and immobile which makes it hard to be utilized in a civilian setting. Concrete jersey barriers are commonly used in civilian settings for crowd control. However, they do not provide much protection from blast waves due to their short vertical dimension. Hussein et al. (2019 & 2020a) developed a barrier made from low-tech common materials pulling motivation from a HESCO. The sandwich structure design utilized two orientated strands board (OSB) face sheets and a sand interlayer to act as an absorbing layer. Figure 5-1 shows the experimental wall that was tested.

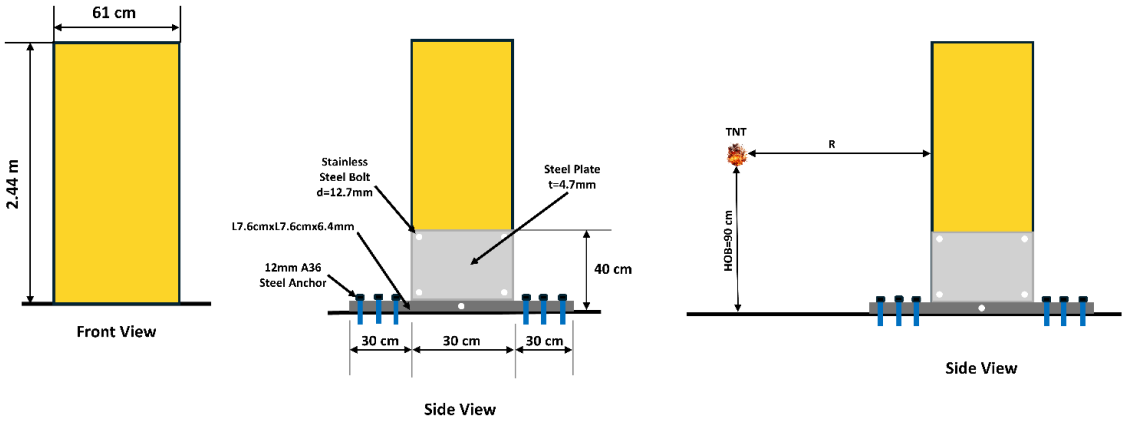

Figure 5-1: Wood-sand-wood wall experimentally tested in (Hussein, 2019; Hussein et al., 2020a).

The results of Hussein's study demonstrated that the simple wood-sand barrier could effectively reduce the pressure behind the wall, while limiting fragmentation and shrapnel due to the absorbing nature of the sand layer. However, the wall tested experimentally in the field was not the same as the one developed in the FEA during the study. The experimental wall dimensions did not match that of the one tested in ABAQUS. Additionally, the charges in which the barrier was tested were not realistic size threats. In order to determine how effective a wood-sand-wood barrier was in surviving large scale blast scenarios, the barrier needed to match the model to have more accurate predictions and the charges needed to be scaled up in size.

5.2.2 Finite Element Model Overview

A finite element model was devised and used to evaluate the response of the wood-sand-wood wall to blast loading. The model was developed using the dynamic explicit procedure in ABAQUS 2021 (ABAQUS/Explicit, 2021). A three-dimensional shell model with four-node (S4R) linear doubly curved thin or thick shell elements with reduced integration, hourglass control, and finite membrane strains were used to model the geometry of the wall. A shell model was

chosen as the wall was made up of thin parts with constant thickness allowing for significant computational time savings and mathematical simplification of solid element analysis.

The geometry of the wood-sand-wood model was determined based on the geometry of the wall used in the CTH simulations for the artificial neural network. The wall was 1.829m (6ft) in height, 1.244m (4ft) in width and 0.1524 m wide (6in) in depth as shown in Figure 5-2a). The mesh size used in the study was 2.5cm as shown in Figure 5-2b).

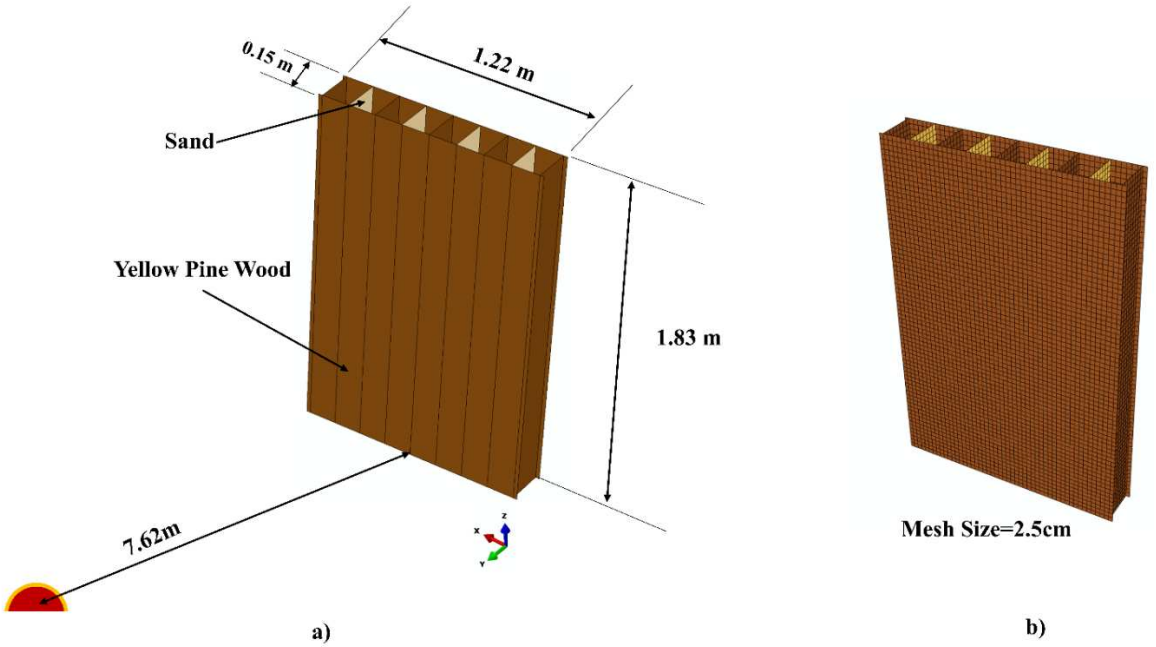

Figure 5-2: Finite element geometrical details for wood-sand-wood wall model.

A transversely isotropic material model for yellow pine was used to define the material behavior for the wood in the elastic zone using *Elastic/Engineering Constants* in ABAQUS. Yellow pine was chosen over the OSB used in Hussein's study as yellow pine is stronger and OSB is considered to be less resistant to water as it swells when exposed to moisture, which can affect the material properties. The material properties for the yellow pine are listed in Table 5-1. The tensile stress vs strain curve is shown in Figure 5-3. These curves were for rate effects at $500s^{-1}$ and blast is typically at a strain rate between 10^2-10^4 s^{-1} (Thornton & Colangelo, 1985). Since there

were no curves for the correct strain rate, the curve without strain rate effects was chosen to be conservative as there was hardly any difference between the curves. The softening part of the yellow pine curve was modeled using *Plastic/Isotropic Hardening* with a *Potential* sub-option in ABAQUS using the properties in Table 5-1. The sand was modeled using the Drucker-Prager plasticity model summarized in Table 5-2 to simulate sliding motion between sand grains (Drucker & Prager, 1952; Hussein, 2019; Hussein, et al., 2020a;2020b). Coupling was used to model the connection between the sand and the wood to limit the degrees of freedom between them to capture the behavior of sand sliding against the wood rather than being fixed to it.

Table 5-1: Mechanical Properties of Yellow Pine (DOT, 2007)

Parameter	Symbol	Value
Parallel Elastic Modulus [MPa]	E_{11} or E_L	11,350
Perpendicular Elastic Modulus [MPa]	E_{22} or E_T	247
Parallel Shear Modulus [MPa]	G_{12} or G_{LT}	715
Perpendicular Shear Modulus [MPa]	G_{23} or G_{TR}	88
Perpendicular Poisson's Ratio	ν_{12} or ν_{LT}	0.16
Yield Strength [MPa]	σ_y	150
Hill Yield Function Coefficients	R11	0.68
	R22=R33	0.061
	R12=R13=R23	0.206

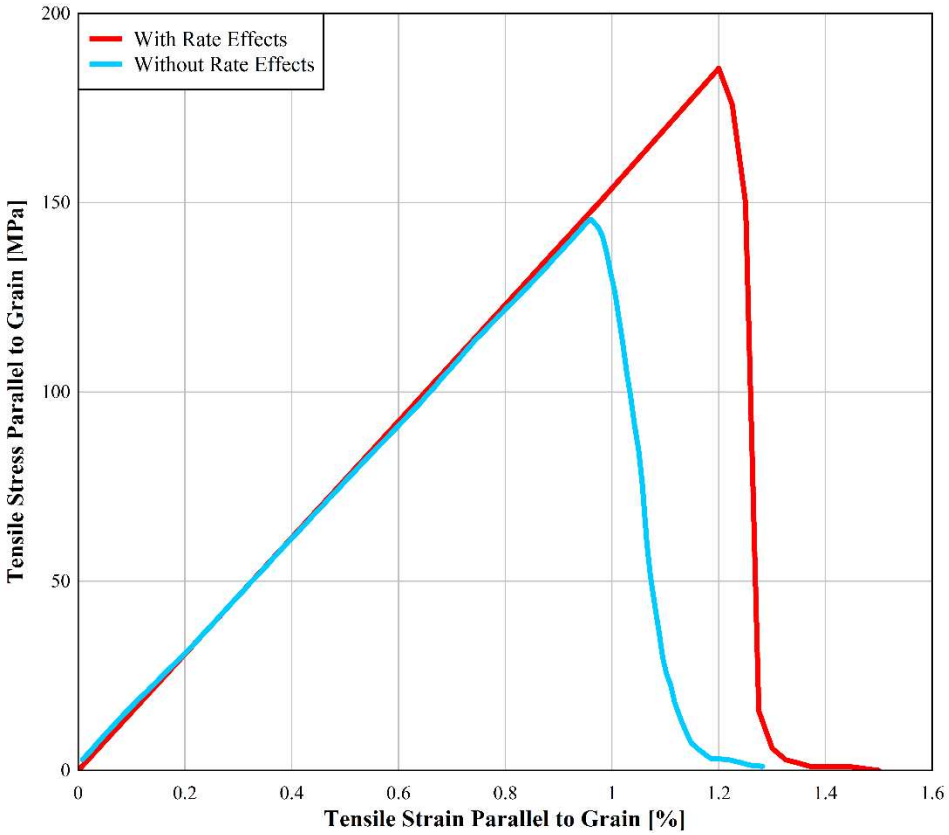

Figure 5-3: Tensile stress vs. strain curve for yellow pine at $500s^{-1}$ *modified from*:(DOT, 2007).

Table 5-2: Mechanical Properties of Sand and Drucker-Prager Parameters (Drucker & Prager, 1952)

Parameter	Symbol	Value
Density [kg/m^3]	ρ	1800
Modulus of Elasticity [MPa]	E	50
Poisson's Ratio	ν	0.3
Drucker Prager Plasticity Model		
Yield Stress [kPa]	σ_y	100
Dilation Angle	ψ	10°
Angle of Internal Friction	ϕ	30°
Material Constant	K	0.8

Since the bottom section of the wall was encased with the two angles, failure of the barrier where the angles were located was not expected to occur as highlighted in Chapter 6. Accordingly, modeling the angles was unnecessary. Instead, an encastre boundary condition was applied to the

bottom of the sand and wood sections of the model to encase the bottom of the barrier as it would be held in between metal angles in the field, to enforce a fixed boundary condition on the wall. The blast shock wave was modeled using the built-in blast model ConWep. The ConWep model in ABAQUS imposes a pressure loading due to an explosion in air defined by the location of the explosion, the time of detonation, and the loading surfaces. The blast type can either be air blast (spherical charge in air) or surface blast (hemispherical charge on the ground) defined by the equivalent mass of TNT. The CONWEP model was applied to the front surface of the barrier only. The wraparound of the wave over the top of the barrier as it hits the back surface of the barrier was not included in the analysis as an understanding of the mechanics, time history of the blast pressure wave and the area the wraparound pressure would be in contact with needs to be determined in order to accurately apply the load to the back side of the barrier. To do this a trial-and-error process could be used in conjunction with an accurate displacement time history curve from the barrier to adjust the area and percentage of the peak pressure to apply to the back surface in order to capture the correct displacement of the barrier.

A fixed standoff of 7.62m (25ft) on the ground was set for all tests for a variety of scaled standoff distances between 7.62m/kg$^{1/3}$ (19.21ft/lb$^{1/3}$) and 1.19m/kg$^{1/3}$ (3ft/lb$^{1/3}$) from the CTH simulations to be tested by only having to change the charge size (lbs or kg of TNT). The connection between the sand and wood panels was defined as a pin using a coupling constraint to allow for movement between the sand and wood. The movement of the sand was limited as the sand was completely encased inside the wood and was compacted, so it was able to rotate but unable to displace due to the wood barrier confinement. Total load time was calculated in the ConWep program, but each model was run for a total of 0.1 seconds to allow for the full response

of the wall to be captured. A mesh size study was conducted to examine convergence and stability of the model. The mesh size varied between 10cm and 1cm. It was found that a mesh smaller than 3cm resulted in stress variation of less than 2%. As result, a mesh size of 2.5cm was used.

5.2.3 Finite Element Model Results

The developed FEM was used to assess the survivability of the wall to blast loading using the Von Mises invariant failure criterion. The Von Mises failure criterion uses the in-plane stress components (σ_x, σ_y, τ_{xy}) of the wall. The Von Mises failure criterion is one of the best predictors, outperforming other criteria including Tsai-Hill, Van der Put, linear, and quadratic models, in determining failure for on-axis tension of wood components when the loading is parallel to the direction of the grains in wood members (Aicher & Klöck, 2001; Cabrero & Gebremedhin, 2010).

The Von Mises yield equation for predicting yielding is shown in Equation 5.1.

$$\sigma_v^2 = \sigma_x^2 - \sigma_x\sigma_y + \sigma_y^2 + 3\tau_{xy}^2 \tag{5.1}$$

The equation for the failure index (IF) is calculated by normalizing the stresses to the respective strength components for the on-axis case using Equation 5.2.

$$\left(\frac{\sigma_x}{f_x}\right)^2 - \frac{\sigma_x\sigma_y}{f_x f_y} + \left(\frac{\sigma_y}{f_y}\right)^2 + 3\left(\frac{\tau_{xy}}{f_v}\right)^2 \tag{5.2}$$

Where σ_x, σ_y and τ_{xy} are on- axis stresses and f_x, f_y are on-axis normal strengths and f_v is the on-axis shear strength. The strengths needed for the analysis were all found in (DOT, 2007) where the material properties for yellow pine were taken from. The IF increases from IF=0 which indicates no stress on the barrier, to IF=1 which indicates yielding of the barrier. In between IF=0 and IF=1, the value of the IF represents the combined stress state of the barrier as it uses the invariants to assess failure meaning the overall yield strength of the material may not be reached. The stresses used to assess the Von Mises failure criterion did not include those that were a result

of the fixity of the boundary conditions since these stresses are unrealistically high as a result of not modeling the bottom angle.

In addition to the Von Mises failure criterion, the displacement of the barrier was assessed at the back center of the barrier to determine the maximum deflection of the barrier. The failure index versus the scaled standoff distance Z is shown in Figure 5-4. The deflection and failure index for each standoff tested is summarized in Table 5-3. From the numerical analysis in ABAQUS, the wood wall could survive blast shock up to Z=3.66m/kg$^{1/3}$ (9.23ft/lb$^{1/3}$). This resulted in a deflection of 0.01m (0.4in). As the scaled distance Z was increased by lowering the charge weight, the deflection in the wall decreased and so did the failure index as the stress on the wall was decreased.

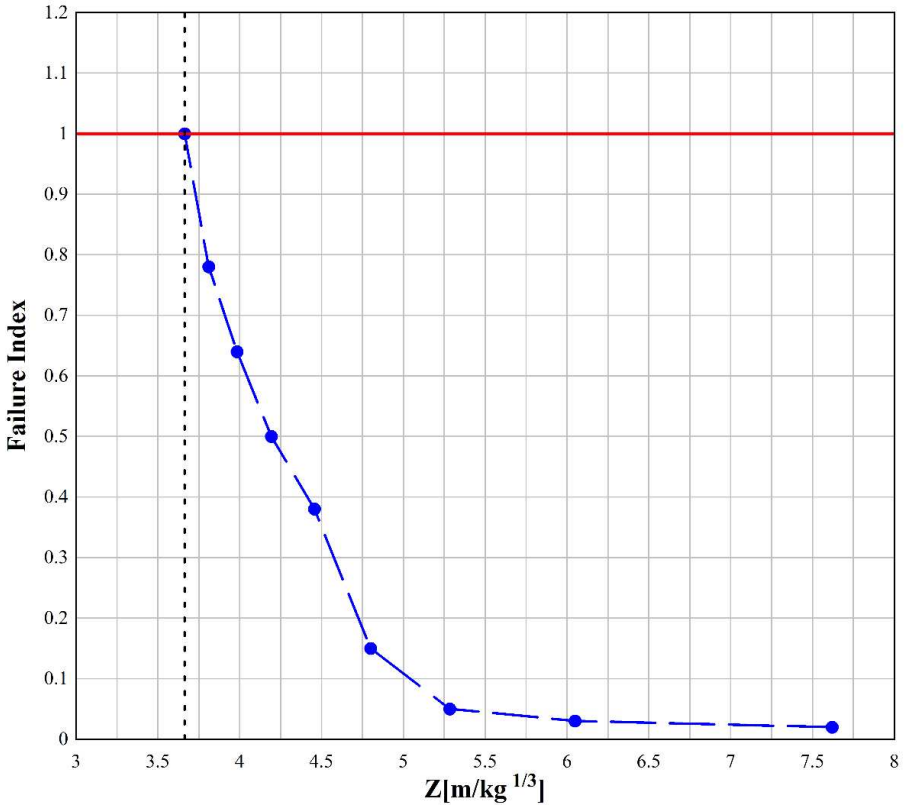

Figure 5-4: Numerical failure index of wood-sand-wood wall.

Table 5-3: Deflection and failure criteria for standoffs tested in ABAQUS.

Z [m/kg$^{1/3}$]	**Deflection [m]**	**IF**
7.62	0.0014	0.02
6.05	0.0021	0.03
5.28	0.0029	0.05
4.80	0.0038	0.15
4.46	0.0048	0.38
4.19	0.0059	0.5
3.98	0.0073	0.64
3.81	0.0088	0.78
3.66	0.010	1.0
3.54	0.012	1.0
3.43	0.013	1.0
3.33	0.015	1.0
3.24	0.017	1.0
3.16	0.019	1.0
3.09	0.021	1.0
3.02	0.023	1.0

Figure 5-5a) shows the displacement time history for Z=5.25 m/kg$^{1/3}$ (13.23ft/lb$^{1/3}$). The displacement curve from ABAQUS exhibits the expected oscillating response as the wall deflects and returns to its original state as no softening or yielding has occurred to the structure. Figure 5-5b) depicts the stress distribution of the wall from the FEM from the same standoff. The wall experienced the most stress at the fixed bottom of the wall while the rest of the wall experienced low stress as the wall deflected minimally.

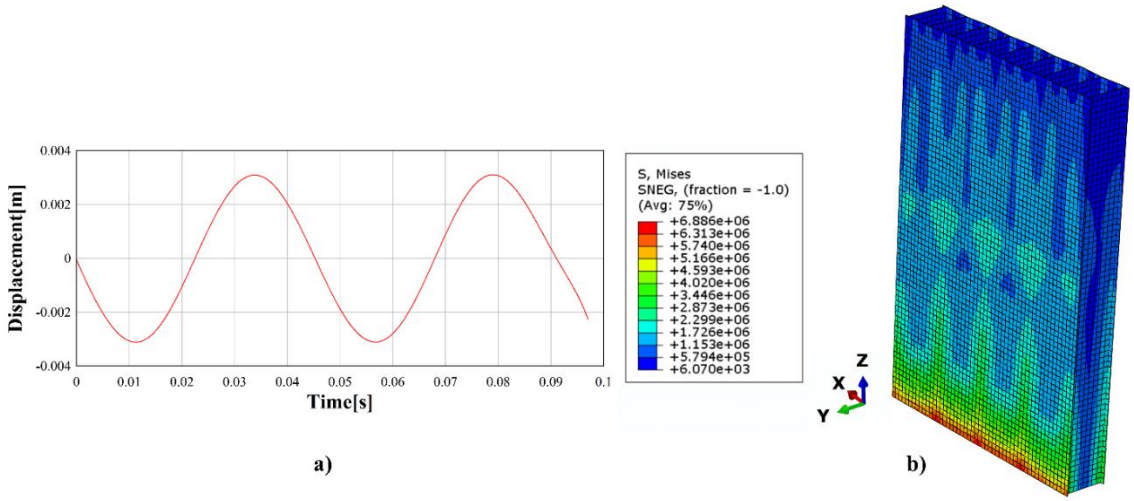

Figure 5-5: a) Elastic deflection response and b) Von Mises stress distribution for finite element model results Z=5.25 m/kg$^{1/3}$ (13.23ft/lb$^{1/3}$).

In contrast, Figure 5-6a) shows the displacement time history for a Z=3.02 m/kg$^{1/3}$ (7.61ft/lb$^{1/3}$). The displacement curve from ABAQUS experiences plasticity in its response due to the non-oscillatory response and that the curve has a clear maximum deflection with a final non-zero displacement around 0.0175m. The curve does not return to 0m displacement indicating permanent deformation of the barrier. Figure 5-6b) is the stress distribution of the wall from the same standoff. The stress distribution shows significantly higher stresses along the fixed bottom of the wall that stretches up the length of the wall putting more stress on the structure.

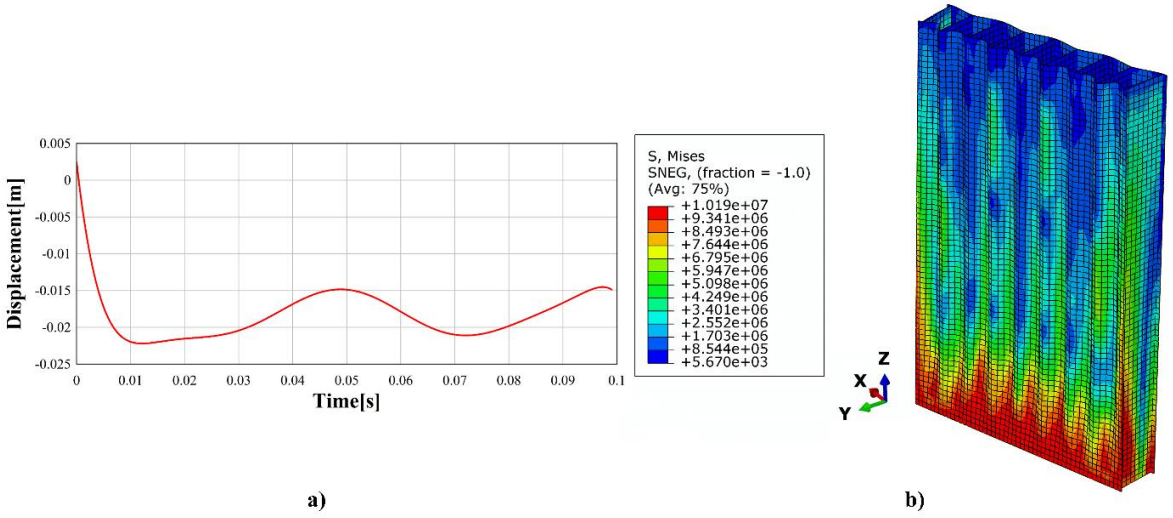

Figure 5-6: a) Time-history response and b) Von Mises stress distribution for finite element model results Z=3.02 m/kg$^{1/3}$ (7.61ft/lb$^{1/3}$).

Along with the failure index analysis, the force versus displacement curve was graphed to verify when yielding and failure occurred in the model. Figure 5-7 shows the resistance curve of the barrier from the ABAQUS model. From the change in slope at a displacement of 0.01m (0.39in), the elastic zone ends, and plastic deformation begins. The slope of the elastic zone represents the stiffness of the barrier in the elastic zone at k=3E+04kPa/m. The slope of the plastic region has two different stiffnesses as the displacement gets larger. From displacement of 0.01m (0.39in) to 0.0315m (1.24in) the stiffness decreases to k=1E4kPa/m while after 0.0315m (1.24in) the stiffness decreases further to 6E+03kPa/m.

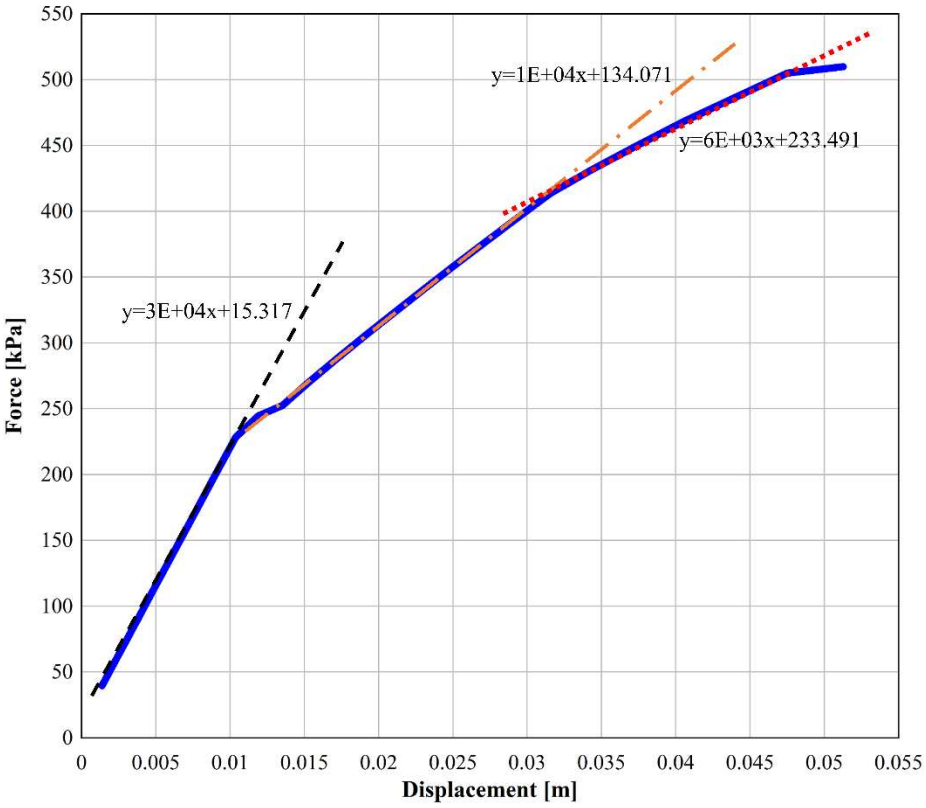

Figure 5-7: Force vs displacement curve for wood-sand-wood model.

5.3 Summary and Conclusions

The main goal of this chapter was to build a finite element model of a wood-sand-wood barrier that could be used to predict the response of the sandwich structure style barrier to various blast loading scenarios. The developed model provides a tool for analysis of a non-rigid barrier against blast loading to assess alternative methods for mitigating the effects of blast loads. Using the model allows for analysis of the structural properties, failure limits and maximum peak deflections. These predictions provide valuable information that can be used in other aspects of the analysis for this dissertation.

The following summary points and conclusions can be drawn from the developed model:

- A 3D dynamic shell model of the wood-sand-wood wall was modeled in ABAQUS using the same materials and geometry as those used in the field. Material models and connections were set up to mimic those of the real interactions as close as possible to capture the response the wall could have and assess its effectiveness in a variety of blast scenarios.
- The Von Mises failure criterion was used to assess the yielding of the barrier and the onset of plastic deformation. The failure criterion found the elastic limit of the wood barrier to be at a $Z=3.66 m/kg^{1/3}$ ($9.23 ft/lb^{1/3}$) when the back center of the barrier was deflected to x=0.01m (0.39in).
- After the elastic limit, the sinusoidal response of the barrier becomes a single maximum deflection with a permanent deformation less than the original max deflection.
- The loads and displacements for the FEM barrier were recorded to create a resistance curve. The slope of the resistance curve can be used to determine the stiffness of the barrier in different regimes of the analysis. The elastic limit was confirmed with the change in slope of the resistance curve at a displacement of x=0.01m (0.39in). The stiffness of the barrier in the elastic region was around K=3E7Pa/m while the stiffness in the plastic regime reduced to 1E7Pa/m.
- The developed FEM of the wood-sand-wood wall was able to model both elastic and plastic response of the wall to blast loading. This model can be used as a baseline to determine the test matrix for full scale testing in Chapter 6.

CHAPTER 6: LARGE SCALE EXPERIMENTATION OF BARRIER DESIGN FOR BLAST MITIGATION

6.1 Introduction

Through the years, many studies have investigated how structural systems and barriers behave when subjected to blast, using experimental or analytical methods to show the effectiveness of a single barrier in reducing the blast shockwave (Goel & Matsagar, 2014b; Xiao et al., 2017). Different shapes, sizes, and materials have been tested to determine new innovative ways to provide protection (Bahei-El-Din & Dvorak, 2008; Dharmasena et al., 2008; Hussein, et al., 2020). Numerous studies have been conducted over the years to understand the impact a barrier has on the blast shock wave. Isaac et al. (2023) conducted an extensive literature review concerning blast-structure interaction. It is well known that when a blast wave impinges upon a rigid structure reflection, rarefaction, and diffraction of the blast wave can occur (Remennikov & Carolan, 2005). The resulting behavior of the blast wave depends on the size, geometry, and material of the structure. The level of amplification depends on factors such as the angle of incidence of the incident wave, the incident pressure of the shockwave, and the compliance of the structure (DOD, 2008; Kinney et al., 1985). The geometry and height of the barriers have an effect on the diffraction and intensity of the blast wave pressure as well (Shirbhate & Goel, 2021).

In the past, the use of non-rigid materials for blast barriers is not uncommon, as it could provide a way to increase energy absorption to attenuate the propagation and duration of the blast wave rather than extend and amplify it. One of the most common forms is a sandwich structure as presented in section 2.6.1 of this dissertation. The idea is that as the barrier plastically deforms, it can dissipate energy reducing the magnitude and duration of the shock wave. Many authors have

studied the design and materials of different sandwich structures (Bahei-El-Din & Dvorak, 2008; Drdlová et al., 2015; Hajek et al., 2016; D. Lee & O 'Toole, 2014).

Historically, natural materials such as water, sand and soil have been successful in significantly mitigating blast waves. Some studies have looked at the effectiveness of using water as an interlayer of a barrier to mitigate a blast wave (Chen et al., 2015; Sugiyama et al., 2014). Sand and soil have been used extensively as an interlayer for temporary barriers such as HESCO's. These individual containers are stacked to form a wall. Hussein et al. (2020a; 2020b) developed a sandwich structure design that utilized two orientated strands board (OSB) face sheets and a sand interlayer to function as an absorbing layer.

The focus of this chapter is to present the full-scale experimental testing of a wood-sand-wood blast barrier based on the FEM in Chapter 5 of this dissertation. Chapter 6 addresses the second portion of the objective of investigating an absorption focused barrier for application against PBIED threats. The experiments conducted and barriers constructed were on a larger scale than previously tested to assess a more realistic blast scenario to determine the barrier's effectiveness in surviving a blast loading event and, in the ability, to attenuate the blast wave. The four goals of the large-scale experimental barrier testing were to (1) assess the charge scenarios for which the expedient light weight wood-sand-wood barrier remains rigid and fixed during the positive phase of the blast to match the assumptions of CTH modeling and the ANN, (2) assess the structural response of a wood-sand-wood barrier subjected to large blast loading, (3) obtain pressure measurements to establish experimental data to validate effectiveness in the barrier in reducing pressures, and (4) assess the effectiveness of an expedient light weight barrier made of commonly available materials.

6.2 Field Experimentation

6.2.1 Physical Barrier Design and Materials

The barrier tested in these experiments was as close as possible to the barrier designed in Chapter 5. The geometrical dimensions were 1.83m (6ft) in height, 1.22m (4ft) in width and 15.24cm (6in) in depth as shown in Figure 6-1a). Five wood barriers were constructed as stud walls as shown in Figure 6-1b) with yellow pine 5.08cm x 10.16cm (2in x 4in) lumber and 1.905cm (3/4in) thick plywood. The studs divided the walls into four enclosed cells that would ultimately be filled by sand.

a) b)

Figure 6-1: a) construction of wood barriers and b) constructed wood barrier with no sand.

Once the walls were constructed, the empty walls were then transported to the testing site where the cavities were filled with densely packed concrete masonry sand as shown in Figure 6-2a). Figure 6-2b) shows that the walls were filled up to the top but still allowed for the top piece of lumber to be placed as a lid.

a)

b)

Figure 6-2: a) Filling the wood barriers with concrete masonry sand and b) filled wood barrier with top removed to see sand level in each section of the barrier.

The sand used for all experiments was concrete masonry sand (ARCOSA, 2023). The gradation data was provided by the manufacturer plotted in Figure 6-3. Two samples were taken for moisture content analysis as it rained between experiments 3 and 4 soaking the sand. The moisture content of the sand used in experiments 1-3 was 2.29% and while the moisture content of the sand used in experiments 4-5 was 8.98%.

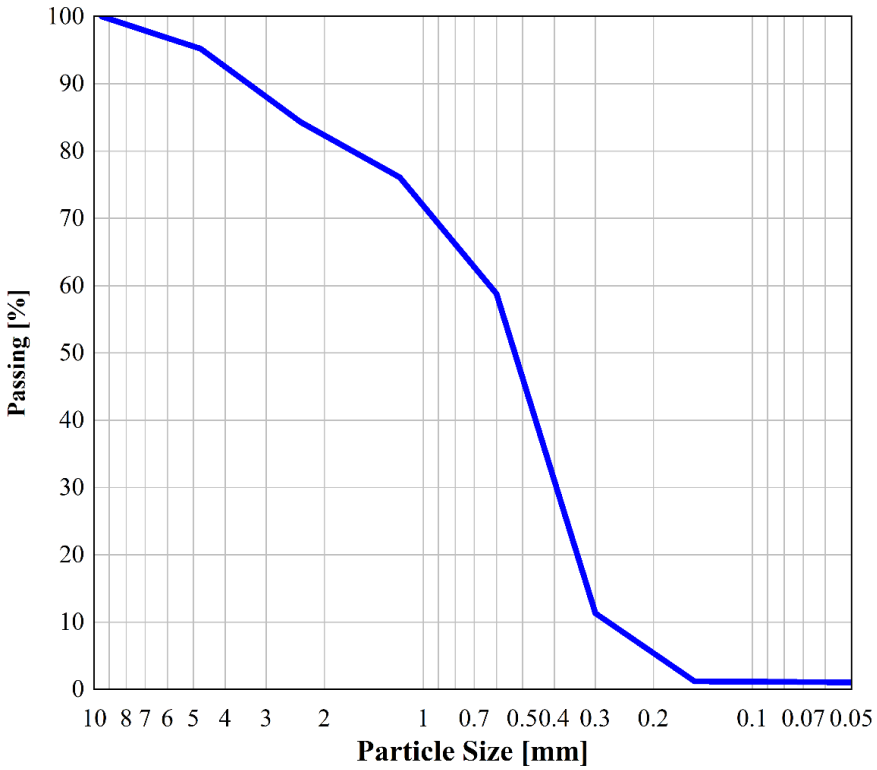

Figure 6-3: Graduation curve for particle distribution of sand.

The barrier was held in place by a metal sleeve constructed out of a 1.22m (4ft) by 2.44m (8ft) by 0.95cm (3/8in) thick steel plate with two 1.27cm (1/2in), 15.24cm (6in) angles welded to the center of the plate as shown in Figure 6-4. The metal sleeve was similar in dimension to the FEM of the wood barrier in Chapter 5 that encased the bottom of the barrier to the same height as the angles to apply a fixed boundary condition to the wall. Eight 1.43cm (9/16in) holes spaced in pairs spaced 8.57cm (3.375in) apart with a gap between pairs of 20.96cm (8.25in) on center across the width of the angles for bolting the barrier to the sleeve. The walls were held upright by attaching the angles to the wood walls using 1.27cm (1/2in)-13 24.13cm (9.5in).

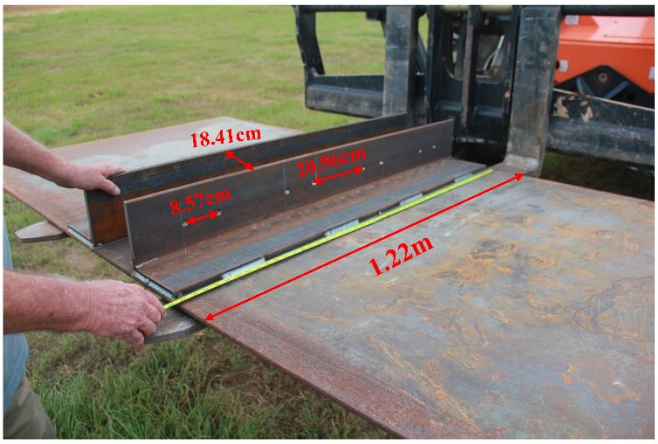

a)

b)

Figure 6-4: a) Metal sleeve to hold barrier during tests and b) the metal sleeve holding a wood barrier with bolts at the bottom.

6.2.2 Experimental Set Up

The ERDC testing site at Fort Johnson in Louisiana was used for the full-scale tests of the wood-sand barriers. A section of a field was graded and leveled for testing. Four Alaska barriers were buried into the ground so that 1.83m (6ft) of the top of the barrier remained above ground to function as clearing walls around the side of the barriers and to simulate as if multiple wood-sand-wood sandwich walls were placed next to each other, to replicate a realistic perimeter barrier. As shown in Figure 6-5, the metal sleeve and wood-sand barrier were placed in the center of the four Alaska barriers to create a continuous surface and eliminate the potential for the blast wave to wrap around the sides of the wood-sand-wood wall. Before the metal sleeve was placed between the Alaska barriers in the field, the ground was leveled and smoothed to produce an even surface for the walls to rest on. The metal plate was not fixed in place, but the metal sleeve was overdesigned and comprised of large mass to prevent translation (i.e., sliding) and rotation. Thin aluminum

flashing was used during each test to fill the seams between the wood barrier and the Alaska barriers to prevent the shockwave from passing through.

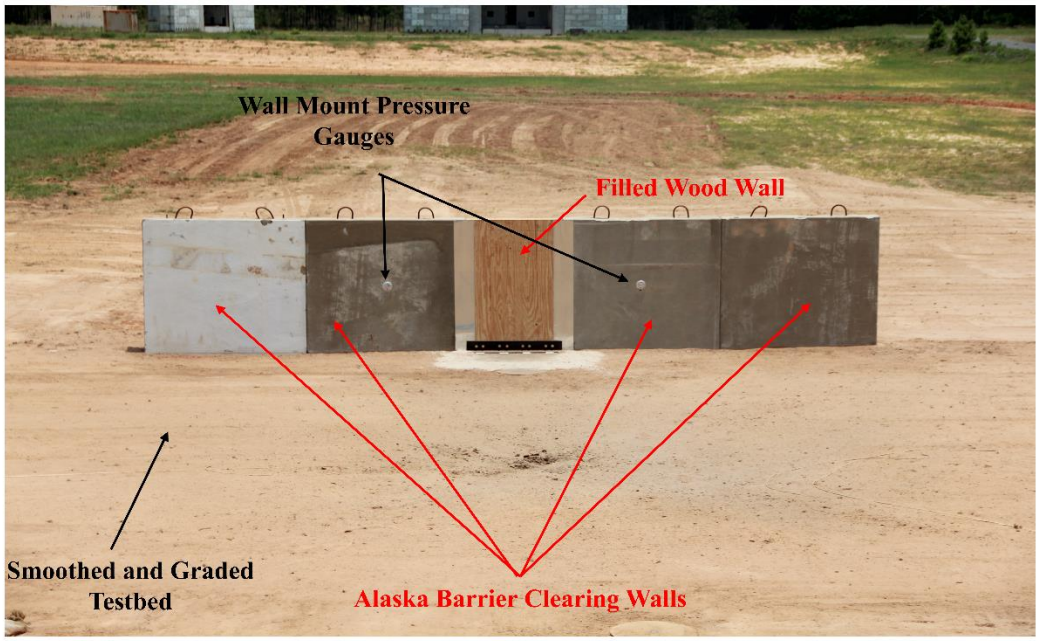

Figure 6-5: Graded field-testing plot with Alaska barriers buried as clearing walls.

The charge was placed at a fixed distance away from the center front surface of the barrier for each experiment. This allowed for the scaled standoff distance of Z to be changed for each test by only changing the charge weight and keeping the pressure gauges and barriers in the same place.

6.2.2.1 Instrumentation

Eight model HKS-375 pressure gauges manufactured by Kulite Semiconductors, Inc., were installed in different locations in the field. The pressure gauge thresholds ranged from 172.4 kPa (25 psi) – 689.5 kPa (100 psi) depending on the location in the field to prevent the pressures from exceeding the ideal range of each gauge (between 10% - 50% of the gauge maximum threshold).

Figure 6-6 shows the layout of the pressure gauges on the field for all the tests. Gauges 1, 2, 3, 5 were ground mount gauges flush with the surface of the ground. Gauge 3 was installed to capture the incident pressure of the incoming blast wave as close to the front of the wood barrier as possible. Gauge 5 was on the back side of the barrier to assess how much the pressure was reduced. Gauges 1 and 2 were "free field" gauges at the same distance from the charge as gauges 3 and 5, respectively to see how the barrier either amplified or reduced the pressure compared to if there was no barrier present. Gauges 7 and 8 were located in the clearing walls to the right and left of the wood barrier 91.44cm (3ft) up off the ground. Gauges 4 and 6 were elevated gooseneck gauges located at a height of 91.44cm (3ft). Gauge 4 was a free field gauge at the same distance as gauges 7 and 8 to assess the amplification of the pressure. Gauge 6 was a validation gauge to compare hydrocode and neural network predictions from the earlier developed models in this dissertation. Table 6-1 summarizes the scaled distances of the gauges for each of the 5 experiments completed.

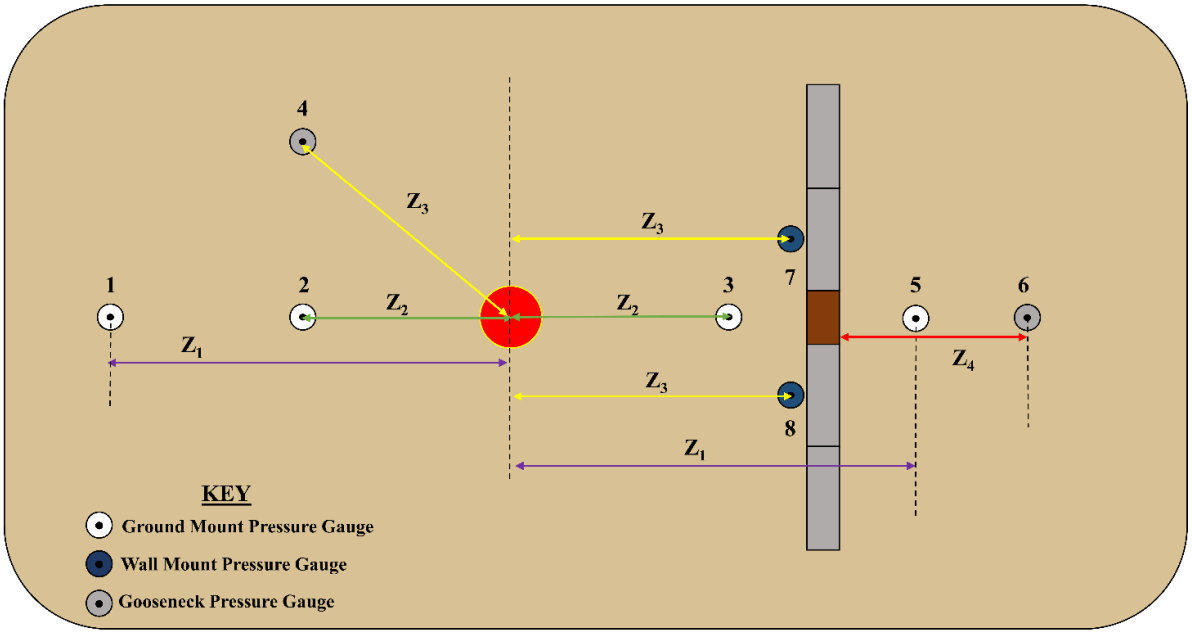

Figure 6-6: Plane view of pressure gauge locations on the field for all experiments.

Table 6-1: Gauge standoff distances for different experiments

Gauge Number	Test 1 Z	Test 2 Z	Test 3 Z	Test 4 Z	Test 5 Z
1	9.57 (24.13 ft/lb$^{1/3}$)	9.57 (24.13 ft/lb$^{1/3}$)	7.05 (17.76 ft/lb$^{1/3}$)	4.75 (11.98 ft/lb$^{1/3}$)	3.08 (7.76 ft/lb$^{1/3}$)
2	6.38 (16.08 ft/lb$^{1/3}$)	6.38 (16.08 ft/lb$^{1/3}$)	4.69 (11.84 ft/lb$^{1/3}$)	3.17 (7.98 ft/lb$^{1/3}$)	2.05 (5.17 ft/lb$^{1/3}$)
3	6.38 (16.08 ft/lb$^{1/3}$)	6.38 (16.08 ft/lb$^{1/3}$)	4.69 (11.84 ft/lb$^{1/3}$)	3.17 (7.98 ft/lb$^{1/3}$)	2.05 (5.17 ft/lb$^{1/3}$)
4	7.98 (17.97 ft/lb$^{1/3}$)	7.98 (17.97 ft/lb$^{1/3}$)	5.88 (14.82 ft/lb$^{1/3}$)	3.96 (9.98 ft/lb$^{1/3}$)	2.56 (6.47ft/lb$^{1/3}$)
5	9.57 (24.13 ft/lb$^{1/3}$)	9.57 (24.13 ft/lb$^{1/3}$)	7.05 (17.76 ft/lb$^{1/3}$)	4.75 (11.98 ft/lb$^{1/3}$)	3.08 (7.76 ft/lb$^{1/3}$)
6	11.98 (30.18 ft/lb$^{1/3}$)	11.98 (30.18 ft/lb$^{1/3}$)	8.82 (22.22 ft/lb$^{1/3}$)	5.95 (14.99 ft/lb$^{1/3}$)	3.85 (9.71 ft/lb$^{1/3}$)
7	7.98 (17.97 ft/lb$^{1/3}$)	7.98 (17.97 ft/lb$^{1/3}$)	5.88 (14.82 ft/lb$^{1/3}$)	3.96 (9.98 ft/lb$^{1/3}$)	2.56 (6.47ft/lb$^{1/3}$)
8	7.98 (17.97 ft/lb$^{1/3}$)	7.98 (17.97 ft/lb$^{1/3}$)	5.88 (14.82 ft/lb$^{1/3}$)	3.96 (9.98 ft/lb$^{1/3}$)	2.56 (6.47ft/lb$^{1/3}$)

Gauge 6 was placed behind the barrier a distance of 2H back from the back surface of the wall to look at how the pressure behaves 2x the wall height behind the barrier in experiment 1 as shown in Figure 6-7a). In experiments 2-5, gauge 6 was replaced by a rack and pinion shown in Figure 6-7b) to determine the magnitude of deflection of the wall to compare to the ABAQUS model. The gear on the rack and pinion was connected to a potentiometer. The potentiometer works as a variable resistor that as the rack is pushed through the gear the voltage on the potentiometer is changed. That voltage change can then be correlated to a distance. This relationship between voltage and distance is determined by running one foot of the rack through the gear to determine the voltage change to correctly set the potentiometer to read the displacement of the barrier during the test. The rack and pinion was set to measure the displacement at the center back surface of the barrier at 91.44cm (3ft) up from the ground and 61cm (2ft) in from the edge of the barrier.

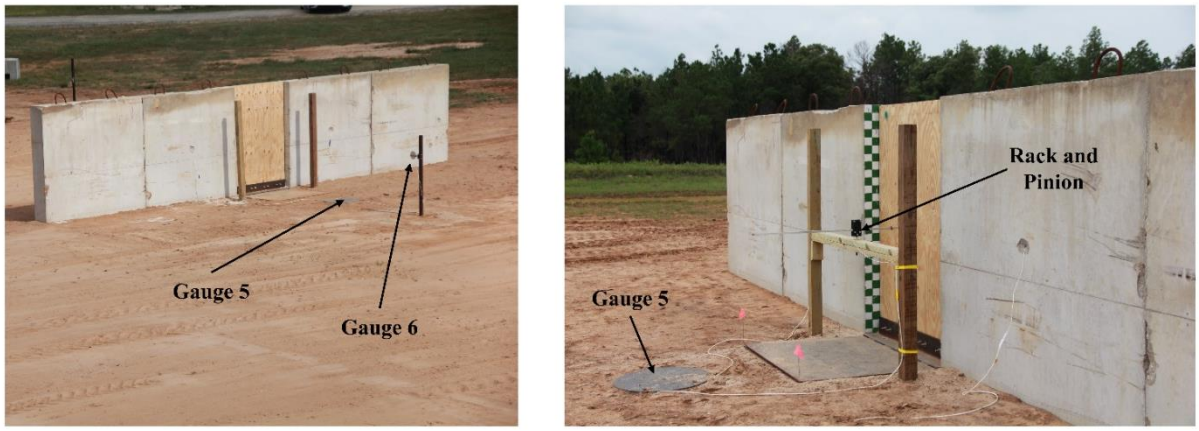

Figure 6-7: a) Pressure gauges behind the wall for experiment 1 and b) Rack and Pinion set up on the back center of the wall for experiments 2-5.

Three high speed Phantom video cameras were used to capture a variety of views of the field testing as shown in Figure 6-8. Figure 6-9a) shows that camera one was at 45° angle on the front side of the barrier. Camera one had a resolution of 1280x720 with 4000fps. Camera two (resolution 800x600 with a 4000fps) was located in line with the back side of the barrier to capture the displacement of the wall as shown in Figure 6-9b). Camera two was zoomed in to focus on the back surface of the barrier. A checkered surface with 6.35cm (2.5in) squares was painted on the extended edge of the Alaska barrier to function as a scale to assess the barrier deflection from camera two and three. Similar to camera one, camera three had a resolution 800x600 with a 4000fps, was located at a 45° angle on the backside of the barrier to capture displacement of the wall and the shockwave passing over the structure as shown in Figure 6-9c).

Figure 6-8: Field location of all three high speed cameras relative to the barrier structure.

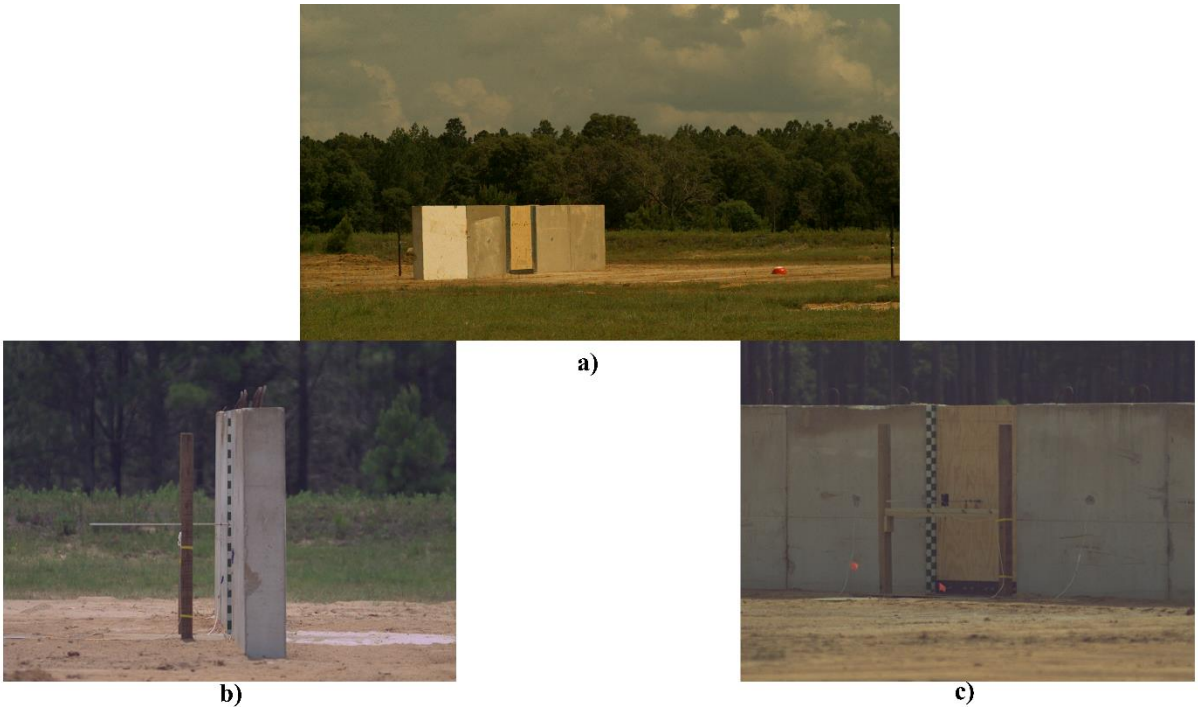

Figure 6-9: a) View from camera one, b) view from camera two and c) view from camera 3.

6.2.2.2 Test Matrix and Testing Procedure

Using the finite element model developed in Chapter 5, a test matrix, with a total of five experiments, was created for testing of the barrier in the field. The FEM in ABAQUS predicted that a 3.66 m/kg$^{1/3}$ (9.23 ft/lb$^{1/3}$) would cause the barrier to fail by yielding with a deflection of

0.01m (0.393in). As a result, it was decided to test the wall well below the elastic limit for 3 of the tests (experiment 1 with no rack and pinion), 1 test slightly below the elastic limit and 1 above the elastic limit. Table 6-2 shows the test matrix completed in the field.

Table 6-2: Test matrix for full scale wood wall experiments

Test Number	Z_TNT[m/kg$^{1/3}$]
1	7.98 (20.11 ft/lb$^{1/3}$)
2	7.98 (20.11 ft/lb$^{1/3}$)
3	5.88(14.82 ft/lb$^{1/3}$)
4	3.96 (9.99 ft/lb$^{1/3}$)
5	2.56(6.47ft/lb$^{1/3}$)

For each of the experiments, the crater from the previous charge was filled in and packed. The test bed was then graded and smoothed to produce an even surface. The location of the charge was measured from the front of the wood barrier and the end corners of the clearing walls to ensure it was centered and in line with the gauges and the center of the barrier at 7.62m (25ft). Before each of the experiments the barriers were inspected and cracks and defects in the front and back panels of the wood, similar to those seen in Figure 6-2b), were marked with a permanent marker to be able to assess any new cracks or splitting after each experiment.

6.3 Results and Discussion

6.3.1 Visual Barrier Damage

After each experiment, the barrier was assessed to determine if additional cracking, splintering, or damage occurred to each barrier. Any new damage was marked in a new color to differentiate between the before and after. In experiments 1-4, no new additional cracking occurred. On the barrier tested in experiment 5, elongation of the existing cracks and formation of new cracks occurred. However, no splitting or splintering of the front or back panels occurred in

any of the experiments including experiment 5. Figure 6-10 and Figure 6-11 show the cracking on the front and back side of the barrier before and after experiment 5, respectively. A significant amount of small new cracks occurred along the top of the front and back side of the wall.

a) **b)**

Figure 6-10: a) Cracking on the front side of the barrier before experiment 5 marked in blue and b) after experiment 5 with new cracks marked in red and initial cracks marked in blue.

a) b)

Figure 6-11: Cracking on the back side of the barrier a) before experiment 5 marked in blue and b) after experiment 5 marked in red.

Around the bolt holes minor damage was observed for all experiments, but no pull out or bolt shear failure occurred as shown in Figure 6-12. The flashing used to cover the seam between the wood barrier and the concrete Alaska barriers did not detach on experiments 1-4. However, in experiment 5 the flashing became detached from the concrete and the wood barrier.

a)

b)

Figure 6-12: a) Bolt hole damage from experiment 5 and b) detached flashing from front side of barrier after experiment 5.

The final aspect of visual damage to the barrier from the experiments was the inspection of any permanent deformation of the barrier after experiments. The checkerboard gauge painted on the side of the Alaska barrier was used as a guide for visual damage assessment. The squares of the checkerboard gauge were 6.35cm (2.5in) as shown in Figure 6-13a). Experiments 1-4 did not exhibit any permanent damage and the checkerboard gauge was still fully visible posttest. In experiment 5, the barrier experienced permanent deformation and did not return to the original starting point as experiments 1-4 did. Figure 6-13b) shows the final deformation of the top of the back surface of the wood barrier. The top of the barrier was deflected back from where it started at the front edge of the Alaska barriers by 2.54cm (1in) as seen by the resulting section of the checkerboard gauge only being 10.16cm (4in) rather than the full checkerboard (5in). This was expected as the ABAQUS model predicted yielding and failure of the wall at a Z=3.66m/kg$^{1/3}$ (9.23ft/lb$^{1/3}$) and experiment 5 was at a Z=2.56 m/kg$^{1/3}$ (6.47 ft/lb$^{1/3}$).

a) b)

Figure 6-13: a) Checkerboard gauge pretest measurement and b) barrier permanent deflection of 0.024m (1in) from experiment 5 posttest.

6.3.2 Barrier Response

The rack and pinion for experiments 2-5 recorded the maximum displacement at the back center of the barrier. The rack and pinion was not used in experiment 1 in order to use additional elevated pressure gauges which is presented in section 6.3.3 below. Table 6-3 summarizes the maximum experimental deflection and the maximum ABAQUS deflection for each experiment. Experiment 2 had a displacement of 0m recorded from the rack and pinion. Small displacements were recorded for experiments 3-5. Experiments 3 and 4 did not exceed the predicted elastic limit of the barrier at a maximum deflection of 0.00791m (0.31in). Experiment 5 did exceed the elastic limit with a maximum of 0.05m (1.97in). Figure 6-14 shows the displacement time histories for the rack and pinion and the ABAQUS model for experiment 5. Both the ABAQUS model and rack and pinion experienced the same peak deflection; however, the time-history response for each curve was different. The rack and pinion exhibited an oscillation with large amplitude resulting in a permanent deformation around 0.01m (0.5in) similar to what was experienced in the field. The ABAQUS model has a smaller oscillation amplitude around the same as the maximum deflection of 0.05m (2in). The ABAQUS model is not able to capture the correct permanent deformation of the barrier that was experienced in the field. This difference in behavior between the ABAQUS

model and the rack and pinion was also experienced in Pezzola (2018) when the rack and pinion was compared to LSDYNA displacements. The rack and pinion for experiments 3 and 4 do not exhibit the behavior experienced in the field as the rack and pinion predicted that a permanent deformation was experienced for all experiments when permanent deformation did not occur for experiments 3 and 4. This was believed to be due to the rack and pinion having trouble picking up such small displacements. Due to this the peak deflections were able to be compared but the displacement time histories were not. The rack and pinion curves for experiments 3 and 4 are shown in the appendix of this dissertation.

Table 6-3: Experimental and ABAQUS FEM deflections for experiments 3-5 at the back center of the barrier

Experiment Number	**Experimental Deflection [m]**	**ABAQUS Deflection [m]**	**% Difference [%]**
1	NA	NA	NA
2	0.0	0.00114 (0.045in)	NA
3	0.00291 (0.114in)	0.00316 (0.093in)	8.59
4	0.00791 (0.311in)	0.00740 (0.291in)	6.45
5	0.05019 (1.98in)	0.0513 (2.01in)	2.21

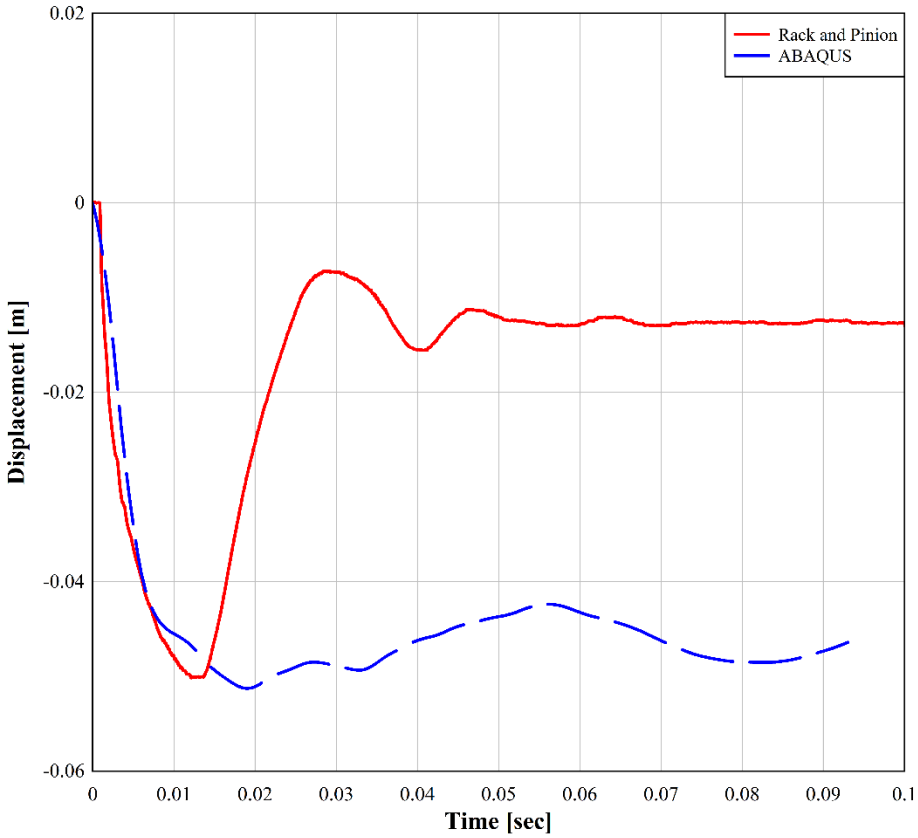

Figure 6-14: Rack and Pinion displacement time history plotted with ABAQUS displacement time history for experiment 5.

Analysis of the videos from experiment 5 showed the displacement of the barrier. Figure 6-15 shows the barrier as it deflects during experiment 5 taken from camera 3 high speed video. Figure 6-15a) was the starting location of the barrier before detonation. Both squares on the checkered scale were showing completely. After detonation and after the shockwave has hit the front of the barrier, Figure 6-15b) shows the barrier in motion. The barrier has deflected at the top 0.0635m (2.5in) to completely cover the first block on the checkered scale. Figure 6-15c) shows the point of maximum deflection of the barrier when the top of the barrier has deflected to half of the second block of the checkered scale which was around 0.09525m (3.75in). The ABAQUS model predicts the maximum deflection of the top of the backside of the barrier to be around

0.08619m (3.39in). After reaching its maximum deflection, the barrier came to rest 0.024m (1in) with about half of the first block on the checkered scale showing again as shown in Figure 6-15d).

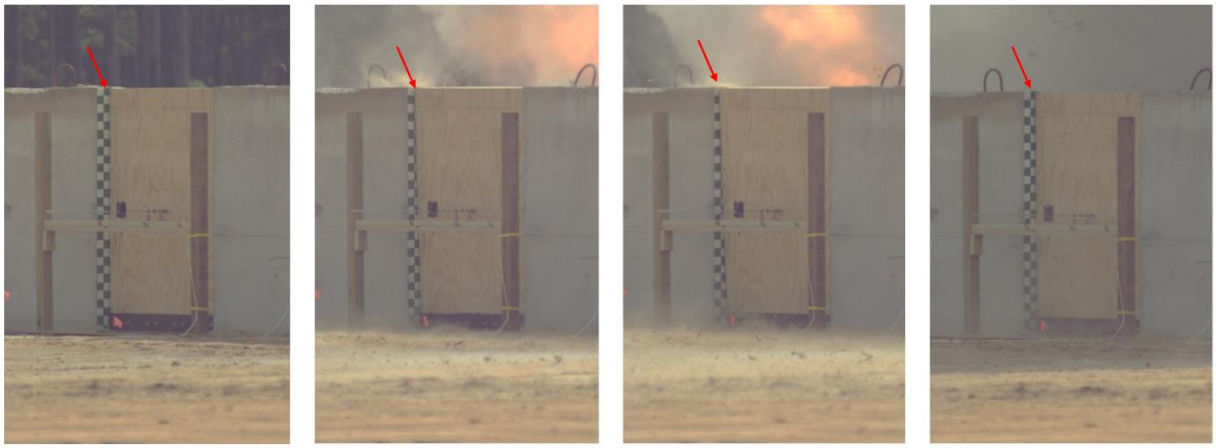

a) b) c) d)

Figure 6-15: a) barrier location before detonation, b) barrier while in motion, c) max deflection of the barrier, and d) final location of barrier.

6.3.3 Pressure Comparisons

After evaluating the barrier's response to the blast loading, the analysis of the pressure readings from the gauges throughout the field can be used to assess the effectiveness of the barrier in reducing pressure behind the structure. Since ConWep was used in the FEM model in Chapter 5, the pressures were first compared to ConWep for the gauges for which it was applicable. For the free field gauges of 1, 2, and 4 ConWep predicted the pressure within 20% error for all experiments. For the wall gauges of 3, 7, and 8 the error between the experimental pressures and ConWep was much larger with the largest discrepancy being for experiment 5 in gauge 7 with a 57.2% error. The hydrocode CTH was run with the same set up as experiments 1-5 to compare the pressures to numerical predictions. The CTH models were in a 2DC axisymmetric domain, similar to that used in Chapters 3 and 4. The meshing, EOS, and material definitions were the same as previously described. The model domain was set up to match the field set up with free field and wall gauges in-front and behind a single rigid barrier. Gauge 6 was only used in experiment 1 due

to the implementation of the rack and pinion for experiments 2-5 effecting the flow field. Gauge 5 behind the barrier remained for the rest of the experiments along with the rack and pinion as it was in the ground not an elevated gauge and showed minimal effects of the rack and pinion on the pressures in experiments 2-5. For this analysis, gauges 1, 2, and 4 were considered "free field gauges" and gauges 3, 5, 7 and 8 were considered to be "wall gauges". Table 6-4 summarized the normalized peak pressure predictions of the CTH hydrocode simulations for all experiments to their matching pairs by dividing the wall gauge by the free field gauge. If the normalized pressure was below 1.0 it meant the wall gauge experienced a reduced pressure compared to the free field gauge. A value of 1.0 meant the wall gauge experienced a pressure the same as a free field gauge and a value greater than 1.0 meant the wall gauge has an amplified pressure greater than the free field gauge. The CTH simulations were set up to match the gauge distances from the field experiments. Similarly, Table 6-5 summarizes the normalized peak pressures experienced in the field experiments. The first column in the tables is gauge 3/gauge 2. Gauge 2 was the free field pressure the same distance away from the charge as gauge 3 which was about 1.5m (5ft) in front of the barrier. As seen in Table 6-4, the peak normalized pressures were around 0.70-0.80. In all the experiments, gauge 3 was slightly farther away from the charge than gauge 2, which resulted in the normalized pressure being less than 1. In Table 6-5, the peak normalized pressure was closer to 1 as the pressures were closer in value than predicted in the CTH simulations. The variation in the field readings could have been from numerous causes including the location of the charge, the locations of the gauges, how flush the gauge was with the mount holding it, or even the location of the detonator in the charge.

The second column in the tables is gauge 5/gauge 1. Gauge 1 was the free field pressure gauge the same distance away from the charge as gauge 5 which was behind the barrier. The

normalized peak pressures in both Table 6-4 and Table 6-5 were between 0.28-0.47. Since the value was less than 1 that means the value at gauge 5 was less than it was in the free field without the protection of the barrier. This indicates the barrier was successful in providing protection and reducing the pressures experienced behind the barrier. The third and fourth column compare the pressures from the wall mount gauges 7 and 8 to the free field pair gauge 4. In the CTH simulations, the normalized peak pressure ratios were the same for both columns as the blast was perfectly hemispherical and the gauges were the same distance from the charge on either side of the wood barrier. In the field experiments in Table 6-5, there was a considerable amount of variation between gauges 7 and 8. For all experiments, the normalized pressures were above 1 for these two columns. This was due to the amplification of the pressure wave caused by the reflection off the wall and the pressure being larger than the free field reading at gauge 4. In experiment 1 and experiment 4, gauge 7 had a larger normalized pressure than gauge 8. Experiments 2 and 3 had slight variation but experiment 5 had a large difference between the two gauges of 0.41. This variation again can be attributed to the expected variances in explosive testing such as the causes listed above as well as slight asymmetric placement of the charge center or misalignment of gauge mounts.

Table 6-4: Hydrocode Simulations Normalized Pressure Pairs

Experiment #	**Gauge 3: Gauge 2**	**Gauge 5: Gauge 1**	**Gauge 7: Gauge 4**	**Gauge 8: Gauge 4**
1	0.80	0.38	2.06	2.06
2	0.80	0.38	2.06	2.06
3	0.79	0.39	2.16	2.16
4	0.77	0.43	2.38	2.38
5	0.72	0.47	2.87	2.87

Table 6-5: Experimental Field Normalized Pressure Pairs

Experiment #	Gauge 3: Gauge 2	Gauge 5: Gauge 1	Gauge 7: Gauge 4	Gauge 8: Gauge 4
1	0.98	0.28	2.02	1.98
2	1.11	0.35	1.85	1.96
3	1.31	0.45	2.23	2.26
4	0.93	0.41	2.32	2.08
5	0.80	0.44	2.39	2.80

Another way to assess the pressures from the field experiments was to compare the pressures to the CTH predictions directly. Table 6-6 shows the field pressures normalized to the CTH simulations. Overall, the normalized pressures were around 1 which means the CTH simulations predicted pressures similar to those experienced in the field. Gauge 3 had the largest variation in normalized pressures as all experiments were above 1. This means the field pressures were elevated compared to the hydrocode predictions in this location. Gauge 6 did not have a matching free field gauge which was why it was not presented in Table 6-4 and Table 6-5. Here it can be seen that in the field experiments, gauge 6 was only slightly elevated but was close to the CTH prediction with a normalized pressure of 1.09.

Table 6-6: Experimental to CTH Normalized Pressures

Experiment #	Gauge 1	Gauge 2	Gauge 3	Gauge 4	Gauge 5	Gauge 6	Gauge 7	Gauge 8
1	1.35	1.07	1.32	1.02	1.02	1.09	0.99	0.98
2	1.05	0.97	1.34	1.07	0.97	-	0.96	1.02
3	0.94	0.97	1.60	1.04	1.06	-	1.07	1.08
4	0.98	0.95	1.15	0.99	0.94	-	0.97	0.87
5	0.98	0.93	1.03	0.93	0.92	-	0.77	0.90

6.4 Summary and Discussion

The main goal of this chapter was to present the full-scale experimental testing of a wood-sand-wood blast barrier based on the studies in Hussein et al. (2020a & 2020b) and FEM in Chapter 5 of this dissertation. The experiments conducted were used to assess larger scale, more realistic blast scenarios than previously tested in order to assess the barrier design. The following conclusions can be drawn from these experiments:

- From the results of Chapter 5 and the full-scale experiments, the barrier was able to remain elastic for scaled distance $Z \geq 3.66 m/kg^{1/3}$ ($9.23 ft/lb^{1/3}$). Anything smaller than $Z \geq 3.66 m/kg^{1/3}$ the barrier will experience plastic deformation.
- The barrier response was recorded during field experimentation using a rack and pinion. The barrier maximum deflections matched the predictions from the ABAQUS FEM within 0.001m for all tests.
- When tested for a $Z=2.56 m/ kg^{1/3}$ ($6.47 ft/lb^{1/3}$), the barrier deflected to a max deflection of 0.05m (1.975in) at the center of the backside of the barrier. The barrier was permanently plastically deformed by 0.0254m (1in) at the top edge of the barrier.
- Pressure measurements taken in the field around the barrier and in the free field were compared to assess the effectiveness of the barrier in reducing pressure. The pressure behind the barrier was reduced to between 55-72%.
- When the pressures recorded in the field were compared to CTH predictions, CTH predicted most pressure within 10% of the pressure experienced within the field for both barrier gauges and free field gauges. Gauge 3 the pressure varied the most with a max difference of 38% for experiment 3.

- The wood-sand-wood barrier was effective in reducing pressure and providing protection from a range of blast scenarios. The barrier was able to plastically deform past the elastic limit of 0.01m to still provide protection at smaller scaled distances (Z).
- The assumption used in the ANN that the barriers remained rigid, and these full-scale tests proved that the barriers were not rigid as they do displace even for smaller PBIED threats. However, the pressures predicted from the ANN were similar to those experienced in the field even with a non-rigid barrier proving the displacement was not significant enough to impact the flow field.

CHAPTER 7: PERFORMANCE BASED ASSESSMENT-PROBABILISTIC ANALYSIS FOR SURVIVABILITY AND RISK

7.1 Introduction

Most design scenarios utilize a deterministic approach in which the probability of exceeding a particular limit state is not evaluated. In the case of blast loading, deterministic values for the blast load and structural capacity are typically chosen as a simplified, conservative approach. This use of deterministic values is due, in part, to the lack of data on probability density functions of hazards or materials (Olmati et al., 2014). However, the use of deterministic analysis does not allow for the uncertainties associated with the loading characteristics and material properties to be included in determining the most probable failure load and damage state (Hussein et al., 2020).

Probabilistic approaches have been extensively used in the performance-based design of structures under a variety of hazards including earthquakes (Cornell & Krawinkler, 2000; Mahmoud & Cheng, 2017; Memari & Mahmoud, 2018), wind (Petrini & Ciampoli, 2012; Spence & Gioffrè, 2012), fire (Memari & Mahmoud, 2018) and hurricanes (Barbato et al., 2013). The use of performance-based blast design and probabilistic methods has grown in blast resistant design over the years as researchers have used it to assess the reliability and failure probability of different blast-resistant systems including concrete slabs, glazing and windows, and sacrificial cladding (Chang & Young, 2010; Linkute et al., 2013; Low & Hao, 2001; Ma et al., 2023; Olmati et al., 2014; Stewart & Netherton, 2008).

Fragility analysis is a powerful statistical representation of the probability of exceeding different performance limit states that is commonly used in performance-based design. Structural fragility analysis is expressed as the cumulative probability of exceeding a certain damage limit

state, conditional to the intensity measure of the hazard in question (Ellingwood et al., 2004, 2007; Olmati et al., 2014). Fragility analysis is well known and developed for predicting the probability of failure of structures subjected to natural hazards (Olmati et al., 2014).

The goal of this chapter is to perform fragility analysis for performance-based blast design of the wood-sand-wood barrier under a variety of standoff distances (Z) and blast loads (W). The fragility functions are determined using a simplified, equivalent SDOF model of the wood-sand-wood barrier. Fragility analysis for survivability and primary blast injury potential are completed and reported as it relates to a double-barrier system as well.

7.2 Single Degree of Freedom Model of Wood Barrier

Single-degree-of-freedom (SDOF) models are a common approach to determine the response of a structure to blast loading. To determine the blast response of a structure, the solution to Newton's equation of motion, shown in Equation 2.24, was required. Due to the impulsive nature of the blast load, damping was ignored. Damping is typically ignored in blast analysis as it has little to no effect on the system response since the peak response of the wave, which governs design, occurs within milliseconds from onset of the blast before the damping forces can absorb much energy and have an impact on the response of the system. The blast pressure-time history was represented by an equivalent triangular linear pulse, illustrated in Figure 7-1, and shown in Equation 7.1, which was scaled to the magnitude and duration of the positive phase of the blast wave from the ANN predictions. The negative phase was neglected in most design approaches as the loads were typically much lower and do not have as strong of a contribution to the response compared to the positive phase (DOD, 2008).

$$F(t) = \begin{cases} F_0(1 - \frac{t}{t_0}) & 0 \le t \le t_0 \\ 0 & t \ge t_0 \end{cases} \tag{7.1}$$

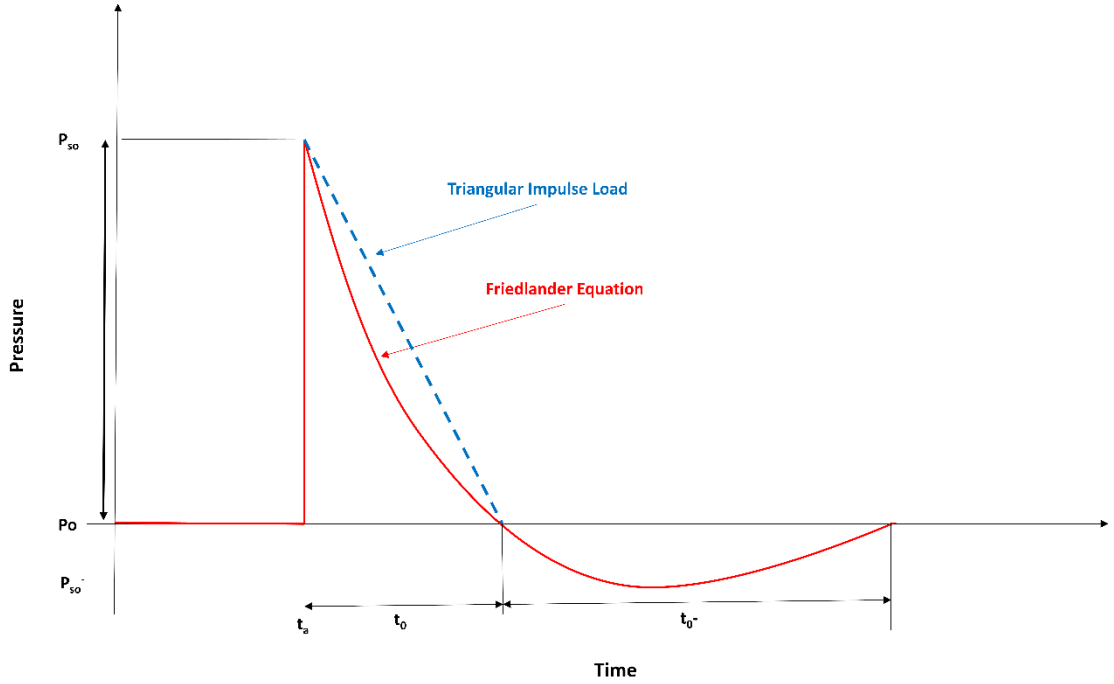

Figure 7-1: Simplified triangular linear impulse load compared to Friedlander equation for blast pressure time history.

The response of the undamped SDOF system subjected to triangular impulse was as follows when solved using Duhamel's integral:

$$x(t) = \frac{F_0}{k}\left(1 - \frac{t}{t_0} - \cos(\omega t) + \frac{1}{t_0\omega}\sin(\omega t)\right) \quad 0 \le t \le t_0 \tag{7.2}$$

$$x(t) = \frac{F_0}{k\omega t_0}\left[\sin(\omega t) - \sin\big(\omega(t - t_0)\big) - \omega t_0 \cos(\omega t)\right] \quad t \ge t_0 \tag{7.3}$$

where $\omega = \sqrt{\frac{k}{m}}$ is the natural frequency of the system, t_0 is the positive phase duration and F_0 is the max overpressure. The mass m was taken from the FEM in Chapter 5 of this dissertation. The stiffness k was taken from the resistance function developed for the wood-sand-wood wall in Figure 5-7 for the corresponding regimes of elastic and plastic. The different stiffness regimes were determined in the code by the elastic limit found in Chapter 5 of $x = 0.01$m

deflection at the center back of the barrier. The peak pressure F_0 was taken from the ANN predictions developed in Chapter 4 of this dissertation. This allowed the SDOF to be scaled to the FEM for the blast barrier and utilize the computationally efficient pressure predictions already developed in the ANN. The response of the SDOF model was calculated at the back center of the barrier using MATLAB code and compared to the FEM response found in Chapter 5.

The calculated response of the SDOF model was compared to the FEM response results from Chapter 5 for the center back of the wood-sand-wood barrier in the elastic region. As noted in Chapter 6, the peak deflections of the ABAQUS FEM model matched those of the experiments. The results of the SDOF model showed good agreement with the FEM results as shown in Figure 7-2. Figure 7-2a) shows the response curves for Z=5.88m/kg$^{1/3}$ (14.82ft/lb$^{1/3}$). The maximum amplitude of the response of the SDOF was off by 3.9% and the natural period was off by 4.8% compared to the finite element model. Similarly, Figure 7-2b) shows the response for Z=3.96 m/kg$^{1/3}$ (9.98ft/lb$^{1/3}$). Again, the SDOF showed good agreement with the ABAQUS finite element response. The peak amplitude of the SDOF was off by 10.8% while the natural period was off by 2.5%.

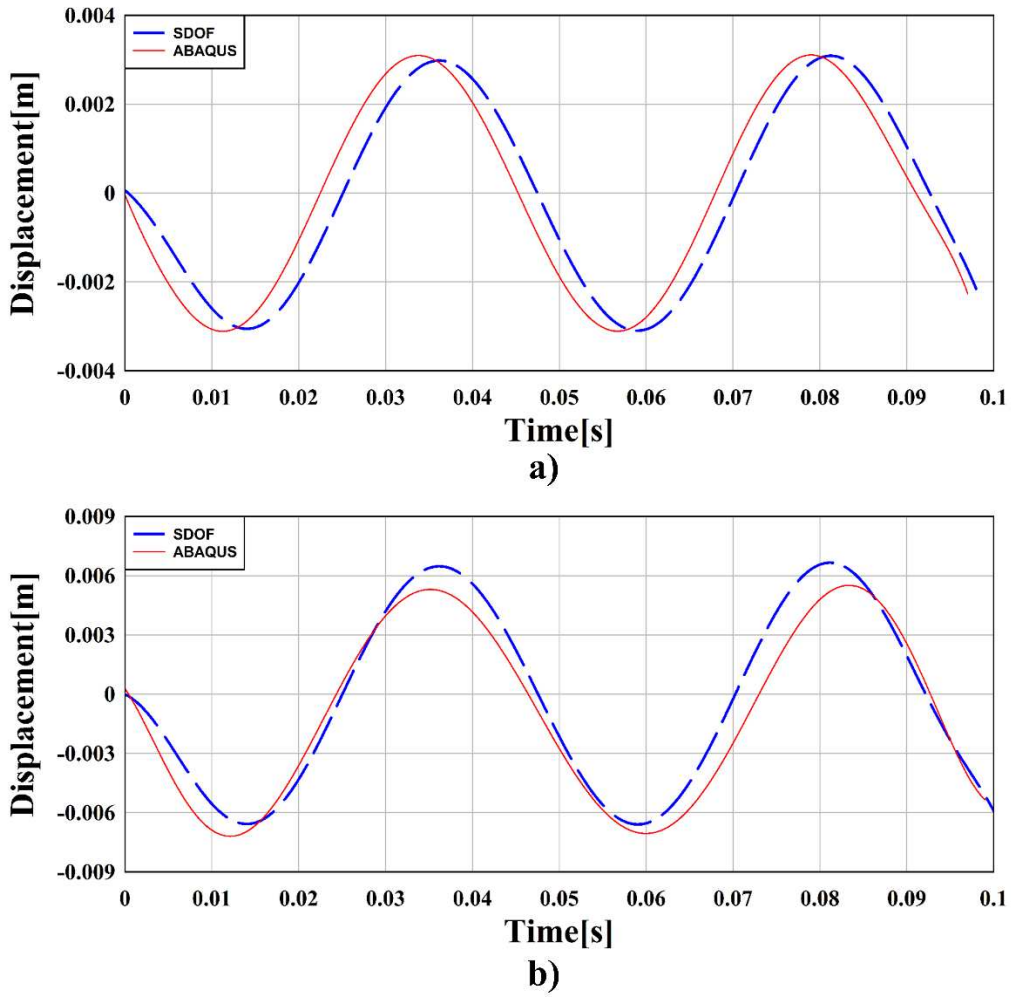

Figure 7-2: ABAQUS FEM displacement compared to SDOF deflection for a) Z=5.88m/kg$^{1/3}$ (14.82ft/lb$^{1/3}$) and b) for Z=3.96 m/kg$^{1/3}$ (9.98ft/lb$^{1/3}$) in the elastic region.

The SDOF results were then compared to the results of the experiments from Chapter 6. These results are summarized in Table 7-1. For Z=5.88m/kg$^{1/3}$ (14.82ft/lb$^{1/3}$) the SDOF was only 4.4% off from the value experienced in the field for the back center of the barrier. At Z=3.96 m/kg$^{1/3}$ (9.98ft/lb$^{1/3}$), the difference between the SDOF deflection of 0.0066m and field experiments deflection of 0.00791m (0.31in) was larger at 18.08%. In experiment 5 at Z=2.57 m/kg$^{1/3}$ (6.47ft/lb$^{1/3}$), the barrier experienced plastic deformation. The SDOF was able to accurately predict the maximum deflection of the wall at 0.0520m (2.05in) which was 3.58% off from the field experimental deflection of 0.0502m (1.98in).

Table 7-1: Deflection magnitudes for experimental testing, ABAQUS model, and SDOF model

Experiment Number	Z [m/kg$^{1/3}$]	Experimental Deflection [m]	ABAQUS Deflection [m]	SDOF Deflection [m]
3	5.88m/kg$^{1/3}$ (14.82ft/lb$^{1/3}$)	0.00291 (0.11in)	0.00316 (0.12in)	0.00304 (0.12in)
4	3.96 m/kg$^{1/3}$ (9.98ft/lb$^{1/3}$)	0.00791 (0.31in)	0.00740 (0.29in)	0.00660 (0.26in)
5	2.57 m/kg$^{1/3}$ (6.47ft/lb$^{1/3}$)	0.0502 (1.98in)	0.0513 (2.02in)	0.0520 (2.05in)

As only 3 experiments had displacements that could be compared to the ABAQUS and SDOF models, with only 1 of those experiencing plastic deformation, the SDOF was compared to the peak deflection of ABAQUS simulations between Z=3.66 m/kg$^{1/3}$ (9.23ft/lb$^{1/3}$) and Z=2.57 m/kg$^{1/3}$ (6.47ft/lb$^{1/3}$), in which plastic deformation would take place. The summary of these results is in Table 7-2. The SDOF predicted the maximum deflection within 10% accuracy of the finite element model within the plastic regime of the barrier's response. The deflection for Z=3.66 m/kg$^{1/3}$ (9.23ft/lb$^{1/3}$) had the highest error between ABAQUS and SDOF. This was because the SDOF model predicted the deflection at 0.0093m (0.37in) which means the barrier had not reached the elastic limit of x=0.01m (0.39in) in the SDOF model. This meant the stiffness has not decreased to the stiffness for plastic deformation. Overall, the SDOF model was able to replicate the behavior of the barrier from the ABAQUS finite element model and field experimentation for experiments 3-5 within acceptable accuracy for both the elastic and plastic regimes given the simplicity of the SDOF model, computational efficiency over the FEM, and cost efficiency over field experimentation.

Table 7-2: Deflection magnitudes ABAQUS model and SDOF model with plastic deformation

Z **[m/kg$^{1/3}$]** (ft/lb$^{1/3}$)	**ABAQUS Deflection [m]**	**SDOF Deflection [m]**	**Error [%]**
3.66 (9.23)	0.0104	0.00935	10.9
3.33(8.39)	0.0153	0.0152	0.59
3.09(7.79)	0.0211	0.0201	4.92
2.91(7.34)	0.0273	0.0259	5.24
2.76(6.96)	0.0344	0.0373	8.09
2.64(6.65)	0.0440	0.0422	4.25
2.57(6.47)	0.0513	0.0520	1.36

7.3 Probabilistic Analysis of Barrier Survivability

7.3.1 Monte Carlo Simulation Method

The Monte Carlo Simulation (MCS) method was used to conduct probabilistic and fragility analysis on the survivability of the wood barrier and for injury prediction. The MCS method is the most commonly used method across various fields to predict the probability of failure of structural systems. The MCS predicts multiple outcomes and the probability of each outcome based on random sampling of variables where the samples are generated in accordance with their probabilistic distribution, mean, and coefficient of variation (COV) (Ding et al., 2017; Memari & Mahmoud, 2018). Using the MCS method, the probability of failure is estimated using Equation 7.4:

$$P_F = \frac{1}{N}\sum_{i=1}^{N} I_F(\theta^i) \tag{7.4}$$

Where P_F is the failure probability, N is the sample size, θ^i represents uncertain parameters, I_F is the failure indicator function. If an uncertain parameter θ^i is estimated to be in the failure zone, the failure indicator function $I_F = 1$ otherwise $I_F = 0$.

7.3.2 Fragility Analysis

In this study, fragility analysis was considered using Monte Carlo simulation in two ways: first for the equivalent SDOF of the wood barrier from Chapter 5 and 6, and secondly for the primary blast injury thresholds for the human body. The probability of failure conditional on the occurrence of a specific threat scenario was calculated using the following relation:

$$P_f I\theta_{i,j} = \sum_{s=0}^{\infty} P_r[G(X) < 0|S] = sP_r[S = s] \tag{7.5}$$

Where P_f is the probability of failure, $\theta_{i,j}$ is the threat scenario (i: explosive mass, j: Standoff distance), $G(X)$ is the limit state function where X is the vector of all relevant variables, and $P_r[S = s]$ is the probability density of uncertainty parameters (Stewart et al., 2006).

The variability and uncertainty in this study was broken into two categories: blast loading parameters and structural properties. Similar to earthquakes and wind loading, the blast load cannot be completely certain, especially in the case of terrorist IEDs, and is subject to variability and uncertainty (DOD, 2008; Si et al., 2024; Twisdale et al., 1994). Blast parameters include variability and uncertainty in the factors such as charge weight (W), charge shape, charge orientation, detonation point location, and standoff range (R) (Netherton & Stewart, 2010; Si et al., 2024; Stewart & Netherton, 2008). Structural properties of the wood barrier include variability and uncertainty in the elastic modulus (E), mass (m), length or geometry (L), and stiffness (k). In this study, the charge weight (W) and elastic modulus (E) were represented as probabilistic distributions. The UFC 3-340-02 manual states: “Unknown factors can still cause overestimation of a structures capacity to resist the effects of an explosion. Unexpected shock wave reflections,

construction methods, quality of construction materials, etc., vary for each facility. To compensate for such unknowns, it is recommended that the TNT equivalent weight be increased by 20 percent." Other studies have found the coefficient of variation for blast parameters to range between 0.13-0.32 depending on standoff distances (Bogosian et al., 2002; Low & Hao, 2001; Twisdale et al., 1994). For the elastic modulus, a distribution for the elastic modulus of yellow pine was found from the United States Department of Agriculture Forest Service (1960). The distributions used in this study are summarized in Table 7-3 and shown in Figure 7-3 and Figure 7-4.

Table 7-3: Statistical Distributions for elastic modulus and charge weight (DOA, 1960; DOD, 2008)

Symbol	Description	Mean	COV	Distribution
E [MPa]	Elastic Modulus of Yellow Pine	10,400	0.206	Normal
W[kg]	Charge Weight of TNT	2.3kg=Pipe Bomb 9kg=Suicide Vest 23kg= Suitcase	0.2	Normal

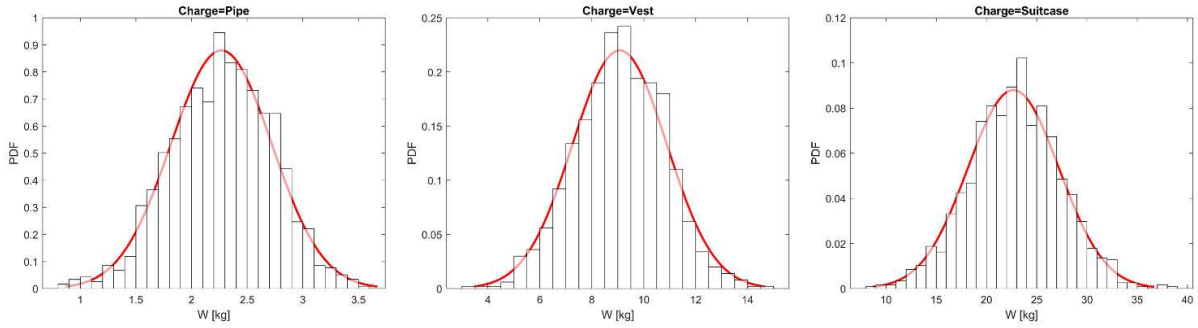

a) b) c)

Figure 7-3: Normal distributions for charge weights of a) 2.3kg, b) 9kg and c) 23kg used in fragility study.

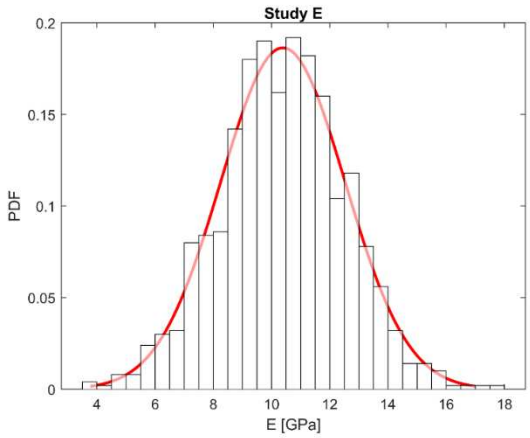

Figure 7-4: Normal distribution for yellow pine elastic modulus.

The failure limit state was calculated according to the displacement of the back center of the wood barrier compared to the elastic limit of $x = 0.01$m (0.39in). This limit state was used as a conditional statement in the framework of the probabilistic and fragility analysis presented in Figure 7-5.

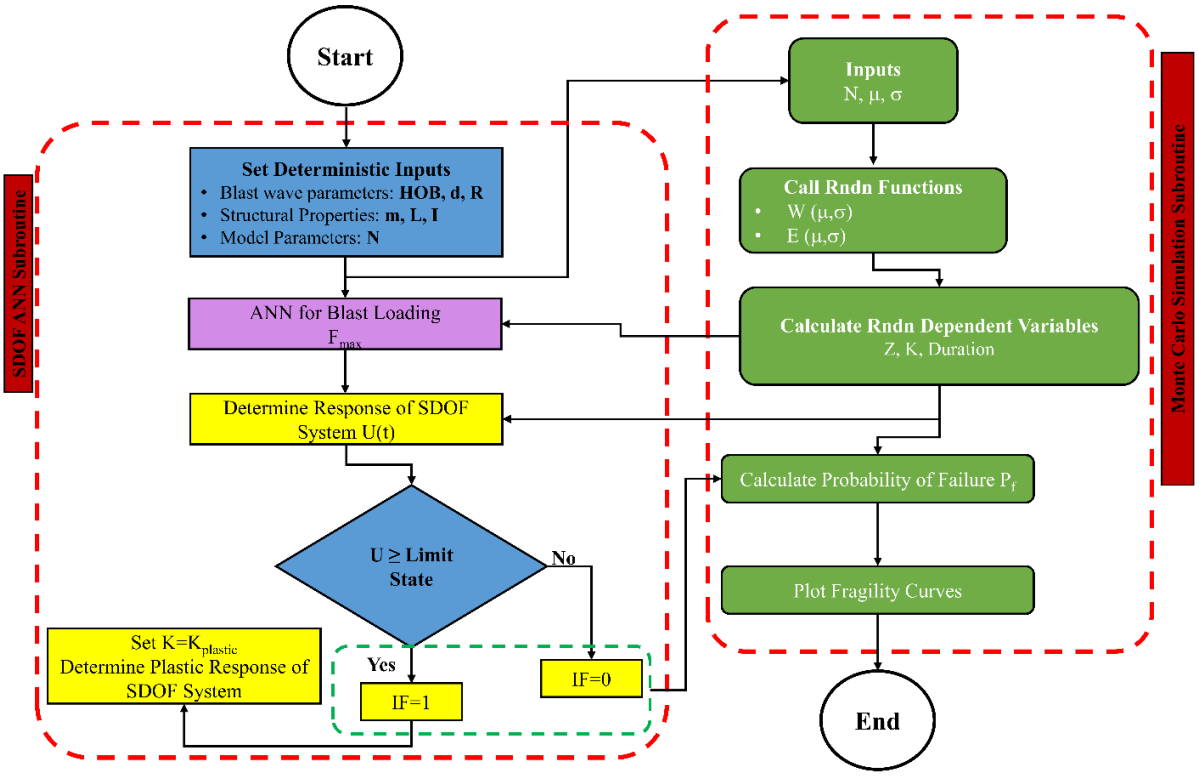

Figure 7-5: Fragility Analysis Computation Flowchart.

7.3.2.1 Charge Analysis

The probability of failure for the equivalent SDOF system of the wood barrier was estimated for range of standoff distances R, at three different HOBs for three different PBIED charge scenarios. The fragility charge analysis is shown in Figure 7-6. Figure 7-6a) shows the fragility curve for the wood barrier across an increasing range of distances for a pipe bomb (μ=2.3kg (5lb)) threat. From the curves, the barrier was best used beyond 5m (16.4ft). The fragility curve for the wood barrier across a range of distances for a suicide vest bomb (μ=9kg (20lb)) threat is shown in Figure 7-6b). From the curve the survivable distance for the wood barrier was found to be around 10m (32.8ft). Finally, Figure 7-6c) shows the fragility curve for the wood barrier for an increasing range of distances for a suitcase or briefcase IED bomb (μ=23kg (50lb)). As expected with a larger charge weight, the survivability of barrier was a further distance away around 12m (39.3ft). Across all images in Figure 7-6 it can be seen as the range increases the probability of failure decreases to 0 across all charge weights. This means regardless of the charge size, the closer to the charge, the higher chance the elastic limit of the barrier will be exceeded, and the barrier will fail. For example, at a range of 7.5m (24.6ft) and HOB=0, at a pipe bomb level threat, the probability of failure of the barrier is 0%, at a suicide vest level threat the probability of failure of the barrier was 58.9%, and a suitcase level threat the probability of failure of the barrier was 100%. It can be seen that as the HOB increases for a specific range, the probability of failure increases. This means a higher HOB results in a higher risk of failure for the barrier and was potentially more dangerous. For example, for a suicide vest level threat, the probability of failure for the barrier at a range of 8m (26.2ft) increases from 42.5% at HOB=0m to 54.6% at HOB=0.91m to finally 59.8% at HOB=1.5m as seen in Figure 7-6b).

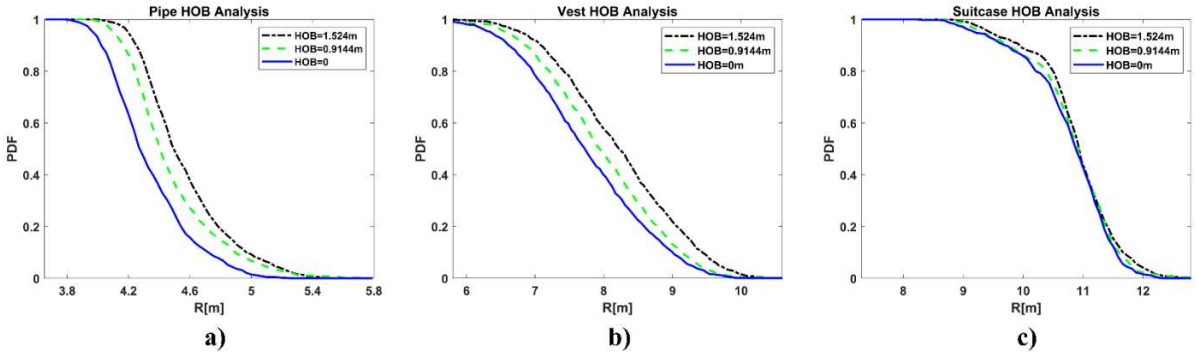

Figure 7-6: HOB analysis for a) pipe bomb charge distribution over a range of distances, b) vest charge distribution over a range of distances and c) suitcase charge distribution over a range of distribution.

7.3.2.2 Range Analysis

The probability of failure for the equivalent SDOF system of the wood barrier was estimated another way. Rather than varying the range, the charge was varied instead. Figure 7-7 and Figure 7-8 show the fragility curves for a range of PBIED charge weights (W) for various ranges (R) for a HOB=5. The different graphs in Figure 7-7 and Figure 7-8 were broken up by increments of charges by 2.27kg (5lbs) from 2.27kg (5lbs)-22.68kg (50lbs). Figure 7-7a) shows the ranges that the barrier has a probability of failure between 0 and 1 for W=2.27kg (5lbs)-4.5kg (10lbs). The smallest range of R=4.27m (14.0ft) had a probability of failure of 23.3% for a 2.27kg (5lb) charge. At the same range, a 2.72kg (6lbs) charge had a 97.7% probability of causing failure in the barrier. Many of the ranges started on one figure for one section of charges with low probability of failures and then continued onto another figure to another section of charge weights. For example, R=7.01m (23ft) started on Figure 7-7b) and reached a maximum probability of failure of 8.25% for a charge weight of 6.8kg (15lbs). The same curve continued onto Figure 7-7c) where it reached 100% probability of failure of the barrier at 9.07kg (20lbs). The larger charge weights are in Figure 7-8a) and Figure 7-8b). In Figure 7-8b), the ranges of R=10.97m (34ft)-11.89m (39ft) did not reach a probability of failure of 100% at the highest charge of 22.68kg (50lbs). The maximum probability of failure reached for R=10.97m, 11.28m, 11.58m and 11.89m

were 82.6%, 58.9%, 24.3% and 18.5%, respectively. In order to reach 100% probability of failure of the barrier at those ranges the charge weight would need to be increased further from 22.68kg (50lbs).

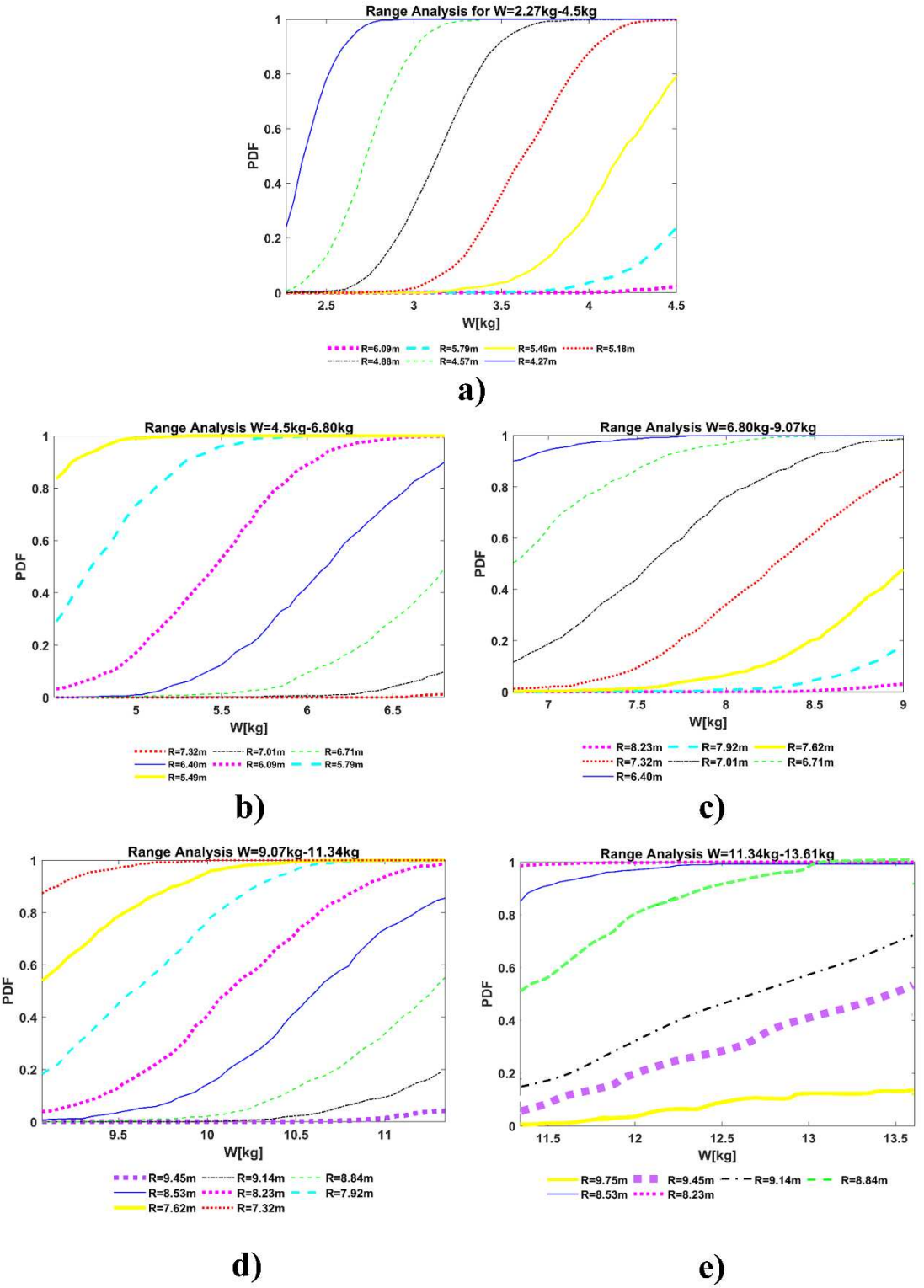

Figure 7-7: Fragility curves for a) 2.267-4.5kg (5-10lb), b) 4.5-6.8kg (10-15lb), c) 6.8-9.07kg (15-20lb) and d) 9.07-13.61kg (20-25lb).

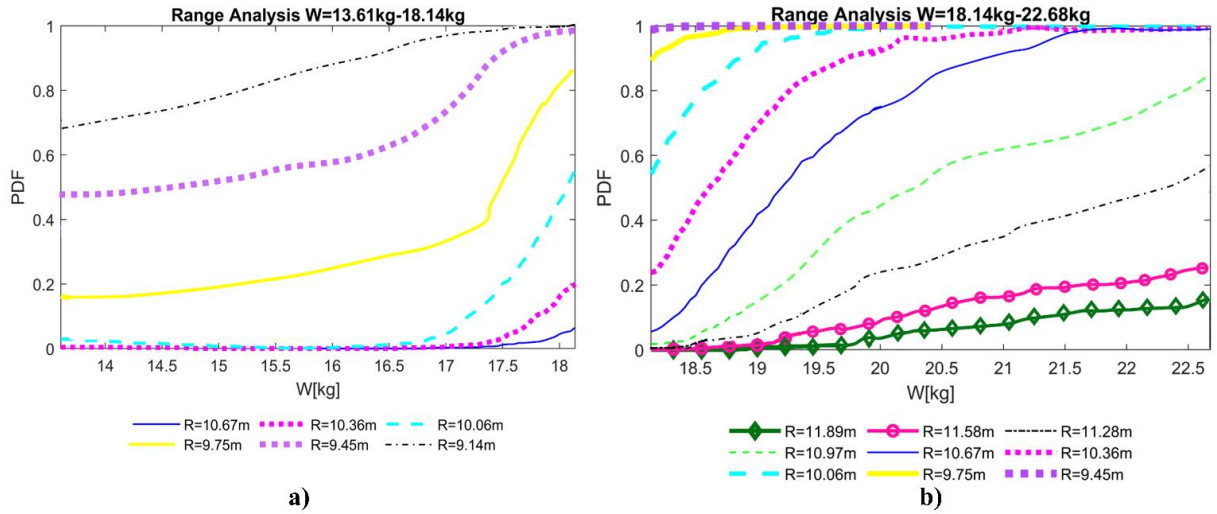

Figure 7-8: Fragility curves for barrier survivability for a) 13.61-18.14kg (30-40lb) and b) 18.14-22.68kg (40-50lb).

7.4 Probabilistic Analysis of Human Survivability and Injury

To highlight another potential use of the ANN from Chapter 4 and probabilistic analysis, the probability of primary blast injuries can be predicted using the same framework. Primary blast injuries are caused as a direct effect of the blast and blast wave as the overpressure exerts force on the body (See Chapter 2, section 2.5.2).

To determine the injury threshold values for primary blast injuries such as ear drum rupture and blast lung damage, the Bowen curves (Bowen et al., 1968) were used. Curve fits for the threshold lung damage and 99% survivability Bowen curves for both the free field and the near reflecting surface graphs were created as shown in Figure 7-9. The duration of the positive phase of the blast wave for the distances and charge weights in this study range between 1msec and 15msec.

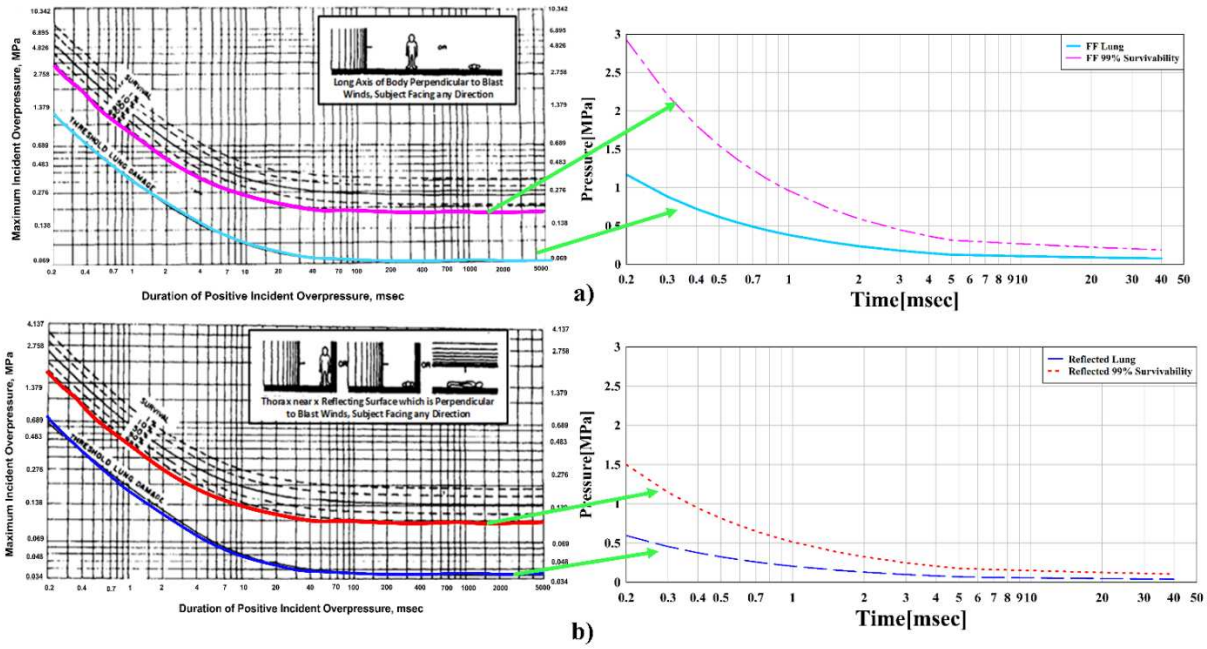

Figure 7-9: Curve fits to Bowen curves for lung and 99% survivability thresholds for a) free field and b) near a reflective surface *modified from:*(Bowen et al., 1968).

The curves provided a deterministic value for the pressure thresholds for each positive phase duration. Those values were used as the mean for the distribution for pressure threshold values for different injuries. Assuming that the biological tissue behaved as a membrane subjected to axial loading, the threshold pressure values were related to the strength of the corresponding biological tissue through a simplified relationship of

$$\sigma = \frac{F}{A} \tag{7.6}$$

Assuming the area of the tissue remained constant under loading, the strength and force was considered directly proportional. The variation in the strength of the tissues can be correlated to the variation in the elastic modulus which was found to vary under different strain rates (Luo et al., 2016; Rashid et al., 2014). When describing the elastic moduli of biological tissues typically the values follow a lognormal distribution (Millet, 2021). In a study, by Luo et al (2016) the elastic modulus for the blast-exposed human ear drum varied between 20-40%. For this study, to be

conservative a COV of 0.25 was chosen. The distribution to describe pressure thresholds used in this study, based on the information described above, is given in Table 7-4.

Table 7-4: Statistical distribution for pressure thresholds for biological tissues

Symbol	Description	Mean	COV	Distribution
P [psi]	Pressure Thresholds for Primary Blast Injuries	Determined from curves in Figure 7-9	0.25	Lognormal

7.4.1 Wood Barrier

Utilizing the SDOF for the wood barrier developed in section 7.3, analysis of the effectiveness of the wood barrier in providing protection from injury can be assessed along with the injury potential from the blast wave itself. To assess the worst-case scenario, a HOB=1.52m (5ft) was chosen with a suitcase charge distribution (μ=22.68kg (50lbs)). Based off the results of Figure 7-7 and Figure 7-8, for the barrier to survive, Z will need to equal Z=4.29m/kg$^{1/3}$ (Z=10.83ft/lb$^{1/3}$) or larger. If the barrier does not survive there are many problems that arise with this analysis. First, in the ANN the barriers were assumed to remain rigid so if the barrier fails and does not remain fixed in place and rigid the ANN pressure predictions are no longer valid for this analysis. Second, if the barrier fails there would be a greater risk of injury in the form of secondary blast injuries (fragmentation if the barrier fractures and breaks) or tertiary blast injuries (if the barrier tips onto or slides into someone). Neither of these events can be accounted for in this analysis and have the ANN and SDOF predictions be valid. In order to assess the effectiveness of the wood barrier the R was varied between Z=4.29m/kg$^{1/3}$ (Z=10.83ft/lb$^{1/3}$) and 5.95m/kg$^{1/3}$ (Z=15ft/lb$^{1/3}$). To assess the potential for injury in various locations in the blast wave field, five tracer sets were defined as described in Figure 7-10. Since the pressures behind the barriers were

of interest, the gap (d) between the two barriers had to be varied in the analysis. Figure 7-10a) shows the tracer sets used in the analysis when d=0.61m (2ft), the smallest gap possible between the barriers. Sets 2 and 4 were not used as part of this analysis as it was unlikely three people could fit in a 0.61m (2ft) gap. Figure 7-10b) and Figure 7-10c) show the tracer sets used in the analysis when d=2.13m (7ft) and d=3.66m (12ft), respectively. Both use all five tracer sets to assess the potential injuries that a person could experience standing in various locations around the barriers.

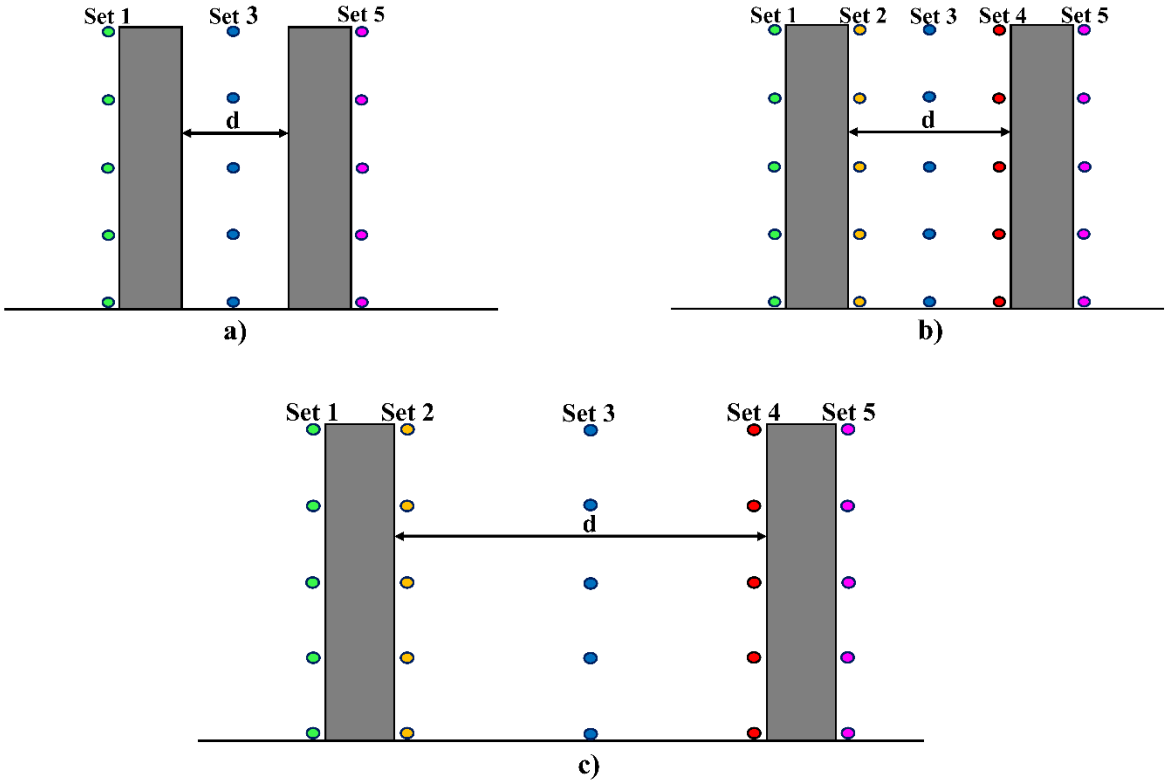

Figure 7-10: Tracer sets for injury analysis for a) d=0.61m (2ft), b) d=2.13m (7ft), and c) d=3.66m (12ft).

Figure 7-11 shows the probability of injury with the wood barriers for the suitcase charge distribution (μ=22.68kg (50lbs)) for the five different tracer sets for three different gap (d) distances. Figure 7-11a) shows the probability of injury for set 1 tracers which were in front of the first barrier. All curves for ear drum and lung damage had a probability of injury at 100% for all scaled distances between Z=4.29m/kg$^{1/3}$ (Z=10.83ft/lb$^{1/3}$) and 5.95m/kg$^{1/3}$ (Z=15ft/lb$^{1/3}$). As set 1

tracers were in front of the first barrier, it was expected the pressures would be much higher and could have a potential for causing death as there was no protection from the blast. The variation in the three different gap distances was a result of the probabilistic distributions varying the charge weight and the pressure thresholds predicting slightly different outcomes and standoff distances each time.

Between the three tests, the probability of injury ranged between a maximum of 35.6%-53.7% at 4.29m/kg$^{1/3}$ (Z=10.83ft/lb$^{1/3}$) and 0% at Z=5.95m/kg$^{1/3}$ (Z=15ft/lb$^{1/3}$). Figure 7-11b) shows the probability of injury for set 2 tracers which was directly behind the first barrier. Directly behind the first barrier when the gap distance was d=2.13m (7ft) or 3.66m (12ft) was a good place to be as the probability of ear drum damage, lung damage or death were all 0. This same result was seen in Figure 7-11e) for set 5 tracers directly behind the second barrier. The highest amount of protection was directly behind barriers 1 and 2 as long as the barrier remains rigid and fixed in place.

The probability of injury for set 3, in the middle of the two barriers was predicted in Figure 7-11c). The potential for death and lung damage were predicted at 0%, which meant the first barrier provides a significant drop in pressure compared to the location of set 1, similar to what was seen in Chapter 3 tabletop testing. Ear drum damage was still present in all cases for set 3. The tests with d= 0.61m (2ft) and d=2.13m (7ft) produced low probability of injury for ear drum damage with maximums of 38.6% and 21.2% respectively for Z=4.29m/kg$^{1/3}$ (Z=10.83ft/lb$^{1/3}$). Both quickly dropped to 0% probability of ear drum injury around Z=4.47m/kg$^{1/3}$ (Z=11.26ft/lb$^{1/3}$). The gap distance of d=3.66m (12ft) had a much higher probability of ear drum injury that ranged between 82.7%-9%. This could be due to the reformation of the wave between the two barriers for the larger gap distance or the stagnation of the elevated pressures between the barriers. This was

also shown in Chapter 3 with the tabletop testing results for larger gap distances. These same phenomena can be seen in Figure 7-11d) for set 4 which was directly in front of the second barrier in the gap between the two barriers. Set 4 has elevated ear drum probability of injury for both gap distances before quickly dropping to 0% probability around Z=5.05m/kg$^{1/3}$ (Z=12.72ft/lb$^{1/3}$).

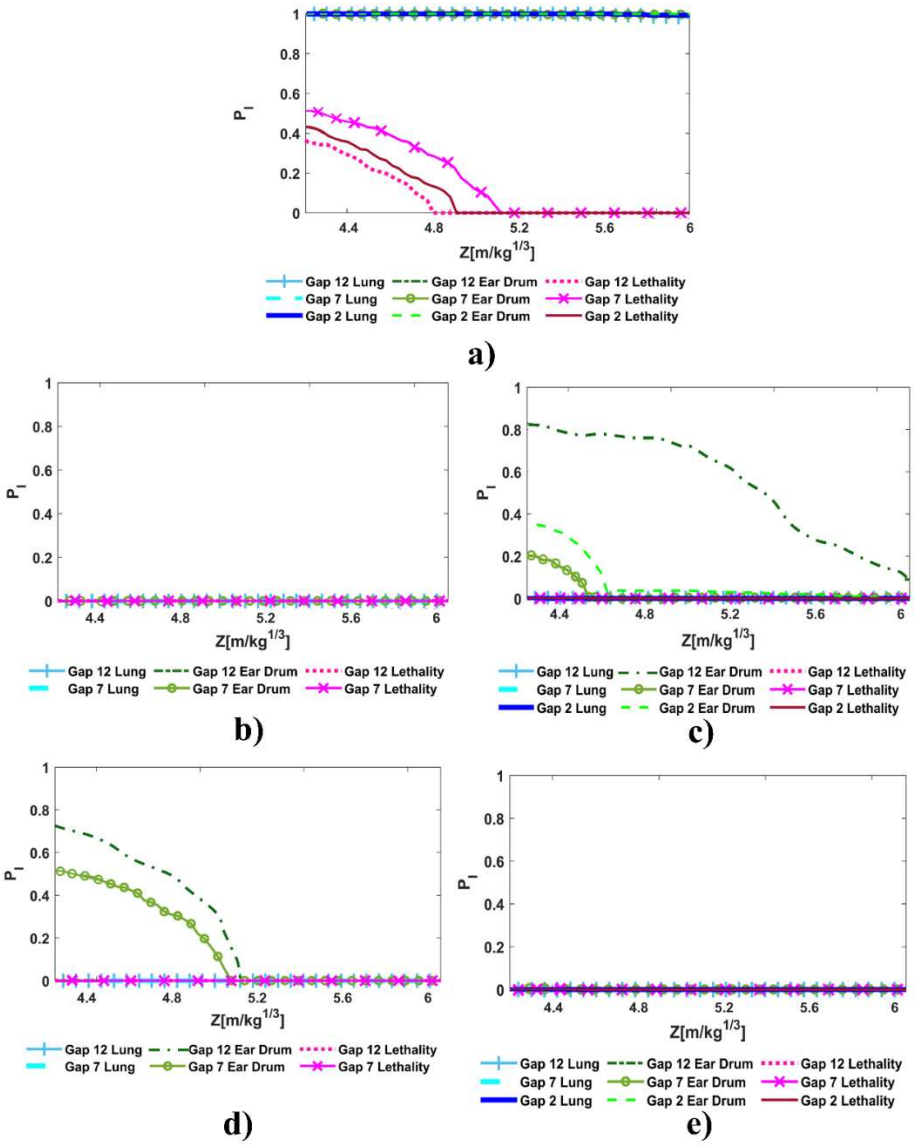

Figure 7-11: Injury probability for gaps d=2ft (0.61m), d=7ft (2.13m) and d=12ft (3.66m) for a) set 1 tracers in front of the first barrier, b) set 2 tracers directly behind the first barrier, c) set 3 tracers in the middle of the two barriers, d) set 4 tracers directly in front of the second barrier and e) set 5 tracers directly behind the second barrier with wood barriers.

7.4.2 Alternate Barrier System

To further assess the ability to predict the probability of injuries in the vicinity of the blast using the developed performance-based design framework, a new scenario was assessed. Excluding the wood barrier and assuming an alternate barrier system of two barriers that will remain rigid and fixed for Z= 1.19m/kg$^{1/3}$ (Z=3ft/lb$^{1/3}$) – 5.95m/kg$^{1/3}$ (Z=15ft/lb$^{1/3}$), a wider range of analysis could be completed on injury prediction potential and assessment of the effectiveness a double-barrier system had on providing protection and reducing pressures from blast events. Similar to Figure 7-11, Figure 7-12 shows the probability of injury for a double-barrier system for the five different tracer sets for three different gap (d) distances. Figure 7-12a) shows the probability of injury for set 1 tracers in front of the first barrier. At Z≤3.60m/kg$^{1/3}$ (Z=8.11ft/lb$^{1/3}$), ear drum, lung and death probability were all 100%. At Z=3.60m/kg$^{1/3}$ (Z=8.11ft/lb$^{1/3}$), the probability of death begins to decrease toward 0%, while the probability of ear drum injury and lung damage remains at 100% until Z=6.52m/kg$^{1/3}$ (Z=14.68ft/lb$^{1/3}$). Directly behind the barrier there was potential for ear drum damage when the gap distance was larger as shown in Figure 7-12b) for set 2 tracers. The probability of ear drum injury drops from 100% to 0% by Z=3.32m/kg$^{1/3}$ (Z=7.48ft/lb$^{1/3}$). For the remaining tracers sets 3, 4, and 5 shown in Figure 7-12c), Figure 7-12d) and Figure 7-12e) respectively, ear drum damage was present with increasing probability with smaller gap distances between the barriers. For example, Figure 7-12c) the ear drum damage for gap 2 (d=2ft (0.61m)) has a higher probability for larger Z values than both gap 7 and gap 12 tests. Additionally in Figure 7-12e), gap 2 ear drum damage was the only injury probability that was not 0 for all Z values tested behind the second barrier as it ranges from 71.2% to 0% between Z= 1.19m/kg$^{1/3}$ (Z=3ft/lb$^{1/3}$) – 2.29m/kg$^{1/3}$ (Z=5.16ft/lb$^{1/3}$).

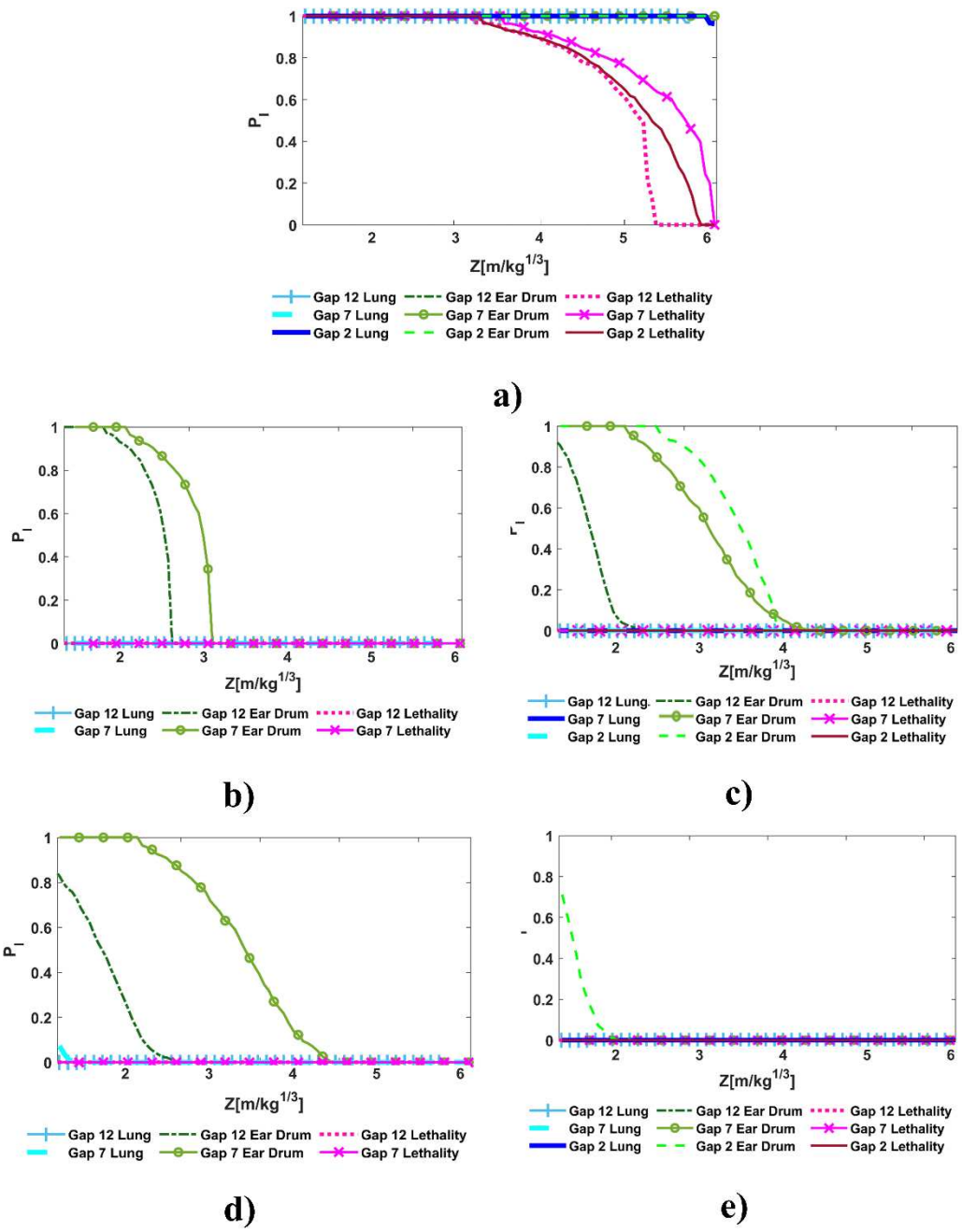

Figure 7-12: Injury probability for gaps d=2ft (0.61m), d=7ft (2.13m) and d=12ft (3.66m) for a) set 1 tracers in front of the first barrier, b) set 2 tracers directly behind the first barrier, c) set 3 tracers in the middle of the two barriers, d) set 4 tracers directly in front of the second barrier and e) set 5 tracers directly behind the second barrier with the alternate barrier system.

7.5 Summary and Conclusions

In this chapter, performance-based design was performed using probabilistic analysis to develop fragility curves for the wood barrier design in this dissertation and for injury potential using a double-barrier system in blast events. The framework was developed to first probabilistically evaluate the performance of the proposed barrier wall accounting for uncertainties in the blast loading and the structural properties of the barrier. The framework was then used to probabilistically predict the potential for injuries using a double-barrier system accounting for uncertainties in blast loading parameters, structural properties of the barrier and injury thresholds. The following conclusions can be drawn from the analysis performed:

- The equivalent SDOF system for the wood barrier accurately predicted the response of the displacement of the barrier with good agreement with the finite element model from Chapter 5 in the elastic region. The peak amplitude was off by less than 11% and the natural period was off by less than 5%.
- The SDOF predicted similar results to the FEM for the plastic deformation regime of displacement. The largest error of 10.9% occurred at the elastic limit Z=3.66 m/kg$^{1/3}$ (Z=9.23ft/lb$^{1/3}$).
- The equivalent SDOF system was similar to the three field experimental deflections with the largest error being 18.08% for a Z=3.96 m/kg$^{1/3}$ (Z=9.983ft/lb$^{1/3}$). The other experiments had an error of less than 5%.
- The equivalent simplified SDOF can predict both the field and FEM response within good accuracy. The largest amount error occurs with the SDOF model around the elastic limit deflection of x=0.01m (0.39in).

- Fragility curves showed that the wood barrier was best used at R>5m (16.4ft) for smaller charges. As the charge weight increases, the range for the wood barrier to not fail by exceeding the elastic limit increases.
- A higher HOB results in a higher risk of failure for the barrier and was potentially more dangerous.
- Range analysis confirmed that for a fixed range, as the charge weight increases the probability of failure of the barrier increases.
- A double-barrier system reduces the pressures between and behind the barriers, reducing the probability of serious injury.
- The duration of the blast wave was accounted for in using the Bowen injury curves to determine pressure thresholds for the injury analysis. This analysis showed that even for lower pressure threats, such as PBIEDs, due to the duration of the loading, serious injury can still occur.
- Based off injury analysis of the wood barrier and alternate barrier systems, directly behind the first barrier and second barrier were the best place to be to minimize the chance of death, lung, and ear drum damage from a blast event.

CHAPTER 8: SUMMARY, CONCLUSIONS AND FUTURE WORK

8.1 Summary of Current Research

This dissertation was dedicated to the development of a comprehensive framework for predicting blast loading around a double-barrier system and the impact on people in large open areas. The analyses combined numerical, analytical, and experimental methods at multiple scales, to create models to predict and assess the pressures associated with person-borne-improvised-explosive-devices (PBIEDS). The developed models used to predict and quantify the pressures around a rigid double-barrier system and the response of the wood barrier to blast loading were coupled with small- and full-scale experimental testing to validate and assess the accuracy and efficiency of the models. The study showed that a double-barrier system can significantly reduce the pressures experienced between and behind the barriers to prevent significant injury or death. It showed that the distance between the barriers plays a critical role in the pressures and therefore the potential for injury between the barriers.

The upward trend of the use of IEDs around the globe since the September 11th, 2001, attacks present a catalyst for a shift in research methods for blast mitigation techniques to providing protection to people rather than just structures. Both military and civilian settings are in need of more rapid and efficient prediction and mitigation tools to provide better protection. This dissertation utilized a new approach to accomplish that by focusing on reducing the impact the pressure from a blast shockwave can have by developing rapid computational models to predict the pressure field around double-barriers, analyzing a new barrier design that focuses on reducing the energy of the shockwave and by using performance-based design to establish potential risk for various scenarios. From the results of this study, it can be observed how the implementation of a

double-barrier system can significantly reduce the pressure experienced around the barriers, which can lead to less potential for serious injury or damage from blast events. In addition, adopting an innovative approach to blast barrier design to consider more lightweight, commonly available, non-rigid materials to increase the energy absorption to attenuate the blast shockwave rather than just reflect was proven to be beneficial. The wood barrier evaluated in this study was an inexpensive, easily constructed barrier from commonly used materials. The results showed how the barrier can plastically deform, without experiencing severe damage and still mitigate the pressure from the blast shockwave.

8.2 Summary and Conclusions

8.2.1 Small Scale Testing Analysis

The use of a double-barrier system in a large open area was not previously presented in literature to understand how the pressure field moves around the barriers and how it can effectively be used in civilian or military settings to mitigate an explosive attack. In order to understand the pressure field between a double-barrier system, a two-dimensional numerical hydrocode model was developed to establish an understanding of the expected behavior of the air blast pressure. The developed numerical model provided a baseline prediction that needed to be validated with experimental testing. Due to issues of scale, equipment capacity, and availability of research funding the use of small-scale testing was used as an inexpensive and rapid way of testing blast wave parameters.

The application of a new small-scale tabletop testing procedure was used to carry out the test matrix to validate the numerical model. The full-scale setup for testing was scaled down to 1/6

scale to fit on the tabletop. Pressure gauges were used to read the pressures on the surface of the table for 10 different experiments to understand how the double-barrier system impacts the blast flow field. The results of the testing showed the small-scale tabletop could be used for repeatable, efficient testing. It was shown that the numerical model predicted the results of the experimental pressures within 68.9kPa (10psi) 97% of the time and within 34.5kPa (5psi) 94% of the time. The experimental testing validated both the pressures and the impulses predicted by the numerical hydrocode model.

8.2.2 Artificial Neural Network Model Analysis

A hydrocode model, validated using the small-scale testing, was used to build a dataset to train an artificial neural network (ANN) to predict the pressure field for a double-barrier system. An ANN that can predict the pressure field around a double-barrier system allows for rapid and accurate predictions inside the data range to be obtained. This kind of tool would allow decision makers, military officers, and city planners to make informed decisions about protective measures and how to provide protection with multiple barriers.

The ANN model was trained, and a variety of model parameters were optimized including training algorithm, number of layers, number of neurons in each layer, and transfer function. The developed ANN was able to predict the pressure for a double-barrier system with inputs of charge weight (W), standoff distance (Z), height of burst of the charge (HOB) and gap distance between the two barriers (d). The finalized network can predict the flow field within 90% accuracy of the experimental tabletop results and the CTH hydrocode simulation predictions for pressure. Using the ANN model reduced computational cost drastically from 3080 CPU hours to 0.16 CPU hours for the hydrocode simulation versus the ANN, respectively.

8.2.3 Finite Element Model Analysis

The CTH models, used to train the ANN surrogate, assumes the barriers to be rigid and fixed in place. To validate this assumption, the response of the desired barrier was tested in full scale. Small-scale testing was not suitable in validating the assumption of rigidity as structural response was not scalable like blast parameters are. As one of the goals of this dissertation was to provide better protection for people rather than just structures, a sandwich structure barrier built out of wood and sand was tested. The analysis from which the design of the barrier originated had not accounted for plastic deformation in the study. To assess the effectiveness of the barrier at larger, more realistic charge weights and to determine the limit of the barrier, a finite element model was developed before full-scale testing could take place.

The 3D shell model of the wood-sand-wood barrier was tested to determine the elastic limit of the barrier and determine the expected displacements under various blast loads. The barrier was modeled using the same materials and geometry that would be experimentally tested in the field to minimize error and to have as accurate of model and predictions as possible. The model was used to perform failure analysis using the Von Mises stress criterion. From the failure criterion the elastic limit was determined to be at a deflection of x=0.01m. The finite element model was used to create a resistance curve to determine the stiffness of the barrier before and after it experienced plastic deformation.

8.2.4 Full Scale Testing Analysis

After establishing a prediction of the behavior of the barrier from the FEM, the model was used to design the full-scale experimentation of the actual barrier to validate the assumption from the ANN and the accuracy of the FEA model. Unlike the original wood-sand-wood barrier tests from a previous study, the barrier tested in the field was as close as possible in materials and

geometry to the barrier tested in the model. Another significant difference from the previous study was the size and proximity of experiments conducted. In this study, PBIED threats between 2.27kg-22.67kg (5-50lbs) at distances larger than Z=1.19m/kg$^{1/3}$ (3ft/lb$^{1/3}$) were conducted to provide more realistic testing scenarios for the barrier. When Z<1.19m/kg$^{1/3}$ (3ft/lb$^{1/3}$), the blast is considered to be "close in blast". This range was not the focus of this dissertation.

The field experiments verified the results of the finite element model. The finite element model was able to predict the peak deflection of the wood barrier at the back center of the barrier within 8.25% of the field experiments. The failure of the barrier at a deflection of x=0.01m (0.39in) was confirmed with the onset of plastic deformation in the experiment that deflected 0.05m (1.97in) at the back center of the barrier. From the pressure readings during the experiments, the barrier was able to effectively reduce the pressure directly behind the barriers compared to the free field readings the same distance from the charge. Overall, the wood-sand-wood barrier was successful in mitigating the blast wave and providing an effective, lightweight, easily constructed, expedient barrier for blast protection.

8.2.5 Performance-Based Blast Framework Analysis

The main goal of this dissertation was to be able to predict the potential injury of people in the vicinity of a blast with protective barriers present. With the development of the validated models in sections 8.2.1-8.2.4, the performance-based blast design could be completed using an equivalent SDOF for the wood barrier and probabilistic fragility analysis. The equivalent SDOF for the wood barrier was developed and validated against both the field and FEM results. The SDOF was able to predict the peak deflection with less than 18.1% error of the field experiments with the largest discrepancy being around the elastic limit. When compared to the FEM, the SDOF predicted within 11.4% again with the largest error occurring around the elastic limit of x=0.01m

(0.39in) deflection. Probabilistic analysis was used to assess the survivability of the wood barrier under various loading conditions. With failure defined at exceeding the elastic limit and experiencing plastic deformation, the fragility curves showed the wood barrier was best used at R>5m (16.4ft) for smaller charges. It was concluded that higher HOBs result in a higher risk of failure for the wood barrier. In the range fragility analysis, as expected, it was found that as the charge weight increases the probability of failure increases for a fixed range.

Using the same performance analysis, fragility curves for the probability of injury were able to be established for the safe range of distances for the wood barrier and for an alternate barrier system. At a safe distance that allowed the wood barrier to survive, the potential for injury was low directly behind the barriers. Between the barriers, the risk of potential ear drum damage was higher due to the reflections and reformation of the wavefront in the larger gaps between barriers. For the alternate system that remains rigid and fixed at closer in ranges, similar results were found. Ear drum damage was likely between the barriers and death and lung damage are only expected in front of the first barrier. This analysis shows the effectiveness of a double-barrier system as it reduces pressures which in hand reduces potential for injury.

8.3 Future Work

The present study developed a framework for predicting blast loads and the impact on people in large urbans areas with a double-barrier system using a combination of numerical, analytical, and experimental methods. The results of this study show that there are many factors: charge weight, standoff, and barrier material that can have a significant effect on the impact a blast has on the human body and how to effectively reduce that impact. Although this study provided some

insights into predicting blast loading and its effects on people, future research directions can include the following:

- *Charge weights*: For this study, the charge weights stayed between 5-50lbs of TNT to be classified as PBIED. This was chosen to simulate the threat level of terrorist attacks with civilian targets. However, this is not the only level of threat that could have been used. Larger threats such as VBIEDS are of more interest to military operations and even for civilian terrorist attacks similar to the Oklahoma City Federal Bombing. Developing an ANN or fast running model for larger threat levels could be beneficial in multiple capacities.
- *Tabletop Expansion & Wave Reformation:* It is well known that the shockwave reforms behind a barrier at varying distances. This was mentioned in the analysis of the tabletop experiments where an amplification in pressure was observed in front of the second barrier when a larger gap was used. Due to the limitations of the size of the tabletop full comparisons for the ANN distances were not able to be completed. To address the reformation behind the second barrier, a larger testing table or surface would need to be used to allow for more datapoints behind the second barrier to be measured.
- *Alternate Wall System*: Even though the wood barrier in this dissertation performed better than expected and did not catastrophically fail causing fragmentation. The study pointed out the limitations of the designed barrier in closer in Z values where this barrier is necessary for terrorist style attacks similar to the Boston Marathon bombing. The barrier showed promise for a natural material such as sand to absorb energy, allowing for plastic deformation without catastrophic failure of the barrier and further reduced pressure behind the structure. However, to be more useful in terrorist attacks, furthering the development

of a barrier that can withstand between Z=3ft/lb$^{1/3}$ -Z=9ft/lb$^{1/3}$ range is critical. Changing the geometry of the wood barrier to be deeper or to thin sheet metal could be potential solutions that keep the barrier as light as possible.

- *Wood Barrier Fracture Loading*: More field experimentation for the designed barrier is needed to determine the complete failure and fracture point of the barrier. The use of more sensors for barrier deflection, strain, and stress could be beneficial in further expanding the FEM and SDOF accuracy and predictions. In this study, failure was defined as reaching the elastic limit and the onset of plastic deformation. Determining the catastrophic failure point could help define the full resistance curve which could allow the SDOF plasticity model to be expanded more. By expanding the SDOF plasticity model, the predictions for near the elastic limit could improve in accuracy.
- *Close-In Blast*: Another aspect of study that would require full-scale experimentation is to assess the behavior of the wood barrier for close-in blast. For Z<1.19m/kg$^{1/3}$ (3ft/lb$^{1/3}$), the potential for breaching is much higher causing modeling to be much more difficult and complex. It would be beneficial to see how the barrier would do with a charge close to the surface of the barrier.
- *Loading in ABAQUS*: To apply blast loading in ABAQUS the ConWep model was used to calculate the peak pressure and the duration of loading from the range R and charge weight W. This was applied to the front surface of the barrier only. The wraparound of the blast wave on the back side of the barrier is not accounted for in this study even though it is only a fraction of the initial pressure applied to the front. This back pressure and wraparound pressure could be accounted for in a few ways to potentially change the displacement

curves by applying either a net load to the front of the barrier or separate time histories to the front and back surfaces of the barrier.

- *Improvement to SDOF Model*: Another modification to the SDOF could be to use an exponential function for SDOF load rather than a triangular impulse load. The triangular impulse load overestimates the impulse (area under the pressure time curve) compared to the actual pressure time histories experienced in the field (Figure 7-1). As the Friedlander equation is an exponential function, a more general exponential function may be able to capture the trend of the blast load more accurately than a simplified triangular pulse.
- *Detonation Location*: It is well known in research that the shape of the charge can drastically impact the shape of the blast wave and therefore the pressures at different standoff distances. However, the location of the detonator in the charge can have a large effect. There will always be variation in experimentation, and this is just one source of variability and uncertainty. Performing experiments to study the impact of detonation location could be a potential project to understand that impact it can have on the surrounding pressures.
- *Impact of Impulse on Injuries*: Even though most injury thresholds are presented in terms of pressure, impulse is actually of more interest, as it is the amount of time exposed to elevated pressure. The duration of exposure is critical as shown in the thresholds in the Bowen curves even for low pressure ranges experienced with PBIEDS. Impulse is what causes more injuries associated with primary blast injuries. Performing more analysis and developing ANNs and other models to predict the impulse rather than just the pressure, could be extremely valuable in protection of people and structures.

REFERENCES

ABAQUS/Explicit. (2021). *Analysis User's Manual* (7.5). Dassault Systemes Simulia, Inc.

ABC News. (2021, September 9). *As the twin towers burned on September 11, hundreds of people became trapped in narrow stairwells*.

Abraham, A., Sydenham, P. H., & Thorn, R. (2005). Artificial Neural Networks. In *Handbook of Measuring System Design*. Wiley.

Aicher, S., & Klöck, W. (2001). *Linear versus quadratic failure criteria for in-plane loaded wood-based panels*. https://www.researchgate.net/publication/285854046

ARCOSA. (2023). *C03 Specifications for CAIN Construction Quote 2315 Deridder Concrete Sand*.

Arnold, J. (2010, December 11). *Big Chill at the Big House attracts Guinness Book representative, record crowd makes an impression and more*. The Ann Arbor News Web Page.

ASCE. (2009). *ASCE Blast Protection of Buildings Standards*.

Associated Press. (2022, April 18). *The Story: Oklahoma City Bombing*.

Awad, M., & Azizi, S. (2016). *Prediction of Interface Level Height of Stratified Liquid-Liquid Flow Using Artificial Neural Network*. https://www.researchgate.net/publication/307905123

Bahei-El-Din, Y. A., & Dvorak, G. J. (2008). Enhancement of blast resistance of sandwich plates. *Composites Part B: Engineering*, *39*(1). https://doi.org/10.1016/j.compositesb.2007.02.006

Barbato, M., Petrini, F., Unnikrishnan, V. U., & Ciampoli, M. (2013). Performance-Based Hurricane Engineering (PBHE) framework. *Structural Safety*, *45*, 24–35. https://doi.org/10.1016/j.strusafe.2013.07.002

Barinov, R., Gai, V., Kuznetsov, G., & Golubenko, V. (2023). Automatic Evaluation of Neural Network Training Results. *Computers*, *12*(2). https://doi.org/10.3390/computers12020026

Belegundu, A. D., & Rajan, S. D. (2008). *Shape Optimization of Metal Plates Subject to Blast Pressure Loading*.

BERRAIS, A. (1999). Artificial Neural Networks in Structural Engineering: Concept and Applications. *Journal of King Abdulaziz University-Engineering Sciences*, *12*(1). https://doi.org/10.4197/eng.12-1.4

Bevins, T., Armstrong, B., Baylot, J., & Rickman, D. (2003). Multiple building simulations and effect of berms behind blast barrier walls. *2003 User Group Conference*, 250–256.

Bewick, B., & Flood, I. (2010). *First-Principle Simulation of Blast Barrier Effectiveness for the Development of Simplified Design Tools*. https://www.researchgate.net/publication/235171977

Bewick, B. T., & Chen, Z. (2011). *A NEURAL-NETWORK MODEL-BASED ENGINEERING TOOL FOR BLAST WALL PROTECTION OF STRUCTURES (POSTPRINT) AIR FORCE RESEARCH LABORATORY MATERIALS AND MANUFACTURING DIRECTORATE ν Air Force Materiel Command ν United States Air Force ν Tyndall Air Force Base, FL 32403-5323*.

Beyer, M. (1986). Blast Loads behind vertical walls. *DoD Explosives Safety Seminar*, *1*(22nd).

Bogosian, D., Ferritto, J., & Shi, Y. (2002). Measuring Uncertainty and Conservatism in Simplified Blast Models. *30th Explosives Safety Seminar*.

Bowen R Fletcher D R Richmond, G. E. (1968). *Estimate of Man's Tolerance to the Direct Effects of Air Blast*.

British Ordnance Board Minutes, Pub. L. No. 13565 (1915).

Brode, H. L. (1955). Numerical solutions of spherical blast waves. *Journal of Applied Physics*, *26*(6). https://doi.org/10.1063/1.1722085

Broyden, C. (1970). The convergence of a class of double-rank minimization algorithms: general considerations. *IMA Journal of Applied Mathematics*, *6*(1), 76–90.

Buchan, P. A., & Chen, J. F. (2007). Blast resistance of FRP composites and polymer strengthened concrete and masonry structures - A state-of-the-art review. *Composites Part B: Engineering*, *38*(5–6). https://doi.org/10.1016/j.compositesb.2006.07.009

Bueno, J. R., Léger, P., Loriggio, D. D., & Carvalho de Sousa, A. (2018). Code for Blast Analysis using the Finite Element Method. *Simpósio de Aplicações Operacionais Em Áreas de Defesa - XX SIGE*.

Busch, C. L., Aimone-Martin, C. T., & Tarefder, R. A. (2016). Experimental Evaluation and Finite-Element Simulations of Explosive Airblast Tests on Clay Soils. *International Journal of Geomechanics*, *16*(4). https://doi.org/10.1061/(asce)gm.1943-5622.0000629

Cabrero, J. M., & Gebremedhin, K. G. (2010). *EVALUATION OF FAILURE CRITERIA IN WOOD MEMBERS*.

Cernak, I., & Noble-Haeusslein, L. J. (2010). Traumatic brain injury: An overview of pathobiology with emphasis on military populations. In *Journal of Cerebral Blood Flow and Metabolism* (Vol. 30, Issue 2). https://doi.org/10.1038/jcbfm.2009.203

Cernak, I., Wang, Z., Jiang, J., Bian, X., & Savic, J. (2001). Cognitive deficits following blast injury-induced neurotrauma: Possible involvement of nitric oxide. *Brain Injury*, *15*(7). https://doi.org/10.1080/02699050010009559

Chang, D. B., & Young, C. S. (2010). Probabilistic Estimates of Vulnerability to Explosive Overpressures and Impulses. In *Journal of Physical Security* (Vol. 4, Issue 2). http://www.globalsecurity.org/military/system/munition/explosives-anfo.htm

Chapman, T. C., Rose, T. A., & Smith, P. D. (1995). Reflected blast wave resultants behind cantilever walls: A new prediction technique. *International Journal of Impact Engineering*, *16*(3). https://doi.org/10.1016/0734-743X(94)00051-W

Chen, L., Zhang, L., Fang, Q., & Mao, Y.-M. (2015). Performance based investigation on construction of anti-blast water wall. *International Journal of Impact Engineering, 81*, 17–33.

Collins, G. S. (2002). *An Introduction to Hydrocode Modeling*. http://www.lpl.arizona.edu/tekton/sales

Constantinescu, R., Lazarescu, V., & Tahboub, R. (2008). GEOMETRICAL FORM RECOGNITION USING "ONE-STEP-SECANT" ALGORITHM IN CASE OF NEURAL NETWORK. In *U.P.B. Sci. Bull., Series C* (Vol. 70, Issue 2).

Cormie, D., Mays, G., & Smith, P. (2019). Blast Effects on Buildings. In *Blast Effects on Buildings*. https://doi.org/10.1680/beob.61477

Cornell, C., & Krawinkler, H. (2000). Progress and Challenges in Seismic Performance Assessment. *PEER Center News*, *3*, 1–3.

Cranz, K. (1926). *Textbook of Ballistics*. Springer.

Cullis, I. G. (2001). Blast waves and how they interact with structures. In *Journal of the Royal Army Medical Corps* (Vol. 147, Issue 1). https://doi.org/10.1136/jramc-147-01-02

Dayhoff, J. (1990). *Neural Network Architectures: An Introduction*. Van Nostrand Reinhold Co.

Dennis, A. A., Pannell, J. J., Smyl, D. J., & Rigby, S. E. (2021). Prediction of blast loading in an internal environment using artificial neural networks. *International Journal of Protective Structures*, *12*(3), 287–314. https://doi.org/10.1177/2041419620970570

Dennis, A. A., & Rigby, S. E. (2023). The Direction-encoded Neural Network: A machine learning approach to rapidly predict blast loading in obstructed environments. *International Journal of Protective Structures*. https://doi.org/10.1177/20414196231177364

Denny, J. W., Dickinson, A. S., & Langdon, G. S. (2021). *Defining blast loading "zones of relevance" for primary blast injury research: A consensus of injury criteria for idealised explosive scenarios. (Preprint). Defining blast loading "zones of relevance" for primary blast injury research: A consensus of injury criteria for idealised explosive scenarios*.

Denny, J. W., Dickinson, A. S., & Langdon, G. S. (2023). Guidelines to inform the generation of clinically relevant and realistic blast loading conditions for primary blast injury research. *BMJ Military Health*, *169*(4), 364–369. https://doi.org/10.1136/bmjmilitary-2021-001796

DePalma, R., Burris, D., Champion, H., & Hodgson, M. (2005). Blast Injuries. *The New England Journal of Medicine*, *352*(13).

Dewey, J. M., Johnson, O. T., & Patterson, J. D. (1962). *Mechanical Impulse Measurements Close to Explosive Charges*.

Dharmasena, K. P., Wadley, H. N. G., Xue, Z., & Hutchinson, J. W. (2008). Mechanical response of metallic honeycomb sandwich panel structures to high-intensity dynamic loading. *International Journal of Impact Engineering*, *35*(9). https://doi.org/10.1016/j.ijimpeng.2007.06.008

DHS. (2003). *FEMA 426: Buildings and Infrastructure Protection Series Reference Manual to Mitigate Potential Terrorist Attacks Against Buildings Homeland Security Science and Technology FEMA*.

DHS. (2005). *FEMA 452: Risk Assessment How-To Guide to Mitigate Potential Terrorist Attacks Against Buildings*.

DHS. (2006). *FEMA 453: Risk Management Series Design Guidance for Shelters and Safe Rooms*.

DHS. (2021). *IED Attack: Improvised Explosive Devices*. http://www.ready.gov

DHS. (2023). FY2023 Spending Bill Highlights. *Senate Appropriations Committee.*

Ding, Y., Song, X., & Zhu, H. (2017). Probabilistic Progressive Collapse Analysis of Steel Frame Structures against Blast Loads. *Engineering Structures*, *147*, 679–691.

DOA. (1960). *VARIATION OF STRENGTH PROPERTIES IN WOODS USED FOR STRUCTURAL PURPOSES*.

Dobratz, B. (1981). *LLNL Explosives Handbook: Properties of Chemical Explosives and Explosives and Explosives Simulants* (Lawrence Livermore National Lab, Ed.).

DOD. (1986). *TM 5-855-1: Fundamentals of Protective Design for Conventional Weapons.*

DOD. (1990). *TM 5-1300: Structures to Resist the Effects of Accidental Explosions*.

DOD. (2008). *UNIFIED FACILITIES CRITERIA (UFC) STRUCTURES TO RESIST THE EFFECTS OF ACCIDENTAL EXPLOSIONS APPROVED FOR PUBLIC RELEASE, DISTRIBUTION UNLIMITED*. http://dod.wbdg.org/.

DOE. (1981). *A Manual for Prediction of Blast and Fragment Loadings on Structures*.

Dongare, A. D., Kharde, R. R., & Kachare, A. D. (2012). Introduction to Artificial Neural Network (ANN) Methods. *International Journal of Engineering and Innovative Technology (IJEIT)*, *2*(1).

DOS. (2022). *Country Reports on Terrorism 2022*.

DOT. (2007). *Manual for LS-DYNA Wood Material Model 143*.

Dowling, A., & Harding, J. (1967). Tensile Properties of Mild Steel Under High Strain Rates. *1st HERF Conference.*

Drdlová, M., Frank, M., Řídký, R., Popovič, M., & Buchar, J. (2015). Evaluation of static and dynamic properties of energy absorbers for explosion resistant elements. *Advances in Military Technology*, *10*(1).

Drucker, D., & Prager, W. (1952). Soil Mechanics and Plastic Analysis or Limit Design. *Quarterly of Applied Mathematics*, 157–165.

Dusenberry, D. O. (2010). Handbook for Blast Resistant Design of Buildings. In *Handbook for Blast Resistant Design of Buildings*. https://doi.org/10.1002/9780470549070

Ellingwood, B. R., Celik, O. C., & Kinali, K. (2007). Fragility assessment of building structural systems in Mid-America. *Earthquake Engineering and Structural Dynamics*, *36*(13), 1935–1952. https://doi.org/10.1002/eqe.693

Ellingwood, B. R., Rosowsky, D. V., Li, Y., & Kim, J. H. (2004). Fragility Assessment of Light-Frame Wood Construction Subjected to Wind and Earthquake Hazards. *Journal of Structural Engineering*, *130*(12), 1921–1930. https://doi.org/10.1061/(asce)0733-9445(2004)130:12(1921)

Epstein, D., & Kudryavtsev, A. (2012). Shock and Blast Wave Propagation Through a Porous Barrier. In *28th International Symposium on Shock Waves* (Vol. 2). Springer Berlin Heidelberg. https://doi.org/10.1007/978-3-642-25685-1

Fletcher, R. (1970). A New Approach to Variable Metric Algorithms. *The Computer Journal*, *13*(3), 317–322.

Flood, I., & Bewick, B. (2010). *A New Method for Very Fast Simulation of Blast Wave Propagation in Complex Built Environments*.

Flood, I., Bewick, B. T., Dinan, R. J., & Salim, H. A. (2009). Modeling blast wave propagation using artificial neural network methods. *Advanced Engineering Informatics*, *23*(4). https://doi.org/10.1016/j.aei.2009.06.005

Frank P. Lees. (1996). Loss Prevention in the Process Industries Volume 3. *Loss Prevention in the Process Industries: Hazard Indentification, Assessment and Control*, *3*(2).

Furrer, D., & Thaler, S. (2005). Neural-network modeling. *Advanced Materials and Processes*, *163*(11).

Gan, K. L., Brewer, T. R., Pope, D. J., & Rigby, S. E. (2022). Probabilistic analysis of blast–obstacle interaction in a crowded internal environment. *Probabilistic Engineering Mechanics*, *68*. https://doi.org/10.1016/j.probengmech.2022.103227

Gavin, H. (2019). *The Levenberg-Marquardt Algorithm for Nonlinear Lease Squares Curve Fitting Problems*. Duke University.

Gebbeken, N., & Döge, T. (2010). Explosion protection - Architectural design, urban planning, and landscape planning. *International Journal of Protective Structures*, *1*(1). https://doi.org/10.1260/2041-4196.1.1.1

Geman, S., Buntine, W., & Weigand, A. (1991). Bayesian Back-Propagation. *Complex Systems*, *5*, 603–643.

Goel, M. D. (2015). Blast: Characteristics, loading and computation-an overview. In *Advances in Structural Engineering: Mechanics, Volume One* (pp. 417–434). Springer India. https://doi.org/10.1007/978-81-322-2190-6_36

Goel, M. D., & Matsagar, V. A. (2014a). Blast-Resistant Design of Structures. *Practice Periodical on Structural Design and Construction*, *19*(2), 04014007. https://doi.org/10.1061/(asce)sc.1943-5576.0000188

Goel, M. D., & Matsagar, V. A. (2014b). Blast-Resistant Design of Structures. *Practice Periodical on Structural Design and Construction*, *19*(2), 04014007. https://doi.org/10.1061/(asce)sc.1943-5576.0000188

Goldfarb, D. (1970). A Family of Variable-Metric Methods Derived by Variational Means. *Mathematics of Computation*, *24*(109), 23–26.

Gonzalez, D. (2005). Crush syndrome. In *Critical Care Medicine* (Vol. 33, Issue 1 SUPPL.). https://doi.org/10.1097/01.CCM.0000151065.13564.6F

Goodman, H. J. (1960). *Compiled Free-Air Blast Data on Bare Spherical Pentolite*.

Griva, I., Nash, S., & Sofer, A. (2008). *Linear and Nonlinear Optimization* (2nd ed.). Society for Industrial and Applied Mathematics.

Grote, D. L., Park, S. W., & Zhou, M. (2001). Dynamic behavior of concrete at high strain rates and pressures: I. experimental characterization PII: S 0 7 3 4-7 4 3 X (0 1) 0 0 0 2 0-3. In *International Journal of Impact Engineering* (Vol. 25).

Gupta, R. K., & Przekwas, A. (2013). Mathematical models of blast induced TBI: Current status, challenges, and prospects. *Frontiers in Neurology*, *4 MAY*. https://doi.org/10.3389/fneur.2013.00059

Hajek, R., & Foglar, M. (2015). Numerical and Experimental Analysis of the Effect of Rigid Barriers on Blast Wave Propagation. *Journal of Structural Engineering*, *141*(12). https://doi.org/10.1061/(asce)st.1943-541x.0001308

Hajek, R., Foglar, M., & Fladr, J. (2016). Influence of barrier material and barrier shape on blast wave mitigation. *Construction and Building Materials*, *120*, 54–64. https://doi.org/10.1016/j.conbuildmat.2016.05.078

Hallquist, J. O. (1998). *LS-DYNA Theory Manual.* Livermore Software Technology Co.

Henrych, J., & Abrahamson, G. R. (1980). The Dynamics of Explosion and Its Use. *Journal of Applied Mechanics*, *47*(1). https://doi.org/10.1115/1.3153619

Hetherington, J., & Smith, P. (2014). Blast and Ballistic Loading of Structures. In *Blast and Ballistic Loading of Structures*. https://doi.org/10.1201/9781482269277

Hoemann, J. (2023, May 15). The Use of Experimental Scaled Airblast Testing to Support Numerical Validation. *6th Annual Conference on Protective Structures.*

Holgado, D., Montalya, A., Florek, J., El-Domiaty, K., & Calidonna, B. (2022). Deep Neural Network (DNN) model to predict close-in blast load. *Structures Congress*, 10–25.

Homan, B. E., Biss, M. M., & Mcnesby, K. L. (2013). *Modeling of Near-Field Blast Performance*.

Hussein, A. (2019). *PERFORMANCE ASSESSMENT OF SIMPLE BLAST WALL SYSTEMS* [Doctor of Philosophy]. Colorado State University.

Hussein, A., Heyliger, P., & Mahmoud, H. (2020). Structural performance of a wood-sand-wood wall for blast protection. *Engineering Structures*, *219*. https://doi.org/10.1016/j.engstruct.2020.110954

Hussein, A., Mahmoud, H., & Heyliger, P. (2020). Probabilistic analysis of a simple composite blast protection wall system. *Engineering Structures*, *203*. https://doi.org/10.1016/j.engstruct.2019.109836

Isaac, O. S., Alshammari, O. G., Pickering, E. G., Clarke, S. D., & Rigby, S. E. (2023). Blast wave interaction with structures – An overview. In *International Journal of Protective Structures* (Vol. 14, Issue 4, pp. 584–630). SAGE Publications Inc. https://doi.org/10.1177/20414196221118595

ISC. (2021). *The Risk Management Process: An Interagency Security Committee Standard*.

Ivanov, A., Fassardi, N., Scafidi, C., Shemen, T., & Eliasson, V. (2019). Shock wave attenuation using rigid obstacles with large- and small-scale geometrical features. *Multiscale and Multidisciplinary Modeling, Experiments and Design*, *2*(4), 269–279. https://doi.org/10.1007/s41939-019-00053-2

Jack, W. H., & Armendt, B. F. (1965). Measurements of Normally Reflected Shock Parameters from Explosive Charges Under Simulated High-Altitude Conditions. *BRL Report*, *NO.1280*.

Jain, A. K., Mao, J., & Mohiuddin, K. M. (1996). Artificial neural networks: A tutorial. In *Computer* (Vol. 29, Issue 3). https://doi.org/10.1109/2.485891

Jankowiak, T., Lodygowski, T., & Sielicki, P. (2007, June 19). Modeling of pressure distribution after explosion. *CMM 2007- Computer Methods in Mechanics*.

Kang, M. A., & Park, C. H. (2023). Prediction of Peak Pressure by Blast Wave Propagation Between Buildings Using a Conditional 3D Convolutional Neural Network. *IEEE Access*, *11*, 26114–26124. https://doi.org/10.1109/ACCESS.2023.3257345

Khan, R., Farooq, S. H., & Usman, M. (2019). Blast loading response of reinforced concrete panels externally reinforced with steel strips. *Infrastructures*, *4*(3). https://doi.org/10.3390/infrastructures4030054

Kingery, C., & Bulmash, G. (1984). *Airblast Parameters from TNT spherical air blast and hemispherical surface blast*.

Kingery, C. N. (1966). *Air Blast Parameters Versus Distance for Hemispherical TNT Surface Bursts*.

Kinney, G. F., Graham, K. J., & Raspet, R. (1985). Explosive Shocks in Air, 2nd ed. by Gilbert F. Kinney and Kenneth J. Graham. *The Journal of the Acoustical Society of America*, *80*(2). https://doi.org/10.1121/1.394030

Kong, S. Y., Remennikov, A. M., & Uy, B. (2011). The effect of medium strain rates on the mechanical properties of high-performance steels. *Incorporating Sustainable Practice in Mechanics of Structures and Materials - Proceedings of the 21st Australian Conference on the Mechanics of Structures and Materials*. https://doi.org/10.1201/b10571-124

Kumar R, A., & Pathak, V. (2021). Shock wave mitigation using zig-zag structures and cylindrical obstructions. *Defence Technology*, *17*(6), 1840–1851. https://doi.org/10.1016/j.dt.2020.10.001

Lahiri, S., & Ho, L. (2011). Simulation of Rapid Structural Failure Due to Blast Loads from Conventional Weapons (Conwep). *3Ds.Com*.

Lee, D., & O 'Toole, B. J. (2014). Energy Absorbing Sandwich Structures Under Blast Loading. *Proceeding of 8th International LS-DYNA Users Conference*, *Detroit, U*.

Lee, E. L., Horning, H. C., & Kury, J. W. (1968). *Adiabatic expansion of high explosives detonation products*.

Lees, F., & Mannan, S. (1996). Chapter 17: Explosion. In *Lees' Loss Prevention in the Process Industries*.

Linkute, L., Juocevičius, V., & Vaidogas, E. R. (2013). A probabilistic design of sacrificial cladding for a blast wall using limited statistical information on blast loading. *Mechanika*, *19*(1), 58–66. https://doi.org/10.5755/j01.mech.19.1.3621

Low, H. Y., & Hao, H. (2001). Reliability analysis of reinforced concrete slabs under explosive loading. *Structural Safety*, 157–178. www.elsevier.nl/locate/strusafe

Lozano, E. (2016). *DESIGN AND ANALYSIS OF A PERSONNEL BLAST SHIELD FOR DIFFERENT EXPLOSIVES APPLICATIONS* [Masters of Science]. Colorado School of Mines.

Luo, H., Jiang, S., Nakmali, D. U., Gan, R. Z., & Lu, H. (2016). Mechanical Properties of a Human Eardrum at High Strain Rates After Exposure to Blast Waves. *Journal of Dynamic Behavior of Materials*, *2*(1), 59–73. https://doi.org/10.1007/s40870-015-0041-3

Ma, L., Wu, H., & Fang, Q. (2023). A unified performance-based blast-resistant design approach for RC beams/columns. *International Journal of Impact Engineering*, *173*. https://doi.org/10.1016/j.ijimpeng.2022.104459

Mahmoud, H., & Cheng, G. (2017). Framework for Lifecycle Cost Assessment of Steel Buildings under Seismic and Wind Hazards. *Journal of Structural Engineering*, *143*(3). https://doi.org/10.1061/(asce)st.1943-541x.0001663

Malvar, L. J., & Crawford, J. E. (1998). *DYNAMIC INCREASE FACTORS FOR CONCRETE*.

MATHWORKS. (2022). *MATLAB* (R2022b). Natick.

McCann, A., McGilvray, K., Troyer, K., Hussein, A., Mahmoud, H., & Heyliger, P. (2018). *Effects of C-1 and TNT explosive pressure on cadaveric ovine auditory tissue*.

McGlaun, J. M., Thompson, S. L., & Elrick, M. G. (1990). *CTH: A Three-Dimensional Shock Wave Physics Code*.

Mcvay, M. K. (1988). *SPALL DAMAGE OF CONCRETE STRUCTURES*.

Memari, M., & Mahmoud, H. (2018). Framework for a performance-based analysis of fires following earthquakes. *Engineering Structures*, *171*, 794–805. https://doi.org/10.1016/j.engstruct.2018.05.099

Meyers, M. A., Marr, L. E., & Lindholm, U. S. (1982). Shock Waves and High-Strain-Rate Phenomena in Metals. *Journal of Applied Mechanics*, *49*(3). https://doi.org/10.1115/1.3162565

Miller, D., Pan, H., Nance, R., Shirley, A., & Cogar, J. (2010). A Coupled Eulerian/Lagrangian Simulation of Blast Dynamics. In *Society for Experimental Mechanics, Inc*.

Millet, A. (2021). A Universal Model for the Log-Normal Distribution of Elasticity in Polymeric Gels and Its Relevance to Mechanical Signature of Biological Tissues. *Biology*, *10*(1), 64.

Møller, M. F. (1993). A scaled conjugate gradient algorithm for fast supervised learning. *Neural Networks*, *6*(4). https://doi.org/10.1016/S0893-6080(05)80056-5

Mustafa, M., Rezaur, R., Saiedi, S., & Isa, M. (2012). River Suspended Sediment Prediction Using various multilayer Perceptron Neural Network Training Algorithms. *Water Resources Management*, *26*, 1879–1897.

Neal, R. M. (1992). *Bayesian Training of Backpropagation Networks by the Hybrid Monte Carlo Method*.

Needham, C. (2009). Blast Loads and Propagation around and over a building. *Shock Waves: International Symposium on Shock Waves.*

Netherton, M., & Stewart, M. (2010). Blast Load Variability and Accuracy of Blast Load Prediction Models. *International Journal of Protective Structures*, *1*(4), 543–570.

Ngo, T. D., & Mendis, P. (2016). *Blast loading and blast effects on structures-An overview Advanced Cement-Based Composite for Construction Industry View project Structures with GFRP bars View project*. https://www.researchgate.net/publication/279897768

Ngo, T., Mendis, P., Gupta, A., & Ramsay, J. (2007). Blast Loading and Blast Effects on Structures. *Electronic Journal of Structural Engineering*, 1359–1364.

Nguyen, T. A., Ly, H. B., Mai, H. V. T., & Tran, V. Q. (2021). On the Training Algorithms for Artificial Neural Network in Predicting the Shear Strength of Deep Beams. *Complexity*, *2021*. https://doi.org/10.1155/2021/5548988

Niollet, J., Yuen, S., & Nurick, G. (2015). A study assesses the use of cylindrical bars as blast barriers. *International Journal of Protective Structures*, *6*(2), 263–286.

Ohrt, A. P., Lunderman, C. V., & Rickman, D. (1998). Miniature-Scale Experiments of Airblast Diffraction Over Barrier Walls. *Proceedings of 69th Shock and Vibration Symposium.*

Olmati, P., Petrini, F., & Gkoumas, K. (2014). Fragility analysis for the Performance-Based Design of cladding wall panels subjected to blast load. *Engineering Structures*, *78*, 112–120. https://doi.org/10.1016/j.engstruct.2014.06.004

Petrini, F., & Ciampoli, M. (2012). Performance-based wind design of tall buildings. *Structure and Infrastructure Engineering*, *8*(10), 954–966. https://doi.org/10.1080/15732479.2011.574815

Pezzola, G. (2018). *EXPERIMENTAL TESTING AND MODELING STRATEGIES OF CARBON FIBER-REINFORCED POLYMER BLAST RETROFITS USING STEEL ANCHORAGE SYSTEMS*.

Pierazzo, E., Artemieva, N., Asphaug, E., Baldwin, E. C., Cazamias, J., Coker, R., Collins, G. S., Crawford, D. A., Davison, T., Elbeshausen, D., Holsapple, K. A., Housen, K. R., Korycansky, D. G., & Wünnemann, K. (2008). Validation of numerical codes for impact and explosion cratering: Impacts on strengthless and metal targets. *Meteoritics and Planetary Science*, *43*(12), 1917–1938. https://doi.org/10.1111/j.1945-5100.2008.tb00653.x

Pilkington, S. F., & Mahmoud, H. N. (2016). Using artificial neural networks to forecast economic impact of multi-hazard hurricane-based events. *Sustainable and Resilient Infrastructure*, *1*(1–2). https://doi.org/10.1080/23789689.2016.1179529

Rashid, B., Destrade, M., & Gilchrist, M. D. (2014). Mechanical characterization of brain tissue in tension at dynamic strain rates. *Journal of the Mechanical Behavior of Biomedical Materials*, *33*(1), 43–54. https://doi.org/10.1016/j.jmbbm.2012.07.015

Razaqpur, A. G., Campidelli, M., & Foo, S. (2012). Experimental versus analytical response of structures to blast loads. *Advances in Protective Structures Research: IAPS Special Publication 1 - Proceedings of the IAPS Forum on Recent Research Advances on Protective Structures*. https://doi.org/10.1201/b12768-7

Razaqpur, G., Mekky, W., & Foo, S. (2009). Fundamental concepts in blast resistance evaluation of structures. *Canadian Journal of Civil Engineering*, *36*(8), 1292–1304. https://doi.org/10.1139/L09-032

Remennikov, A., & Carolan, D. (2005). *Building vulnerability design against terrorist attacks*. https://ro.uow.edu.au/engpapershttps://ro.uow.edu.au/engpapers/2740https://ro.uow.edu.au/engpapers/2740

Remennikov, A. M., & Mendis, P. A. (2006). Prediction of airblast loads in complex environments using artificial neural networks. *WIT Transactions on the Built Environment*, *87*. https://doi.org/10.2495/SU060271

Remennikov, A. M., & Rose, T. A. (2005). Modelling blast loads on buildings in complex city geometries. *Computers and Structures*, *83*(27). https://doi.org/10.1016/j.compstruc.2005.04.003

Remennikov, A. M., & Rose, T. A. (2007). Predicting the effectiveness of blast wall barriers using neural networks. *International Journal of Impact Engineering*, *34*(12). https://doi.org/10.1016/j.ijimpeng.2006.11.003

Rickman, D. D., & Murrell, D. W. (2007). *DEVELOPMENT OF AN IMPROVED METHODOLOGY FOR PREDICTING AIRBLAST PRESSURE RELIEF ON A DIRECTLY LOADED WALL*. https://proceedings.asmedigitalcollection.asme.org

Rose, T. A., Smith, P. D., & Mays, G. C. (1995). *The effectiveness of walls designed for the protection of structures against airblast from high explosives*.

Schmitt, R., Crawford, D., Harstad, E., Hensinger, D., & Ruggirello, K. (2017). *CTH User's Manual and Input Instructions*.

Shahin, M. A., Maier, H. R., & Jaksa, M. B. (2004). Data Division for Developing Neural Networks Applied to Geotechnical Engineering. *Journal of Computing in Civil Engineering*, *18*(2). https://doi.org/10.1061/(asce)0887-3801(2004)18:2(105)

Shanno, D. F. (1970). Conditioning of Quasi-Newton Methods for Function Minimization. *Mathematics of Computation*, *24*(111), 647–656.

Sherman, J. (2011). *Hescos, T-Walls, and a Bunker*. Flickr.

Shirbhate, P. A., & Goel, M. D. (2021). A Critical Review of Blast Wave Parameters and Approaches for Blast Load Mitigation. *Archives of Computational Methods in Engineering*, *28*(3), 1713–1730. https://doi.org/10.1007/s11831-020-09436-y

Si, D., Pan, Z., & Zhang, H. (2024). Probabilistic assessment and expression of load factor design model for explosive blast loading. *Reliability Engineering and System Safety*, *242*. https://doi.org/10.1016/j.ress.2023.109802

Sisemore, C., & Babuška, V. (2020). The Science and Engineering of Mechanical Shock. In *The Science and Engineering of Mechanical Shock*. https://doi.org/10.1007/978-3-030-12103-7

Smith, P. D., Mays, G. C., Rose, T. A., Teo, K. G., & Roberts, B. J. (1992). Small scale models of complex geometry for blast overpressure assessment. *International Journal of Impact Engineering*, *12*(3), 345–360.

Spence, S. M. J., & Gioffrè, M. (2012). Large scale reliability-based design optimization of wind excited tall buildings. *Probabilistic Engineering Mechanics*, *28*, 206–215. https://doi.org/10.1016/j.probengmech.2011.08.001

Stewart, M. G., & Netherton, M. D. (2008). Security risks and probabilistic risk assessment of glazing subject to explosive blast loading. *Reliability Engineering and System Safety*, *93*(4). https://doi.org/10.1016/j.ress.2007.03.007

Stewart, M., Netherton, M., & Rosowsky, D. (2006). Terrorism Risks and Blast Damage to Built Infrastructure. *Natural Hazards Review*, *7*(3), 114–122.

Stoner, R. G., & Bleakney, W. (1948). The attenuation of spherical shock waves in air. *Journal of Applied Physics*, *19*(7), 670–678. https://doi.org/10.1063/1.1698189

Sugiyama, Y., Homae, T., Wakabayashi, K., Matsumura, T., & Nakayama, Y. (2014). Numerical Simulations on the attenuation effect of a barrier material on a blast wave. In *Lees Loss Prevention in Process Industries* (Vol. 32, pp. 135–143).

Svozil, D., Kvasnieka, V., & Pospichal, J. (1997). Chemometrics and intelligent laboratory systems Introduction to multi-layer feed-forward neural networks. In *Chemometrics and Intelligent Laboratory Systems* (Vol. 39).

Swisdak, M. M. (1975). *EXPLOSION EFFECTS AND PROPERTIES PART I-EXPLOSION EFFECTS IN AIR*.

Taha, A. K., Gao, Z., Huang, D., & Zahran, M. S. (2019). Numerical investigation of a new structural configuration of a concrete barrier wall under the effect of blast loads. *International*

Journal of Advanced Structural Engineering, *11*. https://doi.org/10.1007/s40091-019-00252-8

Teledyne. (2023). *RP-81 EBW Detonator*.

Thornton, P., & Colangelo, V. (1985). *Fundamentals of Engineering Materials*.

Trasborg, P. (2014). *Analytical and Experimental Evaluation of Precast Sandwich Wall Panels Subjected to Blast, Breach, and Ballistic Demands* [Doctor of Philosophy, Lehigh University]. http://preserve.lehigh.edu/etd

Twisdale, L. A., Sues, R. H., & Lavelle, F. M. (1994). Reliability-based design methods for protective structures. *Structural Safety*, *15*(2), 17–33.

Tyas, A. (2018). *Experimental Measurement of Pressure Loading from Near-Field Blast Events: Techniques, Findings and Future Challenges*. 471. https://doi.org/10.3390/icem18-05364

United Nations. (2020). *Improvised Explosive Devices (IEDs)*. https://disarmament.unoda.org/convarms/ieds/

Via, A. G., Oliva, F., Spoliti, M., & Maffulli, N. (2015). Acute compartment syndrome. *Muscles, Ligaments and Tendons Journal*, *5*(1). https://doi.org/10.32098/mltj.01.2015.04

Wenzel, A. B., & Esparza, E. D. (1974). PRESSURE AND IMPULSE MEASUREMENTS CLOSE TO EXPLOSIONS IN AIR AND IN EARTH. *ISA Transactions*, *13 n 3*.

Werbos, P. (1990). Backpropagation Through Time: What it does and how to do it. *Proceedings of the IEEE*, 1550–1560.

Wilamowski, B. M. (2009). Neural network architectures and learning algorithms. *IEEE Industrial Electronics Magazine*, *3*(4). https://doi.org/10.1109/MIE.2009.934790

Wolf, S. J., Bebarta, V. S., Bonnett, C. J., Pons, P. T., & Cantrill, S. v. (2009). Blast injuries. In *The Lancet* (Vol. 374, Issue 9687). https://doi.org/10.1016/S0140-6736(09)60257-9

Xiao, W., Andrae, M., Ruediger, L., & Gebbeken, N. (2017). Numerical prediction of blast wall effectiveness for structural protection against air blast. *Procedia Engineering*, *199*. https://doi.org/10.1016/j.proeng.2017.09.432

Yeh, D. D., & Schecter, W. P. (2012). Primary blast injuries - An updated concise review. In *World Journal of Surgery* (Vol. 36, Issue 5, pp. 966–972). https://doi.org/10.1007/s00268-012-1500-9

Ying, X. (2019). An Overview of Overfitting and its Solutions. *Journal of Physics: Conference Series*, *1168*(2). https://doi.org/10.1088/1742-6596/1168/2/022022

Yu, H., & Wilamowski, B. M. (2016). Levenberg-marquardt training. In *Intelligent Systems*. https://doi.org/10.1201/9781315218427-12

Zapata, B. J., & Weggel, D. C. (2008). Computational airblast modelling of commercial explosives. *WIT Transactions on the Built Environment*, *98*, 45–54. https://doi.org/10.2495/SU080051

Zhu, H., & Khanna, S. K. (2016a). A Novel Transparent Glass Fiber-Reinforced Polymer Composite Interlayer for Blast-Resistant Windows. *Journal of Engineering Materials and Technology, Transactions of the ASME*, *138*(3). https://doi.org/10.1115/1.4032882

Zhu, H., & Khanna, S. K. (2016b). A Novel Transparent Glass Fiber-Reinforced Polymer Composite Interlayer for Blast-Resistant Windows. *Journal of Engineering Materials and Technology, Transactions of the ASME*, *138*(3). https://doi.org/10.1115/1.4032882

Zhu, H., & Khanna, S. K. (2016c). Dynamic response of a novel laminated glass panel using a transparent glass fiber-reinforced composite interlayer under blast loading. *International Journal of Impact Engineering*, *89*, 14–24. https://doi.org/10.1016/j.ijimpeng.2015.11.001

Zhu, H., & Khanna, S. K. (2016d). Dynamic response of a novel laminated glass panel using a transparent glass fiber-reinforced composite interlayer under blast loading. *International Journal of Impact Engineering*, *89*. https://doi.org/10.1016/j.ijimpeng.2015.11.001

Zukas, J. (2004). *Introduction to Hydrocodes* (Vol. 49). Elsevier.

APPENDIX A: ADDITIONAL TABLETOP DATA

10.1 Free Field Trends

EXP 1

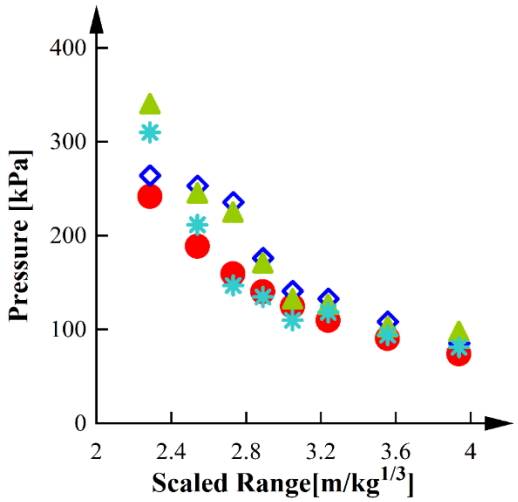

EXP 2

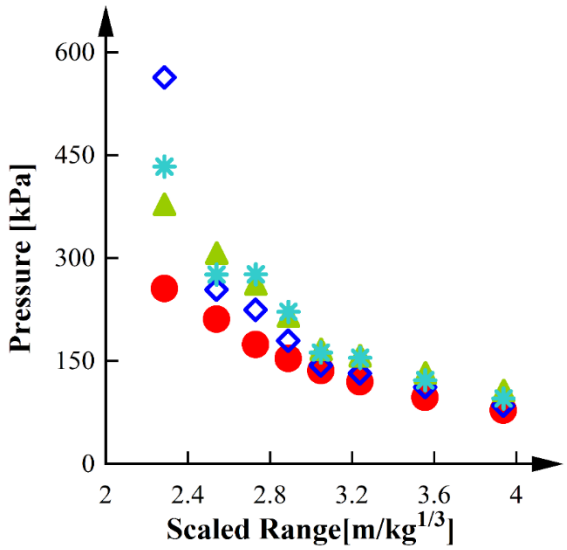

EXP 4

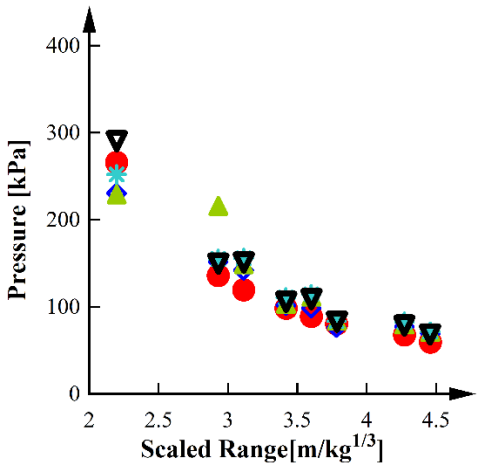

EXP 4

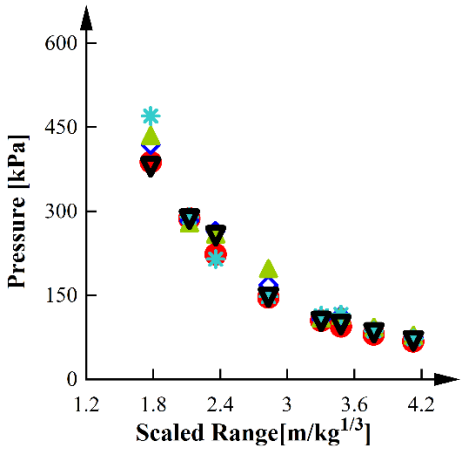

EXP 9

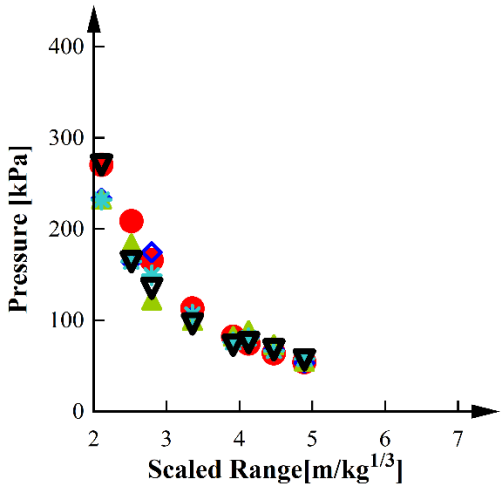

10.2 Tabletop Wall Tests Pressure Time Histories

Each plot is the pressure time histories for a single tracer for a single experiment. The three different shots are plotted together. For example, the first plot under Experiment 1 will be for tracer 1 with curves for shot A, B, and C and the corresponding CTH prediction curves. The experiments correspond to Table 3-2 the test matrix for the tabletop experiments.

EXPERIMENT 1-FF

Tracer 1

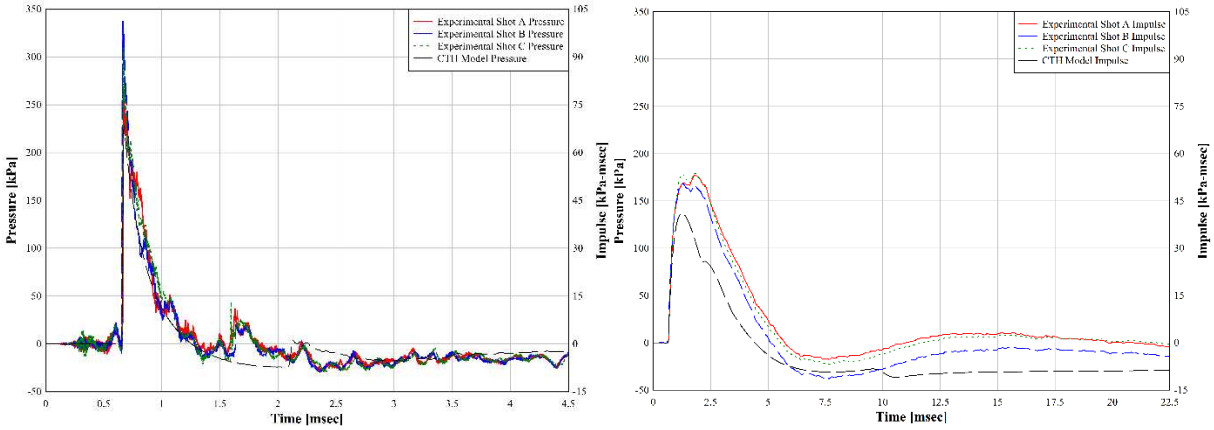

Tracer 2

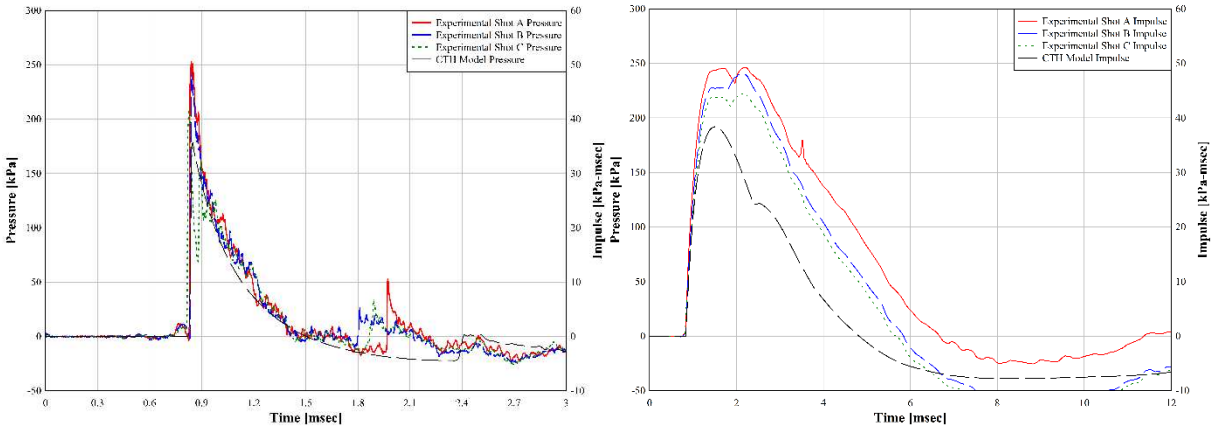

Tracer 3

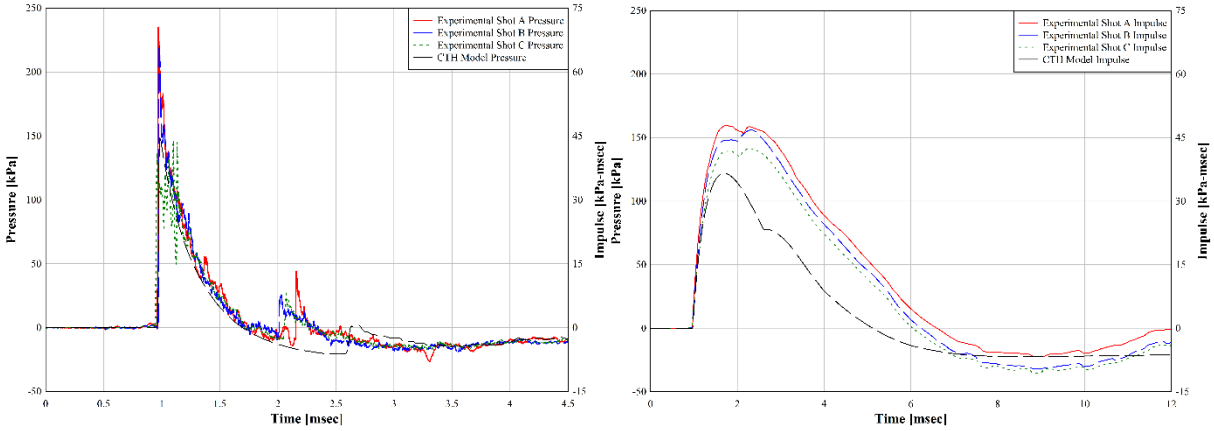

Tracer 4

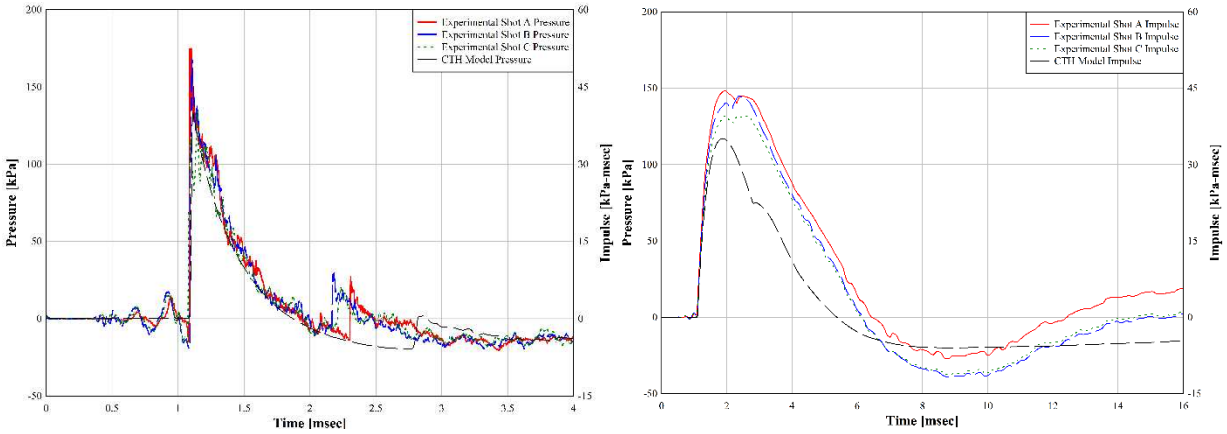

Tracer 5

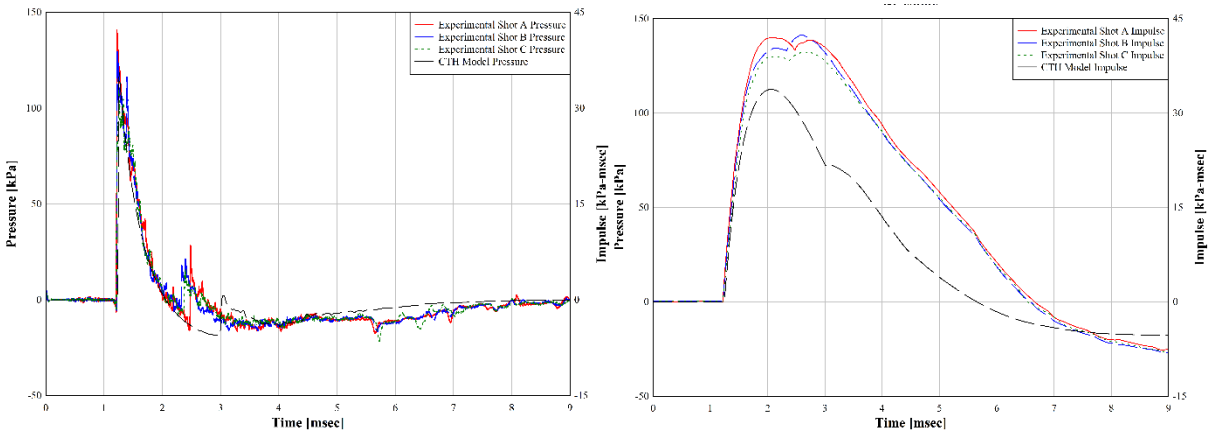

Tracer 6

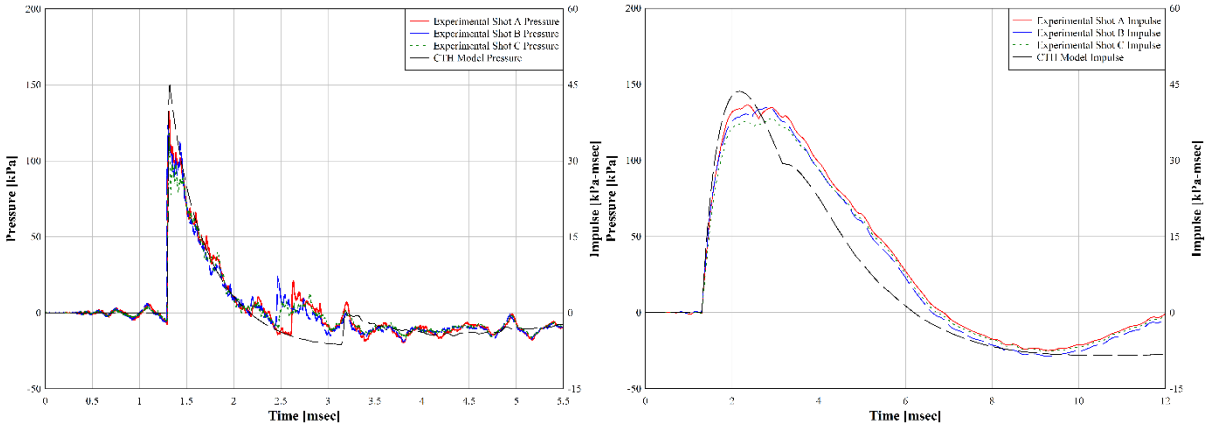

Tracer 7

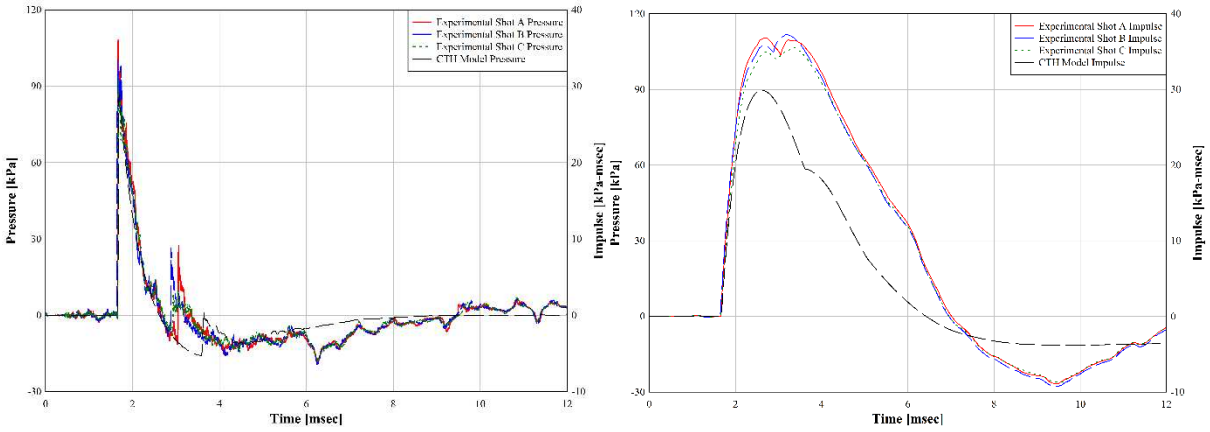

Tracer 8

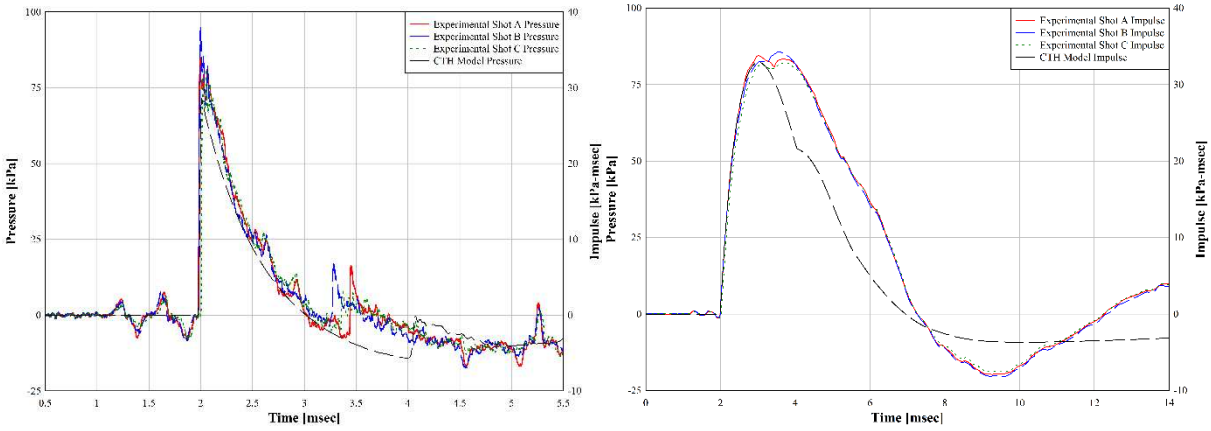

EXPERIMENT 2 -FF

Tracer 1

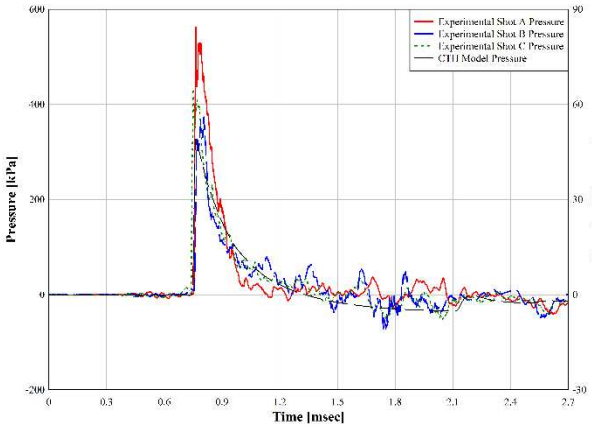

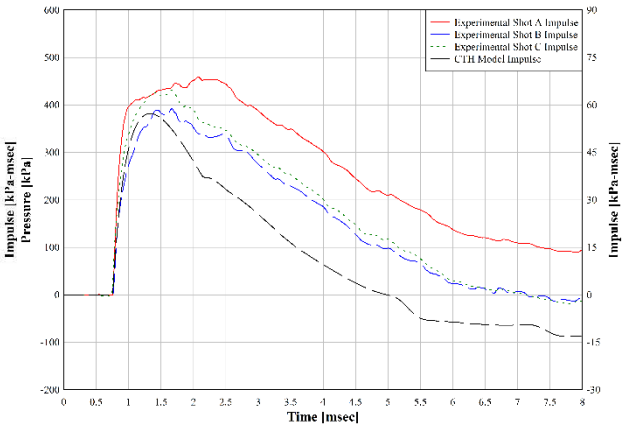

Tracer 2

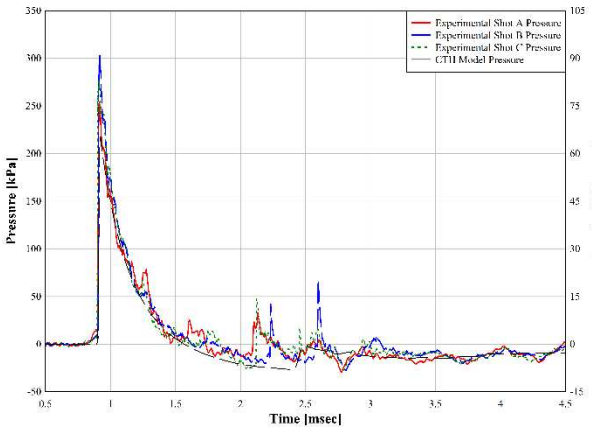

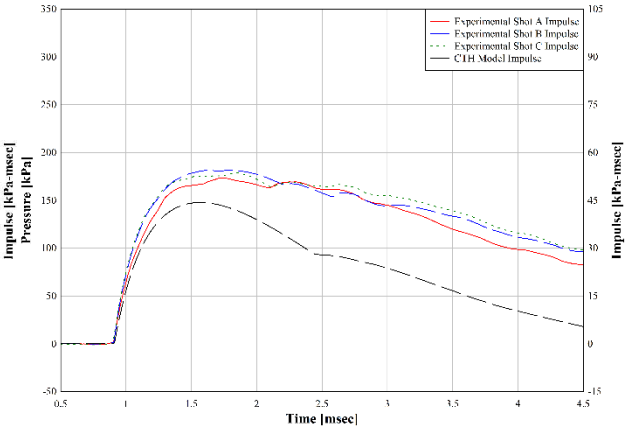

Tracer 3

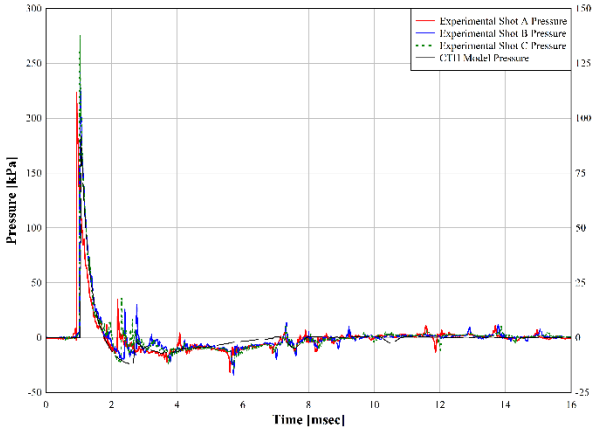

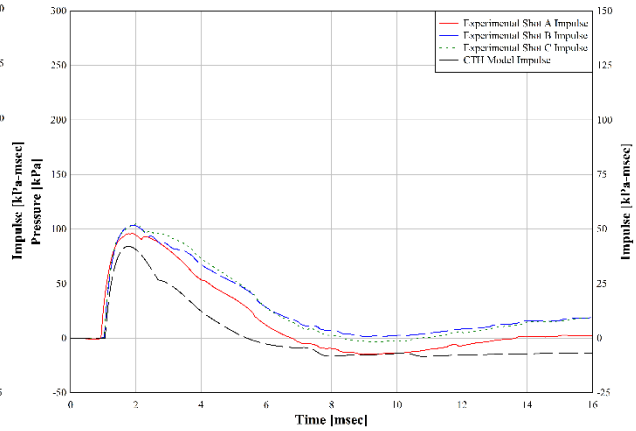

Tracer 4

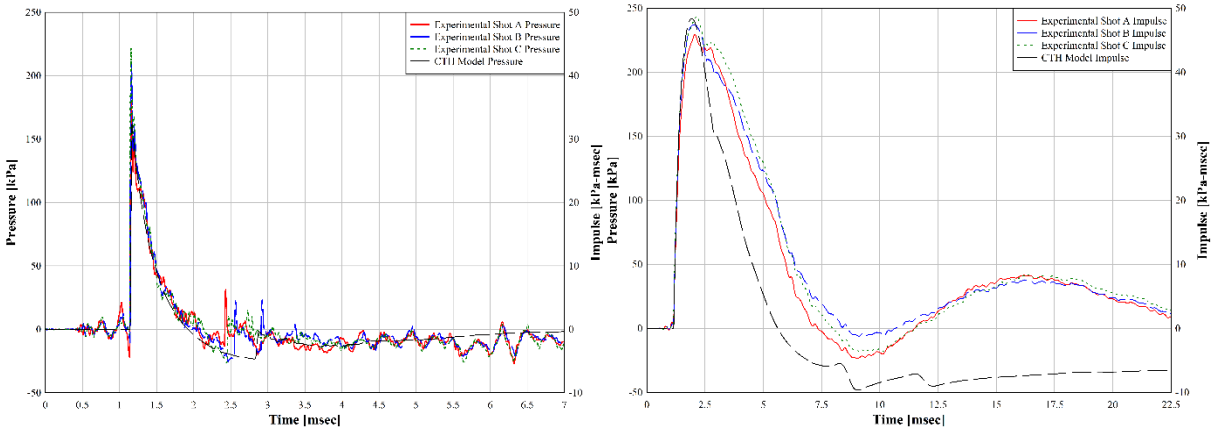

Tracer 5

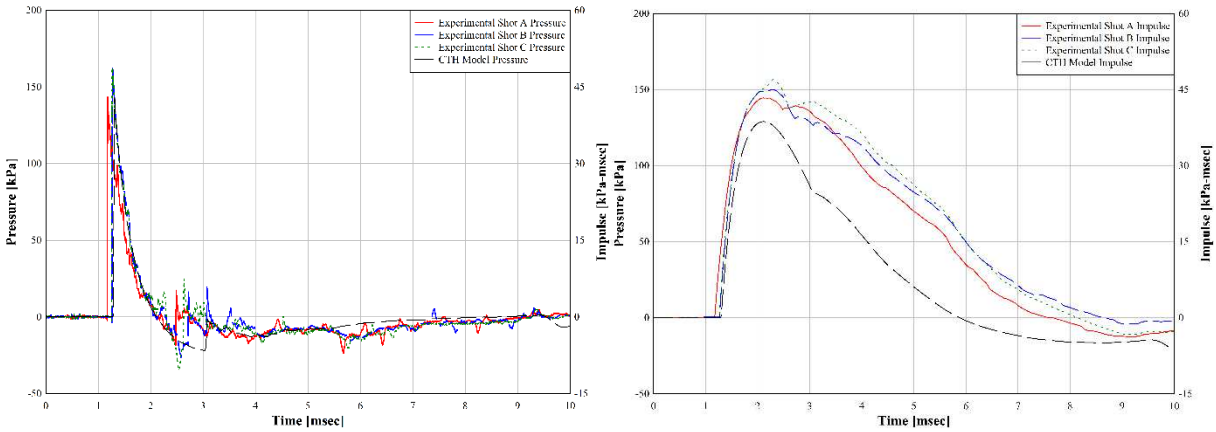

Tracer 6

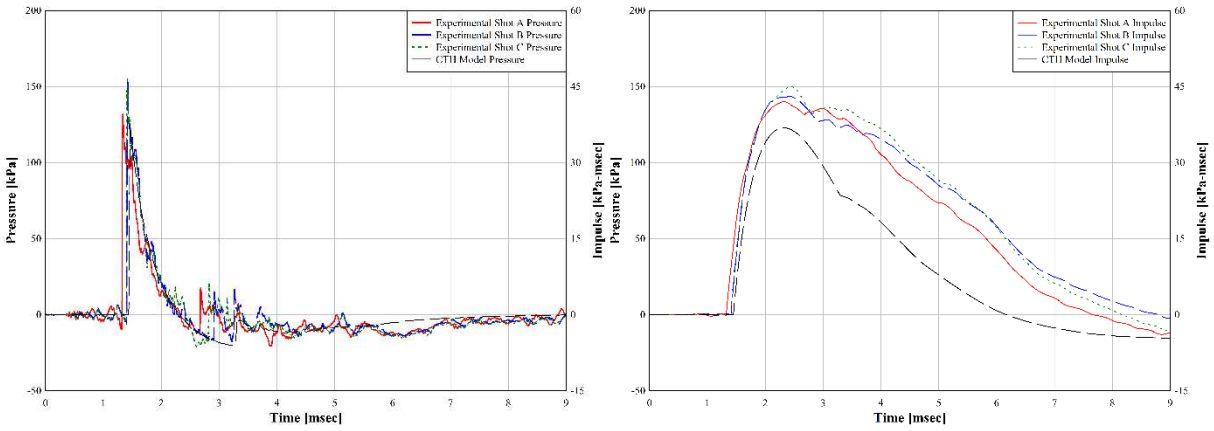

Tracer 7

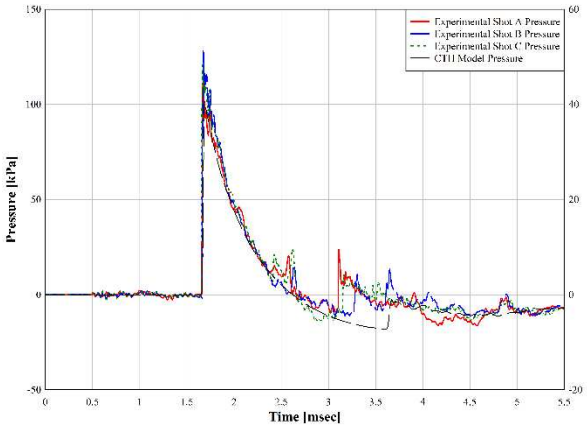

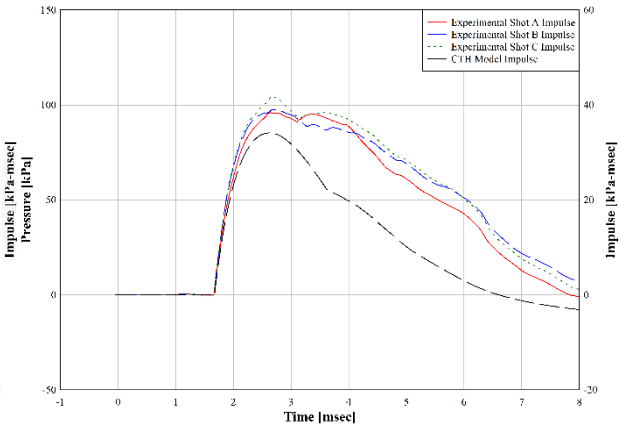

Tracer 8

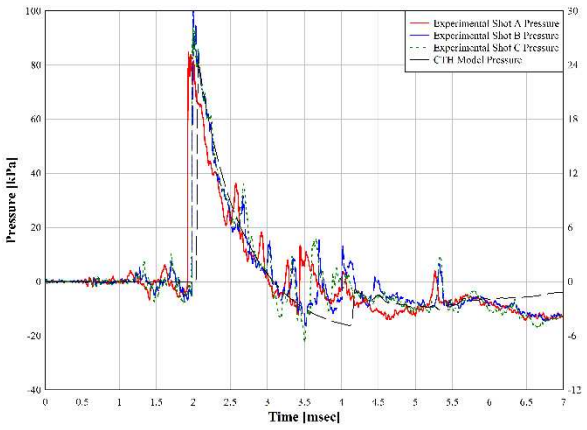

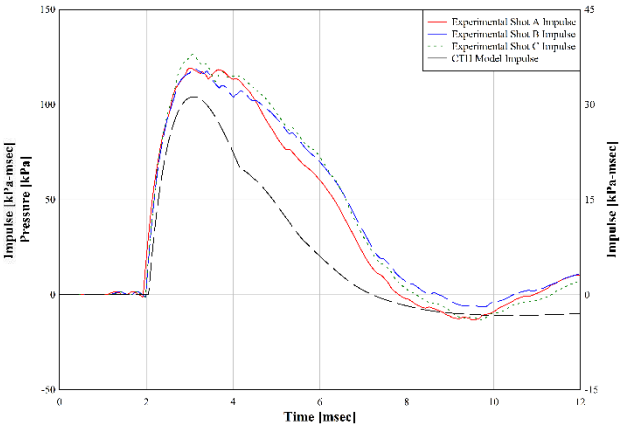

EXPERIMENT 3

Tracer 1

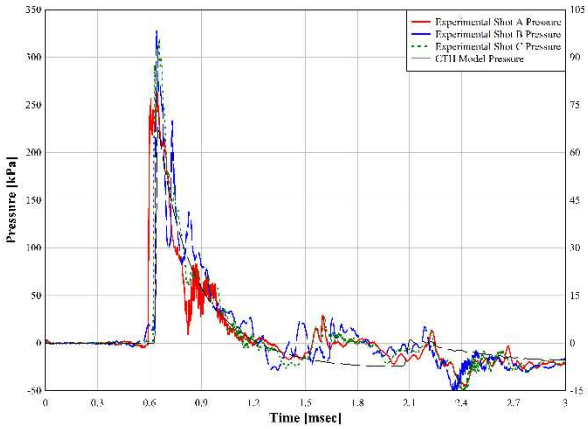

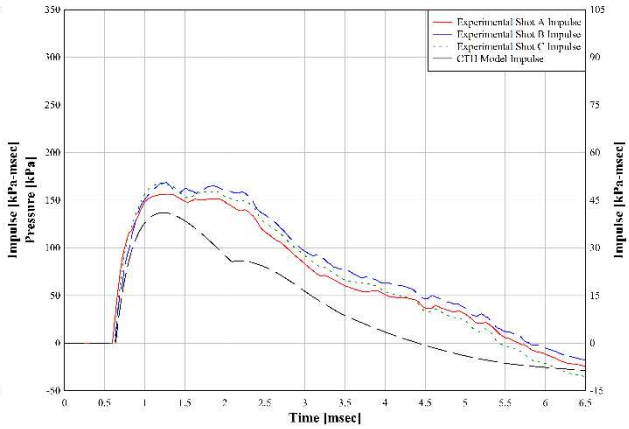

Tracer 2

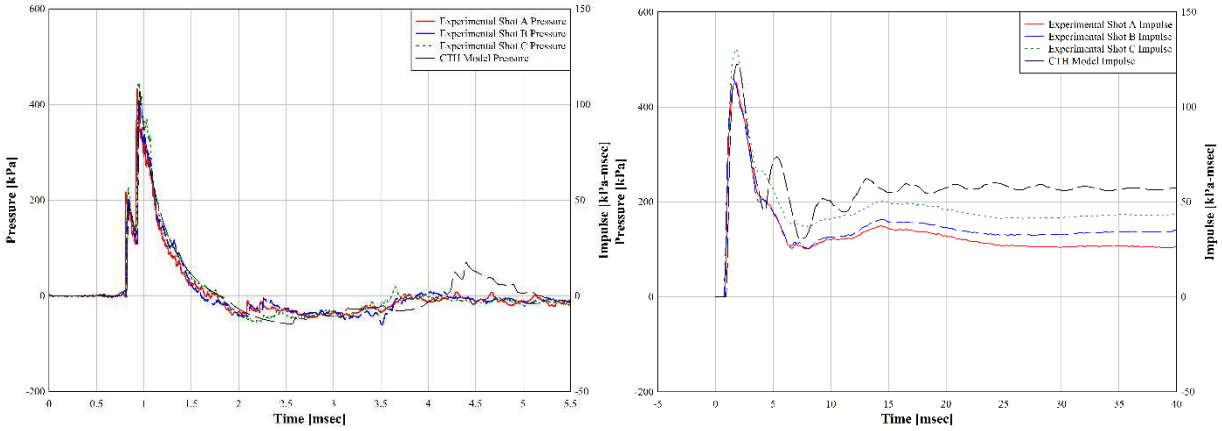

Tracer 3

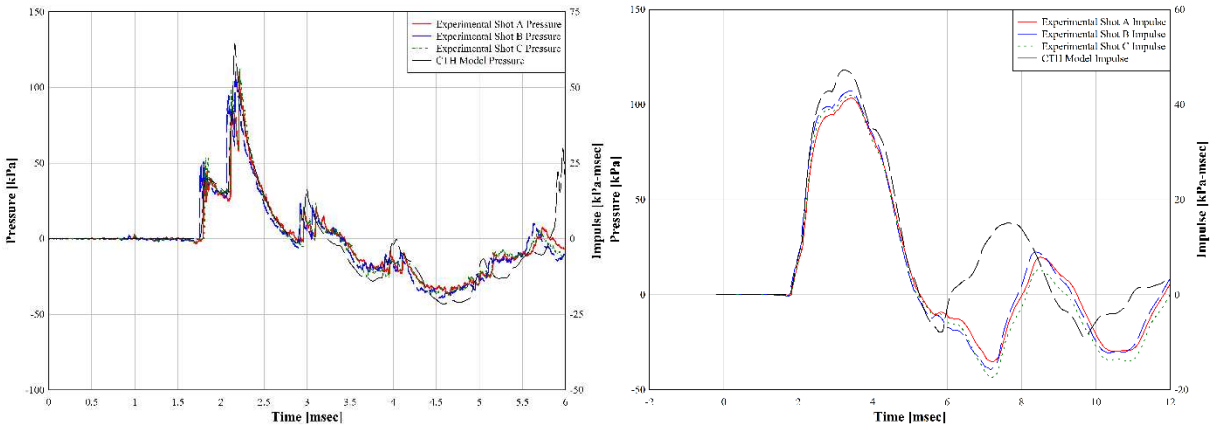

Tracer 4

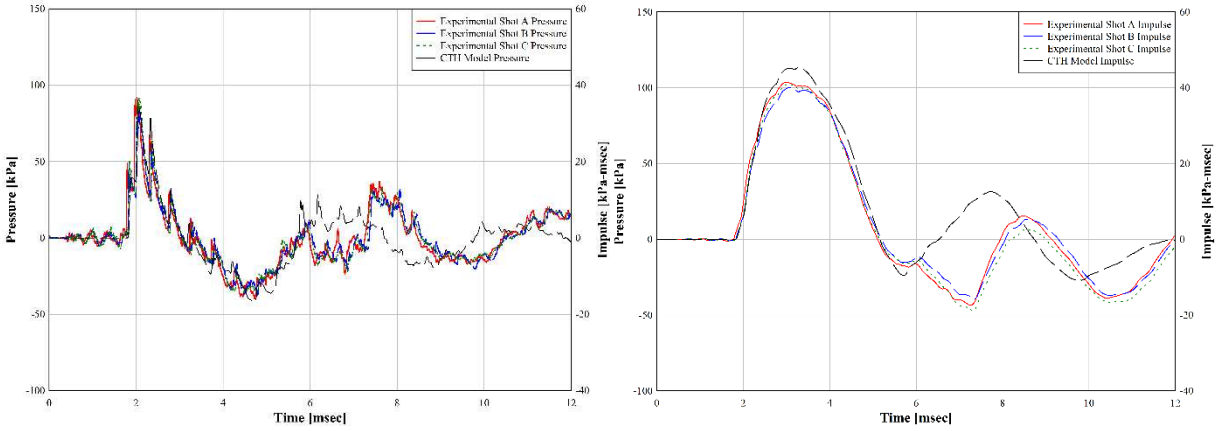

Tracer 5

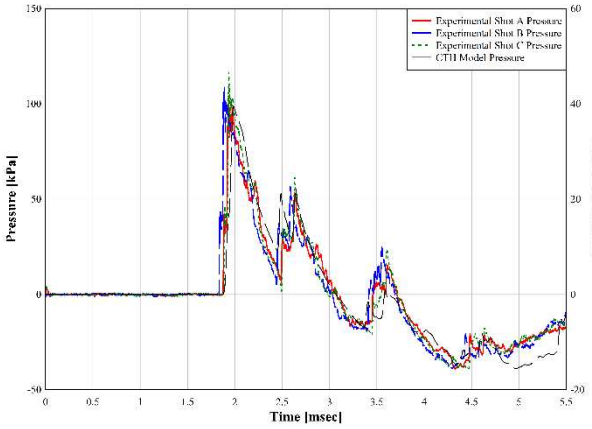

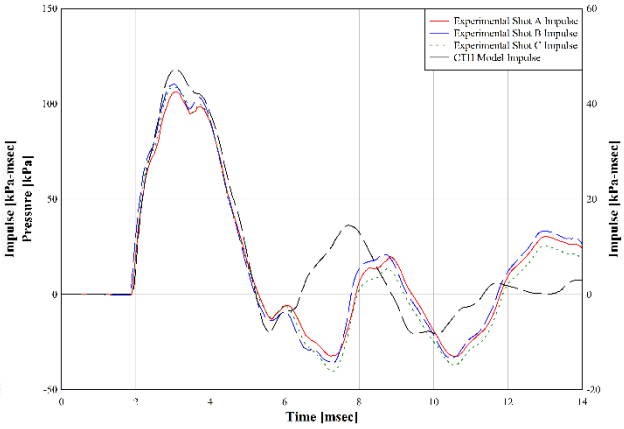

Tracer 6

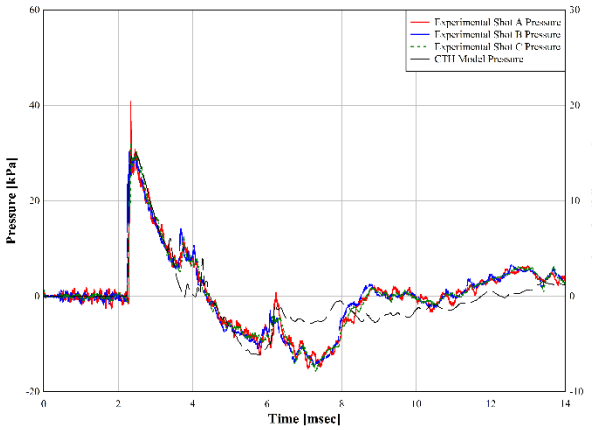

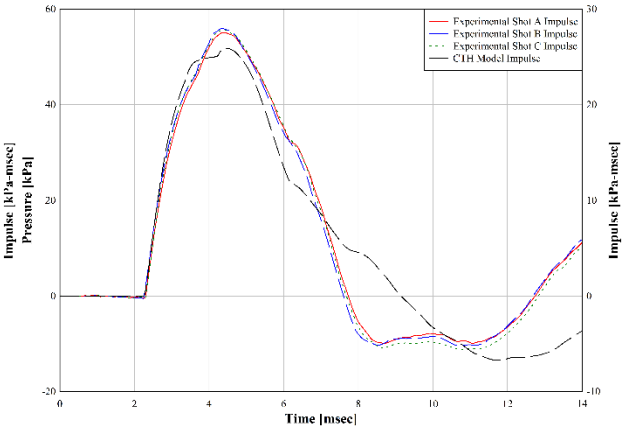

Tracer 7

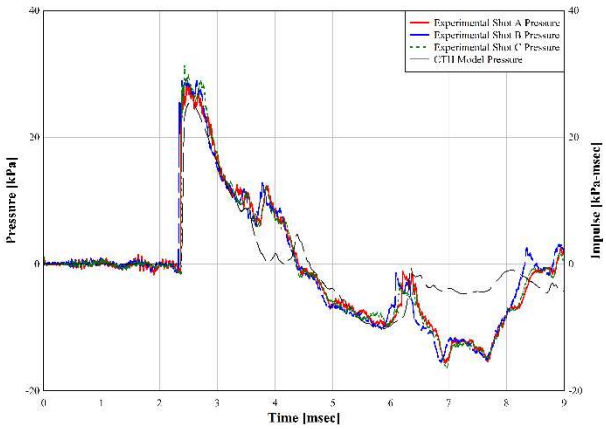

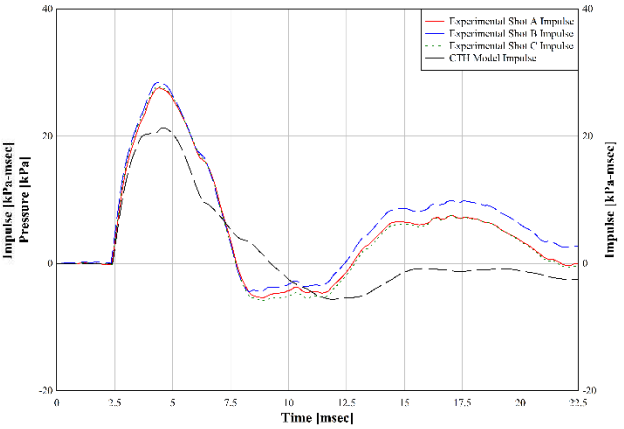

Tracer 8

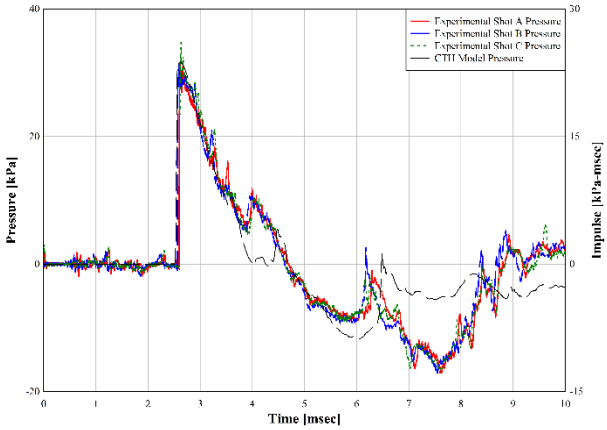

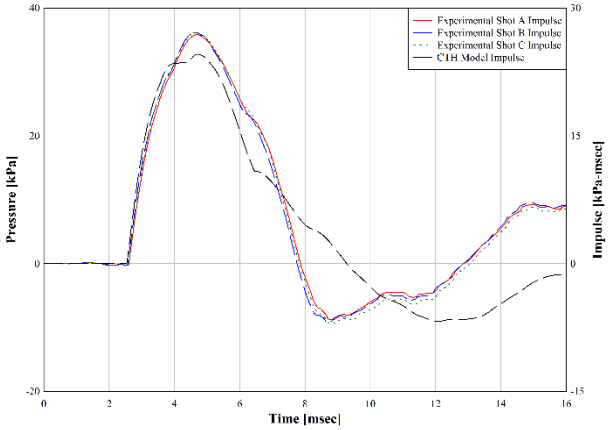

EXPERIMENT 4

Tracer 1

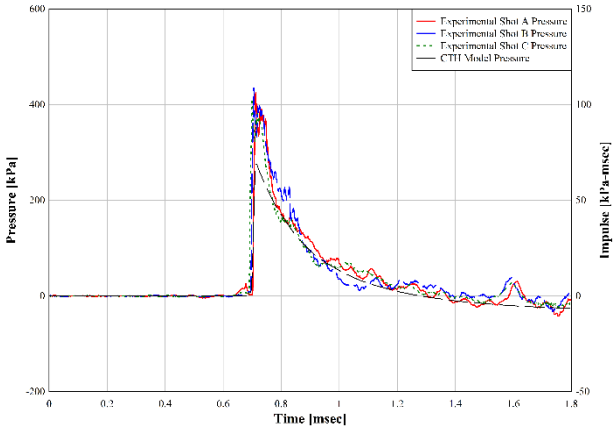

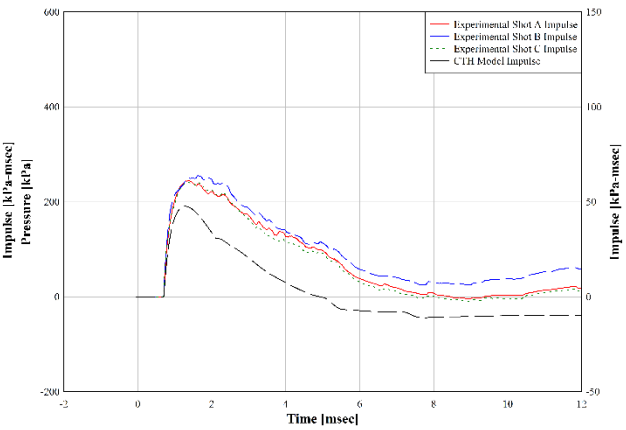

Tracer 2

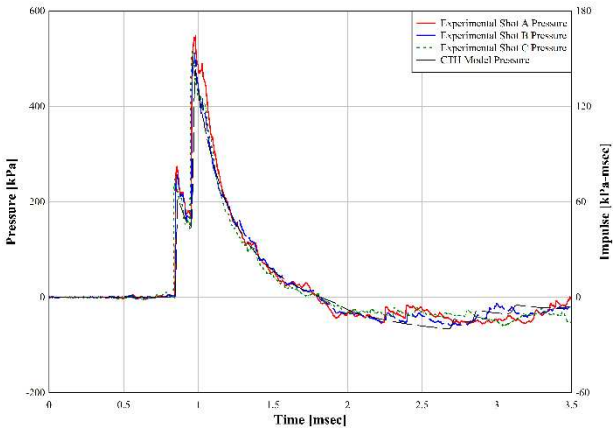

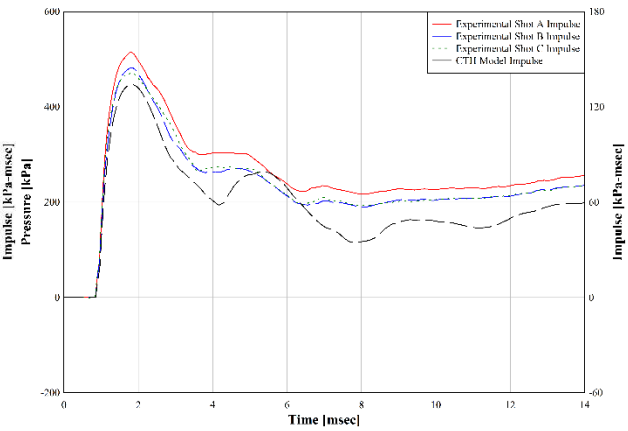

Tracer 3

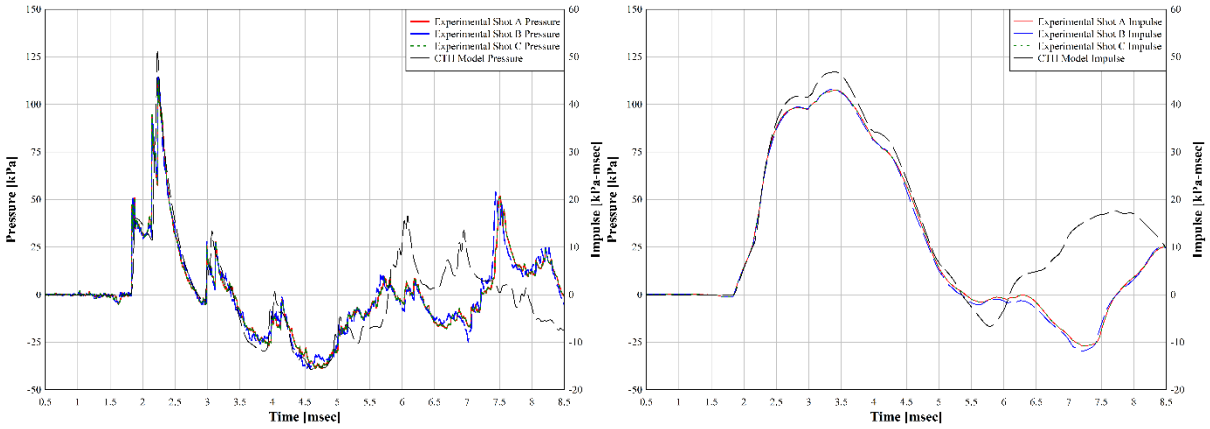

Tracer 4

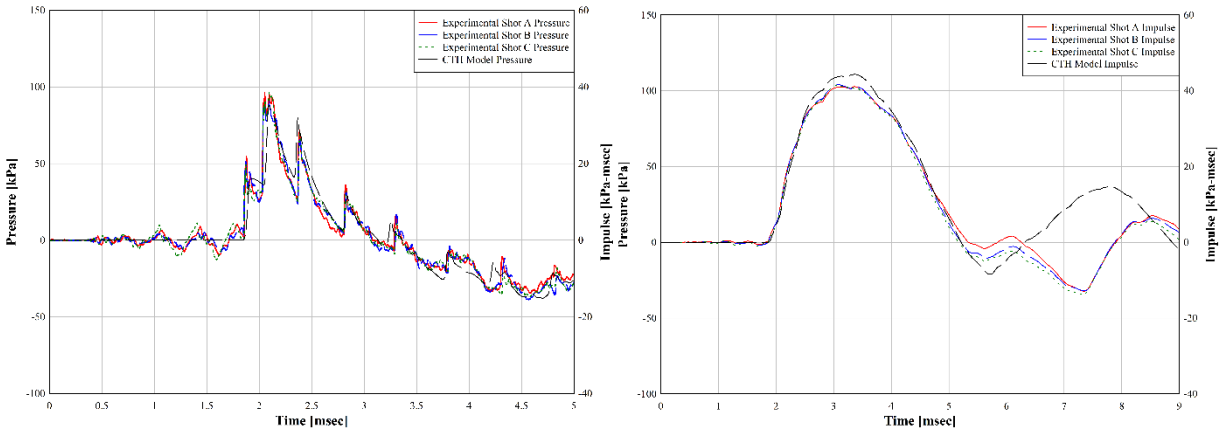

Tracer 5

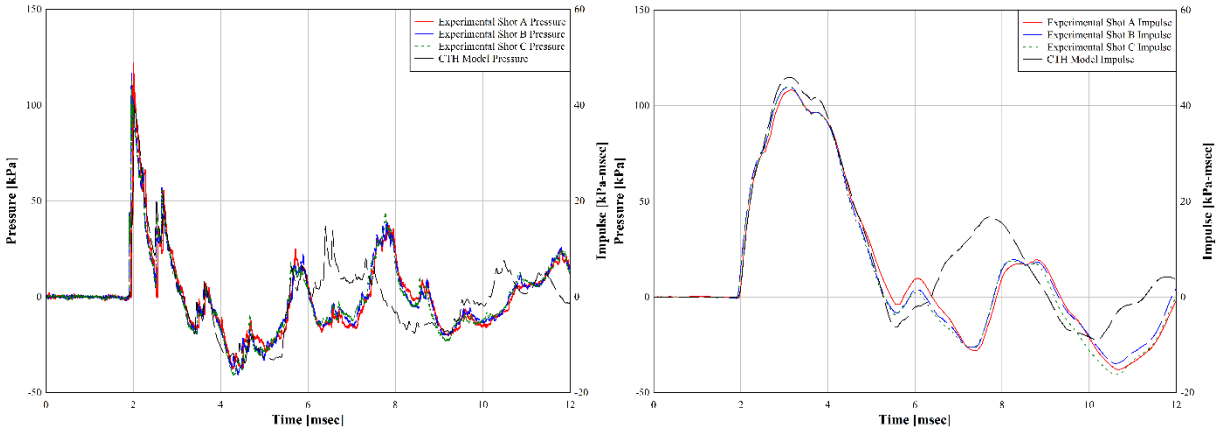

Tracer 6

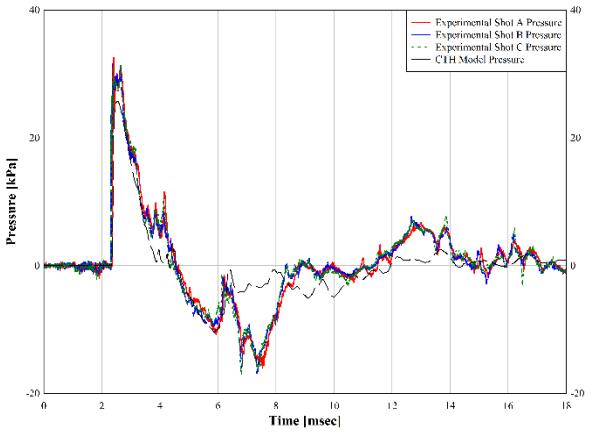

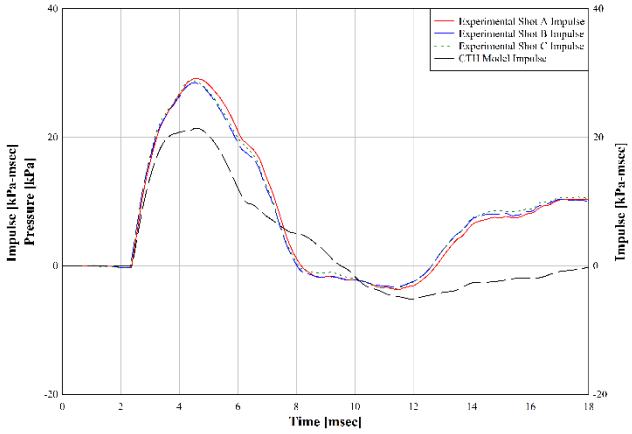

Tracer 7

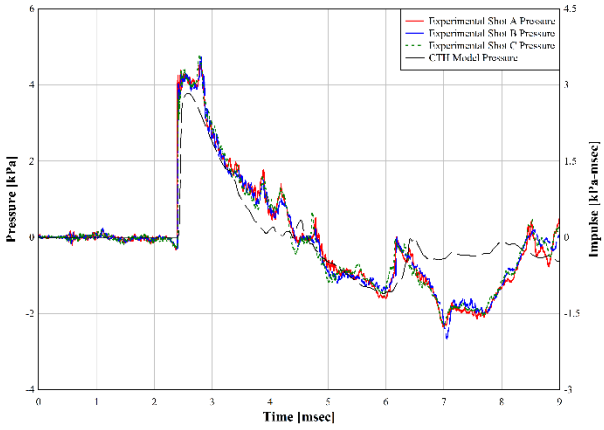

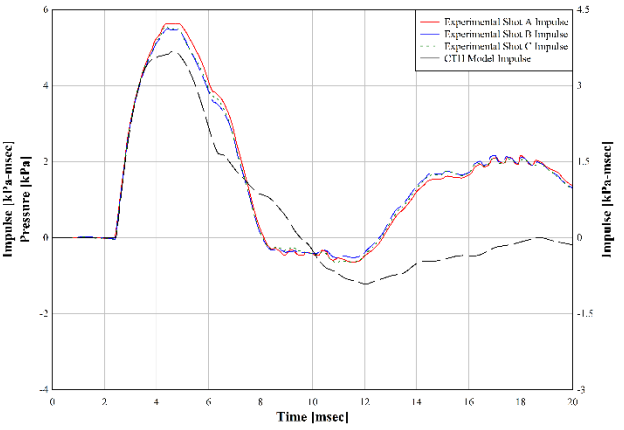

Tracer 8

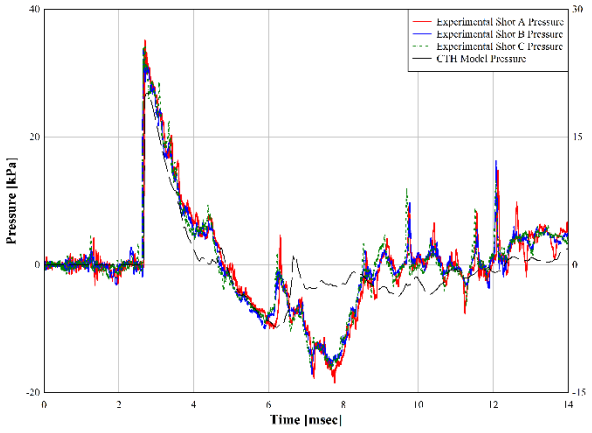

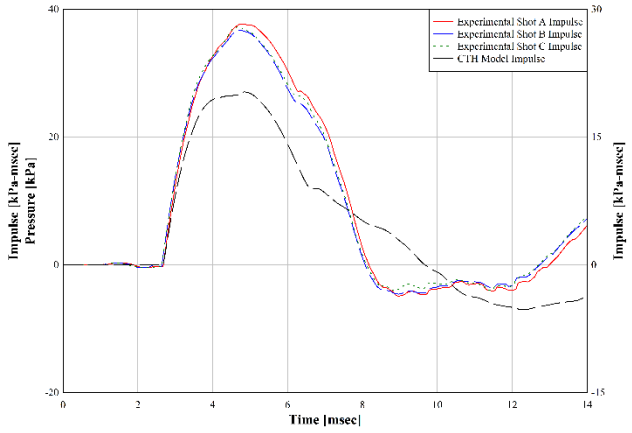

EXPERIMENT 5-FF

Tracer 1

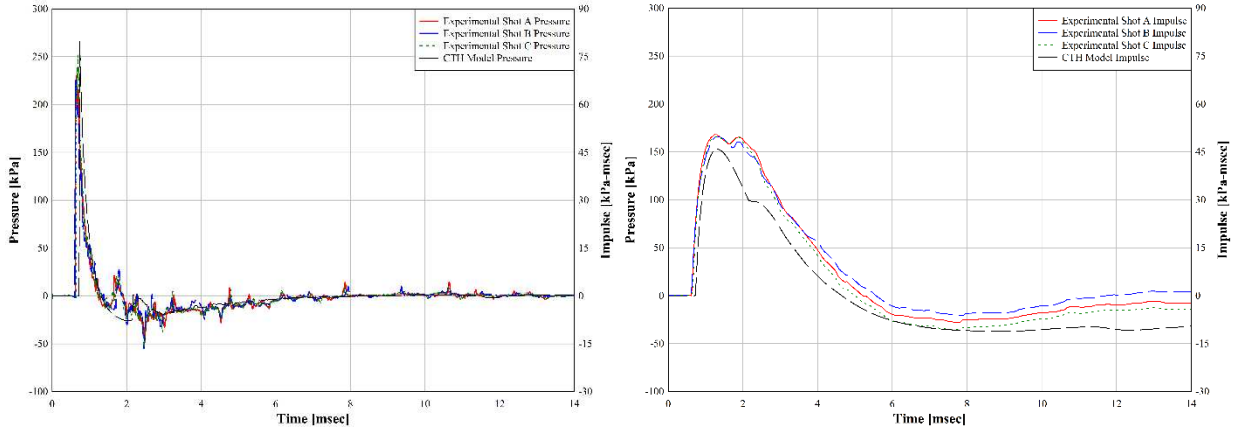

Tracer 2

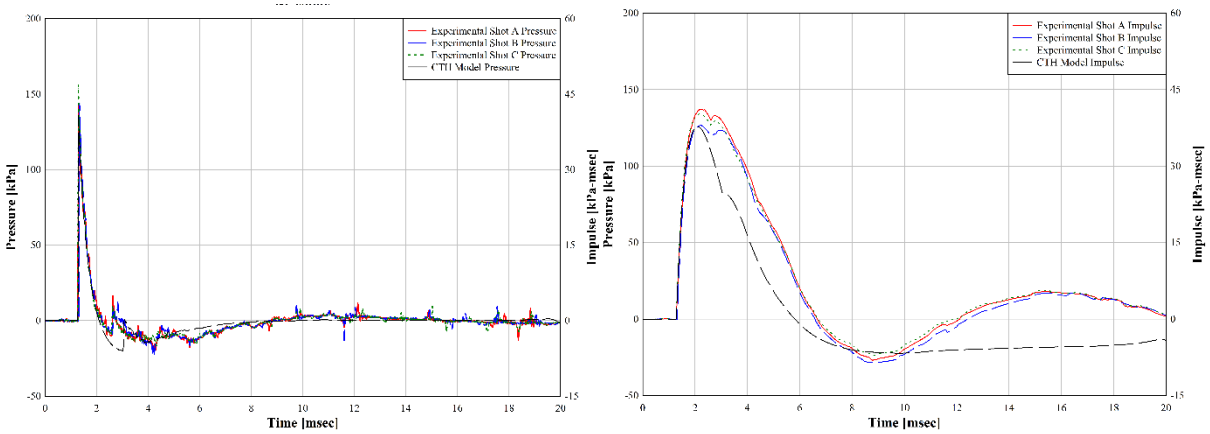

Tracer 3

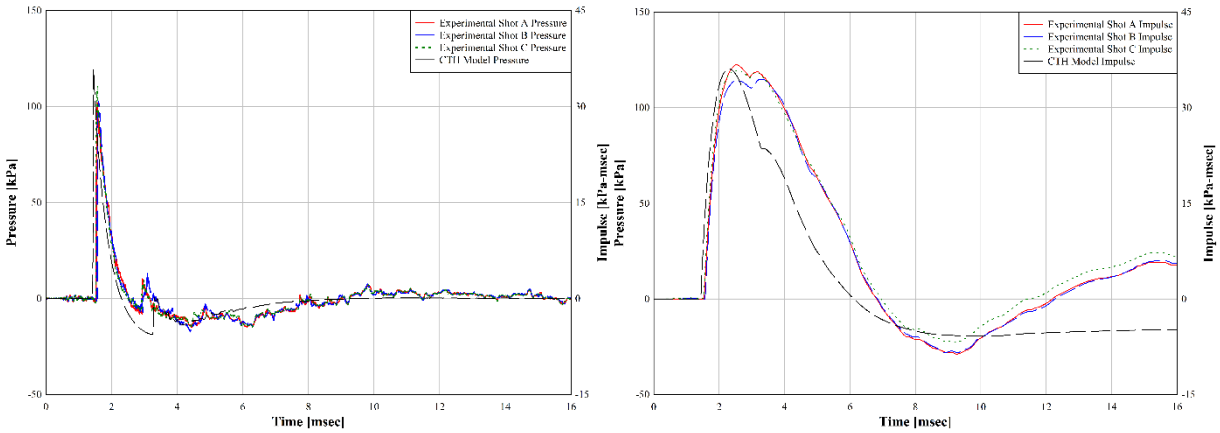

Tracer 4

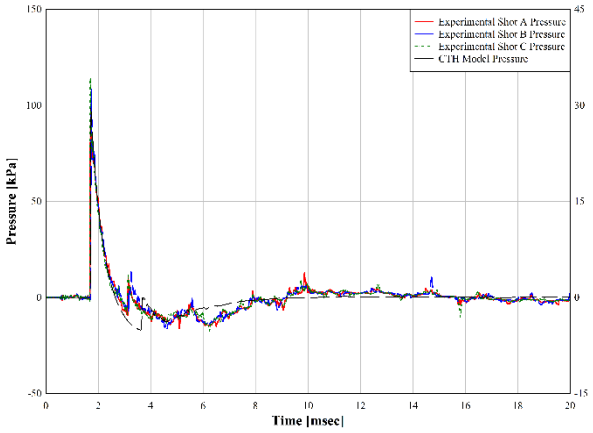

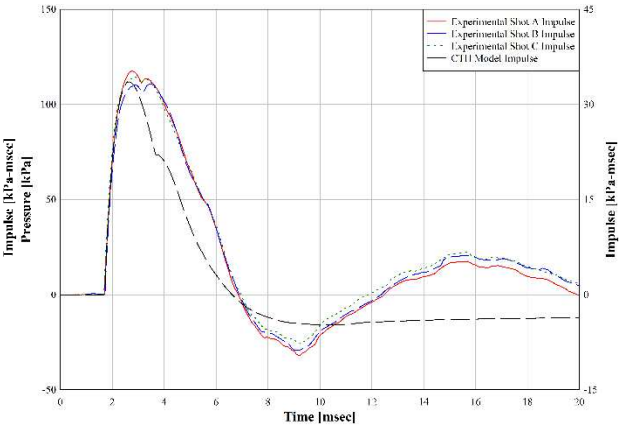

Tracer 5

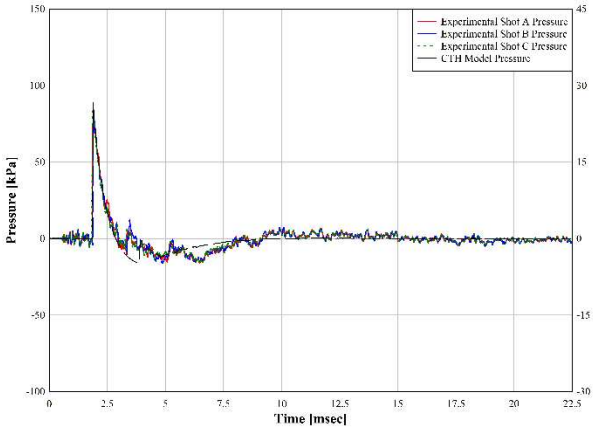

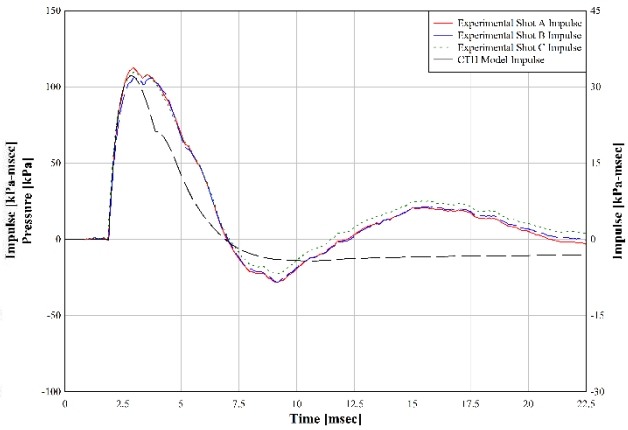

Tracer 6

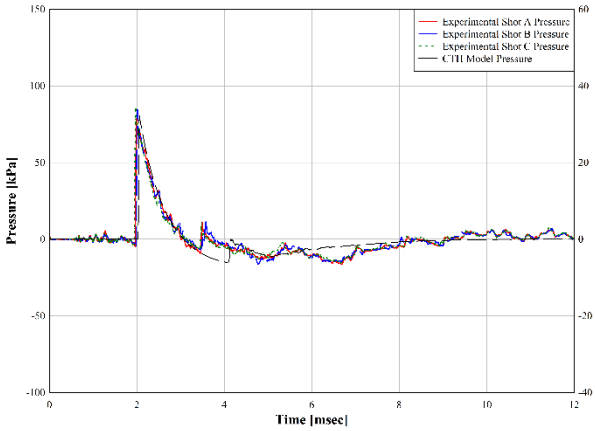

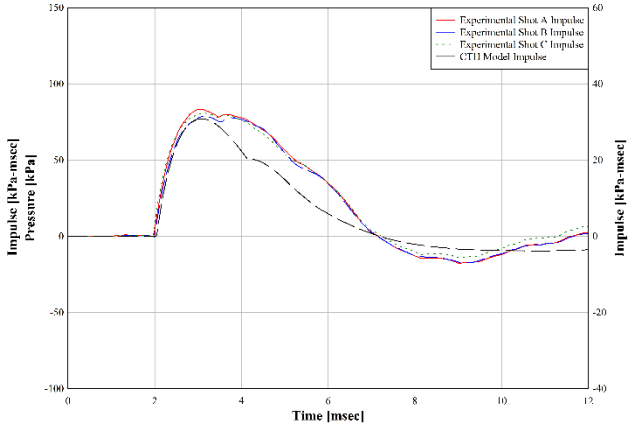

Tracer 7

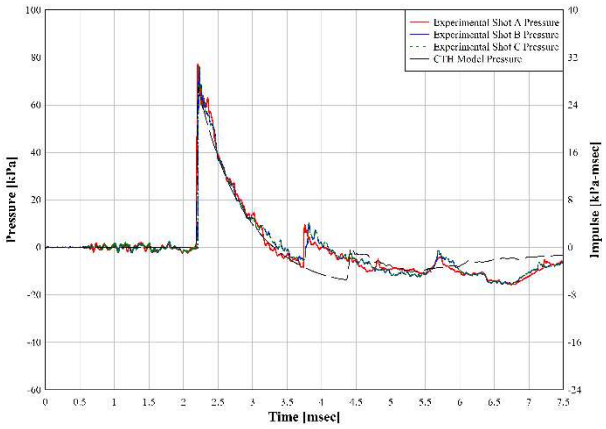

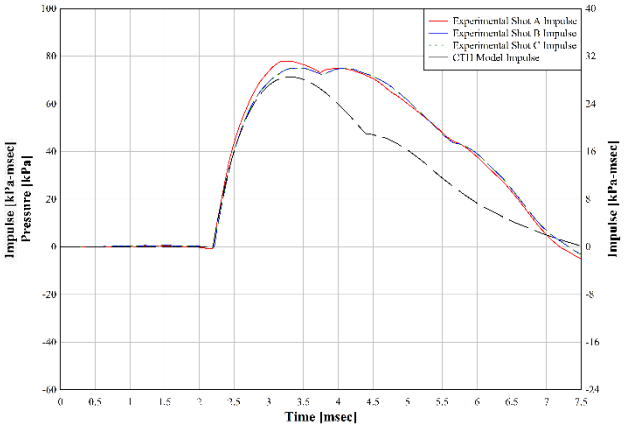

Tracer 8

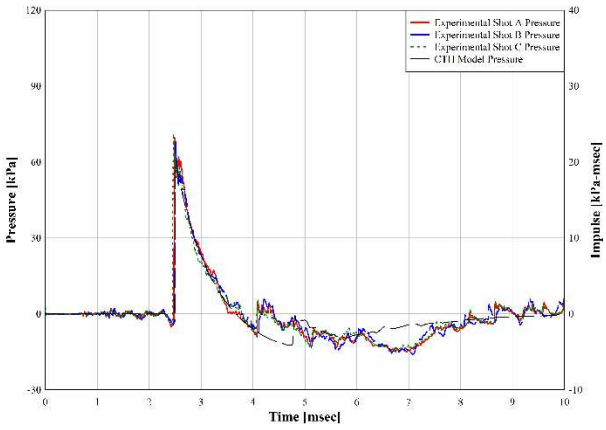

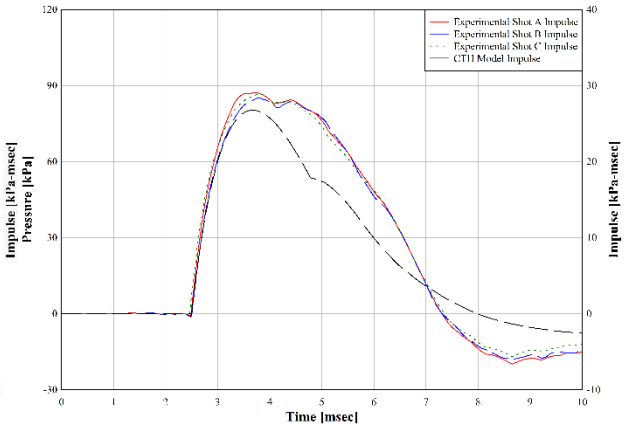

EXPERIMENT 6

Tracer 1

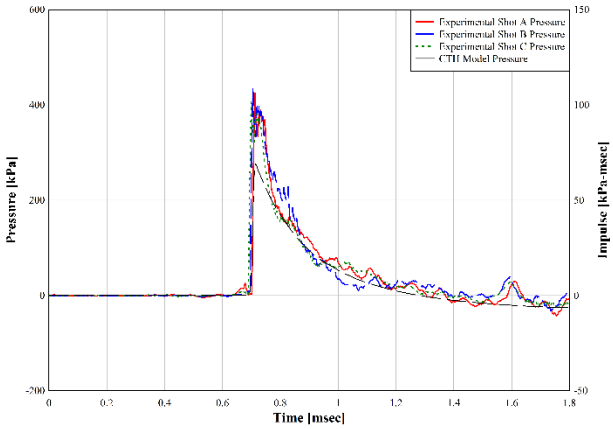

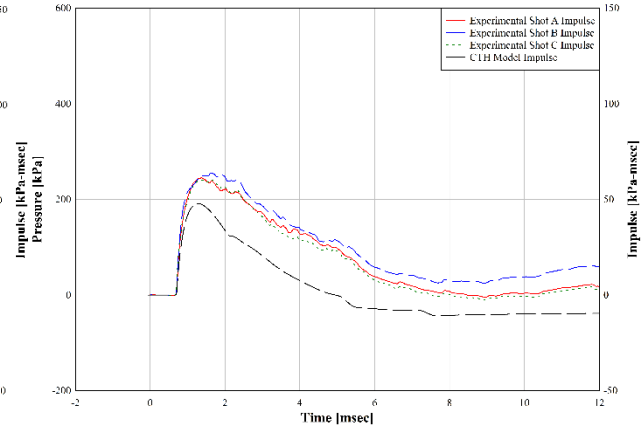

Tracer 2

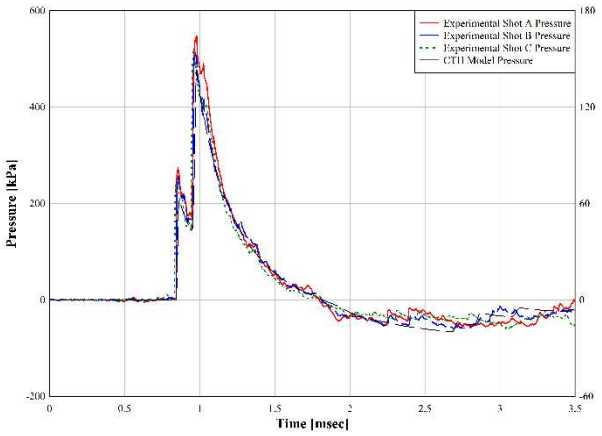

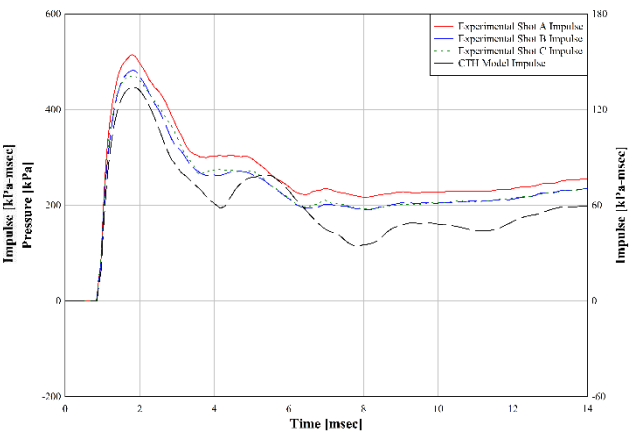

Tracer 3

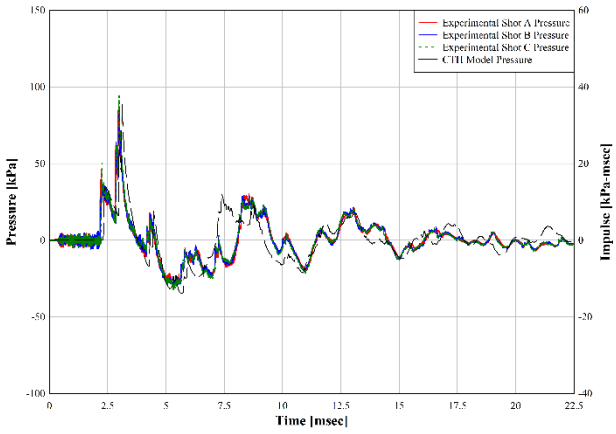

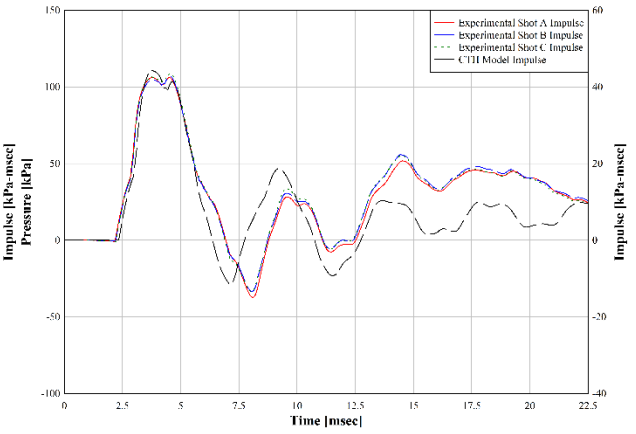

Tracer 4

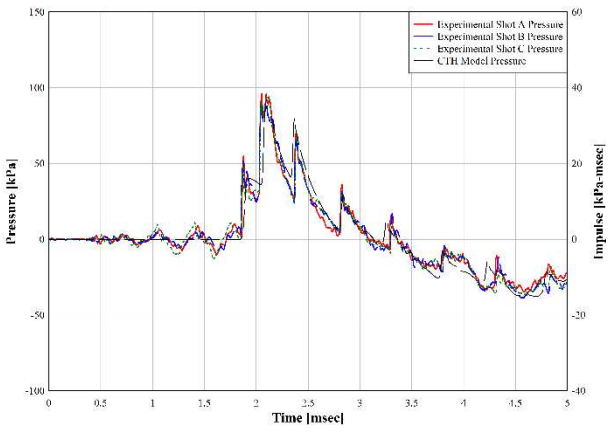

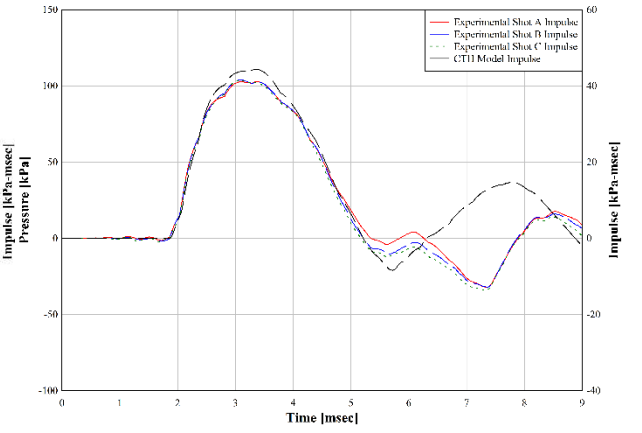

Tracer 5

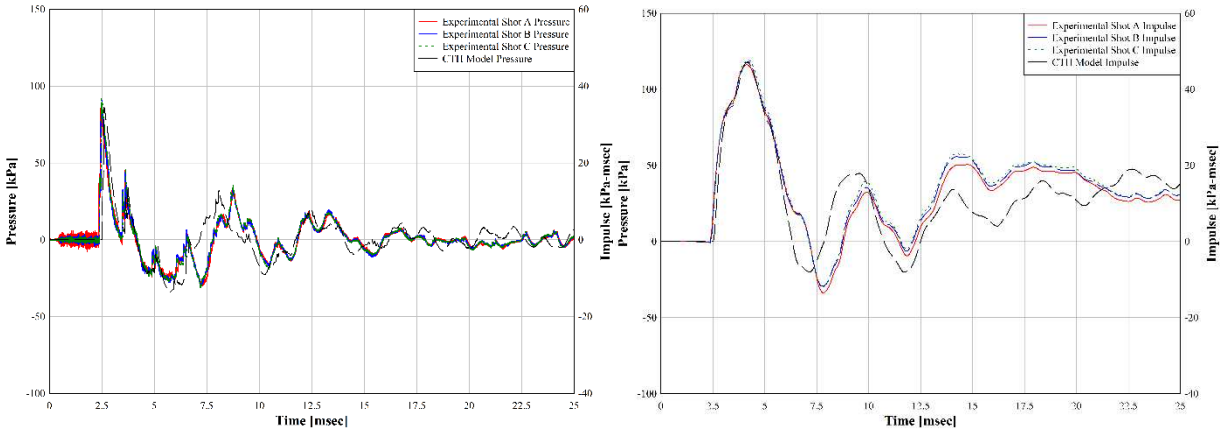

Tracer 6

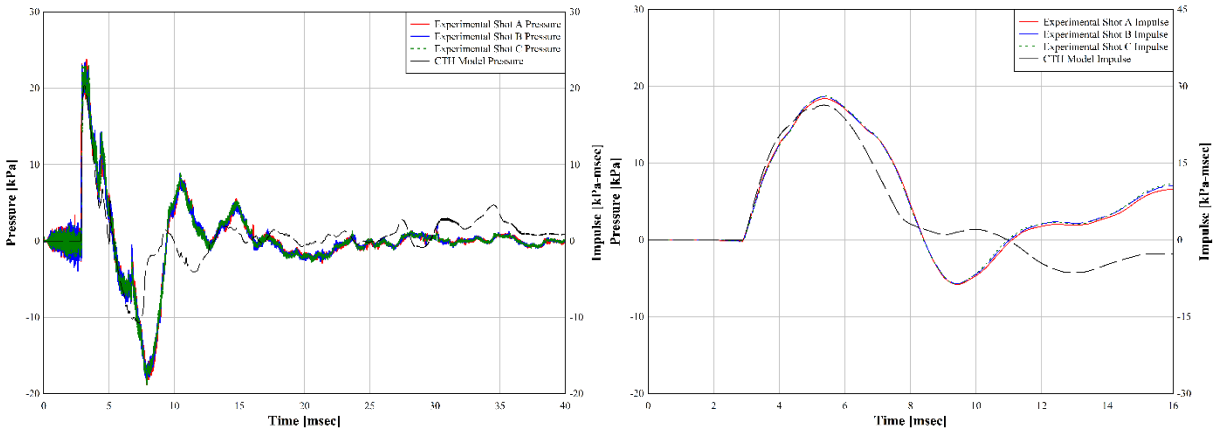

Tracer 7

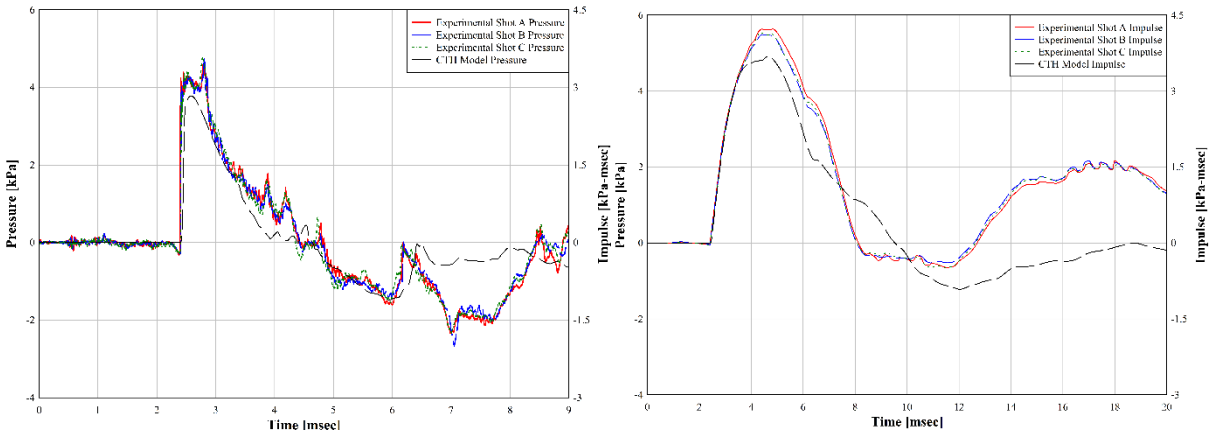

Tracer 8

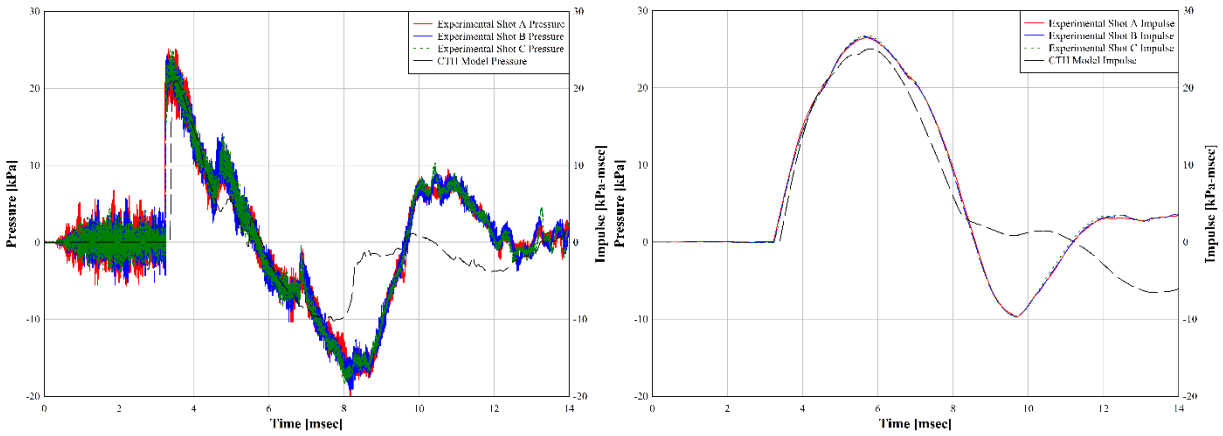

EXPERIMENT 7-FF

Tracer 1

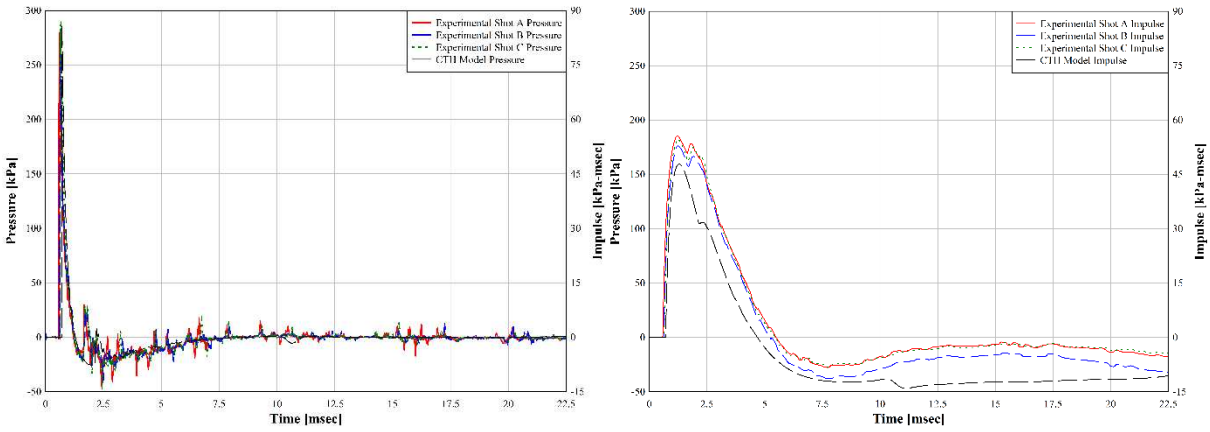

Tracer 2

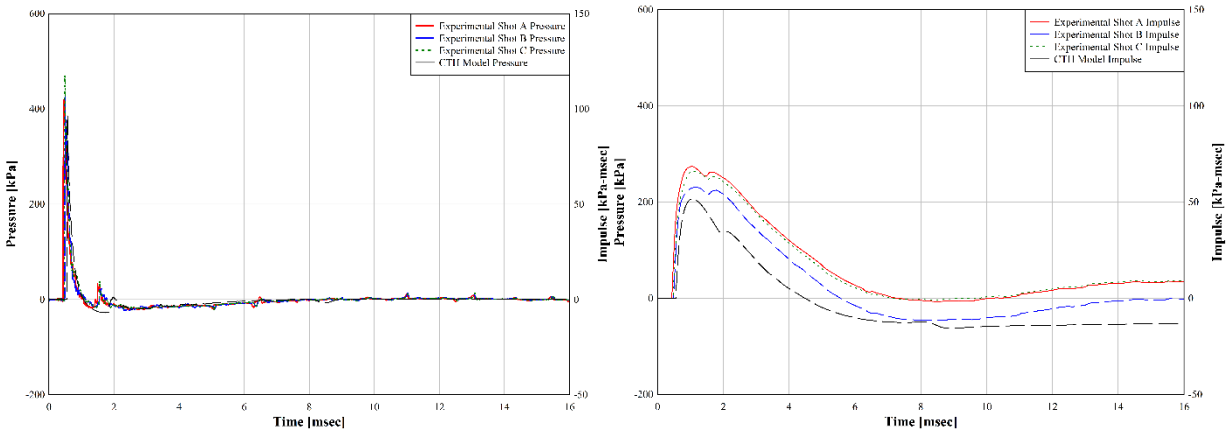

Tracer 3

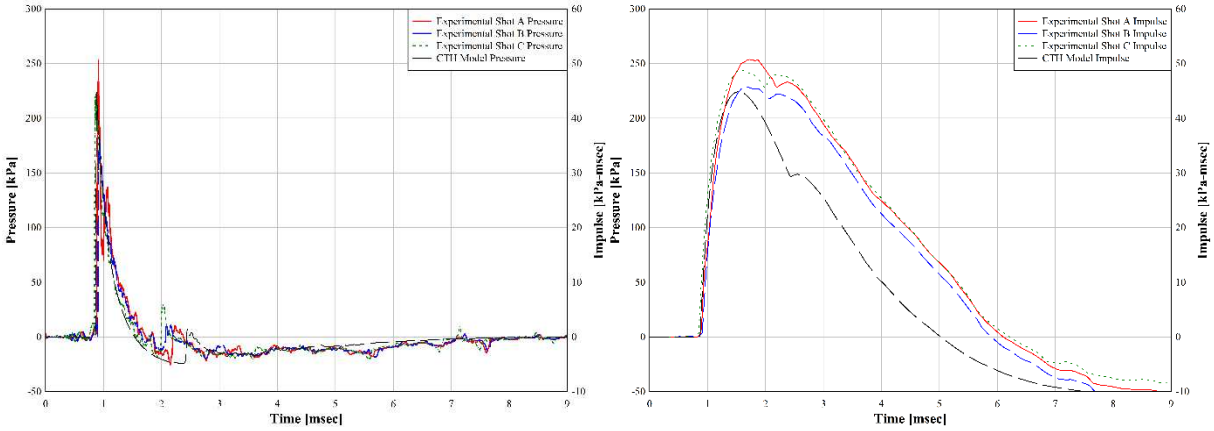

Tracer 4

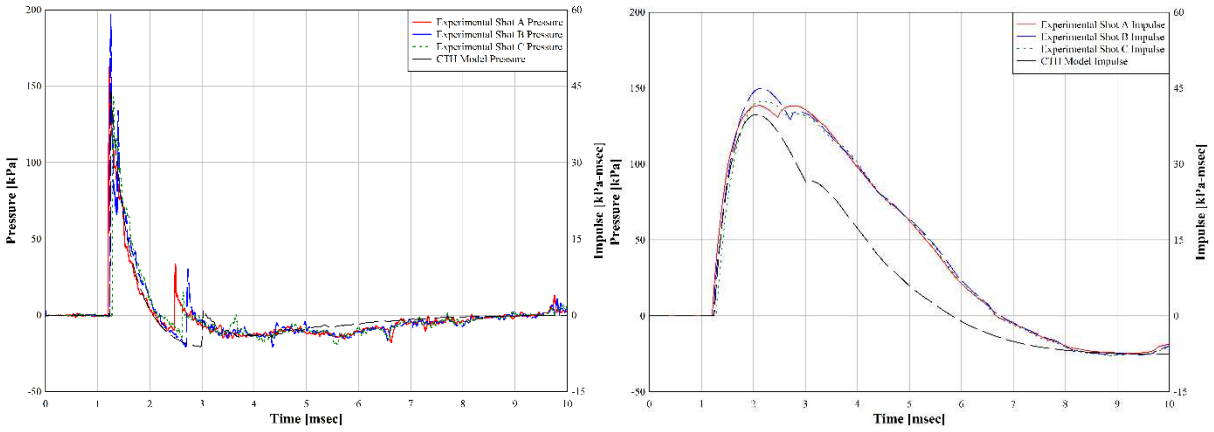

Tracer 5

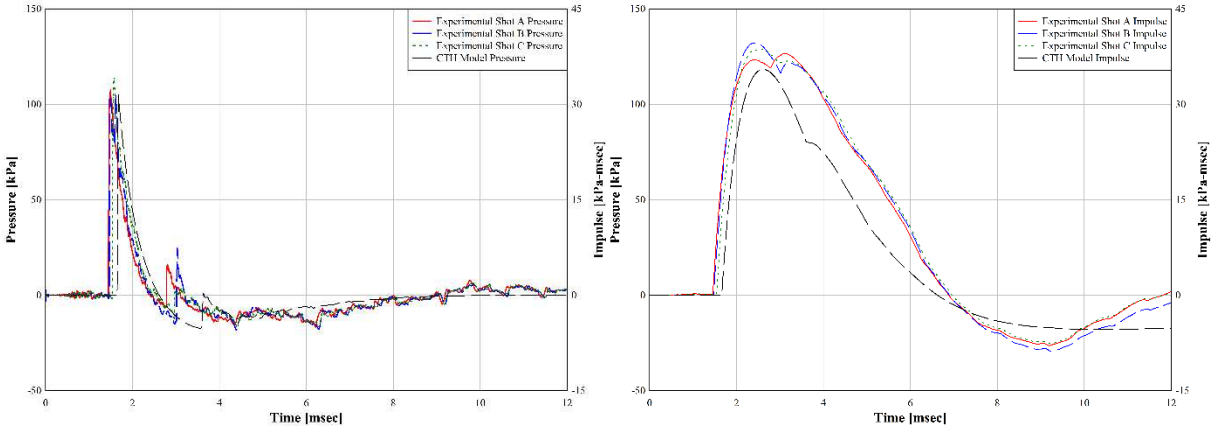

Tracer 6

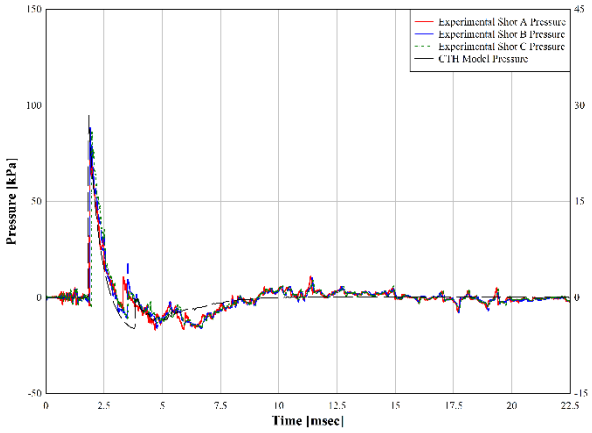

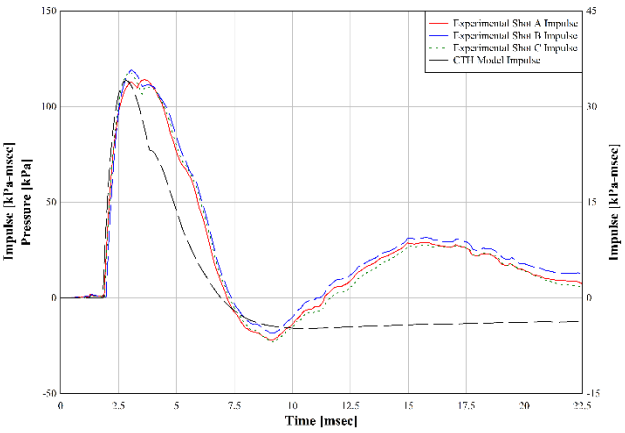

Tracer 7

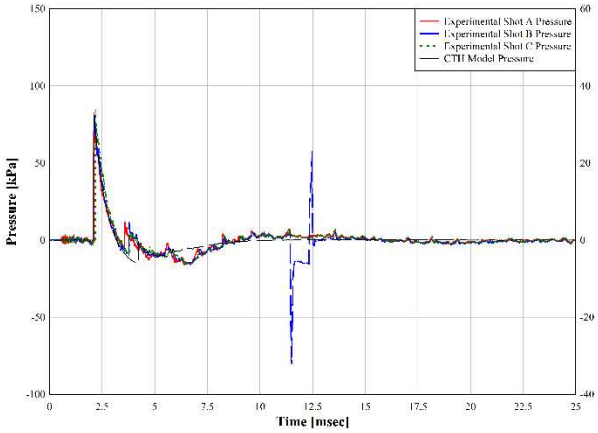

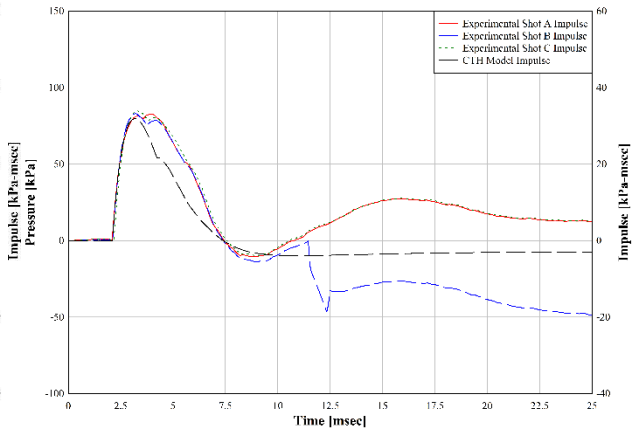

Tracer 8

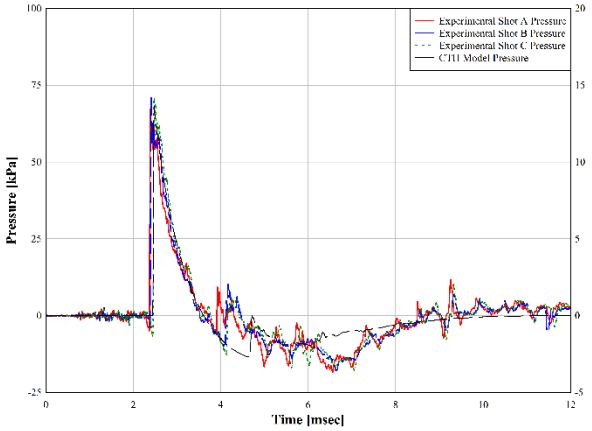

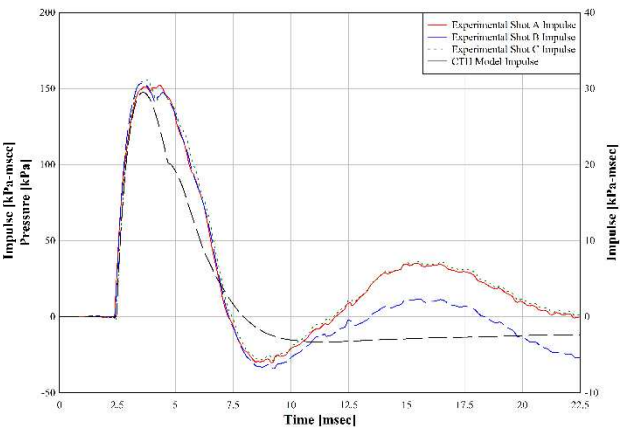

EXPERIMENT 8

Tracer 1

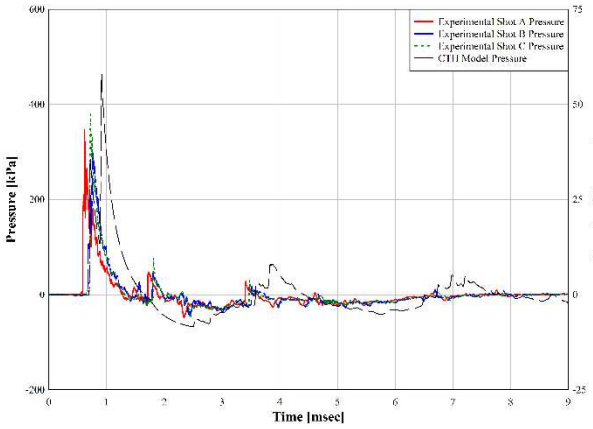

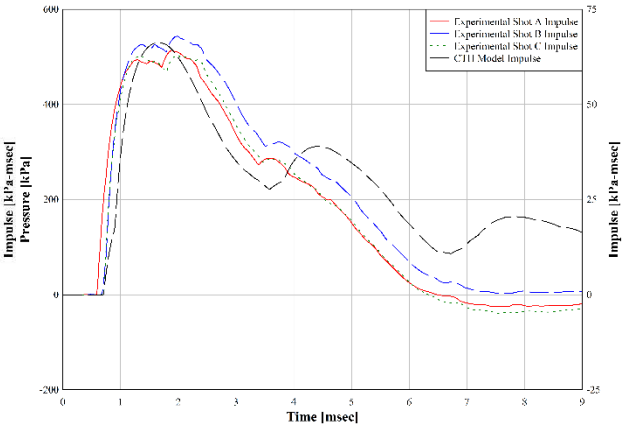

Tracer 2

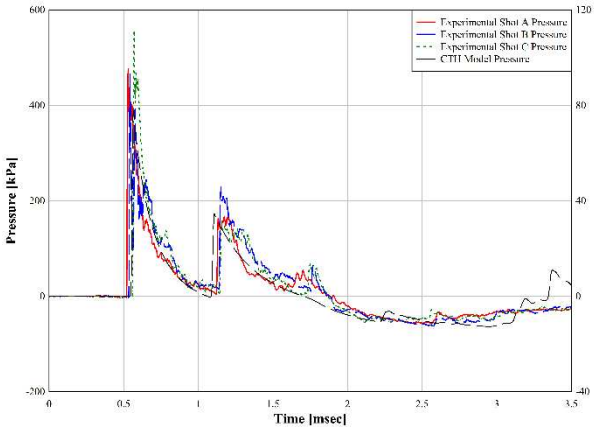

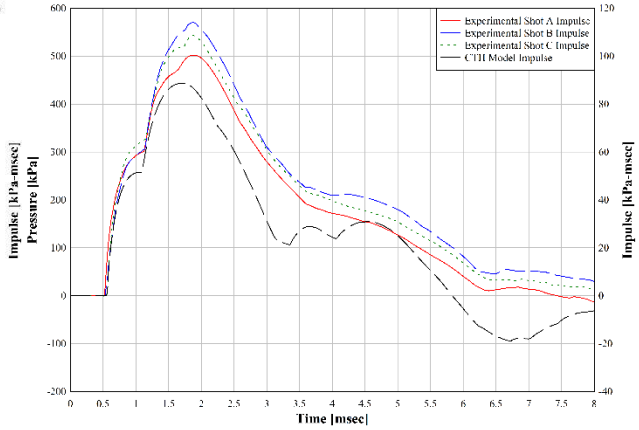

Tracer 3

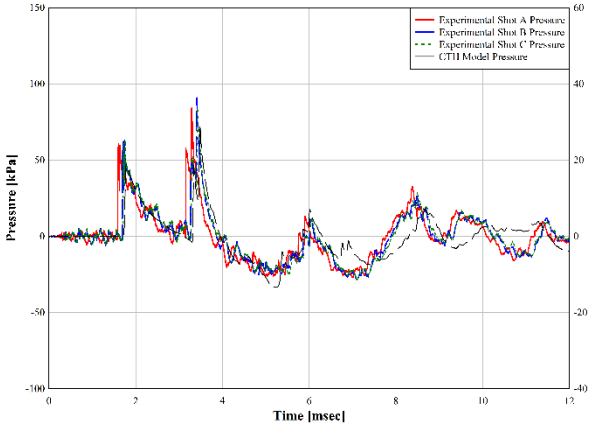

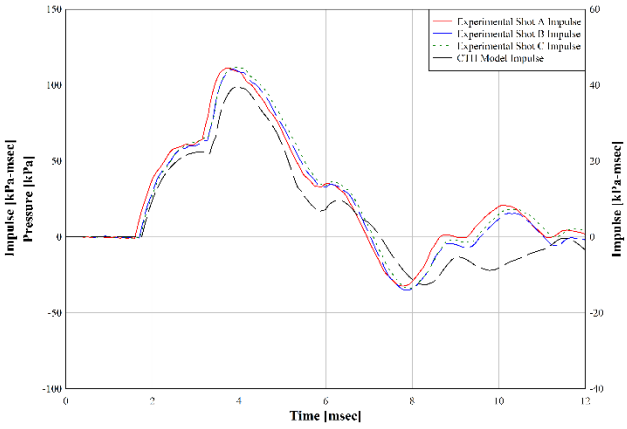

Tracer 4

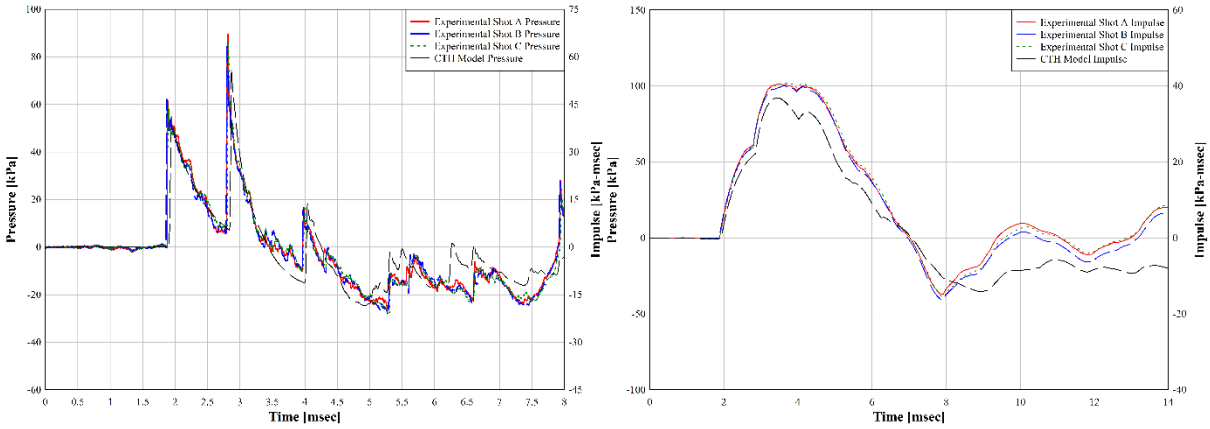

Tracer 5

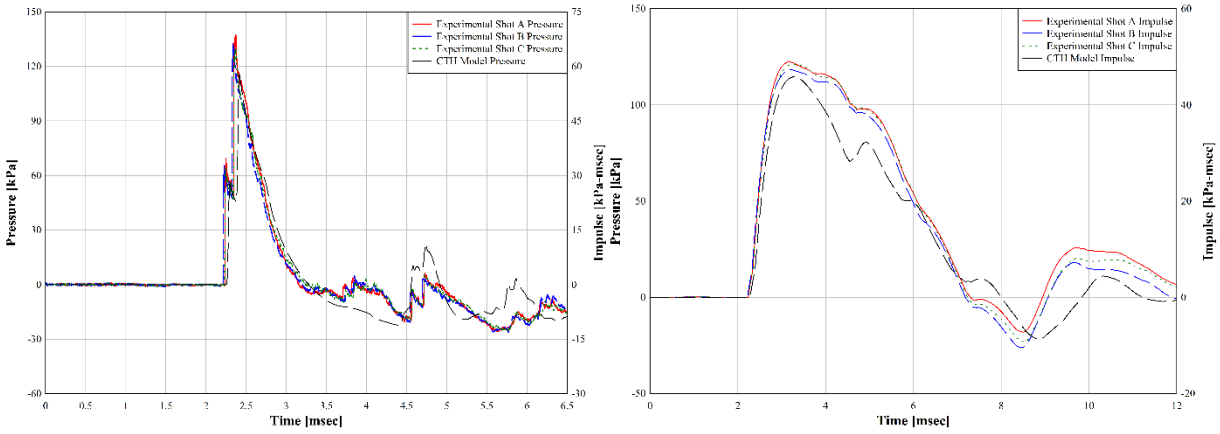

Tracer 6

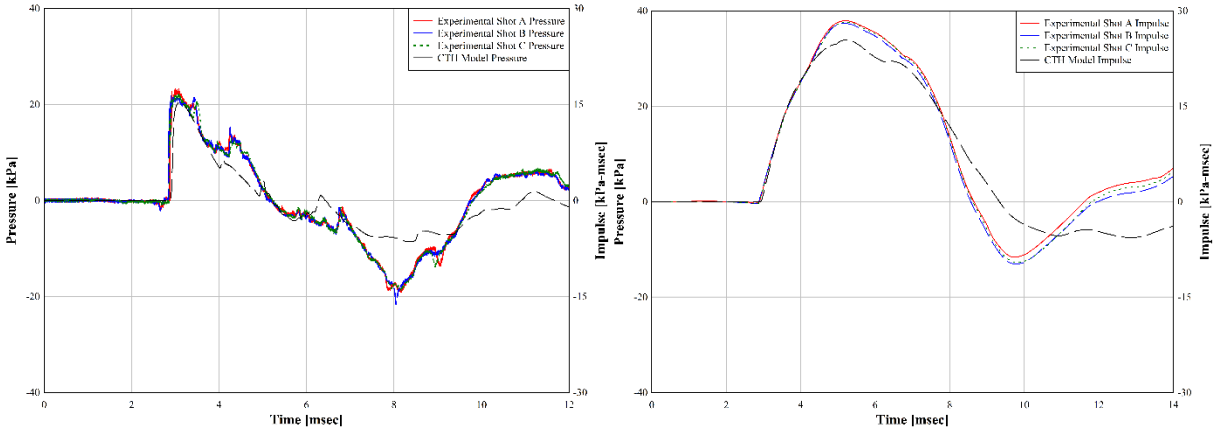

Tracer 7

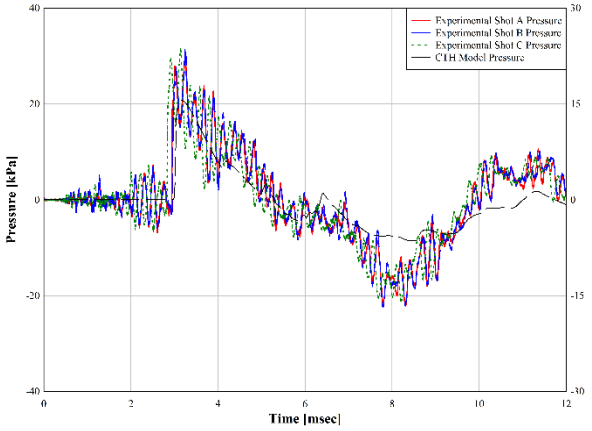

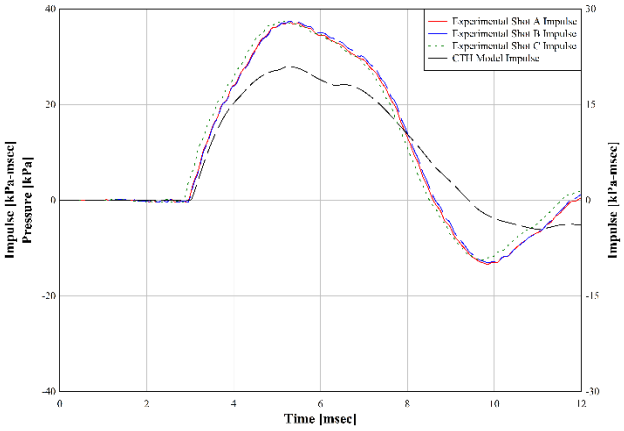

Tracer 8

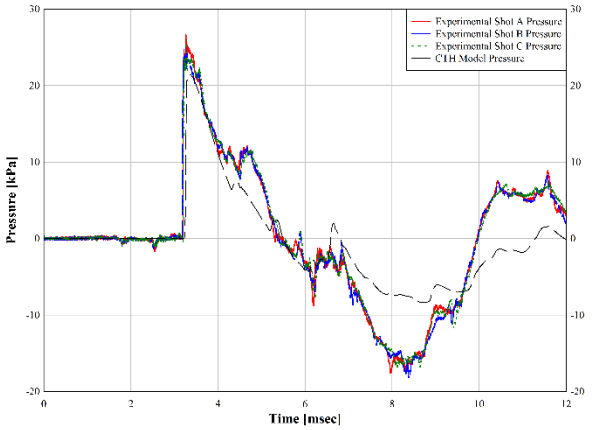

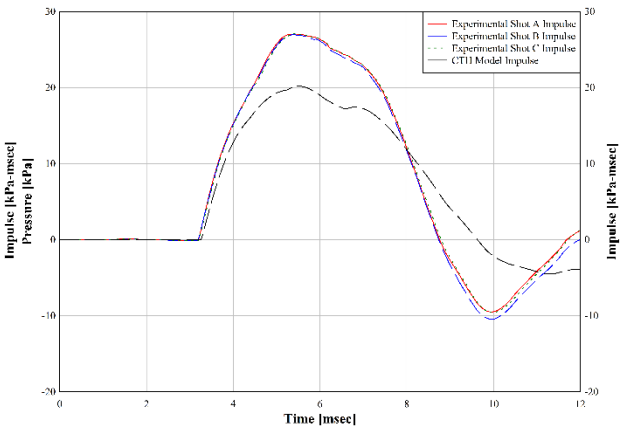

EXPERIMENT 9-FF

Tracer 1

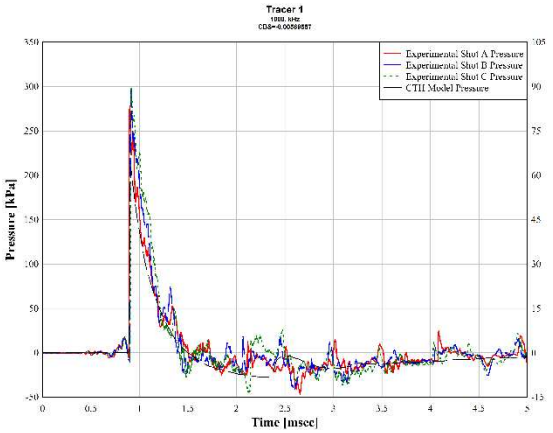

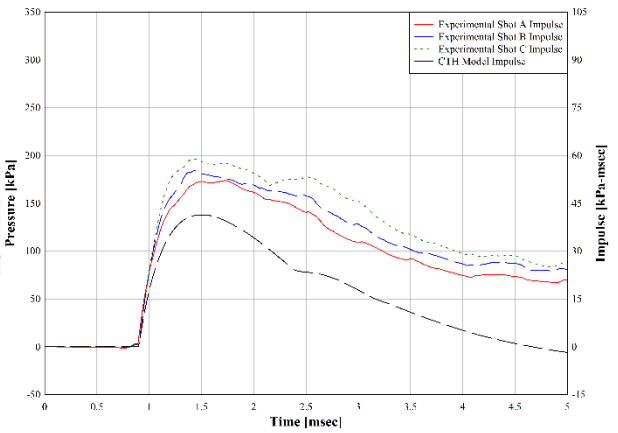

Tracer 2

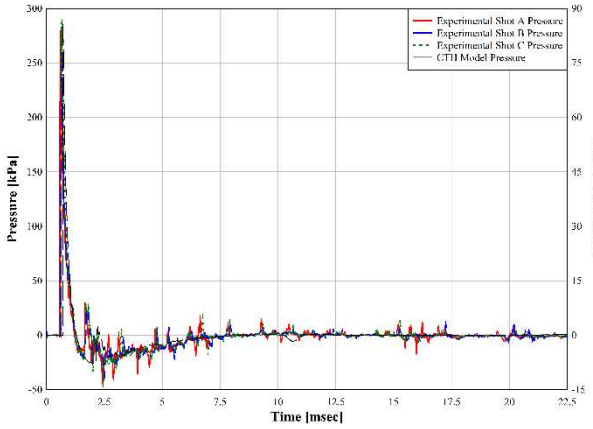

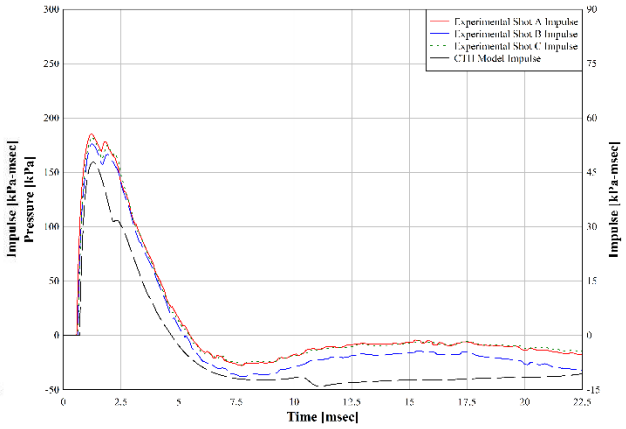

Tracer 3

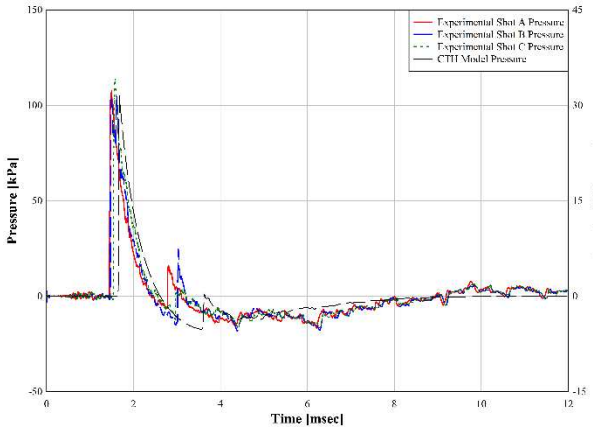

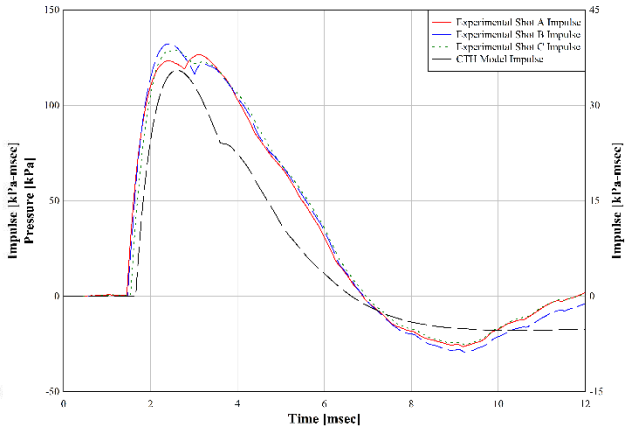

Tracer 4

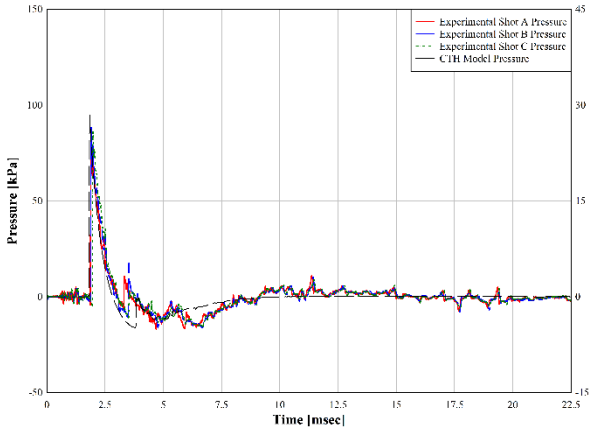

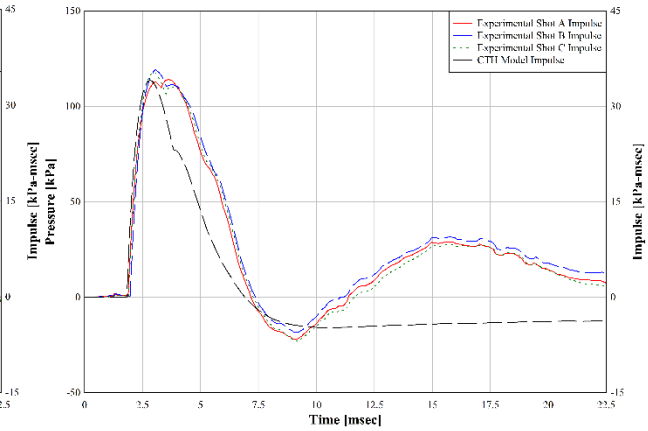

Tracer 5

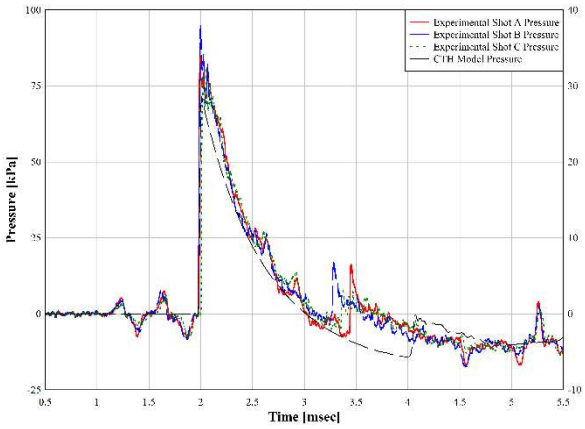

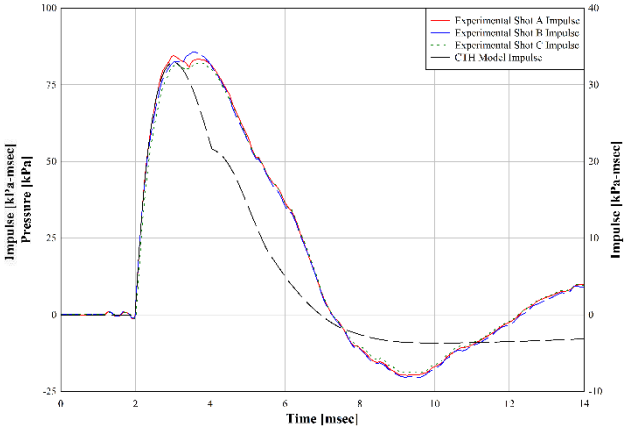

Tracer 6

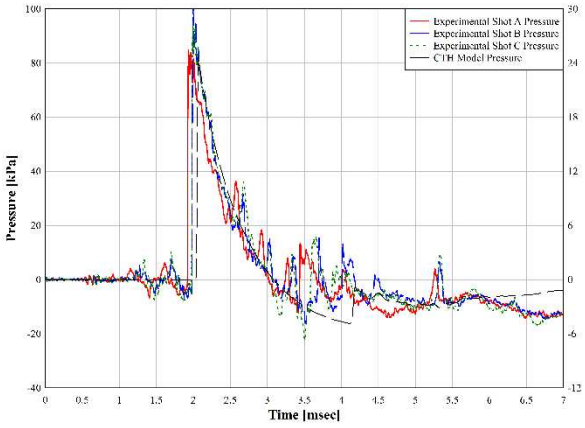

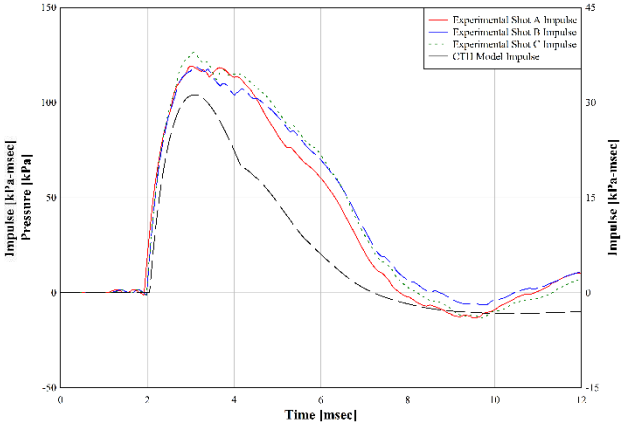

Tracer 7

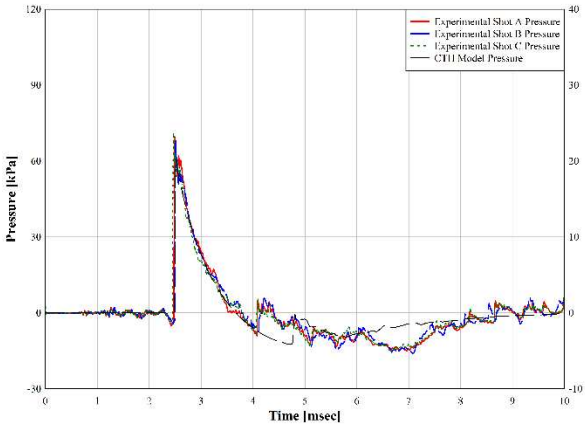

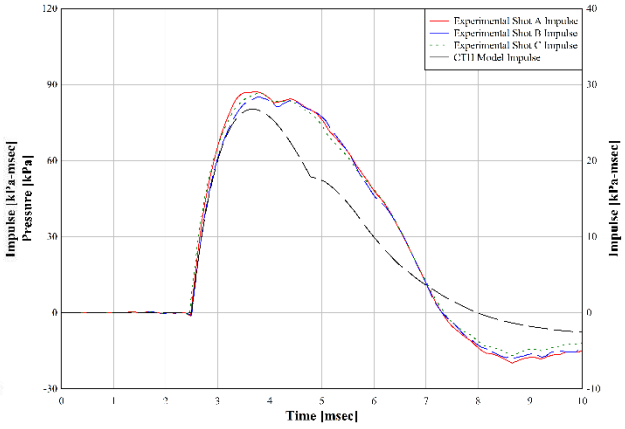

Tracer 8

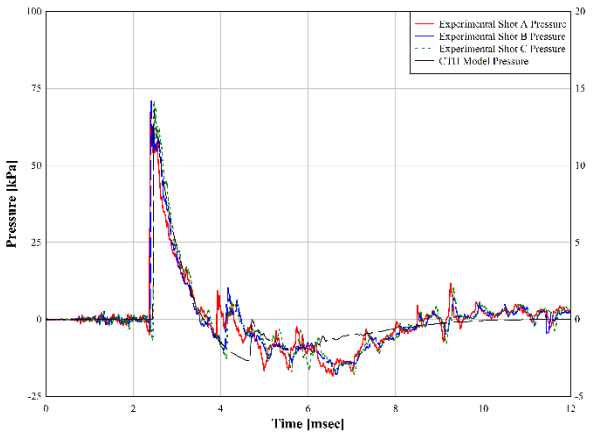

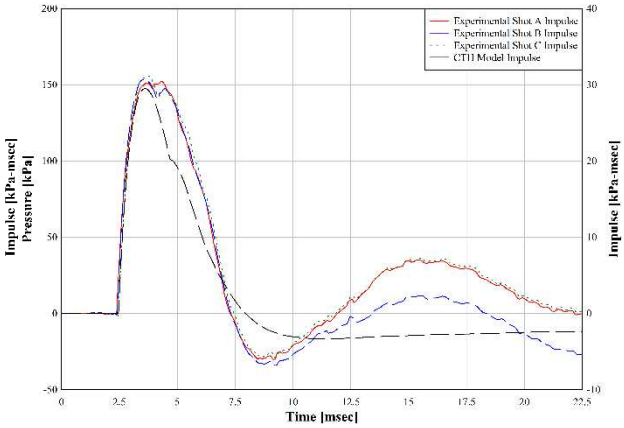

EXPERIMENT 10

Tracer 1

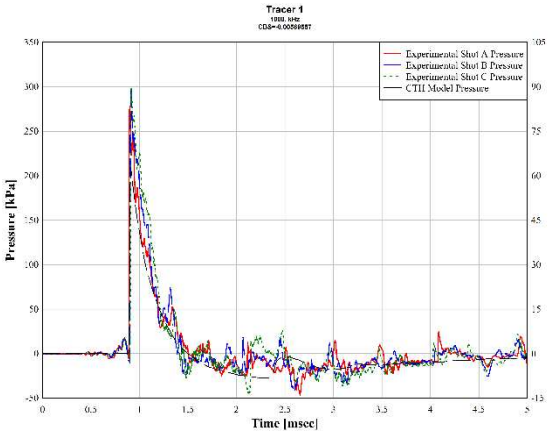

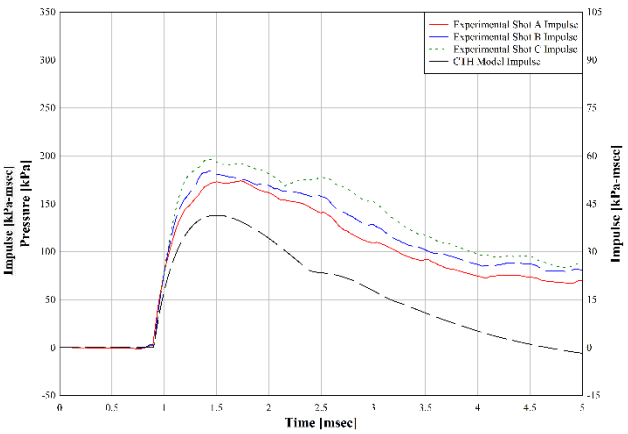

Tracer 2

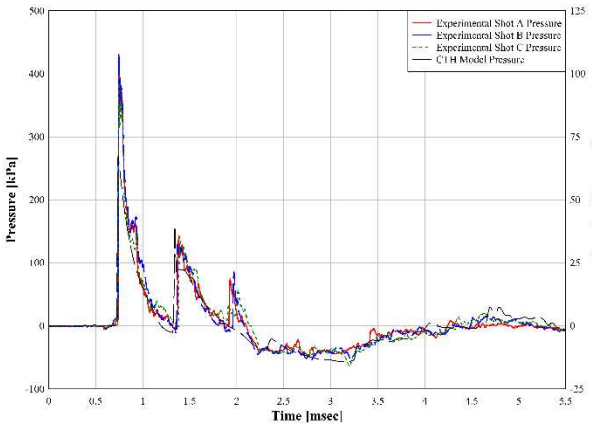

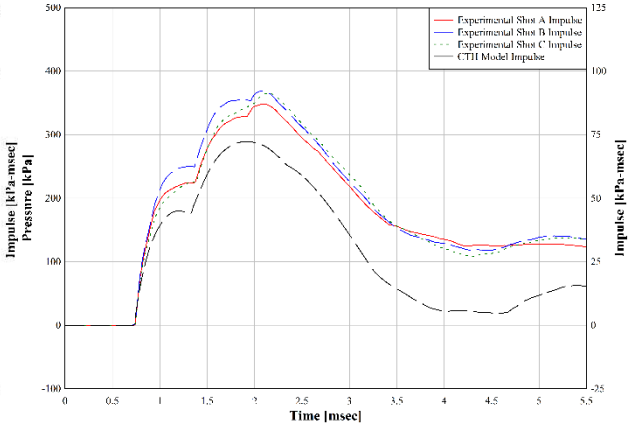

Tracer 3

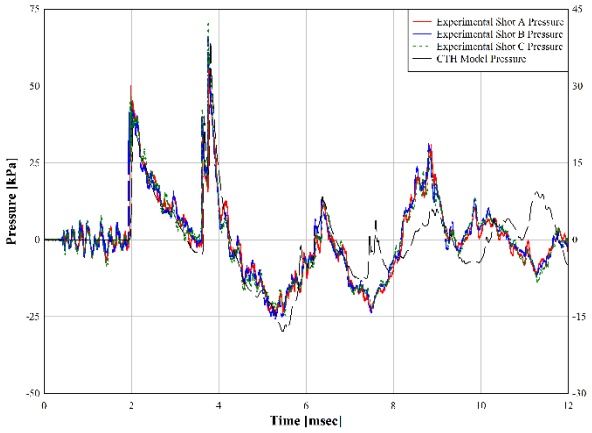

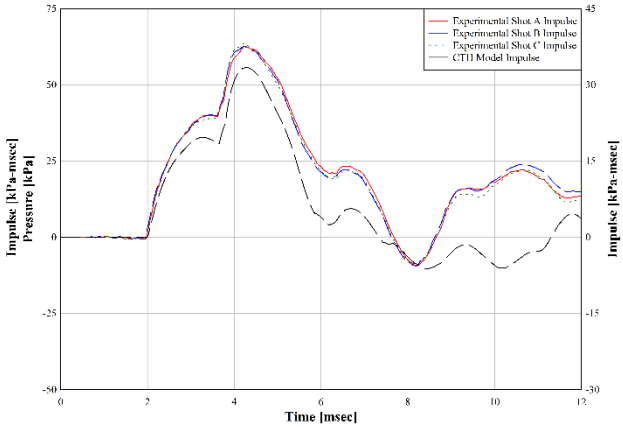

Tracer 4

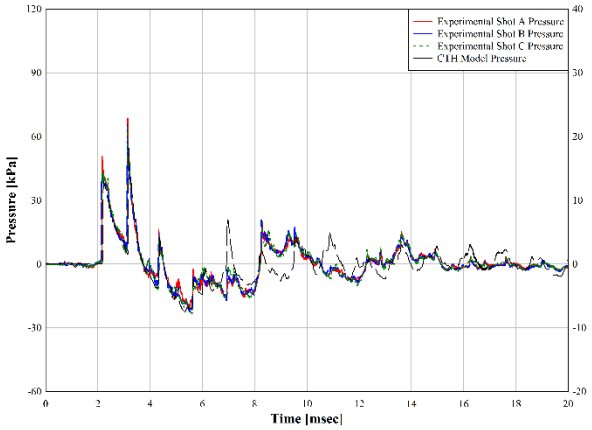

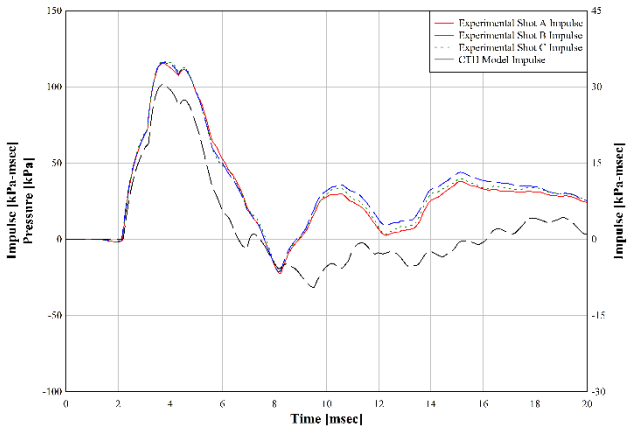

Tracer 5

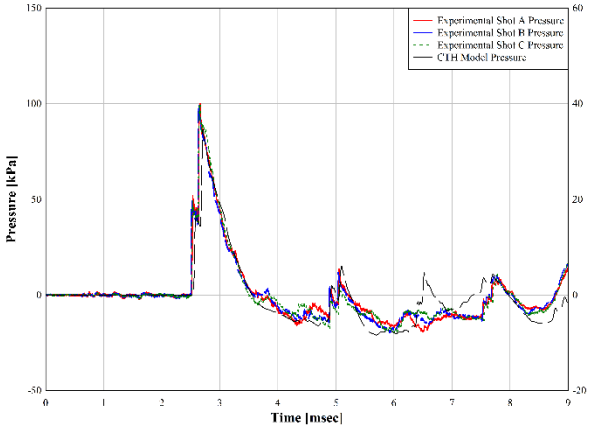

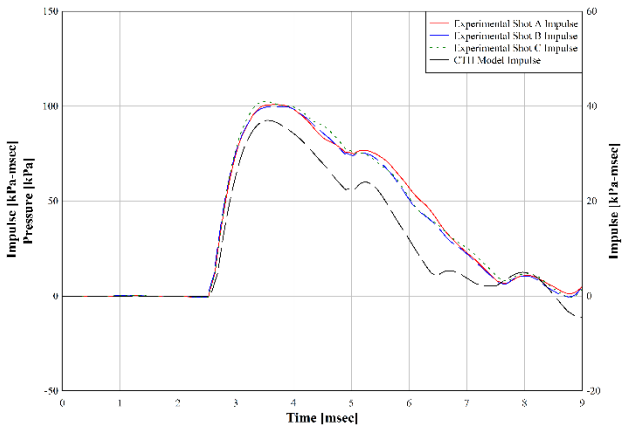

Tracer 6

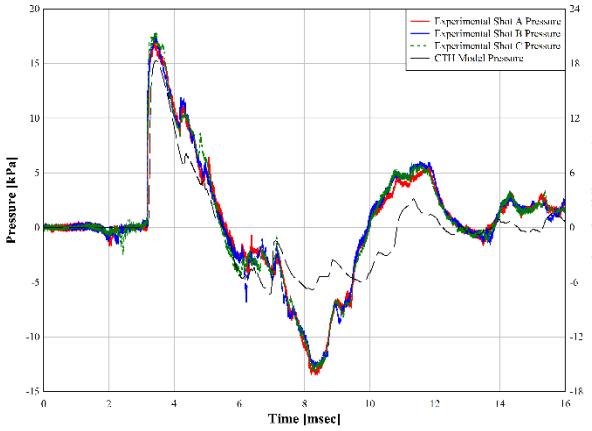

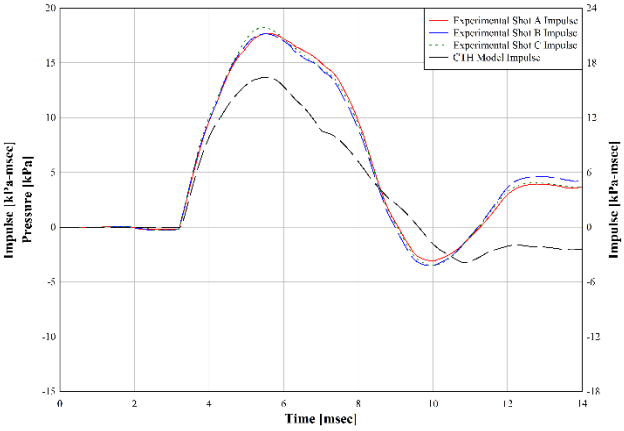

Tracer 7

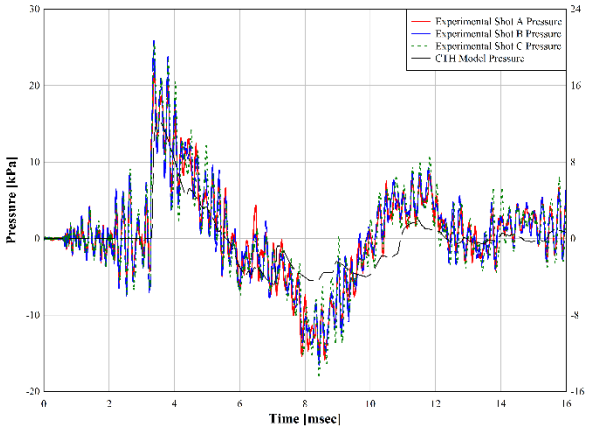

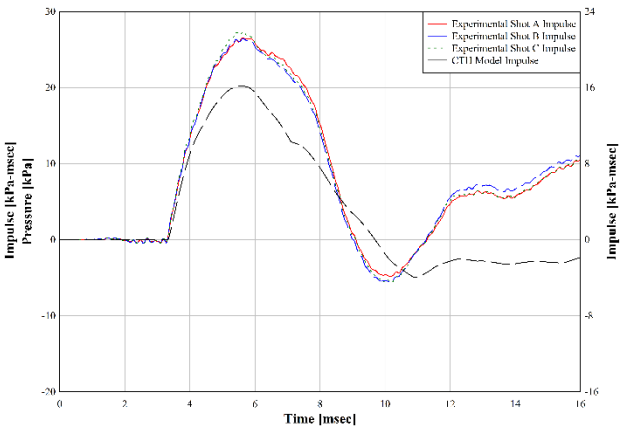

Tracer 8

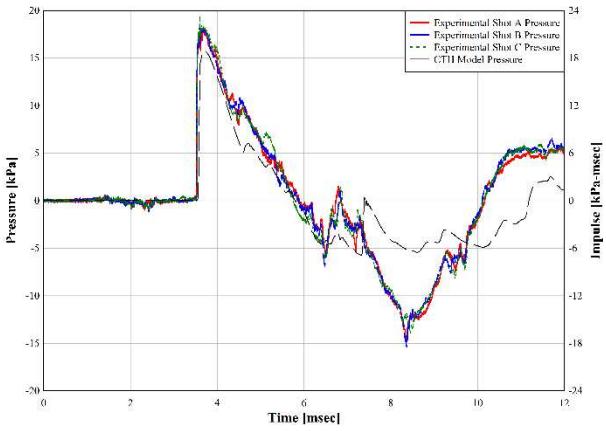

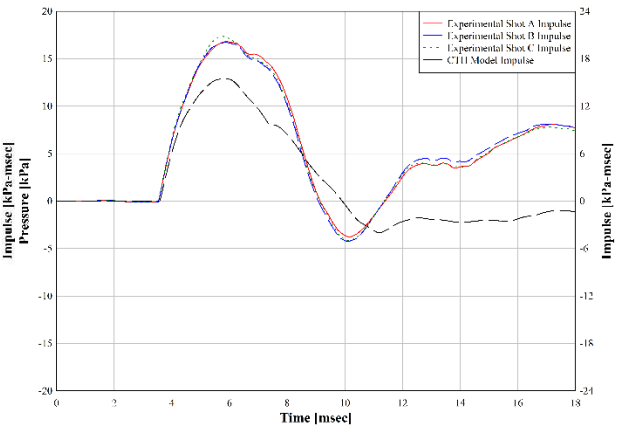

APPENDIX B: ADDITIONAL FULL-SCALE DATA

11.1 Rack and Pinion Displacement Time Histories

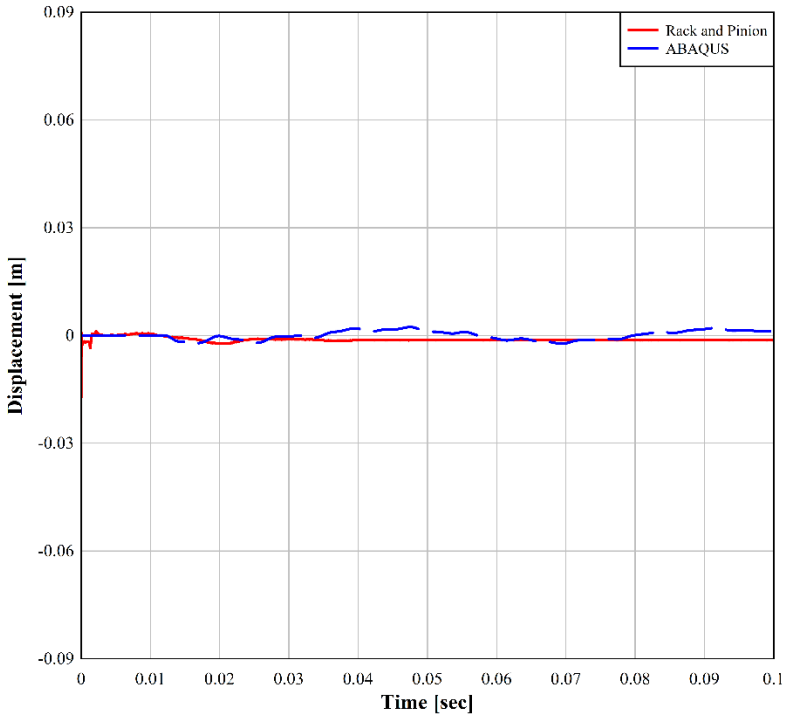

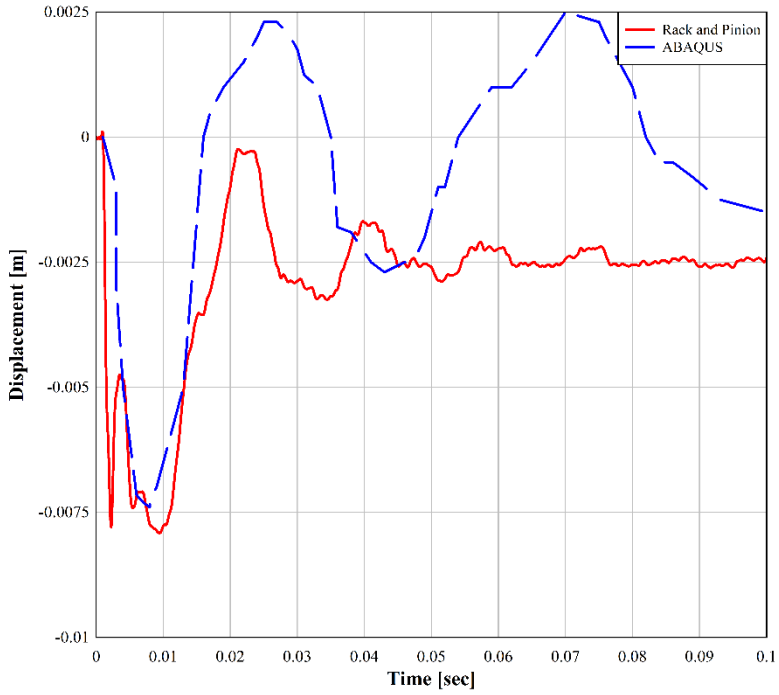

LIST OF ABBREVIATIONS

ACI- American Concrete Institute

AFRL- Air Force Research Laboratory

ANFO- Ammonium Nitrate and Fuel Oil

ANN- Artificial Neural Network

ASCE- American Society of Civil Engineers

ASCI- American Institute of Steel Construction

CBR- Chemical, biological, and radiological

CFD- Computational Fluid Dynamics

CGM- Coarse Grain Model

COV- Coefficient of Variation

DHS- Department of Homeland Security

DOA- Department of Agriculture

DOD- Department of Defense

DOE- Department of Energy

DOS- Department of State

DOT- Department of Transportation

EBW- Exploding Bridge Wire

EOS- Equation of State

ERDC- Engineering Research and Development Center- associated with USACE.

FEA- Finite Element Analysis

FEM- Finite Element Model

fps-Frames Per Second

ft/s=Feet Per Second

FRP- Fiber reinforced polymer

GA- Genetic Algorithm

HE- High Explosive

HME- Homemade Explosive

HOB- Height of Burst

IED- Improvised Explosive Device

ISC- Interagency security committee

JWL- Jones-Wilkins-Lee EOS

LE- Low Explosive

MAE- Mean Absolute Error

MCS- Monte Carlo Simulation

MDOF- Multi Degree of Freedom

MLP- Multi-Layer Perceptron

MSE- Mean Square Error

mps or m/s= Meters Per Second

OSB- Orientated Strands Board

PBIED- Person Borne Improvised Explosive Device

PDC- Protective Design Center

PDF- Probability Density Function

P_I- Probability of Injury

P-I Pressure Impulse Charts

PPE- Personal Protective Equipment

RCC- Reinforced Concrete

RGIN- Radial Gaussian

RSM- Response Surface Models

SBEDS- Single Degree of Freedom Design Spreadsheets

SDOF- Single Degree of Freedom

TBI- Traumatic Brain Injury

TNT- Trinitrotoluene

TSA- Transportation Security Administration

UFC- Unified Facilities Criteria

USACE- United States Army Corp of Engineers

VBIED-Vehicle Borne Improvised Explosive Device